Étude des processus de submersion de protections côtières par les vagues pour des états de mer complexes

Antoine Villefer

École des Ponts ParisTech

THÈSE DE DOCTORAT

de l'École des Ponts ParisTech

Study of wave overtopping processes of coastal protections in complex sea-states

Étude des processus de submersion de protections côtières par les vagues pour des états de mer complexes

École doctorale N°531, Sciences, Ingénierie et Environnement, SIE

Spécialité : Mécanique des fluides

Thèse préparée au Laboratoire d'Hydraulique Saint-Venant (École des Ponts ParisTech et EDF R&D)

Thèse soutenue publiquement le 05/12/2022, par

Antoine VILLEFER

Composition du jury:

Barbara ZANUTTIGH Prof., Univ. Bologne, DICAM (Bologne, IT)	*Rapporteur*
Fabrice ARDHUIN Dir. Rech., LOPS (Brest, FR)	*Rapporteur*
Vasiliki K. TSOUKALA Prof., NTUA (Athènes, GR)	*Examinatrice*
Stéphane ABADIE Prof. Univ., UPPA, SIAME (Anglet, FR)	*Examinateur*
Francisco J. OCAMPO TORRES Dr., CEMIE-Océano (Mexico, MX)	*Examinateur*
Hubert BRANGER Dr., IRPHE, UMR 7342 (Marseille, FR)	*Examinateur/Encadrant*
Michel BENOIT Prof., EDF R&D LNHE & LHSV (Chatou, FR)	*Directeur de thèse*
Damien VIOLEAU Prof., EDF R&D LNHE & LHSV (Chatou, FR)	*Directeur de thèse*

Thèse effectuée au sein du **Laboratoire d'Hydraulique Saint-Venant**

de l'Ecole des Ponts ParisTech et d'EDF R&D

6, quai Watier

BP 49

78401 Chatou cedex

France

Convention CIFRE EDF 2019-1257

Résumé

Près des côtes, dans des conditions de tempête, il est courant d'observer un état de mer bimodal combinant un clapot, caractérisé par des vagues courtes générées localement par le vent, et une houle, caractérisée par des vagues longues générées par des vents lointains en haute mer. Pour dimensionner les protections côtières, la méthodologie actuelle (e.g. guide EurOtop 2018) suggère d'estimer le débit de franchissements pour un état de mer bimodal à l'aide d'un seul jeu de hauteur, période et direction de vagues. Le premier objectif de cette thèse est d'étudier la croissance du clapot en présence d'une houle. Le second objectif vise à étudier les processus de submersion des protections côtières par les vagues dans des conditions d'état de mer bimodales afin d'améliorer la méthode d'estimation du débit de franchissements.

Pour répondre au premier objectif, une série d'expériences a été réalisée dans le canal-soufflerie de l'OSU Institut Pythéas à Marseille en profondeur uniforme (i.e. sans structure côtière) afin d'observer la génération du clapot en présence de vagues longues simulées mécaniquement dans la direction du vent. Différentes vitesses de vent et différents types de vagues de batteur ont été testés. Une analyse spectrale a révélé qu'à vitesse de vent constante, la fréquence pic du clapot sans houle est déplacée vers les basses fréquences en présence des vagues de batteur irrégulières.

Afin de transposer ces résultats à une échelle côtière, nous avons utilisé le modèle spectral d'états de mer TOMAWAC (Benoit et al. 1996). La précision du modèle numérique quant à la simulation d'états de mer bimodaux a été évaluée à l'aide de deux étapes de validation. La première, à l'échelle du laboratoire, visait à reproduire les résultats obtenus dans le canal-soufflerie. La seconde, à l'échelle côtière, visait à reproduire les observations relevées lors d'un événement de la campagne SHOWEX (Ardhuin et al. 2007, Zhang et al. 2009). Des développements récents permettant la modélisation de la dissipation des vagues (Ardhuin et al. 2010) et des interactions non-linéaires entre quadruplets (Gagnaire-Renou et al. 2010) ont montré de bonnes performances pour la reproduction des observations aux deux échelles.

Une seconde campagne d'expériences visait à étudier les processus de franchissements d'une digue par les vagues dans des conditions d'états de mer bimodaux générés uniquement avec le batteur. Une digue à l'échelle 1:25 avec une pente de 3:2 (H:V) a été construite dans le canal-soufflerie. Les débits de franchissements ont été mesurés pour différentes hauteurs de franc-bord, diverses conditions d'états de mer (unimodaux et bimodaux), avec deux types de revêtements : un lisse et un en enrochements. Dans les conditions testées (e.g. états de mer bimodaux), la méthodologie actuelle d'estimation du débit de franchissements est valide pour le cas de la pente lisse. Cependant, en présence d'enrochements, une faible hauteur de franc-bord entraîne une surestimation importante du débit de franchissements pour les états de mer composés d'une forte proportion de clapot. Sur la base des tendances observées avec les différents revêtements, de nouvelles formulations d'estimation des débits de franchissements sont proposées, notamment via une redéfinition

des hauteurs de franc-bord et débits adimensionnels.

Afin de compléter l'utilisation de modèles réduits dans des configurations complexes, le code multiphasique neptune_cfd (Coste et al. 2007) a été appliqué et comparé aux résultats de laboratoire pour la submersion par des états de mer bimodaux. Les débits de franchissements obtenus numériquement sont du même ordre de grandeur que les observations et reproduisent les tendances relatives à l'influence de la cambrure représentative des vagues. Cependant, une légère sous-estimation de l'énergie des vagues est relevée en pied de digue et s'ajoute à une sous-estimation systématique (d'un facteur 1.5 environ) des débits de franchissements adimensionnels.

Mots-clé:

Clapot ; Houle ; Etats de mer bimodaux ; Canal-soufflerie ; Modèles spectraux d'états de mer ; Protections côtières ; Franchissements par les vagues

Study of wave overtopping processes of coastal protections in complex sea-states

Abstract

Near the coast in stormy conditions, it is rather common to observe bimodal sea-state conditions combining short wind-waves, generated by a local wind, and a long swell, generated by far offshore winds across the open ocean. To design coastal protections, the current methodology (e.g. EurOtop 2018 manual) suggests performing the calculation of the wave overtopping rate using a single set of wave height, period, and direction although the sea-sate is bimodal. First, this thesis aims to investigate the wind-wave growth over a background swell. The second objective consists in studying the wave submersion processes of coastal protections in bimodal sea-state conditions to improve the methodology for estimating the wave overtopping rate.

As a first part of the PhD research, a series of experiments was carried out in the OSU Institut Pythéas wind-wave tunnel in Marseilles (France) to study wind-wave growth over following mechanically-generated long-waves in uniform water depth (i.e. without any coastal structure). Various wind speeds and wave conditions have been tested. Based on spectral analysis, it was found that, at a constant wind speed, the wind-wave peak frequency without swell was shifted towards lower frequencies in the presence of a following irregular swell.

To upscale this laboratory results at a coastal scale, the 3rd generation wave model TOMAWAC (Benoit et al. 1996) was used. To assess the reliability of the numerical model to simulate bimodal sea-states, two validation steps were performed. The first one, at laboratory scale, aimed at reproducing the previous experiments in the wind-wave tunnel. The second one was performed at coastal scale against in-situ results from an event of the SHOWEX campaign (Ardhuin et al. 2007, Zhang et al. 2009). The recent parameterization for wave dissipation (Ardhuin et al. 2010) and nonlinear 4-wave interactions (Gagnaire-Renou et al. 2010) showed good performances in reproducing the observations at both scales.

Another series of experiments was conducted to study the wave overtopping rate in bimodal sea-sates conditions. For that purpose, a breakwater with a slope 3:2 (H:V) was built in the wind-wave tank at a scale 1:25. The wave overtopping rate was measured for varying crest freeboards with both unimodal and bimodal wave conditions generated with the wave-make. Two types of slope surfaces were tested: a smooth one and a rock-armoured one. For the smooth slope, the current methodology to calculate the wave overtopping is rather accurate in bimodal sea-state conditions. However, with the rock-armoured slope, it was found that a low crest freeboard causes an important overestimation of the wave overtopping rate for sea states with a high proportion of wind waves. Based on the observed trends with both the smooth and the slope armoured surfaces in bimodal sea-state conditions, new formulations for the non-dimensional wave overtopping rate and crest freeboard are proposed.

To complement the use of physical models, the multiphase code neptune_cfd (Coste et al. 2007) was applied and compared with the laboratory results for the study of coastal wave overtopping

processes in bimodal sea-state conditions. The simulated wave overtopping rates have the correct order of magnitude of the measured ones, together with similar trends regarding the effect of the sea-state steepness as observed during the experiments. However, a slight underestimation of the energy at the toe of the breakwater was observed, together with a systematic underestimation (by a factor of about 1.5) of the relative wave overtopping rates.

Keywords:

Wind waves ; Swell ; Bimodal sea state ; Wind-wave tunnel ; Spectral wave models ; Coastal protections ; Wave overtopping

Remerciements

Je souhaite ici remercier les personnes m'ayant permis de réaliser cette thèse dans les meilleures conditions. Mes premiers remerciements vont aux membres du jury de thèse qui ont animé la soutenance par leurs questions et commentaires. Merci aux rapporteurs Pr. Barbara Zanuttigh et Dr. Fabrice Ardhuin pour leur lecture attentive du manuscrit ayant permis son amélioration et d'entrevoir de nouvelles perspectives aux présents travaux. Merci à Pr. Vasiliki K. Tsoukala, Pr. Stéphane Abadie et Dr. Paco (Francisco J.) Ocampo Torres d'avoir accepté d'examiner ma thèse. En particulier, merci une nouvelle fois à Stéphane et Paco d'avoir veillé au bon déroulement de la thèse par leur participation au comité de suivi dès la fin de ma première année de thèse.

Viennent ensuite les remerciements aux personnes m'ayant accordé leur confiance et dispensé la plus complète des formations qu'un jeune ingénieur-chercheur puisse espérer : les encadrants et contributeurs. Merci aux directeurs Michel et Damien, ces trois années à vos côtés ont été une formidable école. Vous resterez pour moi des modèles de chercheurs et d'encadrants. Merci Maria et Jeff pour votre disponibilité et votre accessibilité pour répondre à mes nombreuses questions, notamment à propos de Tomawac et Code_Saturne. Merci Hubert et Christopher de m'avoir formé aux manips dans la soufflerie mais aussi pour avoir été mes premiers amis à Marseille, autant dans l'effort pour trier et laver des cailloux en plein épisode de Mistral en novembre que dans le réconfort pour observer les vagues depuis un voilier. Merci William pour ton aide indispensable dans la réalisation des simulations neptune_cfd ayant permis la rédaction du chapitre 6. Merci Vito de mettre en avant les travaux des doctorants dans le projet MOISE au sein de EDF R&D.

Merci à tous les collègues qui, par l'animation de la vie de laboratoire et par leurs conseils, ont largement contribué à la réussite de cette thèse : notamment Fatna, Hanna, Jiaze, Teddy, Élie, Bastien, Elisa, Guillaume, Jean-Paul, Marc, Aurélien, Fabien, Sunil, Prokopis. Merci à Christophe d'avoir appuyé ma candidature pour cette thèse. Merci à Paul et Rémi pour vos encouragements à me lancer dans cette aventure de 3 ans ainsi que pour nos nombreuses discussions et aventures partagées. Merci à Thomas, Maxime, Alba, Marie et aux Toms pour les joyeux moments de vie commune en colocation. Enfin, merci à mes proches pour leur soutien et leurs encouragements.

Contents

List of Figures

List of Tables

Nomenclature

Abbreviations

ASIS Air–Sea Interaction Spar

DIA Discrete Interaction Approximation

GQM Gaussian Quadrature Method

HF High-Frequency

JONSWAP JOint North Sea WAve Project

MWL Mean Water Level

NPP Nuclear Power Plant

OSU Observatoire des Sciences de l'Univers

PIV Particle Image Velocimetry

SHOWEX SHOaling Waves EXperiment

SST Sea-Surface Temperature

TOMAWAC TELEMAC-based Operational Model Addressing Wave Action Computation

VDW After van der Westhuysen et al. (2007) wave dissipation model

Roman symbols

a Wave amplitude ..... (m)

a_n Fourier coefficients

B Saturation level

B_r Saturation threshold

$\boldsymbol{C}$ Wave phase celerity ..... (m/s)

$\boldsymbol{C}_g$ Group velocity ..... (m/s)

q Wave overtopping rates ..... (m^2/s or l/s/m)

R_c	Freeboard	(m)
D	Angular distribution function	(rad^{-1})
E	Wave variance density	(m^2/Hz)
f	Wave frequency	(Hz)
f_p	Spectral wave peak frequency	(Hz)
f_p^*	Non-dimensional spectral wave peak frequency	
g	Gravitational acceleration	($\mathrm{m/s}^2$)
h	Water depth	(m)
H_s	Significant wave height	(m)
H_{m_0}	Significant wave height from the spectral zero-order momentum	(m)
k	Wavenumber	(m^{-1})
m_0	Spectral zero-order momentum	(m)
m_0^*	Non-dimensional spectral zero-order momentum	
N	Wave action density	(m^2)
S	Source/sink term (Q in chapter 4)	(m^2)
S_{ds}	Dissipation through whitecapping sink term	(m^2)
S_{in}	Wind energy input source term	(m^2)
S_{nl}	Nonlinear 4-wave interactions source/sink term	(m^2)
s_m	Representative wave steepness	
t	Time	(s)
T_m	Representative wave period	(s)
$u_\star$	Friction velocity at the air/sea interface	(m/s)
U_{10}	Wind velocity at 10 m above MWL	(m/s)
X	Fetch	(m)
X^*	Non-dimensional fetch	
$\boldsymbol{U}_c$	Current velocity	(m/s)
z_0	Aerodynamic roughness	(m)

Greek symbols

α	Breakwater slope angle

α_{p}	Phillips constant
α_c	Charnock constant
β	Miles' parameter
γ	Peak enhancement factor
η	Free-surface elevation ..... (m)
θ	Wave direction ..... (rad or °)
θ_m	Mean wave direction ..... (rad or °)
θ_w	Local wind direction ..... (rad or °)
λ	Wavelength ..... (m)
λ_m	Representative wavelength ..... (m)
λ_p	Spectral wave peak wavelength ..... (m)
ξ	Breaker parameter
σ	Mean angular spread ..... (rad or °)
τ_s	Surface stress ..... ($\mathrm{kg/m/s^2}$)
τ_w	Wave stress ..... ($\mathrm{kg/m/s^2}$)
ϕ	Wave velocity potential ..... ($\mathrm{m^2/s}$)
ψ	Wave phase ..... (rad or °)
ω	Wave angular frequency ..... (rad/s)
χ	Wave age

Chapter 1

Introduction

Pour protéger les zones côtières contre l'aléa de submersion par les vagues en conditions de tempête, des protections côtières sont nécessaires. Celles-ci sont, en grande partie, dimensionnées par rapport à un débit admissible de franchissements par les vagues. EDF a recours très régulièrement à des formules de dimensionnement d'ouvrages de protection contre le franchissement des vagues, dans le cadre de la sûreté des centrales nucléaires contre le risque d'inondations externes. Cependant, l'application de ces formules de dimensionnement à un état de mer bimodal combinant une houle, vagues longues provenant du large, et un clapot, vagues courtes formées par un vent local, pose question. En premier lieu, est-ce que le clapot est généré de la même manière avec et sans houle ? Dans un second temps, est-ce que les caractéristiques moyennes de cet état de mer complexe (i.e. une hauteur et une période caractéristiques) suffisent pour estimer le débit de franchissement ? Ces deux questions composent les deux volets de la thèse : la caractérisation de l'état de mer combinant houle et clapot et l'étude des processus de submersion des protections côtières par les vagues, pour un état de mer bimodal. Chacun des volets est abordé à l'aide de deux approches d'étude complémentaires : une modélisation expérimentale à échelle réduite et un modèle numérique adpaté à la problématique considérée.

1.1 General context

With 40% the World's population living within 100 km of the coastline (2017 UN Ocean Conference), mankind significantly relies on its interactions with oceans and seas. One reason for these interactions consist in the use of the resources available in the maritime environment: not only the sea life feeds mankind but also our machines through oil and gas deposits. More recently, a growing interest in producing electricity at sea arose with the development of marine energies such as offshore wind turbines. A second source of interactions is the worldwide transportation network connecting continents that permitted the development of a global economy. Ports and harbours, located at the boundaries of the marine domain, serve as platforms to connect land and maritime routes, thus generating a considerable human activity easily verified by the fact that three of the five largest cities of the World (Tokyo, Shanghai and São Paulo) are coastal (UN 2018). More recently, industry developed an interest for coastal locations to take advantage of the considerable source of water at hand. It is the case of coastal nuclear power plants (NPP) using sea water as a cooling fluid necessary to control the nuclear reaction. However, oceans and seas can cause great damage to coastal areas through the actions of storms, waves or tsunamis. Storms such as Katrina (2005, Gulf of Mexico and east-coast of the US, 1 836 deaths) or Xynthia (2010, Europe, 65 deaths) caused important human and material losses in coastal zones due to the combination of very strong winds and very severe sea-states (11 m high waves recorded offshore during Katrina). In particular, the recent 2011 Tōhoku earthquake and tsunami, that caused the Fukushima nuclear disaster, is a meaningful example serving as a reminder of how great is the danger for mankind thus how important is the protection of such facilities against natural hazards.

The present thesis focuses on the hazards in relation with ocean gravity waves generated under wind action: tsunamis will not be considered here. In order to protect coastal areas against flooding due to such waves, coastal infrastructures are provided with coastal protections such as dikes or breakwaters. The scientific disciplines involved in the design of such structures are a combination of physical oceanography, in order to characterize the sea-state conditions, and coastal engineering to estimate the protections' dimensions considering the sea conditions. Coastal engineers aim at finding the good balance between safety on the one hand and environmental and economical concerns on the other hand.

First research works dedicated to wave forecast started about 100 years ago in Casablanca, Morocco with the Hydrographic service of the French Navy (Montagne, 1922). The wave prediction techniques then experienced a rapid development that was neither motivated by the beauty of the physical object nor by surfers dreaming for the perfect conditions but by the needs of landing operation during the Second World War (Janssen, 2004). One of the first wave prediction models was based on the use of empirical growth curves yielding the wave significant height and period as a function of wind speed and fetch (Bretschneider, 1952; Sverdrup and Munk, 1944a,b).

Then, Pierson and James (1955) provided the first wave observations based on a spectral analysis. The new concept of wave spectrum permitted to sort the apparent chaos of ocean sea-states as a sum of wave harmonics with different energy levels together with the hypothesis that the wave phases follow a uniform random distribution. These concepts paved the way for the first phase-averaged spectral wave models based on the spectral energy balance equation (Gelci et al., 1957).

However, the spectral energy balance equation, that efficiently handles wave propagation on the basis of the linear theory, greatly relies on source and sink terms to model the physical processes responsible for wave generation, dissipation and resonant interactions between waves. Wave generation processes found a theoretical basis with the distinct works of Miles (1957) and Phillips (1957). Few years later, Hasselmann (1962) followed by Zakharov (1968) derived a theoretical formulation of the nonlinear 4-wave interactions. However, the inclusion of both wave generation and 4-wave interactions theories in operational spectral wave models was not straightforward due to the computational cost and the complexity of the theories.

The development of the Discrete Interaction Approximation (DIA) by Hasselmann et al. (1985) permitted to include an approximated computation of the 4-wave interactions term in spectral wave models triggering the 3rd generation (3G) wave models still in use nowadays. Following Miles (1957) theoretical basis, wave generation source terms were developed with the works of Snyder. et al. (1981) then Janssen (1991). The dissipation sink terms, gathering different physical processes from wave breaking (e.g. whitecapping) to bottom friction are the most empirical terms. Yet, more physical description of wave dissipation and breaking are available but still need to be adapted to spectral wave models (Babanin, 2011). The dissipation processes related to whitecapping used in 3G wave models were first empirically formulated by Komen et al. (1984). Following the works of Alves and Banner (2003) and van der Westhuysen et al. (2007) on a dissipation model partly based on a saturation threshold, the complexity of the physical process was further included in a new formulation developed by Ardhuin et al. (2010). It was still considered as the least understood part of the physics relevant to wave modelling in a state-of-the-art of the discipline performed by the WISE group (Cavaleri et al., 2007). This short story of wave modelling tells the origin of the wave models in use nowadays: WAM (WAMDI Group, 1988), WAVEWATCH III (Tolman and Chalikov, 1996), SWAN (Booij et al., 1999) and TOMAWAC (Benoit et al., 1996). Among them, SWAN and TOMAWAC models resulted from a necessary adaptation for coastal applications.

In ancient times, the only areas that needed protection from the waves were harbours in order to offer calm waters for mooring ships. The typical harbours locations were the areas offering natural protections, such as the Piraeus Port in Athens (Greece) or Alexandria's Harbour (Egypt). However, in coastal areas where natural protections are not sufficient or nonexistent, artificial protections are built. Once the sea-state conditions can be determined with a sufficient accuracy near a coastal area to be protected, the coastal engineering work begins.

Coastal protections are designed considering the required level of safety of the infrastructure (or area) to protect and the most extreme storms that can occur at the selected location based on historical records (e.g. using the so-called return period of such events). The construction of such structures requires a considerable amount of resources. Hence, it is associated to a considerable cost in addition to a significant impact on the environment. Then, the challenge of designing coastal protections relies on finding the good balance in order to maximize the safety level provided by the protections together with a minimal impact on the environment and at a minimal cost. To solve this optimisation problem, coastal engineering largely resort to the use of laboratory experiments using scale models. In addition, the use of numerical models has recently taken an active part in this optimisation process. Both techniques permit to estimate the stability of the structure and wave overtopping rate as a function of a sea-state properties and the protection dimensions. References

such as EurOtop (Pullen et al., 2007; Van der Meer et al., 2018) and The Rock Manual (CIRIA, 2007) gather the knowledge acquired from these experiments and provide recommendations for the design of coastal protections. As regards the impact of waves on coastal protections, the focus of the present thesis is the wave overtopping process: issues related to the stability of coastal structures are barely addressed. Overall, the general methodology going from wave observations and predictions to the use of references gathering the empirical knowledge on the wave overtopping process permits to design quite optimal coastal protections.

1.2 Industrial context

EDF (Électricité De France) constantly resorts to the use of reference empirical formula for the design of the coastal protections built to guaranty the safety of coastal NPP. Five of the NPP run by EDF are located in coastal areas (Gravelines, Paluel, Penly, Flamanville) or estuaries (le Blayais). The protections of these NPP, designed using state-of-the-art recommendations, are regularly challenged by the French nuclear safety authority (ASN) in order to verify, together with EDF, the reliability of the plants. The MOISE project, hosted by EDF R&D, aims at verifying improving the protections of EDF's NPP against floods caused by natural marine hazards. The present thesis has been carried out within the latter project. The financial support of this PhD research program was provided by the French ANRT (Association Nationale de la Recherche et de la Technologie) with CIFRE Grant 2019-1257.

1.3 Problem statement

The occurrence of bimodal sea-state conditions combining two wave systems, namely swell and wind-waves, is rather common near the coast (Thompson et al., 2018). Here, swell and wind-waves systems are characterized by their typical period T: $T > 8$ s for swell (long-waves) and $T < 8$ s for wind-waves (short waves). In essence, swell is a former wind-sea, generated across the open ocean, with wavelength increasing by propagating over long distances under the action of wave-wave interactions and wind forcing. Wind-waves are short waves, somehow younger than the swell, generated by a local wind. Wind-waves are mostly observed when the wind blows whereas swell, appreciated by surfers, is commonly observed in absence of wind.

Based on wind-wave tunnel experiments, several researchers (e.g. Donelan, 1987) observed a significant reduction in wind-wave growth when long monochromatic paddle-waves are added to the system. The various interpretations of the phenomenon relate to each of the physical processes impacting wave propagation:

- Modified wind-wave growth: the presence of paddle-waves creates a sheltering effect reducing the energy available for wind-wave generation,
- Enhanced dissipation: wind-wave dissipation increases under the action of the orbital velocities at the crest of the paddle-waves,
- Detuned nonlinear 4-wave interactions due to the presence of paddle-waves.

These interpretations suggest that the phenomenon could have consequences on bimodal sea-state conditions at coastal or ocean scale. However, the extension of the above laboratory results to real ocean waves with the study of wind-wave growth over swell is not straightforward. On the one hand, the ratio of the swell phase velocity over the wind velocity (i.e. the wave age), which is more than 1 at ocean scale, is usually under 0.2 for paddle-waves in wind-wave tunnels. On the other hand, laboratory long paddle-waves are usually much steeper than common ocean swell. Hence, the extent at which the wind-wave reduction phenomenon observed in laboratory with long paddle-waves can occur at coastal scale with swell remains an open question.

3G wave models have proved their robustness in predicting significant wave heights and representative periods of the sea-states around the globe and in coastal areas. However, their performances regarding the accurate estimation of the spectral and angular distributions of wave energy are more variable. In particular, the simulation of bimodal spectra was recently improved with developments regarding the dissipation and the 4-wave interaction terms (Ardhuin et al., 2010; Gagnaire-Renou et al., 2010). Yet, these recent developments need to be combined in a single wave model and to follow a validation process for the simulation of bimodal spectra.

The recommendations given in reference manuals regarding the design of coastal protections cover a vast range of configurations. The wave overtopping rates are estimated for various breakwater heights, slopes, either with a smooth or armoured-surface, for waves with various incident angles, etc. Yet, most empirical formulas developed in the manuals have been obtained from laboratory experiments exclusively using unimodal sea-state conditions (i.e. either swell only or wind-waves only), but rarely both. Although bimodal sea-state conditions combine two wave systems with distinct heights and periods, the reference formulas estimate the wave overtopping rate as a function of a single wave height, period and direction. Hence, it is necessary to assess the validity of the use of a single wave height, period and direction to estimate the wave overtopping rate in such sea-state conditions.

1.4 Brief review of current knowledge and practice

The wind-wave reduction occurring in wind-wave tunnels in the presence of paddle-waves was further investigated numerically with SWAN by Holthuijsen et al. (2000a) and Booij et al. (2001). They developed a parameterization of Komen et al. (1984) source term in order to account for the enhanced wind-wave dissipation due to the background paddle-waves. However, their parameterization was only used within the SWAN model and lacks of validation. Benetazzo et al. (2019) further investigated the phenomenon in a wind-tunnel with irregular paddle-waves instead of monochromatic (i.e. regular) paddle-waves. They noticed a similar wind-wave growth reduction as Donelan (1987) observed. Shabani et al. (2022), based on similar experiments as Donelan (1987), further argued that the wind-wave growth reduction is due to enhanced wind-wave dissipation at the paddle-wave crest.

van der Westhuysen et al. (2007) and Ardhuin et al. (2010) successively showed that saturation based formulations, to account for wave dissipation in deep water, are more adapted for the simulation of bimodal sea-states with 3G wave models. The development of the Gaussian Quadrature Method (GQM) by Benoit (2005, 2006) and Gagnaire-Renou et al. (2010) improved the simulation

of the wind-wave directional properties during the generation process. The performances of GQM were very recently depicted by Beyramzadeh and Siadatmousavi (2022) by hindcasting recent hurricanes in the Gulf of Mexico. It was shown that the medium resolution setting for GQM have comparable performances as a reference quasi-exact method (WRT), for a computational time 10 times lower.

The wave overtopping rate in the presence of bimodal sea-state conditions has been recently investigated by Orimoloye et al. (2021). They found that the wave overtopping increases with an increasing swell proportion in the bimodal sea-state energy. They introduced a parameterization of the wave overtopping rate estimation (based on EurOtop scaling method) as a function of the swell energy proportion in the total sea state energy and the breakwater slope. However, their recent parameterization lacks of validation. For instance, it has only been tested on smooth slope surfaces: the influence of an armoured surface is still unknown. Furthermore, the definition of a swell proportion neglects the arbitrary difference between swell and wind-waves based on their peak periods: for instance, a swell with a 20 s or a 10 s peak period might not have the same influence on wave overtopping in the presence of wind-waves.

1.5 Objectives

The objectives of the present thesis are separated in two themes:

- Characterization of the bimodal sea-states,
- Study of wave overtopping.

The first theme consists in the study of bimodal wave spectra both experimentally in OSU Institut Pythéas wind-wave tank in Marseilles (France) and numerically through the use of TOMAWAC, a 3G wave model developed by EDF R&D. In order to study the influence of long paddle-waves on wind-wave growth, a series of experiments was carried out in the wave tunnel with the purpose to confirm the previous findings and to further investigate the interactions within bimodal sea-states. Both the influence of monochromatic and irregular paddle-waves were studied.

Then, in order to assess the performances of TOMAWAC for the simulation of bimodal sea-state conditions, two validation cases were identified. The first one consists in the numerical simulation of the above laboratory experiments. The controlled conditions of the laboratory are favorable to a quantitative study of the wave model performances. The second case considers an event of the SHOWEX campaign (Ardhuin et al., 2007) illustrating wind-wave growth in the presence of swell in a coastal area. The final objective in the use of the wave model was to study the influence of swell on wind-wave growth in diverse conditions (i.e. various swell steepnesses, shallow vs deep water conditions, various relative angles between swell and wind directions, etc.) in a generic coastal domain.

As the previous one, the second theme combines laboratory experiments and numerical simulations. A series of experiments was carried out to characterize wave overtopping over a generic breakwater profile considering bimodal sea-state conditions. In the interest of modelling a breakwater with properties as close as possible from the reality, the wave overtopping rates were measured not only

with a smooth slope but also with a rock-armoured slope. The objective of these experiments was to verify the wave overtopping formulas currently in use and to further adapt them to bimodal sea-state conditions. Since laboratory experiments are rather expensive and time-consuming, simulations with a two-phase Navier-Stokes (NS) solver model were performed in order to verify its ability to reproduce these experiments and to keep on improving the wave overtopping formulas with advanced numerical tools.

1.6 Outline of the thesis

Chapters 3, 4 and 5 are articles either published by or submitted to international journals.

- Chapter 2 introduces the general methodology leading to the design of coastal protections. This methodology starts with the sea-state observation techniques that resulted in the first wave prediction models. The improvements of the theoretical ground about wave propagation and interactions with the atmosphere paved the way to the development of several generations of wave models up to the 3G wave models still in use today. The sea-state properties yielded by the wave models are then used in empirical formulas permitting the estimation of the corresponding wave overtopping rate for the design of coastal protections.

- Chapter 3 presents the series of experiments carried out in the OSU Institut Pythéas wind-wave tunnel with the objective to characterize the influence of long paddle-waves on wind-wave growth.

- Chapter 4 deals with TOMAWAC validation for the simulation of bimodal sea-state conditions. The wave model performances were assessed both at laboratory and coastal scales. The satisfying conclusions about the performances permitted to perform a series of numerical experiments using a generic coastal domain to investigate the influence of swell steepness on wind-wave growth.

- Chapter 5 describes the second series of experiments performed in the same wave tank on the wave submersion process over a breakwater model with bimodal sea-state conditions. The results with the rock-armoured breakwater challenge the estimations according to the reference wave overtopping formula. Two methods are suggested to improve the wave overtopping rate predictions.

- Chapter 6 presents the performances of a two-phase code based on NS equations to reproduce wave overtopping observed during the series of experiments described in Chapter 5.

- Chapter 7 summarizes the main findings of this thesis, and discuss a series of proposals for future research.

1.7 Scientific productions during the thesis

In the course of this thesis, 3 journal articles were produced:

- A. Villefer, M. Benoit, D. Violeau, C. Luneau, and H. Branger. Influence of following, regular, and irregular long-waves on wind-wave growth with fetch: an experimental study. *Journal of Physical Oceanography*, 51(11):3435 – 3448, 2021.

- A. Villefer, M. Benoit, D. Violeau, M. Teles. Spectral wave modelling of bimodal sea states at laboratory and coastal scales. *Ocean Modelling*, 183, 102182, 2023.

- A. Villefer, M. Benoit, D. Violeau, M. Teles, and C. Luneau. Wave overtopping of smooth and rock-armoured breakwaters in bimodal sea state conditions. *Coastal Engineering*, submitted, 2022.

The results were presented at 2 international conferences leading to 2 conference papers:

- A. Villefer, M. Benoit, D. Violeau, H. Branger, M. Teles and C. Luneau. Interaction of Short Wind Waves and Swell: An Experimental and Numerical study. In *Proceedings of the 39th IAHR World Congress (IAHR'2022), 19–24 June, Granada (ESP)*, 2022.
  This article received the First Prize of the John F. Kennedy Student Paper Competition, which recognises conference papers from undergraduate and postgraduate students on the basis of written and oral presentations at the IAHR World Congress (https://www.iahr.org/index/dawards/5).

- A. Villefer, M. Benoit, D. Violeau, M. Teles and C. Luneau. Etude expérimentale de submersion de protections côtières pour des états de mer combinant houle et clapot. In *Compte rendu des 17èmes Journées Nationales Génie Côtier - Génie Civil (JNGCGC'17), 11–13 October, Chatou (FRA)*, 2022.
  This article received the Pierre Guével Award 2022, which recognises the best conference paper from PhD students on the basis of written and oral presentations at the JNGCGC conference (https://site.paralia.fr/hommage-a-pierre-guevel.html).

One poster and one oral presentation were presented during WISE 2021 and 2022 international meetings:

- (Poster) A. Villefer, M. Benoit, D. Violeau, M. Teles, J. Harris, H. Branger and C. Luneau. Experimental and numerical characterization of swell-type waves effect on wind-sea growth with fetch. *27th WISE meeting, 5–9 September, Bergen (NOR)*, 2021.

- (Presentation) A. Villefer, M. Benoit, D. Violeau, M. Teles, C. Luneau and H. Branger. Wind-wave growth in the presence of swell: from laboratory observations to coastal scale simulations. *28th WISE meeting, 29 May - 2 June, Brest (FRA)*, 2022.

A presentation and a poster were presented during a workshop in École de physique des Houches (France):

- A. Villefer, M. Benoit, D. Violeau, M. Teles, J.Harris and H. Branger. Influence of swell on wind-wave growth with fetch: an experimental and numerical study. *Air-sea interaction PhD workshop, July, Les Houches (FRA)*, 2021.

Chapter 2

Design of coastal protections: from sea-state observations to the breakwater design

Ce chapitre synthétise l'état de l'art concernant les méthodes de dimensionnement des protections côtières en se limitant à la problématique de submersion par les vagues. En premier lieu, les différentes techniques d'observation des vagues sont décrites en allant des premières observations visuelles aux plus complexes observations par satellite. On présente ensuite les outils mathématiques permettant de décrire les vagues et les états de mer, notamment à l'aide de spectres de vagues. L'analyse spectrale des conditions de mer permet l'introduction des équations à la base des modèles spectraux d'états de mer. Ces modèles permettent notamment la prise en compte des processus suivants, dominants dans la dynamique des états de mer en grande profondeur d'eau : génération des vagues par le vent, dissipation par moutonnement, et interactions non-linéaires entre quadruplets de vagues. Les modèles spectraux sont régulièrement utilisés pour prédire les conditions de mer auxquelles peuvent être confrontées les structures marines et les protections côtières. Dans un second temps, on décrit les différents paramètres permettant d'estimer les débits de franchissements au-dessus d'une protection côtière. Ces estimations sont nécessaires pour le dimensionnement des protections côtières par rapport à des conditions de vagues et de design vis à vis du niveau marin.

2.1 Introduction

Mankind has been attracted by coastal areas since early ages ($\simeq$ 164 kyr ago according to Marean et al. (2007)). At that time, these areas have been determining for mankind survival by providing a crucial food supply (Marean et al., 2007). But the vicinity with oceans and seas also proved to be a crucial hazard endangering mankind with disasters such as storms, waves, hurricanes and tsunamis responsible for the flooding of vast coastal areas. Hence, the protection of coastal areas against ocean and sea hazards is essential.

The coastal engineering discipline addresses this issue by studying the occurrence and the impact of waves, tides, storm surges and tsunamis on coastal areas. Longer processes such as morphodynamic changes, sea level rise and erosion due to salty water are also investigated. Then, these studies permit to conceive sustainable coastal protections depending on the hazards encountered at a specific location.

This thesis aims at assessing the wave overtopping of coastal protections, such as breakwaters, in bimodal sea-state conditions. Here, the bimodal sea-state condition is a combination of two types of waves, wind-waves and swell, identified by their different wavelengths and periods. Eventually, the purpose of the present work is to give recommendations about the design of breakwater structures at locations where the occurrence of a bimodal sea-state is likely.

The objective of this chapter is to describe the coastal engineering methodologies when designing a coastal protection such as the one considered in the present thesis. The different existing tools to evaluate the sea-state conditions and assess the wave overtopping processes are introduced.

Hence, the first stage of the methodology consists in the study of the sea-state through the physical mechanisms at play during the generation and propagation of both wave systems.

This first stage starts with the introduction of different techniques to observe a sea-state from visual observations to in-situ measurements in section 2.2. The infinite diversity of wave and wind conditions in oceans and seas makes the identification of the physical mechanisms responsible for wind-wave generation or dissipation rather difficult. In order to address these scientific questions, wind-wave tunnels have been built in the second half of the 20^{th} century. These facilities, such as the OSU Institut Pythéas wind-wave tunnel in Marseilles (Coantic et al., 1981), permit to observe the latter mechanisms in ideal conditions (e.g. constant air flux, fetch or duration-limited wave conditions) propitious for the development or the verification of wave theories.

The different wave observations techniques are used as an introduction to define the key parameters to describe a sea-state in section 2.3. The differences between wind-waves and swell, crucial in the scope of the present thesis, are discussed. The sea-state description as a stochastic process triggered the development of empirical formulas for predicting wave conditions.

Dedicated research works on the prediction of wave conditions were initiated by the Hydrographic service of the French Navy in Casablanca, Morocco, in the 1920s (Montagne, 1922). It provided swell forecast for harbours (e.g. Casablanca harbour) based on the wave measurements performed in the Azores (see Ardhuin and Orfila, 2018, for more details). Later, it was of great use for the military needs during the landing operations of the Second World War. Since then, disciplines such as offshore engineering and naval architecture also developed an interest in improving these

predictions. One of the first parametric models based on empirical laws for wind-waves and swell was developed by Sverdrup and Munk (1947). Then, the concept of wave spectrum (Pierson and James, 1955) triggered the first wave model essentially based on empirical source terms (Gelci et al., 1957). Based on the wave theories by Miles (1957) and Phillips (1957) for wave generation, spectral wave models were developed in order to forecast the sea-state condition across the globe. Shortly after, the so-called 3G wave models (largely used in the present thesis) arose in the second half of the 20^{th} century from the derivation of the nonlinear transfer (Hasselmann, 1962) in addition to the breakthrough in computing sciences. Nowadays, these wave models are the tools the most soundly based on physics for wave prediction at global scale but still significantly rely on empirical parameterizations. Section 2.4 introduces the theory on which the 3G wave models are based and the different sink and source terms appropriate for the simulation of bimodal sea-state conditions. Recent developments with the purpose to improve wave predictions in bimodal sea-state conditions are also presented.

After estimating the sea-state at the desired coastal location by using a 3G wave model, the second stage of the coastal engineer methodology is to design the breakwater. The design of breakwaters involves different technical aspects including: the stability of the structure, the wave reflection it causes as well as the protection provided against wave overtopping. In the present thesis, only the wave overtopping aspect is considered.

Different empirical formulas, such as the largely validated EurOtop (2018) (Van der Meer et al., 2018), are introduced in section 2.5. Based on the sea-state conditions and the admissible wave overtopping rate at a selected location, these formula permit to calculate the dimensions of the breakwater. The admissible wave overtopping rate mainly depends on the kind of facility to protect (e.g. low admissible rate and high protections for a coastal NPP). However, the accuracy of the current engineering formulas is questionable in the presence of bimodal sea-state conditions.

Section 2.2 introduces the diverse techniques developed for wave observations. In particular, the different observation techniques used in the the present thesis are detailed. Section 2.3 describes different mathematical and physical tools to characterize wave observations. The spectral wave models, widely used to predict sea-state conditions near the coast where breakwater are built, are presented in Section 2.4. Once the different observation and prediction techniques have been defined, the section 2.5 introduces how wave description tools can be used to describe the wave overtopping process, a necessary step in the design of coastal protections.

For more detail about wave observations (Section 2.2), descriptions (Section 2.3) and predictions (Section 2.4), the reader can refer to the following textbooks: Komen et al. (1994), Lavrenov (2003), Janssen (2004), Holthuijsen (2007) and Young and Babanin (2020).

For more detail about the design of coastal protections (Section 2.5), especially since the stability aspect is not addressed here, the reader can refer to the following manuals: TAW (2002), The Rock Manual (2007) (CIRIA, 2007) and EurOtop (2007 & 2008) (Pullen et al., 2007; Van der Meer et al., 2018).

2.2 Wave Observation

2.2.1 Observation Techniques

Visual observation has been the first technique to observe sea conditions. These observations can be performed by everyone from the casual surfer sitting at the beach to the experienced crew member in offshore ships or a wave scientist from an oceanographic ship (Grigorieva and Badulin, 2016) or tower (Cavaleri, 2000). The main information resulting from these observations are an estimation of the wave height (reliable at a good extent) and an idea of the wavelength. The wave periods are rather difficult to estimate with such observations.

The Beaufort scale is a good proof of the power of visual observations. Initiated by the Irish hydrographer Francis Beaufort in 1805, this scale is still in use nowadays. As it can be observed in Figure 2.1, the Beaufort scale permits to describe the wind and sea conditions in a qualitative way. First based on visual observations of the sailing ships, it quickly evolved to visual observations of the sea surface roughness and white breakers coverage. These white breakers are usually called “whitecaps” but can also bear animals names, more or less poetic, such as “whitehorses”, “moutons” (sheeps in French) or “jumping rabbits” in Japanese.

Although meteorological institutes and sailors have great need of visual observations, a record of the water surface elevation as a function of time or as a function of the spatial coordinates at the sea surface is necessary to further understand and predict wave motion.

For that purpose, in-situ measurements near the sea surface can be used. The two main in-situ observation techniques are wave buoys and wave gauges. The most common wave buoys are provided with accelerometers to obtain the buoy vertical acceleration and the free surface elevation in time at a specific location (e.g. Waverider of Datawell, www.datawell.nl). In addition to the surface elevation in time, properties such as the wave directional properties and the short-crestedness of the sea-state can also be estimated by adding extra sensors such as inclinometers or inertial measurement units (IMUs) to obtain the buoy rotations or horizontal motions (e.g. Wavec, Directional Waverider of Datawell). Directional wave data provided by these wave buoys were used in the course of the present thesis. Wave buoys are the most convenient technique to measure waves at sea thanks to the easy set-up (e.g. Spotter buoys of Sofar, www.sofarocean.com).

Fixed platforms at sea such as offshore platforms or spar buoys permit to obtain wave properties using wave gauges. A set of wave gauges consists in vertical wires positioned at the air/sea interface. Figure 2.2 shows the two measurement techniques associated to wave gauges: using (left-panel) the electrical resistance or (right-panel) the capacitance of the water between two electric wires. The second technique, although more expensive and somehow more fragile, is generally more accurate. In order to obtain directional information, a group of at least 3 wave gauges must be positioned in space for instance at the corners of a triangle. The ASIS spar buoy (Graber et al., 2000), from which we used the data in the course of the present thesis, measures wave properties based on the wave gauge technique and provides an accurate estimation of the wave directional properties using a group of eight wave gauges. Most of the buoys cited in this section also measure diverse physical parameters at the air/sea interface such as the sea surface temperature (SST) and the wind velocity as it is shown with the ASIS buoy picture in Figure 2.3.

Figure 2.1: Sea photograph showing example of sea-state conditions corresponding to Beaufort scales 0, 5, 8 and 12. (Source: Wikipedia from NOAA)

Then, by taking a bit of distance from the sea, it is quite obvious to an observer from a plane that the altitude is a great advantage for wave observation as illustrated in Figure 2.4. From a plane, the sea-state seems static so the different shades of blue permit to identify the crests from the trough at a given time over a large area and can inform the observer about the wavelength and the wave height. Remote sensing techniques permit to measure the wave properties from the coast (e.g. LIDAR), from a boat at sea or at high altitude using a plane (Fig. 2.4), and from satellites with active microwave radars.

Ocean observation using satellites has been a rapidly growing technique since the 90s. These missions are more and more numerous and frequent as shown in Figure 2.5. The next one will be the SWOT (Surface Water Ocean Topography) satellite, successor from Topex/Poseidon and Jason series. The SWOT mission is scheduled to be launched in 2022.

The sea surface observation satellites are provided with different generations of active microwave radars such as altimeters permitting to obtain significant wave height and wind velocity all around

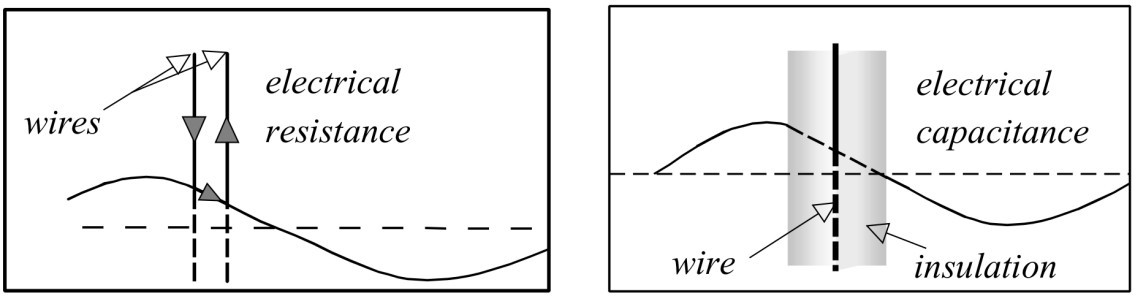

Figure 2.2: Resistance and capacitance-type wave gauges. (Holthuijsen, 2007)

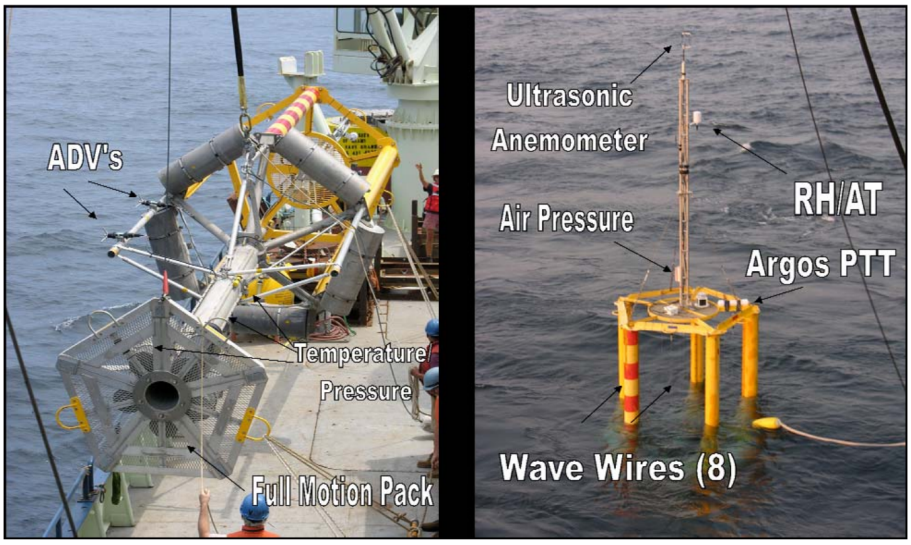

Figure 2.3: Picture of the ASIS buoy deployed at sea. (Graber et al., 2000)

the globe, or scatterometers permitting to obtain wind speed and wind direction. Some of them are also provided with SAR (Synthetic Aperture Radar) or even Interferometric SAR technology permitting to obtain directional spectra or surface water topography with an accurate precision. The CFOSAT (China-France Oceanography SATellite) satellite observes both the sea state (wave height, wave direction, wavelength) and the wind field (speed and direction) using two different kind of scatterometers (Hauser et al., 2017), with a high accuracy. Since remote sensing techniques are not used in the present thesis, the reader is referred to Ardhuin (2021), Le Merle (2019) and Holthuijsen (2007) for more detail.

Optical methods such as the well known particle image velocimetry (PIV) have been recently developed for short time measurements of a sea-state in order to obtain highly accurate temporal and spatial measurements of the free-surface, the wind field just above the waves and the water velocities just below the waves (Kimmoun and Branger, 2007; Reul et al., 2008).

The diverse measurement techniques mentioned in the present section provide a rather large number of ways to obtain ocean wave properties. Yet, even with the great diversity of measuring devices previously mentioned, the understanding of the ocean wave dynamics remains difficult due to the apparent chaotic nature of the climatic conditions in which ocean waves are observed (e.g. wind gustiness, air and sea temperature, currents). In order to theoretically characterize some of the

Figure 2.4: Photograph of a sea-state taken from a plane. (Photo: Hubert Branger)

observed phenomena, the ideal conditions provided by a wave tank or a wind-wave tunnel are often needed.

2.2.2 OSU Institut Pythéas wind-wave tunnel in Marseilles

Studying the air-sea interaction with in-situ experiments is often difficult and costly. In addition, the presence of a ship or a buoy can be responsible for errors in the measured fluxes. Hence, the controlled and repeatable conditions of a laboratory come as a complementary tool in addition to field experiments. In the 60s, small scale wind-wave tunnels were mostly restricted to the study of the momentum transfer at the origin of wind-wave generation (Mitsuyasu, 1966). With the purpose to study the interaction between the atmosphere and the ocean in a larger scope and at a larger scale, the Large Air-Sea Interaction Facility in Marseilles (France) project saw the light of the day. The facility became operational in 1972. In the present thesis, the facility is named "OSU Institut Pythéas wind-wave tunnel" due to the evolution regarding the financial support of the facility and given that the air and water temperature control are no longer functional.

Coantic and Favre (1975) described the facility as a micrometeorological wind-wave tunnel. It aims at studying the energy exchanges between the lower part of the atmoshpere and the upper layers of the ocean through 4 identified processes (Coantic and Bonmarin, 1975):

- Radiative transfer, including absorption of solar short-wave radiation in the sea, and emission and absorption of infrared long-wave radiation by the sea surface and the atmosphere,
- Evaporation and turbulent transfer of water vapor (and latent heat) from the sea surface to the atmosphere,
- Turbulent convective transfer of sensible heat between the atmosphere and ocean,

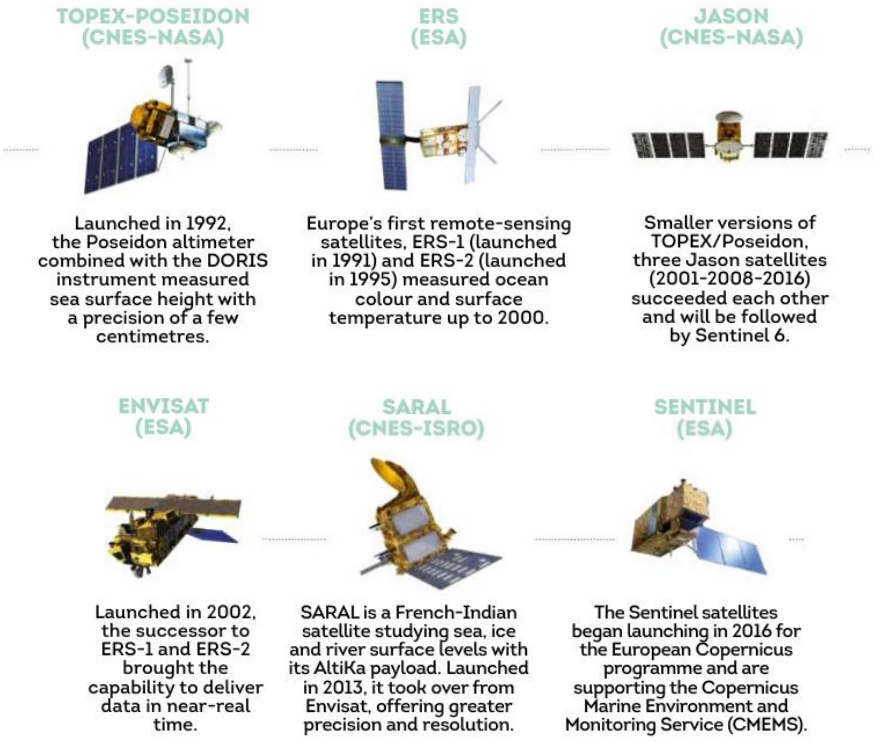

Figure 2.5: Diagram of the different satellites provided with altimeters launched since the 90s. (©CNES MAG #81, August 2019)

- Transfer of kinetic energy and momentum from atmosphere to the sea, leading to the generation of waves and surface drift currents.

Maybe the most ambitious goal of the project was to investigate the coupling between the different processes that happen when heat and mass transfer are combined with wind generation for instance.

In order to simulate sufficiently high dimensionless numbers (e.g. wave age and Froude number when studying wind-generated gravity waves) the facility has been designed with large dimensions. The test section is 40 m long, the water tank section is 2.6 m wide and 0.9 m deep and the airflow section is 3.2 m wide and 1.5 m high.

Figure 2.6 illustrates the different features responsible for the high performances of the facility to reproduce the physical processes listed above. One of the main objectives when designing such a facility is to obtain a homogeneous and regular airflow along the wave tank. For that purpose, the air blower, in the upper section of the tunnel, is followed by a divergent section in which vertical blades (1 in Fig. 2.6) are located. Then, horizontal blades (2 in Fig. 2.6) facilitate the turning of the air flow at the transition between the upper and lower parts of the tunnel. After a second divergent section, the airflow passes through several grids (3 in Fig. 2.6) to break the large vortices and transfer the turbulence to smaller scales. Eventually, the airflow is accelerated by a convergent section at the entrance of the test section (black area in the background of photograph 4 in Fig. 2.6). The piston-type wavemaker, usually used to generate long unidirectional waves, is submerged so it does not disturb the airflow. By design, the mechanically generated waves can only propagate

in the wind direction.

Through the years, many studies have been performed on the physical processes at the air-sea interface. Up to the 90's, when the air and water temperature control were functional, many studies on the heat and mass transfer were performed (e.g. evaporation, gas exchanges). Since then, the most recurrent topics are the study of wave generation, propagation and breaking (i.e. dissipation) and pioneering works on remote sensing of the sea surface by microwave active radars. The facility was also used for small scale modelling with industrial applications such as tidal or wind turbines and, more particularly very recently in the course of the present thesis, a breakwater model.

2.3 Description and statistics of ocean waves

2.3.1 Wave spectrum

Using a wave gauge or a wave buoy, the water surface elevation as a function of time $\eta(t)$ at one location (x, y) can be plotted for a duration D as in Figure 2.7. The first assumption behind the wave spectrum concept (Pierson and James, 1955) is that the plotted surface elevation vs time can be exactly reproduced with a sum of a sufficient number of harmonic wave components (Fourier series) as:

$$\eta(x, y, t) = \sum_{i=1}^{N} a_i \cos(k_i(x \cos\theta_i + y \sin\theta_i) - \omega_i t + \psi_i) \tag{2.1}$$

with a_i the wave amplitude, $\omega_i = 2\pi f_i$ the wave angular frequency (f_i the wave frequency), k_i the wavenumber, θ_i the wave direction and ψ_i the wave phase, and N the number of wave components. After choosing a discrete number of frequencies such as $f_i = i/D$ (i.e. the interval is $\mathrm{d}f = 1/D$), one can perform a Fourier analysis to determine the a_i and α_i (with $\alpha_i = k_i(x \cos\theta_i + y \sin\theta_i) + \psi_i$) associated to each f_i. The amplitude and the phase spectrum corresponding to the latter surface elevation, respectively $a_i(f_i)$ and $\alpha_i(f_i)$, are plotted in Figure 2.7.

In Figure 2.7, it is shown that whereas $a_i(f_i)$ has a characteristic wave distribution around the spectral peak, $\alpha_i(f_i)$ is fully random. This observation is at the base of the wave spectrum concept: since the wave phase distribution is presumed random and uniform over $[0, 2\pi]$ (at least for deep water waves), only the wave amplitude (or energy) distribution over the frequencies and directions is considered. This way of representing the sea-state is often qualified as "stochastic". Then, using Airy linear theory for regular waves, the total energy per surface unit ϵ_{tot} can be formulated, in the discrete case, as:

$$\epsilon_{\mathrm{tot}} = \sum_{i=0}^{N} \frac{1}{2} \rho_w g a_i^2 \tag{2.2}$$

where ρ_w is the water density and g the gravitational acceleration. In the continuous case, one can write:

$$\epsilon_{\mathrm{tot}} = \int_0^{\infty} \int_0^{2\pi} \epsilon(f, \theta) \mathrm{d}f \mathrm{d}\theta \tag{2.3}$$

$\epsilon(f, \theta)$ being the spectro-angular energy density spectrum usually shorten as "energy spectrum".

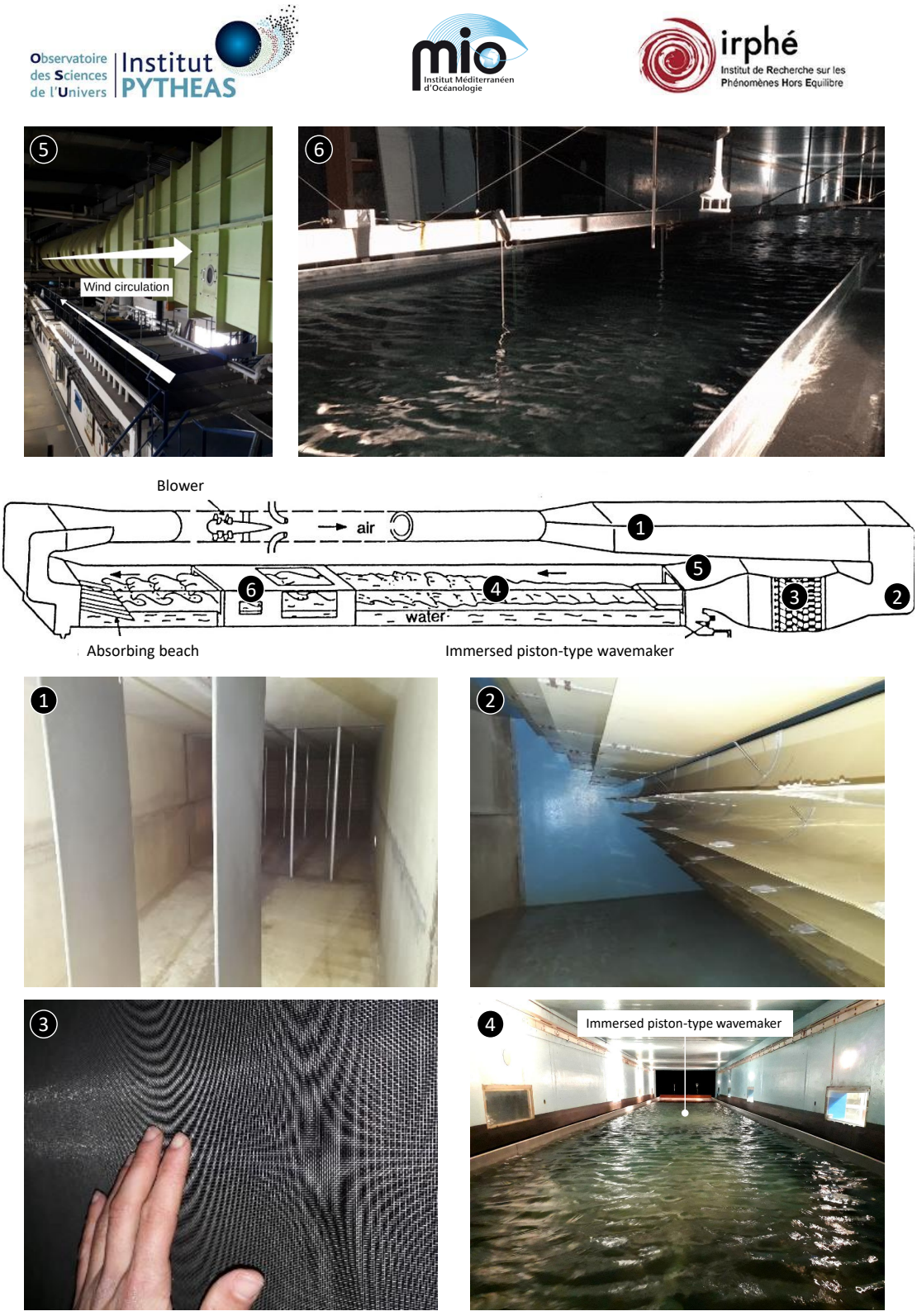

Figure 2.6: Schematic view with photographs of the OSU Institut Pythéas wind-wave tunnel in Marseilles.

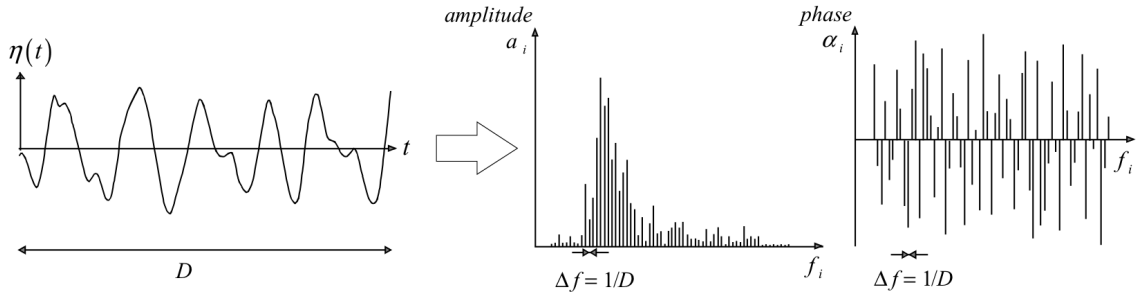

Figure 2.7: The observed surface elevation and its amplitude and phase specta. (Holthuijsen, 2007)

In the literature, the authors usually refer to the variance density spectrum $E(f,\theta)$ defined as:

$$E(f,\theta) = \frac{\epsilon(f,\theta)}{\rho_w g} \tag{2.4}$$

Up to this point, the sea-state has been decomposed as a sum of harmonic wave components in order to define the variance density spectrum E. Across the oceans and seas, waves are often exposed to diverse currents (e.g. tidal currents near the coast). In the presence of such currents, waves propagate in conditions that are no longer homogeneous and steady. Hence, the flux of $E(f,\theta)$ and $\epsilon(f,\theta)$ are no longer conserved. However, the flux of the wave action density $N(f,\theta)$ (Bretherton et al., 1968) is still conserved in inhomogeneous moving media (i.e. if one neglects dynamical processes such as wave generation of dissipation). The wave action density is defined as:

$$N(f,\theta) = \frac{E(f,\theta)}{\sigma} \tag{2.5}$$

where σ is the relative or intrinsic angular frequency, i.e. the angular frequency in a frame moving with the current velocity. An observer from a fixed system of coordinates can measure the absolute angular frequency σ. In order to interrelate the phase parameters within the scope of the linear wave theory, the dispersion relation and a Doppler-type equation can be written as:

$$\sigma^2 = gk \tanh kh \tag{2.6}$$

$$\omega = \sigma + \mathbf{k} \cdot \mathbf{U}_c \tag{2.7}$$

with $\mathbf{k}= (k_x, k_y) = (k\cos\theta, k\sin\theta)$ the wavenumber vector and $\mathbf{U}_c = (U_x, U_y)$ the current velocity vector. In the course of the present thesis, no current will be considered so that $\sigma = \omega$. The notation ω is preferably used in the following.

Whereas the spectral densities have been expressed as a function of the frequencies and the directions, they are often expressed as a function of the wavenumber modulus k and the direction θ or as a function of wavenumber vector only. The relation between the different existing expressions can be obtained (for more details, see Holthuijsen (2007)) using the wave group velocity $C_g = \partial\omega/\partial k$. In the present thesis, the most useful relation is

$$E(f,\theta) = \frac{2\pi}{C_g} E(k,\theta) \tag{2.8}$$

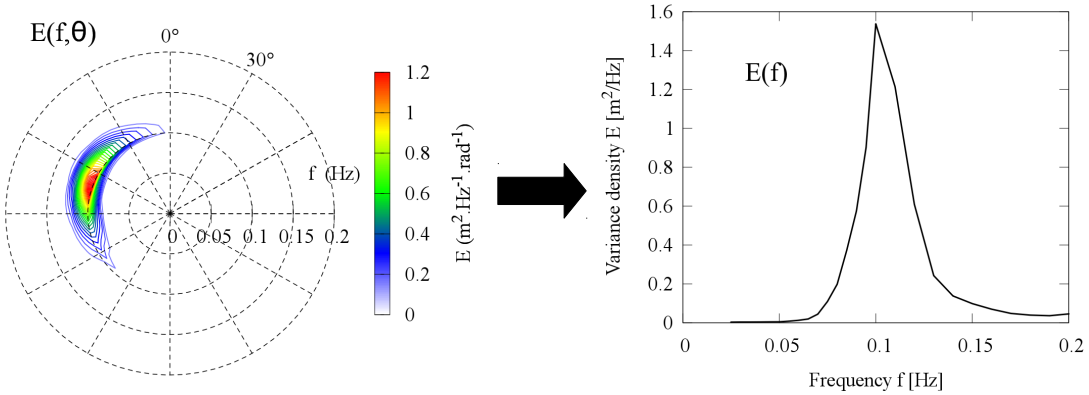

Figure 2.8: Example of a spectro-angular spectrum (left) and the corresponding frequency spectrum (right) obtained from a Directional Waverider buoy during SHOWEX campaign. (Ardhuin et al., 2007)

As mentioned in section 2.2, the directional properties of the observed sea-state are not always available depending on the measurement technique. The variance density spectra is often expressed as a frequency variance density spectrum $E(f)$ either meaning that the directional properties are not available or that the spectro-angular spectrum has been integrated along the directions. Figure 2.8 shows an example of both types of spectra based on the same observation using a Directional Waverider buoy. The directional spectra can be expressed as:

$$E(f,\theta) = E(f)D(f,\theta) \tag{2.9}$$

where $D(f,\theta)$ is the angular distribution function. Since

$$E(f) = \int_0^{2\pi} E(f,\theta)\mathrm{d}\theta, \tag{2.10}$$

D is positive and periodic over $[0, 2\pi]$ and fulfills the following normalising condition:

$$\int_0^{2\pi} D(f,\theta)\mathrm{d}\theta = 1 \tag{2.11}$$

Various empirical expressions for $D(f,\theta)$ can be found in the literature in order to generate realistic sea-states in numerical or physical models for instance.

2.3.2 JONSWAP spectrum

The JOint North Sea WAve Project (JONSWAP) (Hasselmann et al., 1973) was conceived with the purpose to fill the lack of detailed field studies of wave growth and decay. The most noteworthy outcome of this project is a parameterization of a typical wave spectrum developed on the basis of a large number of measured spectra. The proposed formula for the variance density frequency

spectrum $E(f)$ is the following:

$$E(f) = \alpha_p H_s^2 \frac{f_p^4}{f^5} \exp\left[-\frac{5}{4}\left(\frac{f_p}{f}\right)^4\right] \gamma^{\exp\left[-\frac{(f-f_p)^2}{2\sigma^2 f_p{}^2}\right]} \tag{2.12}$$

The JONSWAP recommendations give $\sigma = 0.07$ for $f < f_p$ and $\sigma = 0.09$ for $f > f_p$, $\gamma = 3.3$ is the peak enhancement factor and $\alpha_p = 0.2$ is the Phillips constant. The significant wave height H_s and the peak frequency f_p are the parameters to adjust in order to obtain the desired sea-state. With $\gamma = 1$, one can find the spectrum proposed earlier by Pierson and Moskowitz (1964) corresponding to a fully developed sea-state.

The f^{-5} term in the JONSWAP spectrum, corresponding to the decrease rate of the wave energy at high frequencies (HF), is rather contested in the literature. According to Phillips (1958), $E(f) \propto f^{-4}$ but Toba (1973) proposed $E(f) \propto f^{-5}$. Another formulation of $E(f)$ using Phillips (1958)'s decrease rate was suggested by Donelan et al. (1985).

2.3.3 Integral parameters

Most of the wave parameters used in the present thesis are based on the wave spectrum concept using the n^{th}-order moment m_n obtained with the following expression:

$$m_n = \int_0^\infty f^n E(f) \mathrm{d}f \tag{2.13}$$

Several representative parameters of the sea-state results from this definition. The most common one is the significant wave height based on the variance m_0:

$$H_{m_0} = 4\sqrt{m_0} \tag{2.14}$$

It is useful to note that the zero-order moment is equal to the variance of the free-surface elevation:

$$m_0 = \int_0^\infty E(f) \mathrm{d}f = \overline{\eta^2} \tag{2.15}$$

Regarding the wave period, the most common one to describe a sea-state is the peak period T_p. It corresponds to the spectral period associated to the highest wave energy level in the spectrum. Taking the example of Figure 2.8, the peak frequency f_p is 0.1 Hz corresponding to $T_p = 10$ s. Moreover, several representative mean periods can be defined using spectral moments at different orders. Among these periods, $T_{m_{0,1}}$ and $T_{m_{-1,0}}$ are defined as:

$$T_{m_{0,1}} = \frac{m_0}{m_1} \tag{2.16}$$

$$T_{m_{-1,0}} = \frac{m_{-1}}{m_0} \tag{2.17}$$

$$T_{m_{0,2}} = \sqrt{\frac{m_0}{m_2}} \tag{2.18}$$

The different periods permit to give more or less weight to the HF part of the wave spectrum. For instance, for a typical wave spectrum (e.g. Fig. 2.8) the spectral wave periods can be sorted as follows:

$$T_p > T_{m_{-1,0}} > T_{m_{0,1}} > T_{m_{0,2}} \tag{2.19}$$

Several parameters can be used to describe multidirectional waves (Frigaard et al., 1997). These wave parameters result from a Fourier analysis of the angular distribution function $D(f,\theta)$. The latter function can be expressed as a Fourier series:

$$D(f,\theta) = \frac{1}{2\pi} + \frac{1}{\pi}\sum_{n=1}^{\infty}(a_n(f)\cos(n\theta) + b_n(f)\sin(n\theta)) \tag{2.20}$$

where a_n and b_n are the Fourier coefficients defined as:

$$a_n(f) = \int_0^{2\pi} D(f,\theta)\cos(n\theta)\mathrm{d}\theta \tag{2.21}$$

$$b_n(f) = \int_0^{2\pi} D(f,\theta)\sin(n\theta)\mathrm{d}\theta \tag{2.22}$$

From the Fourier coefficients a_1 and b_1, the angular spread is defined as:

$$\sigma(f) = \sqrt{2\left(1 - \sqrt{a_1^2(f) + b_1^2(f)}\right)} \tag{2.23}$$

The mean frequency averaged angular spread is defined as:

$$\sigma = \frac{\int_f \sigma(f)E(f)\mathrm{d}f}{\int_f E(f)\mathrm{d}f} \tag{2.24}$$

The mean wave direction is defined as:

$$\theta_m(f) = \arctan\left(\frac{b_1(f)}{a_1(f)}\right) \tag{2.25}$$

Lastly, the mean spectral peak direction $\theta_p = \theta_m(f_p)$ and the spectral peak angular spread $\sigma_p = \sigma(f)$ are often used. Other directional parameters cans be found in Frigaard et al. (1997).

2.3.4 Wave steepness

The large panel of tools to describe ocean waves is mostly based on the linear wave theory. When waves are steep, observations prove that waves are no longer sinusoidal: the wave crests are high and sharp whereas the wave troughs are shallow and flat. This is due to nonlinear processes. Overall, the significance of nonlinear processes increases with wave steepness. In order to characterize the limitations of the linear wave theory, the wave representative steepness (s_m or ak) is a useful parameter. It can be defined as the ratio of a significant wave height H_s over a representative wavelength λ_m as:

$$s_m = \frac{H_s}{\lambda_m} = \frac{H_s k}{2\pi} \tag{2.26}$$

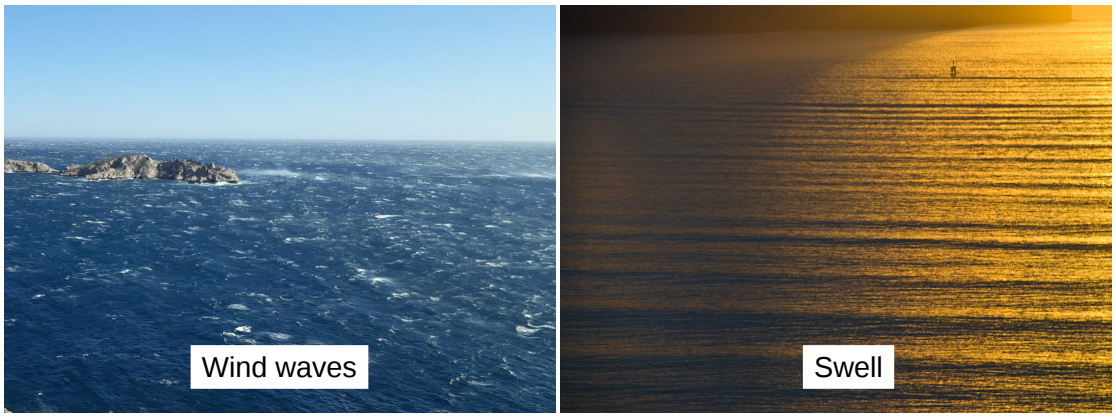

Figure 2.9: Photograph of wind-waves (left panel) and swell (right panel). The left side photograph has been taken during an episode of Mistral wind in Marseilles. (Left photo: Antoine Villefer ; right photo: © Phillip Capper, Wikipedia)

Following the recommendations given to coastal engineers in EurOtop (2018) (Van der Meer et al., 2018), the definitions chosen in the present thesis are: $H_s = H_{m_0}$ and $\lambda_m = \lambda_{m_{-1,0}} = gT^2_{m_{-1,0}}/(2\pi)$.

Another wave steepness definition, commonly used by physical oceanographers, is ak where a is the wave amplitude and k is the wave number. In order to have a common definition for a when observing either regular and irregular waves, the chosen definition is $a = H/2 = H_{m_0}/(2\sqrt{2}) = \sqrt{2m_0}$, where H is the regular wave height.

In the present thesis, ak is used when considering the sea-state only and s_m is used to estimate the wave overtopping of coastal protections. The wave steepness is also used to characterize different types of waves such as wind-waves and swell.

2.3.5 Wind-waves and swell

The distinction between wind-waves (or wind-sea) and swell is a very important notion in the present thesis. Most of the sea-states considered here combine both wave systems: the corresponding spectra have two peaks and are named “bimodal spectra”.

Wind-waves, illustrated in the left panel of Figure 2.9, can be observed in areas where a local wind is blowing. They are characterized by a relatively short wavelength (< 100 m) and a period up to approximately 7 to 8 s. Since they are generally observed in the presence of wind amplifying the waves, they are characterized by a high steepness. Hence, as shown in Figure 2.9, wind-wave observation is often associated with the presence of whitecaps due to wave breaking.

Swell waves, also illustrated in the right side Figure 2.9, are old wind-waves that lengthen by propagating over long distances under the influence of different wind events. They are often observed in absence of wind, near the coast for instance, as illustrated in Figure 2.9. Their characteristic wavelength is generally longer that 100 m and can reach several hundreds of meters in deep water. Their period is approximately over 8 s and can reach 25 s (even sometimes up to 28-30 s).

Another method to differentiate swell from wind-waves is based on the notion of wave age χ defined

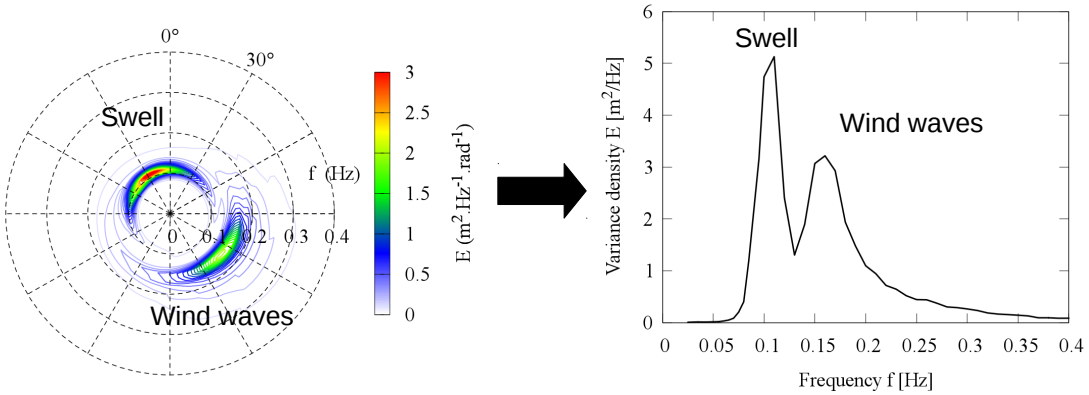

Figure 2.10: Example of a bimodal spectro-angular spectrum (left side) and the corresponding bimodal frequency spectrum (right side) obtained from a Directional Waverider buoy during SHOWEX campaign. Wind-wave and swell systems are clearly separated in terms of direction (left side) and peak frequency (right side) (Ardhuin et al., 2007)

as C/U_{10} or $c_p/u_\star$ with C the wave phase celerity, U_{10} the wind velocity at 10 m above mean water level (MWL) and $u_\star$ the friction velocity. Considering the first definition (i.e. $\chi = C/U_{10}$), waves are considered as wind-waves when $\chi < 1$ and as swell when $\chi > 1$. In other words, according to the latter definition, waves are considered as swell when their crests travel at a speed faster than the wind speed.

An example of bimodal spectrum is given in Figure 2.10. Both wave systems are clearly separated in terms of peak frequencies and directions. However, the separation between wind-wave and swell systems is not always as clear as in Figure 2.10.

2.3.6 Empirical estimations

The combination of observations in open oceans, in large lakes and in wind-wave tunnels led to the development of empirical models for estimating wind-wave growth in specific conditions. For deep water waves, these models are based on a dimensional analysis meaning that the only parameters to affect waves are the wind speed, the fetch X, the duration t (no waves when the wind starts blowing at $t = 0$) and the gravitational acceleration g. The wind speed considered in most cases is U_{10}. Most of the models consider t as sufficiently long so that the waves reach an saturated state and can be estimated with U_{10}, X and g only: these idealised conditions are called "fetch-limited conditions". Following Kitaigorodskii (1961), wind-wave growth in fetch-limited conditions can be characterized using 3 non-dimensional numbers:

$$X^* = \frac{Xg}{U_{10}^2}, \tag{2.27}$$

$$f_p^* = \frac{f_p U_{10}}{g}, \tag{2.28}$$

$$m_0^* = \frac{m_0 g^2}{U_{10}^4}, \tag{2.29}$$

with the non-dimensional fetch X^*, peak frequency f_p^* and total variance of the free-surface elevation m_0^* (proportional to the wave energy). One should note that in Chapter 3, $u_\star$ is used instead of U_{10} for the definition of the above non-dimensional numbers. The non-dimensional significant wave height $H_{m_0}^*$, based on m_0, can also be used instead of m_0^* using the definition:

$$H_{m_0}^* = \frac{H_{m_0} g}{U_{10}^2}. \tag{2.30}$$

Using these non-dimensional numbers, several references proposed parameterizations of the evolution of f_p^* and m_0^* as a function of X^*. An example of commonly used formula, permitting to take into account the stability of the surface between the water and the air, was developed by Kahma and Calkoen (1992) and can be expressed, in its composite way, as follows:

$$m_0^* = 9.31 \times 10^{-4} (X^*)^{0.9} \quad \text{and} \quad f_p^* = 0.4587 (X^*)^{-0.27} \tag{2.31}$$

Such formulas permit a rough estimation of the wind-wave growth when the fetch can be defined. In situations when the definition of the fetch becomes difficult, spectral wave models are used instead of the empirical formulas.

2.4 Spectral wave models

This section is largely inspired by TOMAWAC User manual (2022) and by Gagnaire-Renou (2009).

Spectral wave models have come into existence in the fifties following the works of Gelci et al. (1957). Based on the action balance equation, they solve the propagation of the wind-waves over oceanic or coastal domains. The physical mechanisms such as wave generation, dissipation and nonlinear 4-wave interactions are modelled using source and sink terms. Since the fifties, the developments regarding the modelling of the 4-wave interactions term triggered the breakthrough of 3 generations of these wave models that came in succession. After the 1$^{\text{st}}$ generation wave model following Gelci et al. (1957) work, the JONSWAP experiments permitted an improvement of the 4-wave interactions term that led to the development of 2$^{\text{nd}}$ generation wave models. The approximation of the 4-wave interactions (Hasselmann, 1962; Zakharov, 1968) with the Discrete Interaction Approximation (DIA) method (Hasselmann et al., 1985) then initiated the development of 3G wave models.

2.4.1 The action balance equation

The action balance equation, at the basis of spectral wave models, can be expressed by the following conservation equation:

$$\frac{\partial N(\boldsymbol{k})}{\partial t} + \nabla_{x,y} \cdot ((\boldsymbol{C}_g + \boldsymbol{U}_c) N(\boldsymbol{k})) + \frac{\partial C_\theta N(\boldsymbol{k})}{\partial \theta} + \frac{\partial C_\sigma N(\boldsymbol{k})}{\partial \sigma} = \sum_i \frac{S_i(\boldsymbol{k})}{\sigma} \tag{2.32}$$

with $\boldsymbol{k} = (k_x, k_y)$ the wavenumber vector, $\boldsymbol{C}_g = (C_{g,x}, C_{g,y})$ the group velocity and $\boldsymbol{U}_c = (U_{c,x}, U_{c,y})$ the current velocity. C_θ and C_σ represent the changes of directions and pulsations

(resp.) due to the influence of a current or a depth varying in time or space. Here, the variables N, E and S are function of space (x, y) and time t that are omitted in the equation for convenience matter.

In the general case of waves propagating in a non-homogeneous, unsteady environment (currents and/or sea levels varying in time and space), Equation 2.32 expresses that the wave action is preserved when the right-hand side is zero. Only the source and sink terms S, representing the physical processes, can add or remove wave action in the balance, in the case of wave generation for instance.

In the present thesis, the wave propagation is considered without currents and supposing a constant depth ($C_\theta = C_\sigma = U_{c,x} = U_{c,y} = 0$). Therefore, the equations can be rewritten with the variance density E instead of the wave action N and switching from $\boldsymbol{k}$ to (f, θ):

$$\frac{\partial E(f,\theta)}{\partial t} + C_{g,x}\frac{\partial E(f,\theta)}{\partial x} + C_{g,y}\frac{\partial E(f,\theta)}{\partial y} = \sum_i S_i(f,\theta) \tag{2.33}$$

this equation is later denoted as

$$\frac{\mathrm{d}E(f,\theta)}{\mathrm{d}t} = \sum_i S_i(f,\theta) \tag{2.34}$$

Given the above simplifications, Equation (2.33) describes the transport of the energy of each wave components at the group velocity. On the right-hand side of Equation (2.33), the sum of source and sink terms can be decomposed as:

$$\sum_i S_i(f,\theta) = S_{\mathrm{in}}(f,\theta) + S_{\mathrm{ds}}(f,\theta) + S_{\mathrm{nl}}(f,\theta) \tag{2.35}$$

with S_{in} the wind energy input, S_{ds} the dissipation through whitecapping and S_{nl} the nonlinear 4-wave interactions.

2.4.2 Source terms

2.4.2.1 Wind input

In the present thesis, the model considered for estimating the momentum transfer from the air to the sea is based on Janssen (1991, 2004)'s works. It consists in a quasi-linear theory for modelling the ocean/atmosphere interactions. The linear growth term is ignored and only an exponential energy growth is taken into account, following Miles' results (Miles, 1957). According to Janssen (1991), the wind energy input can be expressed as a quasi-linear source term ($S_{\mathrm{in}} = \gamma E$, with γ the growth rate), function of the directional variance spectrum:

$$S_{\mathrm{in}}^{\mathrm{J}} = \sigma\varepsilon\beta\left(\left[\frac{u_\star}{C} + z_\alpha\right]\max\left[\cos(\theta - \theta_w), 0\right]\right)^2 E \tag{2.36}$$

with $\varepsilon = \rho_{air}/\rho_{water}$ the ratio of air and water specific densities ($\varepsilon = 1.25\ 10^{-3}$), $C = \sigma/k$ the wave phase celerity, θ_w the local wind direction (direction along which it blows), z_α is a constant allowing to offset the growth curve (default value: $z_\alpha = 0.011$) and $u_\star$ the friction velocity, being

linked to the surface stress τ_s by the following relation:

$$u_\star = \sqrt{\frac{\tau_s}{\rho_{air}}}. \tag{2.37}$$

The operator "max" in the source term expression limits the wave generation for the propagation directions included within a $\pm 90°$ angular sector with respect to the local wind direction.

In Equation (2.36), the Miles' parameter β can be expressed as follows:

$$\beta = \frac{\beta_m}{\kappa^2} \mu \ln^4 \mu \tag{2.38}$$

with μ the non-dimensional critical height:

$$\begin{aligned} \mu &= \min \left[\frac{g.z_0}{C^2} \exp \left(\frac{\kappa}{\left[\frac{u_\star}{C} + z_\alpha\right] \cos(\theta - \theta_w)} \right), 1 \right] \\ &= \min \left[\Omega.A^2 \exp \left(\frac{\kappa}{[A + z_\alpha] \cos(\theta - \theta_w)} \right), 1 \right] \end{aligned} \tag{2.39}$$

$A = u_\star / C$ is the inverse wage age, $\Omega = (g.z_0)/u_\star^2$ is the wind profile parameter, κ is the Von Karman's constant (default value: $\kappa = 0.41$), z_0 is the aerodynamic roughness and β_m is a non-dimensional growth parameter (constant). β_m has a default value set to 1.2 by Janssen (1991) but it is usually necessary to adjust it to the wind input forcing (Alday et al., 2021).

Janssen's model computes $u_\star$ and z_0 based on τ_s estimation as a function of the wind velocity U_{10} and on the sea-state roughness through the wave stress τ_w. $u_\star$ and z_0 are obtained by solving the following system of equations:

$$U(z) = \frac{u_\star}{\kappa} \ln \left(\frac{z + z_0 + \tilde{z}_0}{z_0} \right) \approx \frac{u_\star}{\kappa} \ln \left(\frac{z}{z_0} \right) \tag{2.40}$$

$$z_0 = \frac{\tilde{z}_0}{\sqrt{1 - \tau_w / \tau_s}} \text{ with } \tilde{z}_0 = \alpha \frac{u_\star^2}{g} \tag{2.41}$$

where α_c is the Charnock constant (default value: $\alpha = 0.01$).

The solution of the system of equations through a Newton-Raphson's iterative method yields τ_s, $u_\star$ and z_0. The initial value of friction velocity $u_\star$ is defined considering a constant drag coefficient: $u_\star = U_{10}\sqrt{C_D}$ using $C_D = 1.2875\ 10^{-3}$ as default value.

τ_w is computed as a function of the variance spectrum E, via the source term S_{in}, using the following relation:

$$\tau_w = \left| \varepsilon^{-1} g \int_0^{2\pi} \int_0^{f_c} \frac{\boldsymbol{k}}{f} S_{\text{in}}(f, \theta) \left(\cos\theta, \sin\theta\right) \mathrm{d}f \mathrm{d}\theta + \varepsilon^{-1} g \int_0^{2\pi} \int_{f_c}^{\infty} \frac{\boldsymbol{k}}{f} \gamma E(f, \theta) \left(\cos\theta, \sin\theta\right) \mathrm{d}f \mathrm{d}\theta \right| \tag{2.42}$$

Since the wave model computes a finite range of discrete frequencies up to the frequency f_c, a parametric tail is applied for the HF portion of the spectrum, assuming a f^{-n} diagnostic tail.

2.4.2.2 Dissipation by whitecapping

Several models exist to take into account the wave dissipation by whitecapping in spectral wave models. However, these models are empirical to a large extent. More soundly physics-based approaches exists but face difficulties in being adapted into operational spectra wave models (Babanin, 2011). Three of these dissipation models are presented below. These models have the property to be particularly adapted to wave propagation in infinite depth.

Komen et al. (1984) model

The dissipation model developed by Komen et al. (1984) and reformulated in Komen et al. (1994) is the most widely used in 3G wave models. Its expression is the following:

$$S_{ds} = -C_{dis}\bar{\sigma}(\bar{k}^2 m_0)^2 \left(\delta\frac{k}{\bar{k}} + (1-\delta)\left(\frac{k}{\bar{k}}\right)^2\right) E \tag{2.43}$$

with $C_{\text{diss}} = 4.5$ a coefficient, $\delta = 0.5$ a weighting parameter, $\bar{\sigma}$ the average intrinsic frequency and $\bar{k}$ the average wavenumber. $\bar{\sigma}$ and $\bar{k}$ are defined as follows:

$$\bar{\sigma} = \left(\frac{1}{m_0}\int_0^{\infty}\int_0^{2\pi}\frac{1}{\sigma}E(f,\theta)df d\theta\right)^{-1} \tag{2.44}$$

$$\bar{k} = \left(\frac{1}{m_0}\int_0^{\infty}\int_0^{2\pi}\frac{1}{\sqrt{k}}E(f,\theta)df d\theta\right)^{-2} \tag{2.45}$$

It should be noted that in Equations (2.44) and (2.45), the integration over the frequencies extends to infinity considering a decreasing variance in f^{-n}.

The above dissipation models showed significant limitations when simulating bimodal sea-state conditions (e.g. Ardhuin et al., 2007; Booij and Holthuijsen, 2002). The model depends to a large extent on the average wave steepness $a\bar{k} = \sqrt{2m_0}\bar{k}$ (raised to the power 4). Hence, in the presence of smooth swell and steep wind-waves, it was found that swell was over-dissipated whereas wind-wave were under-dissipated.

The problem was partly corrected by Bidlot et al. (2007) who redefined $\bar{\sigma}$ and $\bar{k}$ to put more emphasis on the high frequencies:

$$\bar{\sigma} = \frac{1}{m_0}\int_0^{\infty}\int_0^{2\pi}\sigma E(f,\theta)df d\theta \tag{2.46}$$

$$\bar{k} = \left(\frac{1}{m_0}\int_0^{\infty}\int_0^{2\pi}\sqrt{k}E(f,\theta)df d\theta\right)^{2} \tag{2.47}$$

But the deficiencies intrinsic to Komen et al. (1984) model remained, as shown by (Ardhuin et al., 2007). Therefore, the model is not used as defined in Equation (2.43) in the present thesis. Instead, two other models have been used for S_{ds}. Both models are based on a saturation-based formulation

(Alves and Banner, 2003) in which wave components are dissipated when their saturation level B overtakes a saturation threshold B_r.

van der Westhuysen et al. (2007) model

The first one is the van der Westhuysen (VDW) dissipation model (van der Westhuysen et al., 2007), that partly relies on Komen et al. (1984) model, with the following expression:

$$S_{\text{sat}} = -C_{\text{dis,break}} \left(\frac{B(k)}{B_r} \right)^{\frac{p}{2}} \sqrt{gk} E(f,\theta) \tag{2.48}$$

where $B_r = 0.00175$, $C_{\text{dis,break}} = 5.0\ 10^{-5}$ and the saturation level is expressed as follows:

$$B(k) = \frac{1}{2\pi} \int_0^{2\pi} C_g k^3 E(f,\theta) \mathrm{d}\theta = C_g k^3 \frac{E(f)}{2\pi} \tag{2.49}$$

When $B(k) > B_r$, waves break, and the power p is set equal to a constant value p_0:

$$p_0 \left(\frac{u_*}{C} \right) = 3 + \tanh \left[26 \left(\frac{u_*}{C} - 0.1 \right) \right] \tag{2.50}$$

When $B(k) < B_r$, waves do not break and other dissipation processes occur. In that case, p is smoothly set to zero with the function $\zeta(k)$:

$$p = \zeta(k) = \frac{1}{2} + \frac{1}{2} \tanh \left\{ 10 \left[\left(\frac{B(k)}{B_r} \right)^{1/2} - 1 \right] \right\} \tag{2.51}$$

The other dissipation processes are modelled using Komen et al. (1984)'s sink term (S_{K}). The balance between both S_{sat} and S_{K} formulations is given by:

$$S_{\text{ds}}^{\text{VDW}} = f_{br}(f) S_{\text{sat}} + (1 - f_{br}(f))\, S_{\text{K}} \tag{2.52}$$

with $f_{br} = \zeta(k)$.

Ardhuin et al. (2010) model

The second saturation-based model S_{sat}, developed by Ardhuin et al. (2010), is combined with a cumulative breaking term $S_{\text{bk,cu}}$. It has been implemented in the wave model TOMAWAC, described later, during the present thesis. The dissipation model can be expressed as:

$$S_{\text{ds}}^{\text{ST4}}(f,\theta) = S_{\text{sat}}(f,\theta) + S_{\text{bk,cu}}(f,\theta). \tag{2.53}$$

The saturation term can be expressed as follows:

$$S_{\text{sat}}(f,\theta) = -\frac{C_{ds}^{sat}}{B_r}\sqrt{gk}\left\{\delta_d \max[B(k)-B_r,0]^2 + (1-\delta_d)\max[B'(k,\theta)-B_r,0]^2\right\}E(f,\theta) \quad (2.54)$$

Here the saturation level B' is expressed as a normalized velocity variance projected on one direction restricting the projection to the components on the range $[\theta-\Delta_\theta, \theta+\Delta_\theta]$:

$$B'(k,\theta) = \int_{\theta-\Delta_\theta}^{\theta+\Delta_\theta} k^3 \cos^{s_B}(\theta-\theta')E(k,\theta')\mathrm{d}\theta', \quad (2.55)$$

and

$$B(k) = \max\{B'(k,\theta), \theta \in [0, 2\pi[\}. \quad (2.56)$$

The cumulative breaking term accounts for the wave dissipation that occurs when a long wave breaker (k',θ') wipes out a shorter wave (k,θ). The resulting dissipation depends on the relative phase celerity difference $|\boldsymbol{C}-\boldsymbol{C}'|$ between the wave components. It has the following expression (Ardhuin et al., 2010):

$$S_{\text{bk,cu}}(f,\theta) = -1.44 C_{cu}\frac{C_g}{2\pi}E(f,\theta)\int_0^{r_{cu}f}\int_0^{2\pi}\max\left\{\sqrt{B(k',\theta')}-\sqrt{B_r},0\right\}|\boldsymbol{C}-\boldsymbol{C}'|\mathrm{d}\theta'\mathrm{d}k' \quad (2.57)$$

where $C_g = \mathrm{d}\omega/\mathrm{d}k$ is the wave group velocity.

According to Ardhuin et al. (2010), an additional dissipation term S_{out} accounts for the swell dissipation due to the friction with the air over long distances. This term is mandatory when studying wave propagation over distances longer than 1000 km. In the present thesis, this term was not implemented in TOMAWAC because the typical propagation distances are shorter than 200 km.

Ardhuin et al. (2010) adapted S_{in}^{J} to $S_{\text{ds}}^{\text{ST4}}$ with $z_\alpha = 0.006$, $\beta_m = 1.52$ and set a maximum value for z_0 such as $z_{0,\max} = 0.0015$. Furthermore, a sheltering effect (Chen and Belcher, 2000) is taken into account with a new friction velocity $u'_\star$ expressed as a function of the wavenumber:

$$(u'_\star(k))^2 = \left| u_\star^2(\cos\theta,\sin\theta) - |s_u|\int_0^{2\pi}\int_0^k \frac{S_{\text{in}}(k',\theta)}{C}(\cos\theta,\sin\theta)\,\mathrm{d}k'\mathrm{d}\theta \right| \quad (2.58)$$

where $C = \omega/k$ the phase celerity and s_u a sheltering parameter. This sheltering effect is also applied in the high frequency tail. The calculation of the wave stress, in Eq. (2.42), is slightly modified given that the growth rate (γ) resulting from the new friction velocity definition is function of k.

The default values for the calibration parameters according to the "T471" set of parameters given by The WAVEWATCH III (R) Development Group (WW3DG) (2019) are the following:

- Saturation constant: $C_{ds}^{sat} = 2.2\ 10^{-5}$
- Saturation threshold: $B_r = 0.0009$
- Directional width parameter: $\Delta_\theta = 80°$

- Weighting between the isotropic and direction-dependant part of S_{sat}: $\delta_d = 0.3$
- Cumulative breaking constant: $C_{\text{cu}} = -0.40344$
- Sheltering parameter: $s_u = 0.3$

In the present thesis, we focused on the study of bimodal sea-states in infinite depth conditions. To further study the combination of swell and wind-waves in intermediate and shallow waters, the use of parameterizations modelling the dissipation processes from infinite depth to shallow water such as Filipot and Ardhuin (2012) would be of interest.

2.4.2.3 Nonlinear 4-wave interactions

In deep water conditions, ocean waves interact between themselves by resonance. These interactions results in a transfer of energy from one wave component to the other. This energy transfer is conservative: interactions do not add or remove energy from the wave spectrum.

The exact expression of S_{nl} term has been theoretically formulated by Hasselmann (1962) and Zakharov (1968). It consists of a Boltzmann integral for resonant interactions between quadruplets of surface gravity waves. According to Hasselmann (1962, 1963), the theoretical expression can be written as a function of the wave action N as follows:

$$S_{\text{nl}}(N_{\boldsymbol{k}}) = \int_{\boldsymbol{k}_1}\int_{\boldsymbol{k}_2}\int_{\boldsymbol{k}_3} G(\boldsymbol{k},\boldsymbol{k}_1,\boldsymbol{k}_2,\boldsymbol{k}_3)\{N_2N_3(N+N_1) - NN_1(N_2+N_3)\} \times \delta(\boldsymbol{k}+\boldsymbol{k}_1-\boldsymbol{k}_2-\boldsymbol{k}_3)\delta(\omega+\omega_1-\omega_2-\omega_3)d\boldsymbol{k}_1 d\boldsymbol{k}_2 d\boldsymbol{k}_3 \quad (2.59)$$

where $N_j = N(\boldsymbol{k}_j)$, with $j = 1$ to 3, and G is a complex coupling coefficient defined by Hasselmann (1962).

The Dirac functions δ ensures that the energy transfers only occurs when the following resonance conditions are satisfied:

$$\boldsymbol{k} + \boldsymbol{k}_1 = \boldsymbol{k}_2 + \boldsymbol{k}_3 \quad (2.60a)$$

$$\omega + \omega_1 = \omega_2 + \omega_3 \quad (2.60b)$$

Recent references, such as Zakharov et al. (2015), suggests that these interactions play a major role in wind-wave growth. However, the exact calculation of this term requires considerable computing resources. Hence, several methods have been developed to estimate the 4-wave interactions with different levels of accuracy that result in different levels of computational cost. Two of these methods are used in the present thesis:

- DIA (Hasselmann et al., 1985) ($S_{\text{nl}}^{\text{DIA}}$) is the most famous method, due to its determinant role in the development of 3G wave models, but suffers from important shortcomings (e.g. Benoit, 2005).
- The Gaussian Quadrature Method - GQM (Benoit, 2005, 2006; Gagnaire-Renou et al., 2010) ($S_{\text{nl}}^{\text{GQM}}$) is a quasi-exact method computing the 4-wave interactions with a largely improved accuracy compared to DIA. The accuracy level of the method can be chosen by the user with

3 configurations: rough, medium and fine. With the rough configuration, the computing time with GQM is about 50 times longer than with DIA.

2.4.3 Further improvements for bimodal sea-state modelling

In the previous section, recent developments appropriate for the simulation of bimodal sea-states are presented. However, these developments only relate to S_{ds} and S_{nl} terms. Recently, developments with the purpose to improve the estimation of S_{in} have been performed.

Du et al. (2017) developed a wave boundary layer model (WBLM) with the purpose to overcome the shortcomings attributed to Janssen (1991)'s model regarding the overestimation of the wind stress in strong-wind conditions. These shortcomings, already addressed by Ardhuin et al. (2010) through the limitation of the z_0 parameter and the reduction of the wave stress with a sheltering mechanism, is problematic in 3G wave models. In addition to the physical mechanisms taken into account in Janssen (1991)'s model, based on the momentum conservation within the wave boundary layer, Du et al. (2017) model satisfies the conservation of the turbulent kinetic energy (TKE). This model has been implemented in SWAN model (Booij et al., 1999) and showed a wind stress estimation in a closer agreement with measurements than with Janssen (1991)'s model.

Janssen and Bidlot (2021) proposed to further include the effects of nonlinearity in Janssen (1991)'s model. This modification had the effect to reduce the increase of the drag coefficient with wind speed in the range of large wind speeds. This model has been implemented in the WAM version of the ECMWF.

Given the high wind speed considered in both models (U_{10} up to 60 m/s according to Du et al. (2017)), a better estimation of the wind stress in such conditions leads to a better estimation of the momentum transfer from the wind to waves characterized by a low wave-age (C/U_{10}). Hence, these developments might improve the simulation of the HF part of the spectrum in milder wind conditions thus improving bimodal sea-states modelling. Furthermore, when simulating wind-tunnel measurements where the typical wave age is rather low ($C/U_{10} << 1$), these developments might improve the simulations at laboratory scale.

2.4.4 TOMAWAC 3G wave model

TOMAWAC (TELEMAC-based Operational Model Addressing Wave Action Computation), part of the TELEMAC-MASCARET hydro-informatic system, is a 3G wave model developed by EDF R&D within the "Laboratoire National d'hydraulique et Environnement" (LNHE). It was developed by Michel Benoit and Fréderic Marcos between 1995 and 1996 (Benoit et al., 1996). TOMAWAC is used for industrial applications and academic projects by several companies and universities. In particular, the software is commonly used to determine the sea-state conditions impacting coastal areas such as harbours and NPP.

The originality of TOMAWAC lies in the use the finite element method with an unstructured mesh from its initial version back in 1996. The use of this method is rather efficient when meshing coastal domains with a complex contour. Furthermore, the propagation scheme is based on the method of characteristics thus avoiding stability conditions imposed by the Courant number. Further details

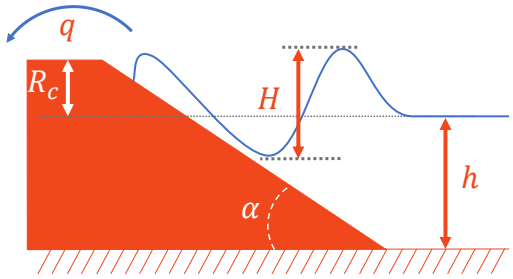

Figure 2.11: Sketch of the wave overtopping process over a breakwater.

regarding the spectro-angular discretization, the solver and the integration of the source terms in TOMAWAC can be found in TOMAWAC User manual (2022).

2.5 Design of coastal protection

Using 3G wave models, the wave spectrum of a sea-state impacting a coastal protection can be predicted. Based on a spectral analysis, the sea-state is usually characterized by parameters such as the significant wave height (H_{m_0}), a representative period (e.g. $T_{m_{-1,0}}$) and the associated mean wave direction. These parameters, describing the sea-state conditions, are required in the design of coastal protections. As a reminder, in the present thesis, the breakwater design is based solely on the wave overtopping process. It should be noted that this consideration is not sufficient to treat in an exhaustive way the problems of design of such structures.

2.5.1 Definitions

The wave overtopping rate q is a key parameter when designing a coastal protection. As shown in Figure 2.11, it characterizes the average water discharge per linear meter. It is usually expressed in m^2/s or in l/s/m. Since the wave overtopping process is highly variable in time and space in real (irregular) wave conditions, q is usually averaged over a long period of time. According to references such as EurOtop (2018) (Van der Meer et al., 2018), this period of time is ideally longer than 1000 wave periods relative to the largest peak period in the wave spectrum (e.g. the swell period in the case of bimodal sea-states).

Once the sea-state conditions are known and the admissible wave overtopping is defined in a specific coastal area, the general shape of the breakwater can be estimated using empirical formulas (see Chapter 5) and dedicated manuals (CIRIA, 2007; Van der Meer et al., 2018). Figure 2.11 shows an example of breakwater profile. The main parameters that determine the wave overtopping rate are the structure freeboard R_c, the slope angle α, the breaker parameter ξ (or Iribarren number) and the breakwater composition. As illustrated in Figure 2.11, R_c is the height of the breakwater relative to MWL. The breaker parameter is used to characterize the different types of wave breaking

and to take into account the effect of the wave period on wave overtopping. It is defined as follows:

$$\xi = \frac{\tan \alpha}{\sqrt{s_m}} \tag{2.61}$$

with s_m the representative wave steepness defined in Equation (2.26).

Depending on the material used for the breakwater construction, the core of the structure can either be permeable or impermeable. Several kinds of materials can be used to cover the breakwater surface in order to improve the damping of the wave energy. For that purpose, rocks of different sizes or shaped blocks (Antifer cubes, Tetrapode, etc) are commonly used to change the roughness, porosity and permeability properties of the slope surface. Then, the stability of the roughness elements under the wave action must be considered as a function of α. Manuals (e.g. CIRIA (2007)) give recommendations regarding the stability of such structures.

2.5.2 Physical modelling

The most common approach to estimate the wave overtopping rate associated to a specific coastal protection under different sea-state conditions consists in performing laboratory experiments with a breakwater model. Froude similarity is used to convert the prototype dimensions at model scale. According to Van der Meer et al. (2018), water depths in the model should be much larger than $h = 2.0$ cm, wave peak periods larger than $T_m = 0.35$ s and wave heights larger than $H_{m_0} = 5.0$ cm to avoid the effects of surface tension.

Most of the empirical formulas to estimate the wave overtopping rate as a function of the wave and the structure properties are based on a regression analysis based on experimental data. Since each run, with a duration equal or longer than 1000 wave periods, is repeated several times, the measurements of the wave overtopping rate can be considered as a stochastic process. Hence, the uncertainties of the estimations can be evaluated with a 90%-confidence band (or 5%-exceedance lines). Making the hypothesis that the data follow a Gaussian distribution centered on the empirical formula obtained with the regression analysis, the 90%-confidence band can be calculated using $\mu \pm 1.64\sigma$ where μ is the value of the parameter obtained from the regression analysis and σ is the standard deviation of the parameter.

When studying the impact of waves on a breakwater, it is necessary to deal with the waves reflected by the structure. Some wavemakers are equipped with an active absorption of these reflected waves. It is not the case of the wavemaker of the wind-wave tunnel of the OSU Institut Pythéas. Hence, the incident waves impacting the breakwater were obtained using a reflection analysis. Among the several methods existing to identify the incident and reflected wave, the type of analysis performed in the present thesis is based on linear wave theory using a least square method on a grid of N wave gauges (Goda and Suzuki, 1976). The N wave gauges are located considering the representative wavelength of the measured waves. For a unimodal spectrum representing unidirectional waves with a peak wavelength λ_p, a minimum of 3 wave gauges should be used with the second and third gauges located at a distance $\lambda_p/4$ and $\lambda_p/3$ (respectively) from the first gauge in the wave direction.

2.5.3 Empirical formulas for bimodal spectrum

To design coastal protections, engineers must be able to predict wave overtopping rates associated to the characteristics of the protections and of the sea-states conditions. For that purpose, numerous laboratory experiments have been carried out with breakwaters models to measure wave overtopping rates in diverse configurations. Based on a dimensional analysis, several semi-empirical formulas have been developed to estimate a non-dimensional wave overtopping rate q^* as a function of a non-dimensional freeboard height R_c^*. The characteristics of the sea-states conditions are included in the formula through the definition of non-dimensional parameters. One of the most recent formula can be found in EurOtop (2018) manual (Van der Meer et al., 2018). Its most simple expression (i.e. for non-breaking waves) is the following:

$$q^* = a \exp\left(-b \left[\frac{R_c^*}{\prod \gamma_i}\right]^c\right) \tag{2.62}$$

with a, b and c three design coefficients and $\prod \gamma_i$ a product of coefficients accounting for specific configurations such as a rough breakwater slope (e.g. with a rock-armour) or direction of incident waves.

The reader is referred to Section 5.1 to find more details about the state-of-the-art regarding the estimation of the wave overtopping rates in bimodal sea-state conditions.

Chapter 3

Influence of following, regular, and irregular long waves on wind-wave growth with fetch: an experimental study

by A. Villefer, M. Benoit, D. Violeau, C. Luneau and H. Branger

Journal of Physical Oceanography, 51(11), 3435 – 3448, 2021.
doi: https://doi.org/10.1175/JPO-D-21-0050.1

Une série d'expériences a été menée dans un canal-soufflerie à Marseille pour étudier l'influence de la présence de houle (représentée par des vagues longues, générées mécaniquement) sur la croissance du clapot dans des conditions de fetch limité. Diverses conditions océaniques et atmosphériques ont été simulées via la génération de houles monochromatiques et irrégulières (avec un spectre de type JONSWAP) en présence de différentes vitesses de vent. Une analyse spectrale des états de mer combinée à des mesures du flux d'air a permis d'étudier l'évolution des deux systèmes de vagues afin d'identifier les mécanismes d'interaction transposables à l'échelle prototype (i.e. océanique ou côtière). En particulier, une méthode originale est utilisée pour séparer les deux systèmes de vagues dans les spectres bimodaux mesurés. Dans des conditions de fetch limité et en absence de houle, la croissance du clapot diffère des observations expérimentales en termes de variations d'énergie et de fréquence avec le fetch. Comme cela a été observé lors d'expériences antérieures, une houle monochromatique provoque une forte réduction de l'énergie du clapot. En revanche, la présence d'un train de houle de type JONSWAP entraîne un décalage du pic de clapot vers les basses fréquences, sans réduction significative de son énergie. Dans l'ensemble, on observe que la présence de houle affecte les variations spatiales de l'énergie et de la fréquence pic du clapot. Enfin, en présence d'un train de houle de type JONSWAP, les variations de l'énergie et de la fréquence de pic du clapot en fonction du fetch semblent étroitement en accord avec la croissance du clapot observée en laboratoire.

Abstract

A series of experiments were conducted in a wind-wave tank facility in Marseilles (France) to study the effects of preexisting swell conditions (represented by long mechanically generated waves) on wind-wave growth with fetch. Both monochromatic and irregular (JONSWAP-type) long-wave conditions with different values of wave steepness have been generated in the presence of a constant wind forcing, for several wind velocities. A spectral analysis of temporal wave signals combined with airflow measurements allowed for the study of the evolution of both wave systems with the aim of identifying the interaction mechanisms transportable to prototype scale. In particular, a specific method is used to separate the two wave systems in the measured bimodal spectra. In fetch-limited conditions, pure wind-wave growth is in accordance with anterior experiments, but differs from the prototype scale in terms of energy and frequency variations with fetch. Monochromatic long-waves are shown to reduce the energy of the wind-waves significantly, as it was observed in anterior laboratory experiments. The addition of JONSWAP-type long-waves instead results in a downshift of the wind-wave peak frequency but no significant energy reduction. Overall, it is observed that the presence of long-waves affects the wind-wave energy and frequency variations with fetch. Finally, in the presence of JONSWAP-type long-waves, variations of wind-wave energy and peak frequency with fetch appear in close agreement with the wind-wave growth observed at prototype scale both in terms of variations and nondimensional magnitude.

3.1 Introduction

The infinite diversity of waves in the ocean makes the understanding of the complex sea-states dynamics rather difficult. Numerous experimental studies both in the field and in laboratories have been carried out over the last decades to improve the knowledge on the particular case of bimodal sea-states or more precisely on wind-wave and swell combination. Many field measurements (Donelan et al., 1997; Hwang et al., 2011; Vincent et al., 2019) show evidence of a modified wind-wave generation in the presence of swell. However, field experiments can hardly be generalized due to the specific wind and atmospheric conditions varying from one experiment to another. In wind-wave tank facilities, wind-wave and swell combination can be studied in controlled conditions using a wave-maker (e.g. a mechanically actuated paddle) for representing swell and a closed-loop air circulation to produce a quality airflow creating short wind-waves above the long mechanically-generated waves (paddle-waves). Thereby, both wave systems are sufficiently separated in frequency to observe a bimodal sea-state. A series of experiments was conducted in a well-controlled laboratory environment in Marseilles (France) with two objectives. The first one was to identify the mechanisms at stake in the interaction between the two wave systems. Assessing the extent at which those mechanisms can be transposed to wind-wave growth in the ocean was the second objective.

The wind-wave generation over a train of long monochromatic paddle-waves propagating along the wind direction is a well-documented experimental configuration (Donelan, 1987; Mitsuyasu, 1966; Phillips and Banner, 1974). In these conditions, a drastic reduction on the energy density of the wind-wave component is unanimously observed. The intensity of this reduction increases with the

long-wave steepness ak (where a is the wave amplitude and k the wave number). Donelan (1987) found a windsea elevation variance reduced by a factor of about 2.5 in presence of long-waves. A similar experiment by Mitsuyasu and Yoshida (1991) with long-waves propagating opposite to the wind direction revealed wind-wave height intensification. More recently, Benetazzo et al. (2019) and Bailey et al. (2020) carried out experiments (in an open-air basin without a closed-loop airflow in the case of Bailey et al.) on wind over irregular (JONSWAP-type) paddle-waves. These latter experiments also showed a reduced wind-wave growth.

Variance density spectrum $E(f, \theta, x, t)$ at a location x and a time t, with f and θ are respectively the wave frequency and direction, is a powerful manner to describe wind-wave growth. For infinite depth, the evolution of $E(f, \theta, x, t)$ is governed by the spectral energy balance involving source/sink terms $S(f, \theta, x, t)$:

$$\frac{dE}{dt} = S_{in} + S_{ds} + S_{nl} \tag{3.1}$$

The left hand side is the kinematic part of the equation while the right hand side includes three source/sink terms corresponding to wind energy input S_{in}, dissipation through white-capping S_{ds} and nonlinear four-wave interactions S_{nl}. Note that among these terms, only the latter one is explicitly formulated based on a weakly nonlinear theory (Hasselmann, 1962) while the formulations used for S_{in} and S_{ds} rely on semi-empirical parametrizations of complex sea-atmosphere interaction processes (see Cavaleri et al. (2007) for a review and discussion of these terms).

Experiments of wind over monochromatic mechanically-generated waves propagating in the same direction have received a lot of attention to provide a physical explanation to wind-wave reduction and to consider at what extent this effect could appear at natural scale. First, the hypothesis of an enhanced wave breaking of the windsea, represented by S_{ds}, due to the addition of wind drift and long-wave orbital velocities, was suggested by Phillips and Banner (1974). This suggestion was later tempered by Wright (1976) arguing that enhanced wave breaking could not account for the magnitude of wind-wave reduction in the case of high wind velocities. According to Masson (1993), nonlinear four-wave interactions (i.e. S_{nl}) is also involved in the physical evolution when the ratio of long-waves over short-waves frequencies is greater than 0.6. This ratio discriminates the interaction between wind-waves and swell in the ocean (ratio lower than 0.6) and in most laboratory experiments (ratio greater than 0.6).

Chen and Belcher (2000) developed a model based on a sheltering effect of the long-waves absorbing momentum from the wind, thus reducing the available momentum for wind-wave generation (i.e. S_{in}). Their model delivered results in accordance with laboratory experiments but closely depending on the growth rate coefficient β formulated by Miles (1957) as $S_{in} = \beta E$, which is known to be highly variable, especially at laboratory scale. The growth rate coefficient itself depends on the long-wave age, $C/u_\star$, with C the long-wave (phase) celerity, $u_\star = (\tau/\rho)^{1/2}$ the friction velocity with τ the total turbulent shear stress at the air-water interface and ρ the air density. Chen and Belcher's results suggest that the wind-wave reduction observed in laboratory environment with young waves ($C/u_\star << 20$) would probably not occur with older ocean swell for which $C/u_\star > 20$. More directly, Chen and Belcher's model predicts that the sheltering effect occurs when the long-waves are, to a good extent, slower than the wind. Lately, Donelan et al. (2010) attributed the wind-wave reduction to both the modified airflow (i.e. S_{in}) and the orbital velocity gradients in the presence of the long-waves.

In our experiment, short waves were generated by the wind in a large closed-loop wind/wave tank facility, and long-waves were generated with a wave-maker, with both cases of monochromatic waves and irregular (JONSWAP-type) waves. All the measurements were carried out on a fetch-limited wave field. The fetch limited case is a generic case of spatial wave evolution consisting in a steady wind forcing over a statistically stationary wave-field. The statistical wave-field can be related to the wave-spectrum notion.

In order to compare our experimental results with other laboratory experiments and field observations, an appropriate scaling has to be applied. Following Kitaigorodskii (1961), the parameters describing wind-wave growth are the total variance of the free-surface elevation $m_0 = \overline{\eta^2}$ and the peak frequency f_p as a function of the fetch X. Those variables are made dimensionless using the friction velocity $u_\star$ and the acceleration due to gravity g:

$$f_p^* = \frac{f_p u_\star}{g} \tag{3.2}$$

$$m_0^* = \frac{m_0 g^2}{{u_\star}^4} \tag{3.3}$$

$$X^* = \frac{X g}{{u_\star}^2} \tag{3.4}$$

Although the wind speed 10 m above the mean free surface $U_{10} = U(z = 10\ \mathrm{m})$ is usually employed as a scaling wind speed, the friction velocity is chosen here since it does not depend on height and it better represents the momentum transfer at the air/water interface (Janssen, 2004).

The facility and the data processing methods are introduced in Section 3.2. The wind profiles determined in presence and in absence of paddle-waves, used as a scaling tool for the subsequent analyses, are presented in section 3. The growth of wind-waves is measured and processed in absence of long-waves in section 4, then in presence of monochromatic waves in section 5 and finally with irregular waves in section 6. A comparison of these different cases and their relation with the prototype scale are discussed in section 7. Section 8 gives a summary of results and their application, followed by a further discussion on future studies on the topic.

3.2 Experimental Facility and Data Processing

3.2.1 The Facility

The IRPHÉ/Pythéas wind-wave tank, see Figure 3.1, consists of a closed-loop tunnel for air circulation with a 1.5-m-high air cavity above a basin with a test section 40-m-long and 2.60-m-wide (sketched in Figure 3.2). The water depth h, set to 0.80 m, was kept constant during all the experiments. For a complete description of the facility, one can refer to Coantic et al. (1981). The wind is generated by an air blower in the upper part of the tunnel and guided through a settling chamber with a honeycomb and a converging nozzle ; this system produces a uniform airflow at the entrance of the water basin. At the upwind end of the basin, an immersed paddle wave-maker (piston-type) can be used for generating either monochromatic or irregular waves propagating along the wind direction. At the downwind end, a permeable absorbing beach with a 6-degrees-slope was installed

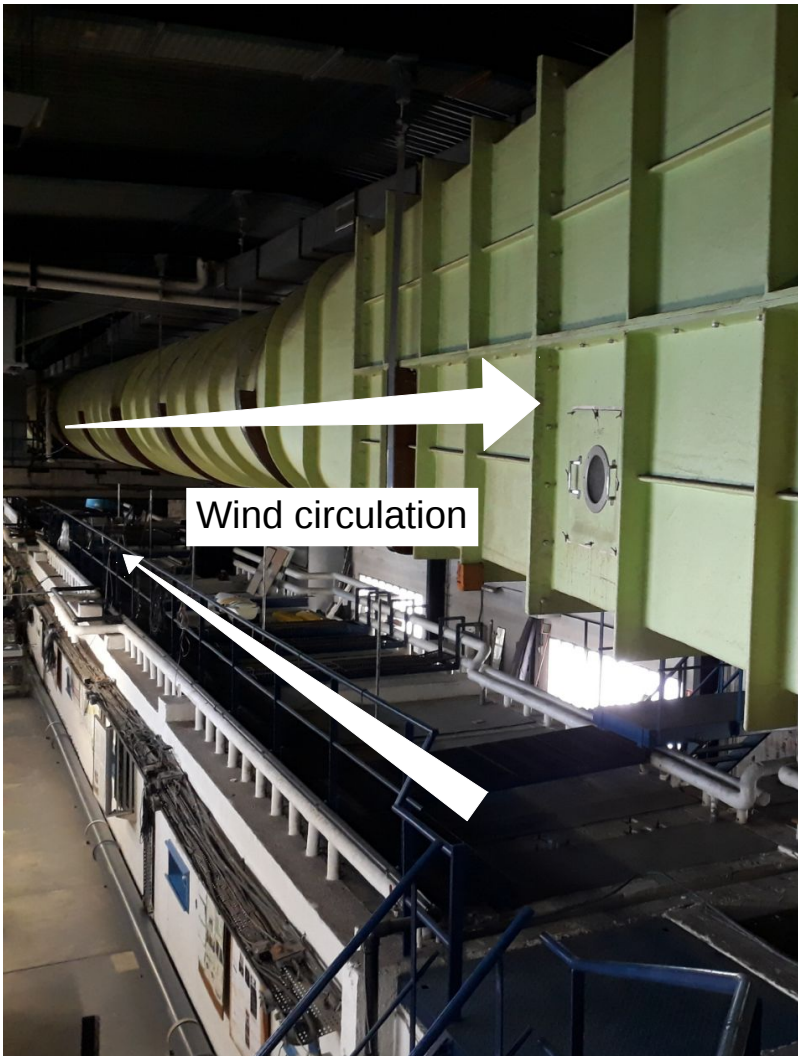

Figure 3.1: Upwind view of the IRPHÉ/Pythéas wind-wave tank in Marseilles. The top and left sides of the closed water+air tunnel can be seen in the lower part of the picture, while the green pipe in the upper part is part of the recirculating air tunnel (see text for additional description).

to minimize wave reflection. The basin side walls are punctuated with windows to observe the water surface. A larger 5-m-long clear glass is situated at the 25-m-fetch to perform measurements that require a sight on the water surface.

For these experiments, eight resistance-type and four capacitance-type wave gauges were distributed along the basin (Figure 3.3) to measure the instantaneous free surface elevation η with a precision of 4.10^{-4} and 2.10^{-4} m respectively. Note that the wave gauges distribution is not uniform: the distance between two consecutive gauges decreases at large fetch (Figure 3.2). Two anemometers were situated in front of the clear glass at a 25-m-fetch (Figure 3.2 and 3.3). Wind reference velocity U_{ref} was measured at approximately 0.5 m above the water surface with a Gill 2D sonic anemometer.

An additional hot film anemometer from E+E Electronik supported by a vertical telescopic pole allowed to measure the vertical profile of the mean (i.e. time averaged) horizontal velocity $U(z)$.

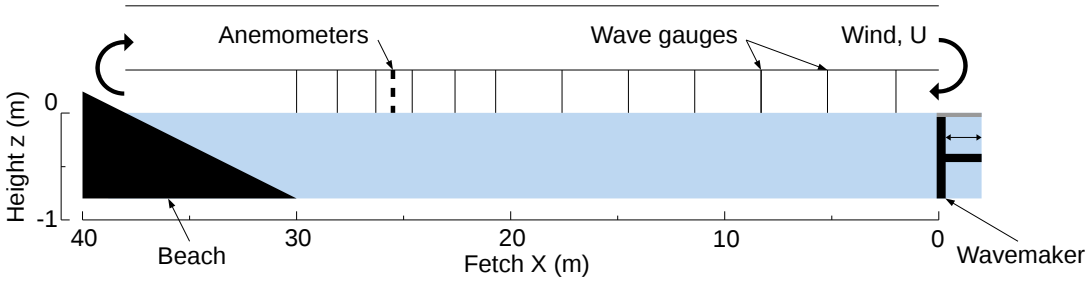

Figure 3.2: Sketch of the IRPHÉ/Pythéas wind-wave tank facility showing the location of the measuring devices. The vertical exaggeration is × 5.

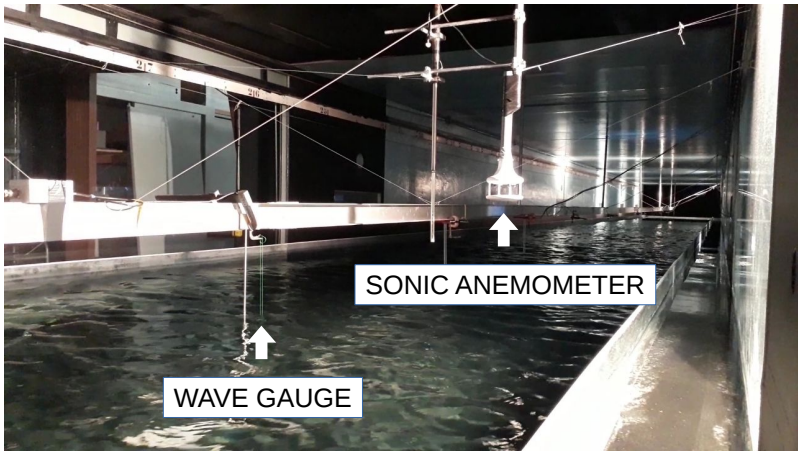

Figure 3.3: Downwind view of the inside of the wind-wave tank with a generic case of long monochromatic paddle-waves and short wind-waves.

Friction velocity and aerodynamic roughness z_0 are determined by fitting the logarithmic profile (see Section 3.3) to the vertical time-averaged wind profile in neutral atmospheric conditions for all the experiments (air and water were roughly at the same temperature). The friction velocity is considered constant along the test section because of the slightly divergence of the air section along the wind-wave tank allowing a zero pressure longitudinal gradient.

Apart from the air blower controlled with a graduated potentiometer, the control of the wave-maker and all the gauges output signals were gathered on a computer using a LabView program. Wind velocity could be generated between 2 and 14 m.s^{-1} (U_{ref}) by regulating the potentiometer.

In order to generate waves, the required temporal free surface elevation was convoluted with the wave-maker transfer function, and then transferred as a voltage signal from the computer to the piston wave-maker, converting the input signal to actual waves. Both regular (Stokes-type) and irregular (JONSWAP-type) wave trains were generated. The JONSWAP spectrum is given by:

$$E(f) = \alpha_p {H_s}^2 \frac{f_p^4}{f^5} \exp\left[-\frac{5}{4}\left(\frac{f_p}{f}\right)^4\right] \gamma^{\exp\left[-\frac{(f-f_p)^2}{2\sigma^2 {f_p}^2}\right]} \tag{3.5}$$

where, using the JONSWAP's recommendations (Hasselmann et al., 1973), $\sigma = 0.07$ for $f < f_p$

and $\sigma = 0.09$ for $f > f_p$, $\gamma = 3.3$ is the peak enhancement factor and $\alpha_p = 0.2$ is the Phillips constant. The significant wave height H_s and the peak frequency f_p are the parameters to adjust in order to obtain the desired sea-state.

To generate the time series of irregular waves, inverse FFT (Fast Fourier Transform) transforms of the complex amplitudes from the JONSWAP spectra (using random phases) were used over the frequency range [0.4-4.0] Hz. This wide range of frequency, which is the recommended mechanical range for the wavemaker, was necessary in order to obtain a smooth transition between the JONSWAP peak and the high frequency waves. However, the wave-maker was able to accurately generate a sea-state corresponding to a JONSWAP-type spectrum over the frequency range [0.4-2.0] Hz. Above 2 Hz the energy distribution could slightly deviate from the f^{-5} desired tail.

Acquisition of wave gauges signals were launched from the computer for a 20 minutes duration at the sampling rate 256 Hz. Before every acquisition, it was verified that the waves in the wave tank were in stationary fetch-limited conditions by waiting a sufficient long time before acquiring data. During the experiments with wind, the instantaneous horizontal wind velocity was measured using the hot film anemometer from the lower point above the water surface (i.e. slightly above the highest wave) at about ten vertically distributed points over a range of 20 cm and a duration of 240 s to obtain the vertical profile of the mean horizontal velocity. In order to be able to differentiate swell from wind-waves, the mechanically-generated wave frequency (respectively the peak frequency for irregular waves) was chosen equal to 0.6 Hz. This choice accounts for the wind-waves lower peak frequency reaching 1 Hz at maximum fetch and maximum wind velocity.

Using the dispersion relation for the long-waves, the non-dimensional depth $kh = 1.33$ corresponds to intermediate water depth. Thus, bottom friction slightly dissipates the paddle-waves as they propagate along the tank. Bottom friction and additionnal dissipation mechanisms, such as sidewalls friction, that occur in laboratory experiments have been quantified using Dorn's formula (Dorn, 1966). At the downwind end of the tank, more than 95 % of the long-wave energy is conserved. Wind-waves, however, are short enough ($kh > 3$) to be considered as propagating in deep water and unaffected by bottom friction. Wind-wave dissipation by sidewalls remains weak since their wavelenghts is much smaller than the channel width (Shemer, 2019). Overall, the dissipation due to bottom and sidewalls friction is relatively low and is not further considered in the present study.

Table 3.1 gathers the characteristics of all the tests presented in this paper.

3.2.2 Spectral Separation Methods

A spectral approach was chosen to characterize the interaction between wave systems. Spectra were calculated using the Welch method (Welch, 1967) by partitioning the surface elevation time records into shorter records of 16384 points with a 50 % overlap and a Hanning windowing. Depending on the sea-states, the resulting spectra were unimodal (wind-waves only, irregular swell only) or multimodal (monochromatic swell with harmonics, swell and wind-waves combination). Separating wave systems in multi-modal sea-states is necessary to have access to their individual characteristics (e.g. significant wave height, peak period, spectral width) in order to compare windsea growth with and without swell for instance. In the literature, this separation is commonly performed using a

U_{ref} (m.s^{-1})		6	10	14
U_{10} (m.s^{-1})		9	13	20
$u_\star$ (m.s^{-1})		0.31	0.48	0.88
$z_0 \times 10^4$(m)		1.4	1.6	9.3
Swell type	ak (%)		$(b \times 10^4, c)$	
Monochromatic	5.6	$(0.13, 1.28)$	$(0.59, 1.05)$	-
	2.7	$(2.00, 0.99)$	$(0.31, 1.29)$	$(4.61, 0.82)$
	0.0	$(\mathbf{0.02}, \mathbf{1.64})$	$(\mathbf{0.11}, \mathbf{1.50})$	$(\mathbf{0.52}, \mathbf{1.30})$
Irregular	2.7	$(2.16, 1.01)$	$(0.96, 1.17)$	$(1.27, 1.18)$
	4.1	$(2.68, 1.01)$	$(7.56, 0.90)$	$(5.47, 0.91)$
Swell type	ak (%)		(d, g)	
Monochromatic	5.6	$(0.60, -0.28)$	$(0.64, -0.30)$	-
	2.7	$(1.68, -0.42)$	$(1.27, -0.38)$	$(0.86, -0.33)$
	0.0	$(\mathbf{3.46}, \mathbf{-0.50})$	$(\mathbf{1.36}, \mathbf{-0.39})$	$(\mathbf{0.89}, \mathbf{-0.33})$
Irregular	2.7	$(0.06, -0.01)$	$(0.28, -0.20)$	$(0.34, -0.22)$
	4.1	$(0.11, -0.11)$	$(0.07, -0.02)$	$(0.21, -0.14)$

Table 3.1: Wind characteristics and corresponding power law coefficients representing the fetch dependence of windsea peak frequency and energy ($m_0^* = b(X^*)^c$ and $f_p^* = d(X^*)^g$). The lines with bold characters refer to the pure windsea cases.

transition frequency that divides the wave spectrum in two parts: swell and windsea. That method works while the peaks of both wave systems are sufficiently separated. In some cases, as it will be shown in this paper, windsea and swell components are overlapping, making difficult the separation with the former method. Two methods to separate the mechanically-generated wave part from the wind-wave part of multi-modal spectra are introduced in this section. The first method deals with the multi-modal sea-states with a monochromatic swell. The second method refers to multi-modal sea-states with a JONSWAP-type swell. Both methods are based on curve-fitting using a nonlinear least square method, and are described below.

The generation of monochromatic long-waves with the wave-maker leads to the generation of additional super-harmonic waves in intermediate depth conditions. These harmonics occupy the same frequency range as the windsea making difficult the distinction between the proper energies and peak frequencies of these overlapping systems. The first stage of the method consists in the removal of the spectral bands containing the frequencies of the monochromatic wave harmonics into the initially measured multi-modal spectrum. The removed number of points depends upon the width of the corresponding harmonic peaks. Thus, although the wind-wave peak then becomes discontinuous at this stage, its shape is conserved. The next stage is to fit the discontinuous wind-wave spectral peak with a JONSWAP-type spectrum initialized with the triplet $(f_p, H_s, \gamma = 3.3)$. The significant wave height H_s is equal to the integral of the spectrum and the peak frequency f_p is equal to the maximum value of the spectrum. The fitted JONSWAP-type spectrum enables to access the energy and the peak frequency of the wind-wave part of the spectrum. Then, the harmonic-only part of the spectrum can be obtained by subtracting the fitted wind-wave part from the measured multi-modal spectrum.

A spectrum combining irregular-swell and wind-waves can be decomposed using the following

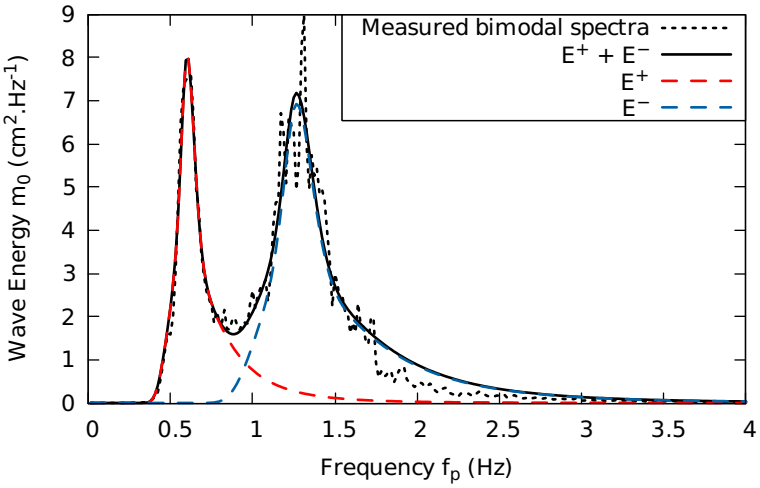

Figure 3.4: Example of spectral separation for a spectrum obtained at a 30-m-fetch with a wind of 10 m.s^{-1} in presence of irregular long-waves of 2.7 % steepness. E^+ and E^- are respectively the JONSWAP fit of the higher and the lower peaks.

procedure inspired from Mackay (2011). First, a unimodal JONSWAP-type spectrum E^+ (see (3.5)) is fitted on the bimodal measured spectrum E_m using the triplet $(f_p^+, H_s^+, \gamma^+ = 3.3)$ as initial values: H_s^+ is determined using the integral of E_m and f_p^+ is equal to the frequency of the higher peak. For this first fit, the peak frequency is a constant parameter in order to fit the higher peak only. The resulting fitted triplet is $(f_p^+, H_s^{+\prime}, \gamma^{+\prime})$ (the prime denoting the fitted parameters). A second triplet $(f_p^-, H_s^-, \gamma^- = 3.3)$ is used as initial value to fit the second (i.e. the lower) peak with H_s^- from the integral of $E^- = E_m - E^+$ and f_p^- as the peak frequency of E^-. Finally, the sum of two JONSWAP-type spectra (i.e. bimodal) $E^- + E^+$ is fitted on the bimodal measured spectrum E_m using both (f_p^-, H_s^-, γ^-) and $(f_p^+, H_s^{+\prime}, \gamma^{+\prime})$ as initial values of the least square algorithm. Thus, the measured spectrum is decomposed in two JONSWAP-type spectra permitting to determine the energy and peak frequency of each wave system.

An illustration of the spectral separation of a measured bimodal spectrum is given in Figure 3.4. The figure shows that the spectra resulting from the spectral separation are an accurate fit for both long-wave and wind-wave peaks but slightly deviate from the measured spectrum in the high frequency range. It is also interesting to note the slight reduction of wind-wave energy at the peak of the wind-wave spectrum whether the spectrum is separated or included in the bimodal spectrum. This last observation proves the necessity of a proper separation of each wave system in a multi-modal measured spectrum so that they can be compared to the wave systems observed individually in unimodal measured spectra as it will be performed in the following.

3.3 Estimation of the Vertical Wind Profile

Among the numerous methods for estimating wind fluxes, the profile method was used for this experiment. Thus, the airflow above water waves is considered analogous to that above a stationary rough surface. Assuming a constant flux layer and using the Monin and Obukhov (1954) turbulence

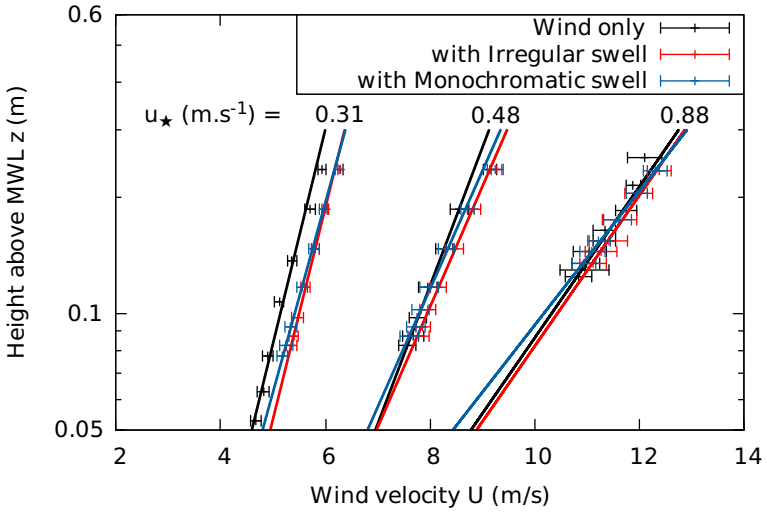

Figure 3.5: Vertical profiles of the averaged horizontal wind velocity with and without paddle-waves associated logarithmic fits. The corresponding friction velocities values (mean slope of the fitted lines) are indicated for each wind only cases.

similarity theory, the vertical velocity wind profile is assumed logarithmic and may be written as:

$$U(z) = \frac{u_\star}{\kappa} \ln\left(\frac{z}{z_0}\right) \tag{3.6}$$

where $\kappa = 0.41$ is the von Karman constant, z is the coordinate on a vertical axis pointing upwards with origin at the mean water level (MWL) (see Figure 3.2) and z_0 is the aerodynamic roughness. The measured vertical evolution of the mean horizontal wind velocity is fitted with the logarithmic turbulent velocity profile (3.6). In that way, the friction velocity and the aerodynamic roughness are found for cases with and without paddle-waves.

Figure 3.5 displays the vertical profiles of the averaged horizontal wind velocity with and without paddle-waves, for monochromatic and irregular waves. The measured wind velocities have an overall tendency to increase when paddle-waves are present. Regarding the fitted logarithmic profiles, paddle-waves have a trend to increase the friction velocity, thus inducing an increase in the total shear stress τ at the air/water interface. This observation is not surprising since the wind stress is mainly supported by waves traveling slower than the wind, which is the case for both wind-waves and paddle-waves in our experiments. Those results are in disagreement with Chen and Belcher (2000) who designed a model for the reduction of wind-waves due to long monochromatic waves based on the absence of variation of the total stress with long-wave steepness.

However, the large error-bars corresponding to the standard deviation in the calculation of the mean horizontal velocity depicted in Figure 3.5 show the uncertainties associated with the logarithmic fit. Thus, there is a high degree of uncertainty in the estimation of $u_\star$. Regarding the measurements, two evaluations of the friction velocity in the same experimental conditions could lead to a 20 % variation in the results. Additionally, water sprays at high wind speed (e.g. $U_{\text{ref}} = 14$ m.s^{-1}) could invalidate the measurements by reaching the hot film and cooling down its temperature, thus measuring abnormally high velocities. Overall, the use of the logarithmic profile method

to determine the friction velocity and the aerodynamic roughness seems questionable since the presence of long-waves propagating slower than the wind is prone to invalidate the analogy with the airflow above a stationary rough plate. A method free from the logarithmic profile hypothesis, such as the eddy-correlation method using a thin cross-X hot wire anemometer, would be more adapted for the characterization of the airflow in the presence of paddle-waves; this is left for further work.

Due to the uncertainties previously mentioned, the measured data will be scaled using a unique friction velocity for each wind speed. This friction velocity is determined using the profile method on pure windsea cases (see Figure 3.5). Thus, the measurement uncertainties added by the presence of long-waves are avoided, and possible effects of such waves on the wind friction velocity will be ignored. Shemer (2019) observed that the friction velocity does not depend notably on the fetch in a similar fetch-limited case. Using this latter observation in our study, the friction velocity is assumed to be constant along the fetch with an impact of the surface drift velocity considered as negligible (Shemer, 2019).

3.4 Wind-Wave Growth

This section aims to verify the similarities on fetch-limited wind-wave growth between our results, anterior laboratory experiments and ocean measurements. In this section, experimental data with wind only (i.e. without mechanically-generated waves) are analyzed.

Laboratory experiments are, on one hand, necessary to facilitate the understanding of wind-wave growth through controlled conditions. On the other hand, limitations are present due the limited size and the peculiarities from a wave tank to another. To quantify these limitations, fetch-limited cases of wind-wave growth under four increasing wind velocities have been carried out in the wind-wave tank. In Figure 3.6, the evolution of the measured dimensionless wind-wave energy and peak frequency are plotted and compared to two selected empirical laws. The first one is Mitsuyasu and Rikiishi (1978) law exclusively based on laboratory experiments:

$$m_0^* = 4.49 \times 10^{-5} (X^*)^{1.282} \quad \text{and} \quad f_p^* = 1.19 (X^*)^{-0.357} \tag{3.7}$$

The second one is Kahma and Calkoen (1992) law for stable stratification (adapted to friction velocity scaling from Komen et al. (1994)) obtained from a collection of laboratory and ocean data:

$$m_0^* = 7.3 \times 10^{-4} (X^*)^{0.85} \quad \text{and} \quad f_p^* = 0.477 (X^*)^{-0.26} \tag{3.8}$$

Figure 3.6 shows the differences in wind-wave growth depending on the wind speed in our experiments. At high wind speed, $U_{\text{ref}} \geq 10$ m.s^{-1}, energy and peak frequency exhibit a linear evolution with fetch in log-log coordinates confirming a power law behavior. Additionally, this power law appears to be in accordance with Mitsuyasu and Rikiishi (1978)'s law.

At lower wind speed, water surface tension affects the evolution of wind-wave energy (Figure 3.6.a), especially because most of the waves are short, hence in the capillary-gravity range, where surface tension strongly modifies the wave dynamics. The case $U_{\text{ref}} = 6$ m.s^{-1} is characterized by a two-

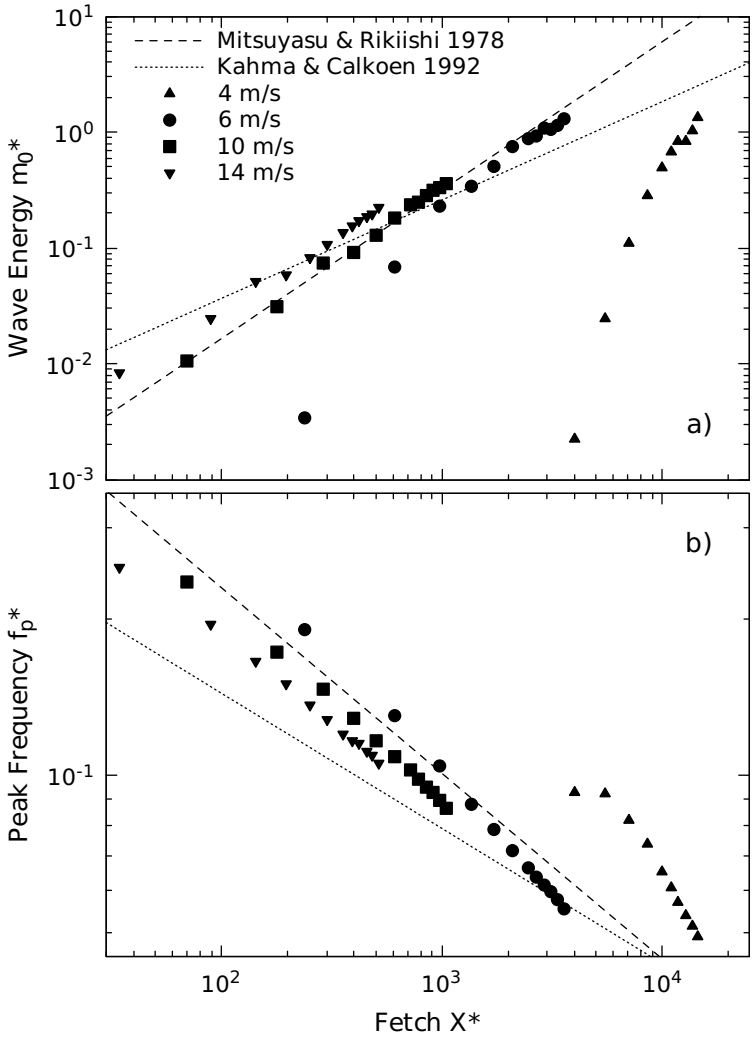

Figure 3.6: Variations of dimensionless wave energy (a) and peak frequency (b) with dimensionless fetch for different reference wind speeds (U_{ref}) compared to empirical laws.

stage evolution that clearly appears in the energy variation: the first stage, $X^* < 10^3$, shows a strong slope which is attenuated, in a second stage, at larger fetches. Surface tension impact thus decreases gradually as the waves grow. The second stage, $X^* > 10^3$, is linear and parallel to Mitsuyasu and Rikiishi's power law indicating that the surface tension effect on waves is lower. Wind-waves generated by a 4 m.s^{-1} wind deviate markedly from both the experimental curves for higher wind speeds and empirical laws: surface tension seems to have a significant effect in that case.

Moreover, both dimensionless energy and peak frequency magnitudes agree reasonably well with Kahma and Calkoen's law. The differences with this latter law lie in the variations of the variables with fetch. Since Mitsuyasu and Rikiishi's law is a good fit for our experimental data variations, absolute value of the power coefficients from Kahma and Calkoen's law (0.85 for the energy, 0.26 for the peak frequency in (3.8)) appear somewhat too low to accurately describe laboratory data (corresponding exponents are 1.282 for the energy, 0.357 for the peak frequency in (3.7)). Recently,

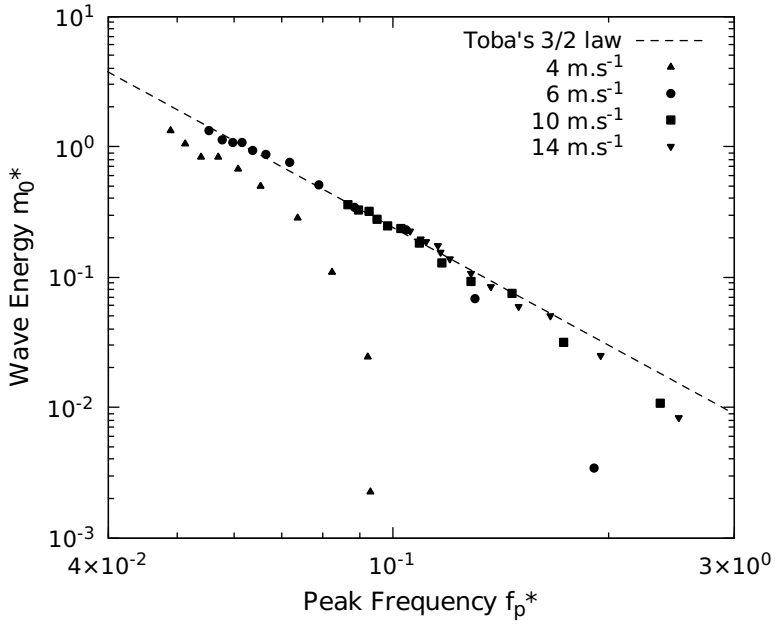

Figure 3.7: Variations of the wind-wave dimensionless energy with the dimensionless peak frequency for different equivalent wind speed (U_{ref}) compared to variations according to Toba's 3/2 law (3.10).

Shemer (2019) also fitted power laws to a set of small-scale experiments, and found exponents in rather good agreement with the values obtained here, namely 1.012 for the energy and 0.27 for the peak frequency.

Another relevant comparison with empirical law can be done using Toba's 3/2 law (Toba, 1997):

$$H_s^* = 0.062(f_p^*)^{3/2} \tag{3.9}$$

or in term of energy formulation

$$m_0^* = 2.4 \times 10^{-4}(f_p^*)^3 \tag{3.10}$$

This law is well adapted to ocean measurements. Contrary to power law previously mentioned the fetch does not appear in this relation. This is a benefit since the fetch is difficult to define in the real ocean because of the wind changing speed and direction. Note that the previous two sets of laws (3.7) and (3.8) disagree with eq. (3.10) in the sense that the ratio of their power coefficients is slightly above the value of 3 as claimed by Toba.

Figure 3.7 shows the agreement between our experimental results and Toba's law. In line with Figure 3.6, Figure 3.7 shows that once wind-waves are long enough to be free from surface tension effect (i.e. below a certain peak frequency or above a certain wind speed) Toba's law is well adapted to describe our experimental data set.

This section proved that laboratory experiments are, to a good extent, appropriate to describe short fetch evolution of a growing windsea in the ocean. From this observation, long mechanically-

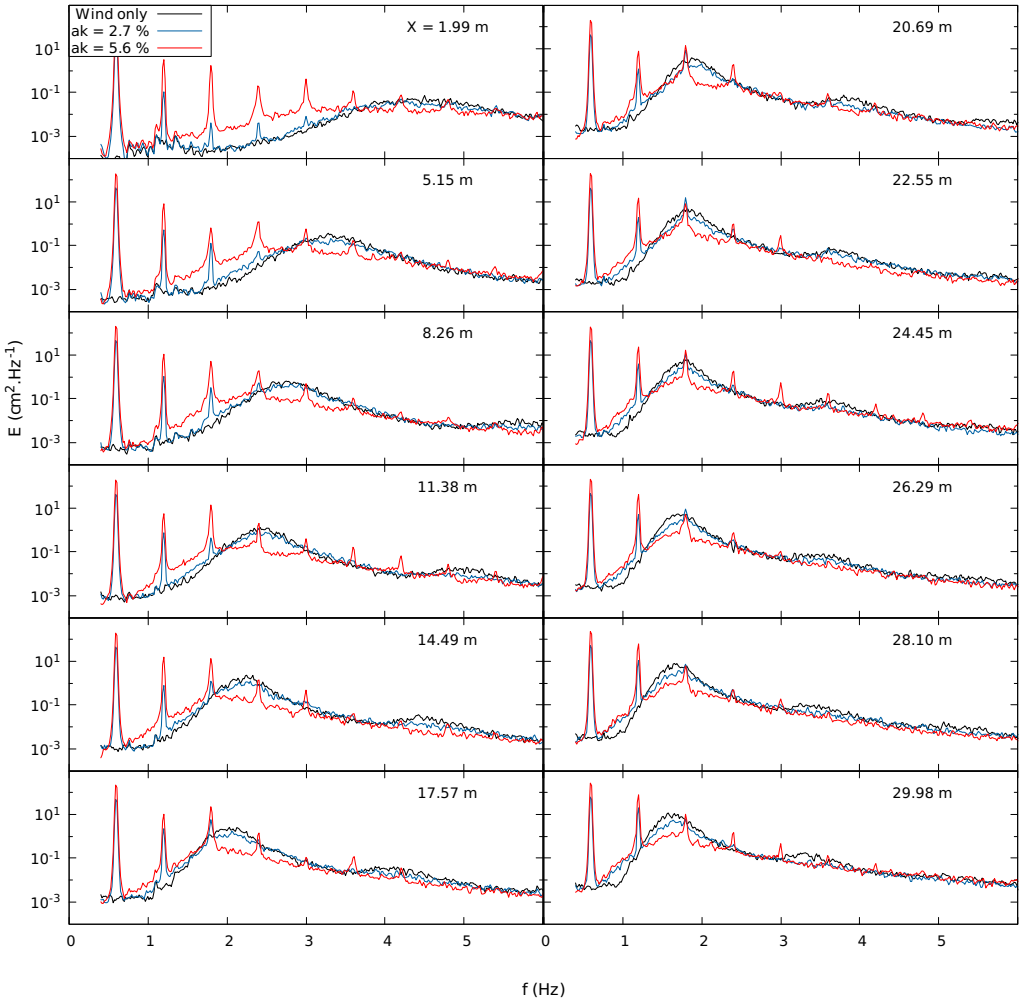

Figure 3.8: The spatial evolution of the variance density spectrum with and without regular paddle-waves of steepness ak and peak frequency 0.6 Hz for a wind speed $U_{\text{ref}} = 10$ m.s^{-1}.

generated waves representing swell are now added to the system in order to observe their effect on the growing windsea.

3.5 Effect of Monochromatic Paddle-Waves on Wind-Wave Growth

To assess the effect of following swell on wind-wave growth we repeated the same wind forcing conditions of the previous section with now long monochromatic paddle-waves generated at $X = 0$ m with the wave-maker. Two values of steepness of these long-waves were considered: $ak = 2.7$ % and $ak = 5.6$ %, with $a = H/2 = \sqrt{2m_0}$ the wave amplitude, corresponding to wave frequency $f = 0.6$ Hz. In both cases, the long-waves have a moderate level of nonlinearity, lying in the validity domain of Stokes' second order wave theory. As will be seen hereafter, harmonic modes of the fundamental forcing frequency will be present in the analyzed spectra.

In the wave tank, the addition of these regular long-waves had the direct and visible effect of attenuating the wind-waves. Figure 3.8 illustrates this interaction through the spatial evolution of the variance density spectrum for the wind speed $U_{ref} = 10$ m.s^{-1}. For that purpose, the pure wind-wave spectrum is compared to the spectrum combining wind-waves and paddle-waves.

The semi-log scale in Figure 3.8 emphasizes the generation of wind-waves at high frequencies. At short fetch (from 0 to 10 m), wind-wave peak frequency in the presence of long-waves deviates from the pure wind-wave peak frequency: the wind-wave peak frequency becomes lower as the steepness of the long-wave increases. This downshift is even more pronounced at a lower wind speed (not shown here). The frequency deviation from the pure windsea growth is also depicted in Figure 3.9.b using the spectral decomposition presented in Section 3.2.3.2.2. A possible explanation for this downshift is the presence of high frequency harmonics initiating wind-wave growth at frequencies lower than in the absence of paddle-waves. The induced frequency shift reduces at larger fetch and eventually vanishes. Thus, the progression of the wind-wave peak towards low frequencies is slowed down in the presence of long monochromatic waves.

Donelan (1987) drew attention to the slowed rate of progression of the paddle-modified windsea peak towards low frequencies with increasing fetch. In his 100-m-long tank, the introduction of long-waves upshifted the windsea peak frequency at large fetch ($X \sim 70$ m). This tendency of the pure windsea peak to overtake the paddle-modified one in its progression towards low frequencies could be imagined as a scenario in our case with an extended fetch: in Figure 3.9.b, an hypothetical spatial extension of the $ak = 5.6$ % peak frequency evolution towards higher fetch would probably lead to the observation of Donelan. According to him, the frequency shift previously described could be due to an alteration of the dispersion relation when a paddle-wave passes through a group of wind-waves, resulting in a detuning of the resonance leading to a modified nonlinear quartet interaction. This hypothesis is also relevant to explain the broadening of the paddle-modified wind-wave peak in its forward face (low-frequency).

Regarding the relative energy of wind-wave, paddle-waves broaden and flatten the corresponding spectral peak (Figure 3.8) resulting in a total energy (m_0, see Figure 3.9.a) smaller than the total energy of pure windsea. This observation is in line with previous studies (Donelan, 1987; Mitsuyasu, 1966; Phillips and Banner, 1974).

In Figure 3.9, the evolution of wind-wave energy and peak-frequency with fetch using log-scaled axes can be approximated by straight lines. In order to extend the previous results for different wind speeds, the wind-wave growth curves observed in the tank are fitted with power laws in the same manner as the previously described empirical power laws. Table 3.1 gathers the power laws parameters providing a summary of our results on wind-wave growth with and without paddle-waves for different wind speeds. In Table 3.1, the absolute values of coefficients c and g with monochromatic swell globally decrease with paddle-waves steepness, showing that both the variations of wind-wave energy and peak-frequency with fetch become milder.

The slowed increase of wind-wave energy with monochromatic paddle-waves, that has been extensively studied in the past, has been related to wind-wave enhanced dissipation (Phillips and Banner, 1974), long-wave sheltering effect (Chen and Belcher, 2000) and nonlinear wave-wave interactions (Masson, 1993). The sheltering effect can be observed in Figure 3.8: at fixed wind speed and for a given fetch, wind-wave total energy decreases as the steepness of the paddle-wave increases.

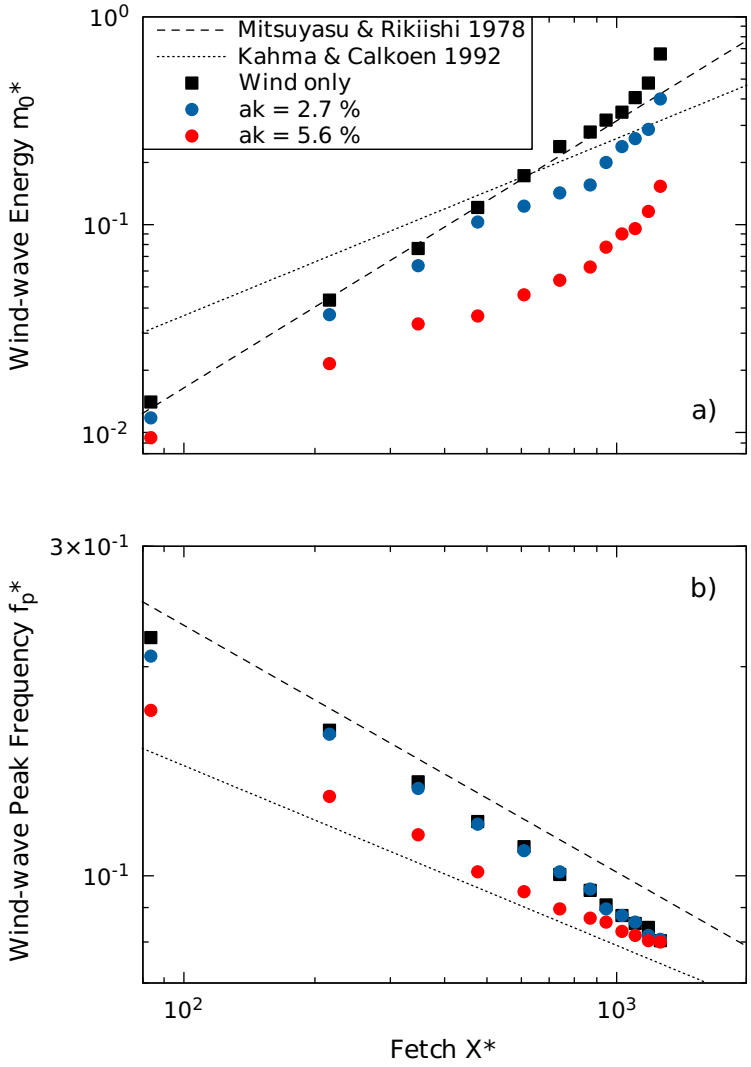

Figure 3.9: The spatial evolution of wind-wave energy (a) and peak frequency (b) with and without regular paddle-waves of steepness ak and peak frequency 0.6 Hz for a wind speed $U_{\text{ref}} = 10$ m.s^{-1}.

However, nonlinear wave-wave interactions are only significant when the ratio of long-waves over short-waves frequencies is greater than 0.6 according to Masson (1993). This condition is not satisfied in our case considering the first harmonic of the monochromatic waves, with a ratio ranging from about 0.1 at X = 1.99 m to less than 0.4 at maximal fetch (Figure 3.8). One can observe the second harmonic of paddle waves lies closer to the wind-wave peak, but this peak corresponds to a bound wave component, so not fulfilling the linear dispersion relation and in principle not prone to resonant interaction with free wind-wave components.

In the high frequency tail of the spectra in Figure 3.8, a small wind-wave harmonic can be observed at about 2 times the wind-wave peak frequency, for the pure wind-wave case, and to a lesser extent with paddle-waves of steepness $ak = 2.7$ %. It is hardly noticeable with paddles-waves of steepness $ak = 5.6$ %. The decrease of this second harmonic peak as the long-wave steepness increases is a consequence of the reduction of the amplitude of the main wind-wave spectral peak with increasing long-wave steepness, resulting in a lower nonlinearity level of the wind-wave component. Except

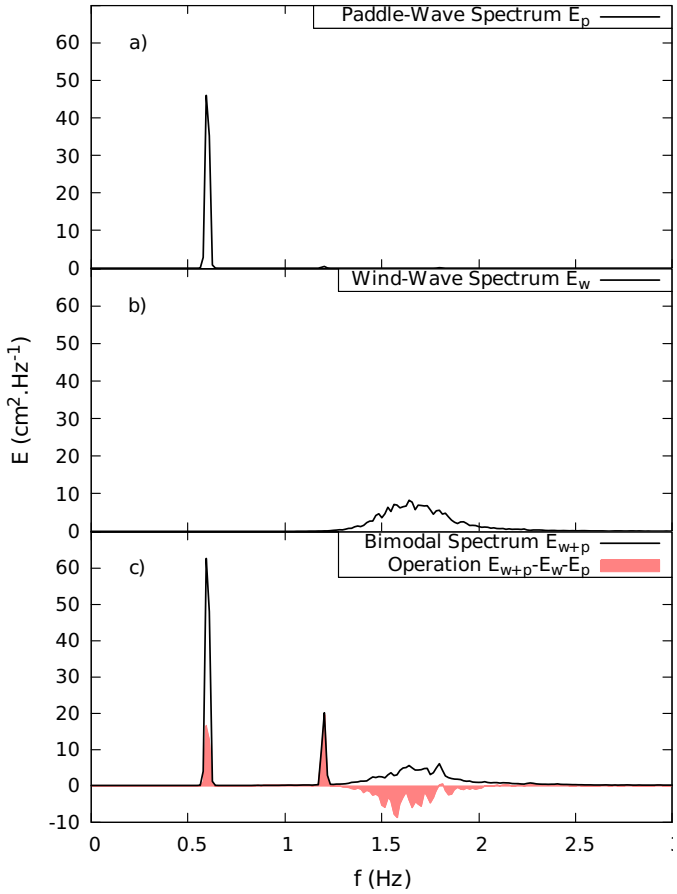

Figure 3.10: Pure paddle-wave spectrum E_{p} (a) and pure wind-wave spectra E_{w} (b) by comparison with the bimodal spectrum $E_{\mathrm{w+p}}$ (c) with monochromatic paddle-waves of steepness $ak = 2.7$ % and peak frequency 0.6 Hz at fetch of 30 m for a wind speed $U_{\mathrm{ref}} = 10$ m.s^{-1}. The pink area is the difference between the bimodal spectrum $E_{\mathrm{w+p}}$ and the sum of the pure spectra $E_{\mathrm{w}} + E_{\mathrm{p}}$.

for this difference, the high frequency tail is not altered in the presence of paddle-waves. This last observation is in disagreement with Donelan (1987) who noticed a higher tail for the cases including paddle-waves.

A semi log-scale is necessary to observe the high frequency behavior of wave-spectra but differences around the spectral peaks are usually less visible. Removing the semi log-scale permits to discern the location of the significant energy in the spectra. Figure 3.10 shows the energy transfers differentiating so called "pure" paddle-waves (a) and "pure" wind-waves (b) cases from the paddle-wave-plus-wind-wave combination (c) using a direct subtraction between the measured spectra.

The pink area is a good illustration of the interaction between long monochromatic waves and short wind-waves. The wind-wave reduction previously observed appears in the negative pink area between 1.25 and 2 Hz. The pink area under the first harmonic shows the amplification of the monochromatic paddle-waves. A striking effect illustrated in Figure 3.10 is the amplification of the second harmonic of the paddle-waves by the wind: negligible in Figure 3.10.a, the second harmonic is prominent and even more amplified than the first harmonic in Figure 3.10.c. This

amplification is a consequence of the frequency of the second harmonic of the fundamental mode of the paddle-waves lying in the frequency band of the wind-wave peak. Though less marked, this effect also manifests on the third harmonic at 1.8 Hz. In the same vein, it is observed in Figure 3.8 that higher-order harmonics of the paddle-waves are significantly amplified (see for instance the spectra with paddle-waves of steepness $ak = 5.6$ % for fetches from 10 to 20 m, for which the third harmonic is highly enhanced so has to become higher than the second harmonic. Thus, higher-order harmonics plays an important role in the interaction between both wave systems. These ideal waves enable a separation of the physical phenomena taking part into wave systems interactions. But adverse effects such as the amplification of wave harmonics can alter the direct comparison with ocean waves.

3.6 Effect of Irregular Paddle-Waves on Wind-Wave Growth

In order to consider a more realistic long-wave system representing swell, a JONSWAP-type sea-state was generated in the wave tank. The spatial evolution of the bimodal sea-states with fetch is compared to the pure windsea case using a spectral representation in Figure 3.11. In this section, the steepness ak of the irregular waves is defined as $a = H_s/(2\sqrt{2}) = \sqrt{2m_0}$ and $k = k_p$. Using this definition, monochromatic and irregular waves with the same steepness have the same energy.

As in Figure 3.8, the spatial evolution of spectra with fetch is shown in Figure 3.11. A striking effect is the downshift of the wind-wave peak frequency in the presence of long irregular waves. This large downshift appears at the earliest stage of wind-wave growth (fetch $X = 1.99$ m in Figure 3.11) and has the tendency to increase with increasing paddle-wave steepness. Thus, the presence of paddle-wave energy in the high frequency range seems to initiate wind-wave growth with a lower frequency than without paddle-waves. This effect, also observed in the monochromatic case, is even more pronounced with irregular long-waves. The downshift then slightly reduces with fetch but remains significant even at the maximal fetch (i.e. $X = 29.98$ m). Figure 3.12.b depicts different slopes in the non-dimensional peak-frequency evolution depending on the presence of paddle-waves and their relative steepness: the progression towards low-frequency is slowed down with increasing paddle-waves steepness.

Regarding the wind-wave energy, a small amplification effect due to long irregular waves is shown in Figure 3.12.a for the wind speed $U_{\text{ref}} = 14$ m.s^{-1}. This amplification, more significant at short fetch, has a tendency to reduce with increasing fetch. This reflects a slower energy variation with fetch in the presence of irregular paddle-waves. At lower wind speed, this small amplification becomes a small reduction at the maximal fetch (see table 3.1).

Overall, the effect of irregular waves on wind-wave energy appears weaker compared to monochromatic waves of the same energy. In the present study, the absence of a clear reduction of the windsea energy due to the presence of irregular paddle-waves is in disagreement with Benetazzo et al. (2019) and Bailey et al. (2020). A plausible explanation for these diverging observations, based on Benetazzo et al. (2019), is an insufficient separation between the wave systems leading to a misinterpretation of the spectra combining wind-waves and paddle-waves. Using Figure 3.11 to illustrate this latter remark, if one only considers the energy at the peak frequency of the pure windsea, the presence of paddle-waves indeed causes a wind-wave reduction at this particular fre-

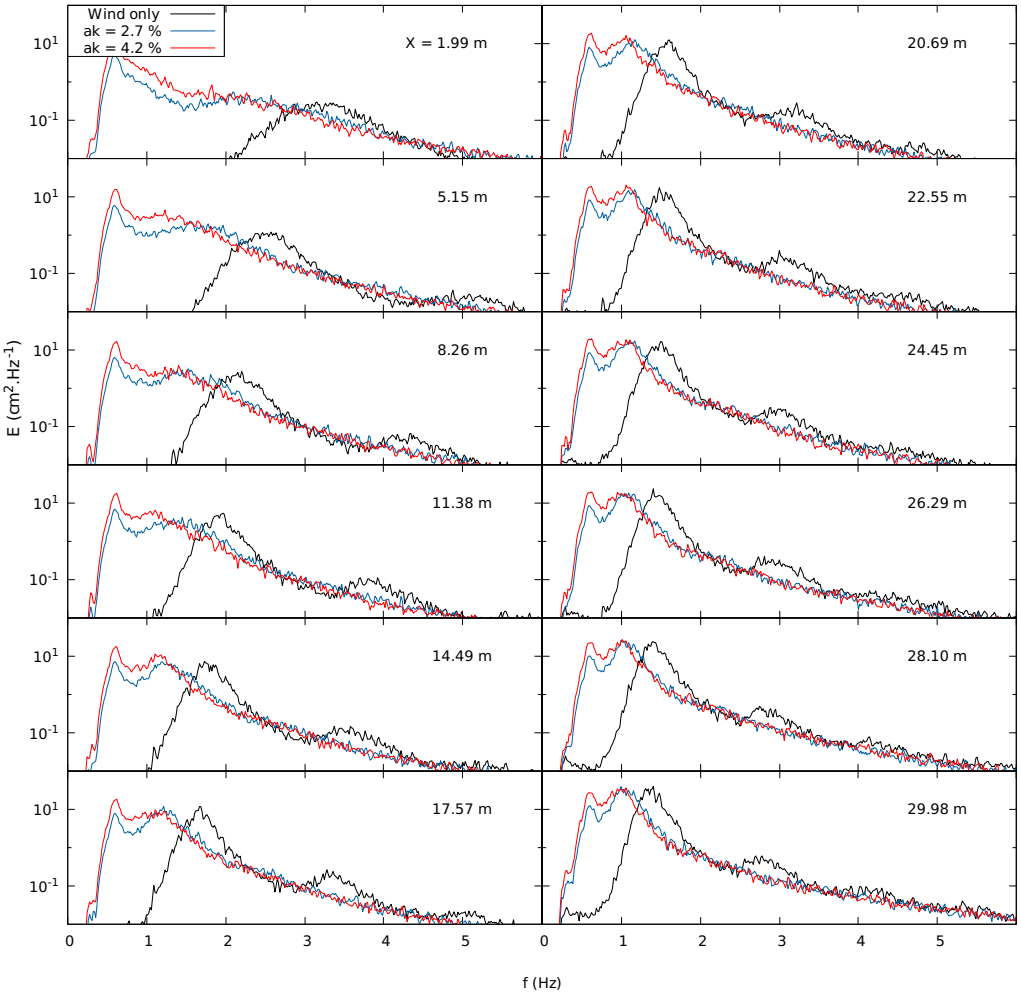

Figure 3.11: The spatial evolution of the variance density frequency spectrum with and without irregular paddle-waves of steepness ak and peak frequency 0.6 Hz for a wind speed $U_{\text{ref}} = 14$ m.s^{-1}.

quency. Thus, it is only by considering the downshift that one can observe wind-wave energy has not been reduced but downshifted towards lower frequencies. Figure 10 in the paper of Benetazzo et al. (2019) shows that the wind-wave peak frequency downshift cannot be observed in their case due to the presence of the paddle-wave peak at 1 Hz. A lower paddle-wave frequency, in our case, permits the observation of this downshift.

The sheltering effect occurs especially with monochromatic paddle-waves. The main characteristic differentiating these latter waves from the irregular waves is the distribution of wave energy over a range of frequencies. The wave trough between two consecutive crests of the dominant wave mode is much deeper with monochromatic paddle-waves than with irregular ones. In the case of irregular paddle-waves, the troughs are often "filled" with other wave modes causing lower height differences between crests and troughs than in the monochromatic case.

Regarding the slowed increase of wind-wave energy with fetch in the presence of irregular waves, since the sheltering effect is certainly reduced due to the spectral property, only enhanced dissi-

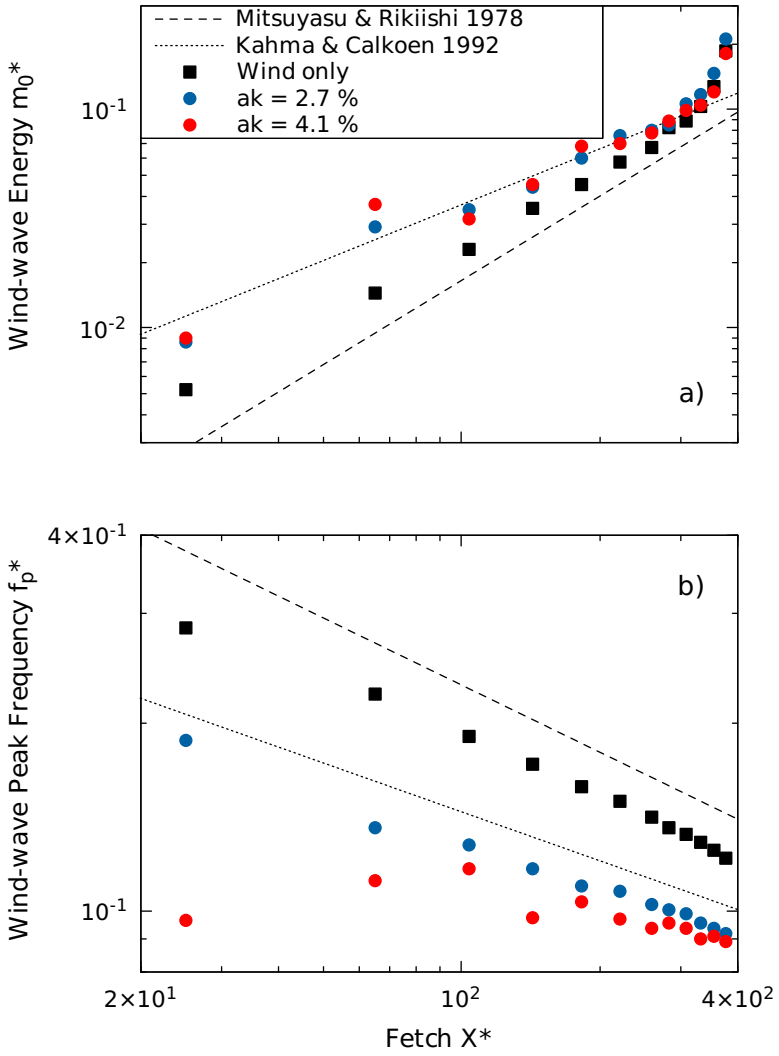

Figure 3.12: The spatial evolution of wind-wave energy (a) and peak frequency (b) with and without irregular paddle-waves of steepness ak and peak frequency 0.6 Hz for a wind speed $U_{\text{ref}} = 14$ m.s^{-1}.

pation and nonlinear wave-wave interaction are possible candidates. In this latter case, Masson's ratio is 0.6 at maximal fetch, implying a weak nonlinear interaction between wave systems. The remaining candidate would be the enhanced wave breaking due to wind-wave interaction with the addition of long-waves orbital velocities and wind drift as formulated by Phillips and Banner (1974).

The slowed rate of progression of the windsea peak towards lower frequencies with increasing fetch can be related to nonlinear interactions. With monochromatic paddle-waves, Donelan (1987) suggested that the wind-wave energy transfer towards low frequencies might be reduced due to wind-waves reduced steepness, thus nonlinearity, compared to pure windsea. This latter suggestion can be illustrated in Figure 3.13 where the wind-wave energy is expressed as a function of the wind-wave peak frequency. In this figure, the points representing wind-wave growth in the presence of paddle-waves (blue and red dots respectively for monochromatic and irregular paddle-waves) are situated below the pure wind-wave growth (black dots). Thus, at a fixed wind-wave energy, the

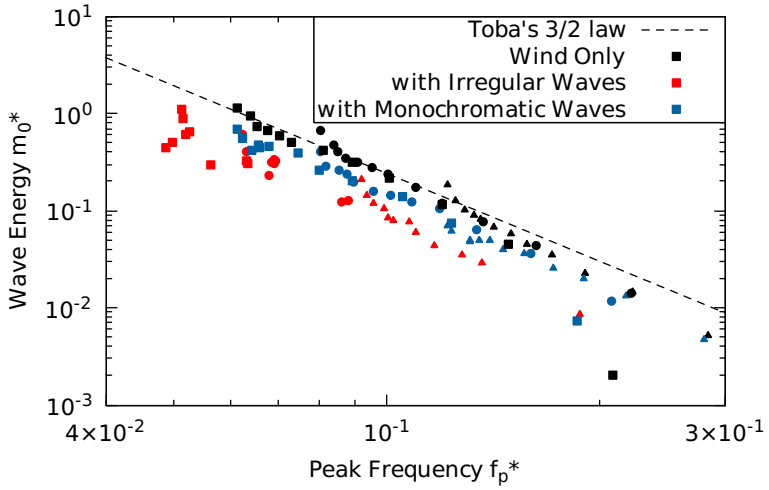

Figure 3.13: Variations of the wind-waves dimensionless energy with the dimensionless peak frequency for different reference wind speeds (squares: $U_{\text{ref}} = 6$ m.s^{-1}, circles: $U_{\text{ref}} = 10$ m.s^{-1}, triangles: $U_{\text{ref}} = 14$ m.s^{-1}) compared to variations according to Toba's 3/2 law.

corresponding wind-wave peak frequencies in the presence of paddle-waves are lower than in the pure wind sea case. Since a lower wave frequency relates to a lower wavenumber k and the wave energy increases with the wave amplitude a, it appears that the wind-wave steepness is reduced in the presence of paddle-waves. Additionally, Figure 3.13 shows that the wind-wave steepness is even more lowered when irregular paddle-waves are present. This latter observation suggests that nonlinear interactions are a good candidate to explain the slowed decrease of wind-wave peak frequency with fetch in the case with irregular waves.

3.7 Extension of the Results to the Prototype Scale

The extent at witch our experimental results, can be generalized at natural scale is discussed in the following. As mentioned in Introduction, the main difference between laboratory and natural scale measurements lies in the wave age of the swell. While the wind velocity conditions produced during the experiment are close to that observed in natural conditions, the mechanically-generated waves representing swell are significantly shorter, thus slower, than the swell conditions encountered in the ocean. Thus, an appropriate scaling was performed to compare our experiments with equivalent natural scale observations. Being aware of the main differences in term of wave age, qualitative comparisons permitted to draw tendencies about the physical processes involved in the interaction between swell and wind-waves at natural scale.

First, an effort was devoted to the determination of the wind friction velocity in order to perform an accurate scaling. Some doubts were formulated regarding the measuring device and the pertinence of the logarithmic profile method to determine the friction velocity in the presence of paddle-waves. Using ocean buoys measurements, Vincent et al. (2019) showed that the friction velocity tends to increase with swell steepness especially at low wind speeds. A similar trend is observed in Figure 3.5 as the friction velocity increases with the long paddle-waves. To confirm the similarities between

both scales, it would be necessary to use a method free from the logarithmic profile analogy for the wind profile characterization.

As it was highlighted in section 3.4, wind-wave growth (without paddle-waves) in laboratories shows similarities with that at natural scale. To observe these similarities, laboratory wind-waves must be long enough to be free from surface tension effects. Then, the wind-wave energy and peak frequency (Figure 3.6) were close to Kahma and Calkoen's empirical relations, representing wind-wave growth at natural scale, but slightly deviated in terms of variations with increasing fetch.

The introduction of paddle-waves, representing swell, significantly modifies the wind-wave field. First, monochromatic paddle-waves cause a reduction of wind-wave energy. This reduction has received numerous interpretations that reached an agreement on the fact that the physical processes responsible for that reduction are proper to steep short waves (equivalent to paddle-waves in natural reservoirs) traveling slower than the wind (i.e. $C << U_{10}$). This wind-wave reduction phenomenon was used to design a reduced wind input model for high frequencies waves (i.e. waves with a wave age equivalent to paddle-wave) and high winds in Ardhuin et al. (2010). Some gray areas remain on the role played by the monochromatic wave harmonics in the modification of the wind-wave growth. The prominence of these harmonics is principally inherent in laboratory steep monochromatic paddle-waves and might damage the relation with wind-waves at natural scale.

Secondly, the wind-wave peak frequency and its variations with increasing fetch are modified in the presence of either irregular or, to a lower extent, monochromatic paddle-waves. In Figures 3.9.b and 3.12.b, the wind-wave peak frequency variations with fetch are closer to Kahma and Calkoen's than to Mitsuyasu and Rikiishi's power laws although the latter is specific for laboratory wind-wave growth. In Table 3.1, the same tendency can be observed by comparing the power law coefficient g in the presence of paddle waves with the corresponding coefficient in Kahma and Calkoen's law ($g = -0.26$). Furthermore, in the presence of irregular paddle-waves, wind-wave energy evolution with increasing fetch follows this agreement with Kahma and Calkoen relations. This accordance can be observed in Figure 3.12.a or by comparing the power law coefficient c in Table 3.1 with the coefficient $c = 0.85$ of Kahma and Calkoen. Finally, irregular paddle-waves seem to restore wind-wave growth as it is observed at natural scale.

3.8 Conclusion

A series of experiments were carried out at IRPHÉ/Pythéas wind-wave tank in Marseilles. The interactions between long paddle-waves, representing swell, and short wind-waves were investigated with both monochromatic and irregular paddle-waves. An analysis was performed in order to identify the interaction mechanisms that can be transposed at prototype scale.

Wind-wave growth was studied in absence of paddle-waves to assess the similarities with existing experiments. It was found that, after the young wind-waves emancipate from the gravity-capillary state, wind-wave growth is in agreement with laboratory based empirical laws but differ from more general laws (i.e. laws valid at prototype scale) in terms of variations with fetch.

By calculating the vertical profile of the wind horizontal velocity using the logarithmic profile

method, the friction velocity had a tendency to increase in the presence of paddle-waves. However, the measurements uncertainties added to the limited validity of the logarithmic profile method to characterize the airflow in the presence of long paddle-waves prevented a more quantitative analysis. The use of a more accurate method, such as the eddy correlation method, is let for further work.

The interactions between wind and paddle-waves have repercussions on the wave systems. The paddle-waves are amplified by the wind which echoes back to the sheltering effect highlighted by Chen and Belcher (2000). With monochromatic paddle-waves, this shelter effect seems to affect wind-wave growth by reducing the quantity of momentum available for wind-wave generation. In this latter case, the wind mostly impacts the wind-wave energy. Thus, the wind-wave peak frequency evolution with fetch is similar to wind only conditions, resulting in a reduced wind-wave steepness in the presence of monochromatic paddle-waves.

The effect of irregular paddle-waves on wind-wave growth is quite different since the wind-wave parameter affected by this interaction is mostly the wind-wave peak frequency. The energy continuum brought by the paddle-waves high frequency tail initiates wind-wave growth at a lower frequency than in the absence of paddle-waves. Thus, it was found that the irregular low frequency waves downshift wind-wave peak frequency in a significant manner. The wind-wave energy being only slightly impacted by comparison with the peak-frequency, irregular paddle-waves reduces wind-wave steepness even more than in the monochromatic paddle-wave case.

The similarities between the action of monochromatic and irregular paddle-waves on wind-wave growth lie in the wind-wave energy and peak frequencies reduced variations with fetch. It is interesting to note that most laboratory measurements, for example Mitsuyasu and Rikiishi (1978), display an accelerated wind-wave growth (i.e. wind-wave energy increases faster and the peak frequency reduces faster) by comparison with ocean measurements, illustrated here by Kahma and Calkoen (1992)'s empirical law. Especially with irregular paddle-waves, which is a more faithful reproduction of a typical ocean sea-state, wind-wave growth is somehow in accordance with Kahma and Calkoen (1992)'s law. A result from this latter observation is that wind-wave growth in laboratories seems closer to wind-wave growth at prototype scale when irregular paddle-waves are present.

Finally, our experiments provide a valuable database for validating a spectral wave model. From this database, spectral wave model performances can be assessed under generic conditions for both wind and wave forcing. Using the separation of the physical mechanisms at the root of wind-wave generation in the spectral energy balance equation (3.1), the ability of the spectral wave model in reproducing wind-wave growth with and without paddle-waves might enable to identify the mechanisms at the origin of the wave systems interactions observed in laboratory. Ultimately, the use of a spectral wave model may help to evaluate the extent at which the mechanisms observed in laboratories can be transposed to prototype scale.

Chapter 4

Spectral wave modelling of bimodal sea-states at laboratory and coastal scales

by A. Villefer, M. Benoit, D. Violeau and M. Teles

Ocean Modelling, 183, 102182, 2023. doi: https://doi.org/10.1016/j.ocemod.2023.102182.

Les expériences en canal-soufferie du chapitre précédent ont mis en évidence un décalage du pic de clapot provoqué par la présence de vagues longues de type JONSWAP générées mécaniquement. Un modèle spectral d'états de mer de 3^e génération, TOMAWAC, est utilisé pour évaluer dans quelle mesure ce décalage fréquentiel peut avoir lieu à l'échelle côtière lors de la génération du clapot en présence de houle. Dans ce but, on a selectionné différentes méthodes et paramétrisations permettant la modélisation des processus physiques intervenant lors de la génération du clapot. Les performances du modèle spectral sont évaluées pour la simulation d'états de mer bimodaux à deux échelles : à l'échelle du laboratoire et à l'échelle côtière. D'une part, nous avons reproduit numériquement les conditions ayant permis d'observer le décalage du pic de clapot en canal-soufflerie. D'autre part, nous avons réalisé des simulations rétrospectives d'un état de mer bimodal observé en zone côtière lors de la campagne SHOWEX (Ardhuin et al., 2007). Dans l'ensemble, un bon accord est obtenu entre les simulations et les observations à l'échelle du laboratoire ainsi qu'à l'échelle côtière. En particulier, un ensemble de paramétrisations à l'état de l'art pour la modélisation de la dissipation par moutonnement et des interactions non-linéaires entre quadruplets de composantes de vagues a montré de bonnes performances par comparaison aux observations. Enfin, sur la base des performances de cet ensemble de paramétrisations, une emprise côtière générique a été définie pour étudier numériquement l'occurrence du décalage du pic de clapot en zone côtière. Cette dernière étude révèle un décalage de la période pic du clapot de 5 s sans houle à plus de 6,5 s en présence d'une houle de 2 m de hauteur significative.

Abstract

A downshift of the wind wave peak frequency was observed in a wind wave tunnel when irregular long paddle-waves (i.e. generated mechanically with a plane wave-maker) are added in the sea state. The 3rd generation spectral wave model, TOMAWAC, is used to assess the extent at which this peak frequency downshift can take place at prototype scale in bimodal sea-state conditions involving swell and wind wave systems. Several parameterizations of the modelled physical processes are selected to numerically reproduce the laboratory experiments in the first place. Then, the model performances are further inquired in reproducing coastal observations during a specific event combining a wind wave and a swell system. Overall, a good agreement is obtained between the simulations and the observations both at laboratory and coastal scale. In particular, a set of parameterizations combining one of the latest developments in spectral wave models for the whitecapping dissipation and the nonlinear 4-wave interactions reveals high performances in reproducing the observations. Lastly, based on the performances of this latter set of parameterizations, a generic numerical domain with typical coastal scale dimensions is created to inquire the occurrence of the downshift at prototype scale. This last study reveals a wind wave peak period shift from 5 s without swell to more than 6.5 s with a 2 m high swell.

4.1 Introduction

Sea states combining several wave systems, such as swell and wind waves, are very common both in open oceans and in coastal areas (Mason et al., 2008; Thompson et al., 2018). Although the occurrence of these complex sea states has been addressed several times in the literature, it is not quite settled whether the wind waves are generated the same way with or without a background swell. The purpose of this paper is to evaluate 3rd generation (hereafter denoted 3G) wave models performances for bimodal sea states modelling, given recent improvements in wind wave generation parameterizations. Then, such a model is further used to investigate the physics behind the combinations of both wave systems.

With the purpose to study wind wave growth in the presence of swell, a preliminary approach consists in studying the generation of short wind waves in the presence of a longer wave system in the well controlled conditions of a wind wave tank. Such facilities allow the combination of both wave systems generated using an air blower and a mechanical paddle-wave-maker, respectively (Donelan, 1987; Mitsuyasu, 1966; Phillips and Banner, 1974; Villefer et al., 2021). Yet, the long paddle-waves generated in wind wave tanks are significantly different from ocean swell in terms of wave age $\chi = C/U_{10}$, with C the peak phase celerity and U_{10} the wind velocity at 10 m above the mean water level (MWL). Respective wave ages are larger than 1 for typical ocean swell and generally lower than 0.5 for paddle-waves in wind wave tanks to avoid surface tension effects. Therefore, the different wave systems generated in a wind wave tank should be considered as different components of the wind sea (with lower and higher peak frequencies), rather than real swell and wind sea. Hereafter, for readability reasons, short wind-generated waves are denoted "wind waves" and long mechanically-generated waves are denoted "paddle-waves".

Donelan's (1987) wind wave tank experiments revealed a reduction of the wind-sea variance by

a factor of about 2.5 in the presence of following monochromatic paddle-waves. Replacing the monochromatic waves by JONSWAP-type paddle-waves, Villefer et al. (2021) showed that the wind wave peak frequency is shifted towards lower frequencies due to the background paddle-waves. However, the extension of these results for the study of wind wave growth over real ocean swell is complicated by the high steepness and the low wave age of the laboratory paddle-waves compared to open-ocean swell.

At prototype scale, a common approach to physically characterize such a bimodal sea state involves in-situ observations of its spatial development. Thus, the conditions for these observations must be in a coastal area where a wind is blowing steadily offshore (i.e. fetch-limited conditions) and opposing a swell directed inshore (Ardhuin et al., 2007; Hwang et al., 2011). These very specific conditions make the characterization of bimodal sea states rather difficult at natural scale. Some observations showed a modification of wind wave growth in the presence of swell (Donelan et al., 1997; Hwang et al., 2011; Vincent et al., 2019). According to Hwang et al. (2011), wind wave generation and development are enhanced with an opposing background swell. These observations lead to physical interpretations: swell is expected to modify the wind velocity profile (Chen and Belcher, 2000; Donelan et al., 1997), to increase the breaking of the wind sea (Phillips and Banner, 1974) and to alter the nonlinear 4-wave interactions (Masson, 1993). However, based on observations in the North Carolina continental shelf during the Shoaling Waves Experiment (SHOWEX), Ardhuin et al. (2007) showed that a moderate swell has no significant effect on the bulk parameters characterizing the wind sea.

Both the idealized laboratory conditions and the realistic in-situ observations are necessary to understand the processes at play when wind waves are generated over a preexisting swell. With the purpose to unify the different observations, our approach is based on the use of the 3G spectral wave model TOMAWAC (part of the TELEMAC-MASCARET hydro-informatic system) (Benoit et al., 1996) to upscale Villefer et al. (2021) laboratory results to the coastal scale. The model is used to numerically reproduce first the laboratory experiments and then an event during the SHOWEX campaign. Taking advantage of the physical processes separation involved in wind wave generation, the laboratory experiments hindcast aims to assess the extent at which the observed spectral downshift can occur at prototype scale.

However, the accuracy of 3G wave models remains questionable for a simulation including more than one wave system as shown in latest developments in 3G wave models (Ardhuin et al., 2010; Gagnaire-Renou et al., 2010). While the integral parameters such as the significant wave height and representative periods can be well predicted for this kind of sea states, the frequency and directional distributions of the wave energy remain rather inaccurate. However, these distributions are of prime importance for applications such as the design of coastal protections or offshore structures.

Recent developments in wave models proved that improving the whitecapping dissipation modelling was necessary to better simulate the combination of swell and wind sea. This dissipation process is considered as the least understood part of the physics relevant to wave modelling by Cavaleri et al. (2007).

The first operational dissipation parameterization in 3G wave models was the one developed by Komen et al. (1984) loosely following Hasselmann (1974)'s work in which whitecaps act as a pressure pulse countering the rise of the sea surface. In the case of swell and wind wave combination, the

main weakness of this parameterization is the use of an averaged wave steepness to determine the dissipation rate. Since swell and wind waves have a low and high steepness respectively, the presence of swell leads to anomalously high wind waves due to a lack of dissipation and vice-versa. Bidlot et al. (2007) partly corrected this issue by re-defining the averaged steepness used in the latter parameterization to increase the dissipation at higher frequencies (i.e. wind wave frequencies).

To further solve this issue, dissipation models using a local saturation spectrum rather than an integral wave steepness have been developed based on the work of Alves and Banner (2003). First, van der Westhuysen (2007) combined the advantages of a saturation model (van der Westhuysen et al., 2007) and a model based on the average wave steepness of the sea state (Komen et al., 1984). Secondly, Ardhuin et al. (2010) developed a new set of source/sink terms taking into account the breaking threshold approach with a saturation term, the dissipation of short waves by larger breakers and the swell dissipation over long distances.

Another improvement in the bimodal sea state modelling regards the nonlinear 4-wave interactions. An exact equation with Boltzmann-type integral describing these interactions has been proposed by Hasselmann (1962) and Zakharov (1968). Since then, a substantial work has been devoted to find a good balance between a computationally efficient and an accurate resolution of these interactions. Masson (1993) showed that nonlinear 4-wave interactions are involved in bimodal spectra evolution when the ratio of long-wave to short-wave frequencies is greater than 0.6. The standard Discrete Interaction Approximation (DIA) method, that triggered the outbreak of 3G wave models, is a computationally efficient method to estimate these interactions. However, it suffers from many shortcomings regarding the frequency and directional distribution of wave energy compared to exact methods (Benoit, 2005). According to Masson's work, a more accurate method to solve the nonlinear 4-wave interactions might be required for bimodal spectra simulations. Based on the Gaussian Quadrature Method (GQM) (Lavrenov, 2001), Gagnaire-Renou et al. (2010) developed an algorithm using numerical integration methods of high accuracy. In the following, this original method is used to assess wind wave growth in the presence of swell both at laboratory and coastal scales.

To compare the simulations with observations, an appropriate scaling is applied following Kitaigorodskii (1961). In the present study, wind wave growth is described in two manners both based on a spectral analysis of the sea states: on the one hand using the variance density spectrum $E(f,\theta,x,t)$ at a location x and a time t, where f and θ are the wave frequency and direction respectively, on the other hand using the fetch X, peak frequency f_p and the total variance of the free-surface elevation $m_0 = \overline{\eta^2}$. Those variables are made dimensionless using U_{10} and the acceleration due to gravity g:

$$X^* = \frac{Xg}{{U_{10}}^2} \tag{4.1a}$$

$$f_p^* = \frac{f_p U_{10}}{g} \tag{4.1b}$$

$$m_0^* = \frac{m_0 g^2}{{U_{10}}^4} \tag{4.1c}$$

In the present paper, section 2 presents the laboratory experiments (see Villefer et al. (2021)

for a more complete description) and the SHOWEX event (Ardhuin et al., 2007) against which TOMAWAC's hindcast performances are evaluated. Section 3 gives an overview of the physics at play in the wave model in order to introduce the different sets of parameterizations later used for the simulations. Then, after a description of the numerical characteristics, the results of the simulations at laboratory and at coastal scales are discussed in sections 4 and 5, respectively. In light of the preceding discussion, a generic numerical domain is created to assess wind wave growth modifications in the presence of a following swell at coastal scale in section 6. Section 7 summarizes the present findings and introduces recent 3G wave model developments that could further improve the simulation of bimodal sea state conditions.

4.2 Bimodal sea states data sets

This section introduces two bimodal sea state data sets, used to evaluate the performances of TOMAWAC, during the wave generation process, at laboratory and coastal scales, respectively. It is important to note that these data sets are not comparable since they differ in at least two ways:

- a short and a long wind wave systems are combined in the wind wave tank whereas wind waves and oceanic swell coexist at coastal scale,
- both wave systems have the same direction in the wind wave tank whereas they have nearly opposed directions at coastal scale.

The extension of the laboratory results (i.e. the peak frequency downshift phenomenon) at coastal scale is investigated in Section 4.6.

4.2.1 Experimental study in a wind wave tank

The first dataset consists in a series of experiments carried out in the controlled conditions of the Institut de Recherche sur les Phénomènes Hors-Equilibre (IRPHÉ)-Pythéas 40 m long wind wave tank in Marseilles, France. The use of such a facility permitted to study wind wave growth in the presence of following long paddle-waves. The facility and the results are described and discussed in Villefer et al. (2021). Twelve wave gauges distributed along the test section enabled to obtain the fetch-limited evolution of the wind waves with and without monochromatic or irregular (JONSWAP-type) paddle-waves.

For the present study, only the spectra depicting wind waves in the presence of irregular paddle-waves are considered using the wave gauge situated at the maximal fetch of 30 m. Figure 4.1 introduces the 6 cases of interest for this study. The frequency wave spectra are considered for three wind-speed settings, $U_{\text{ref}} = 6$, 10 and 14 m/s, with and without paddle-waves. Here, U_{ref} is a reference wind speed measured by a sonic anemometer at 1 m above MWL. Two different values of paddle-wave steepness ak of 2.7 and 4.2%, with the wave amplitude $a = \sqrt{2m_0} = H_{m_0}/(2\sqrt{2})$ and the wavenumber $k = k_p$ (i.e. the peak wavenumber), are considered.

For each wind velocity in Figure 4.1, the comparison between spectra with and without paddle-waves highlights the downshift of the wind wave frequency peak in the presence of paddle-waves.

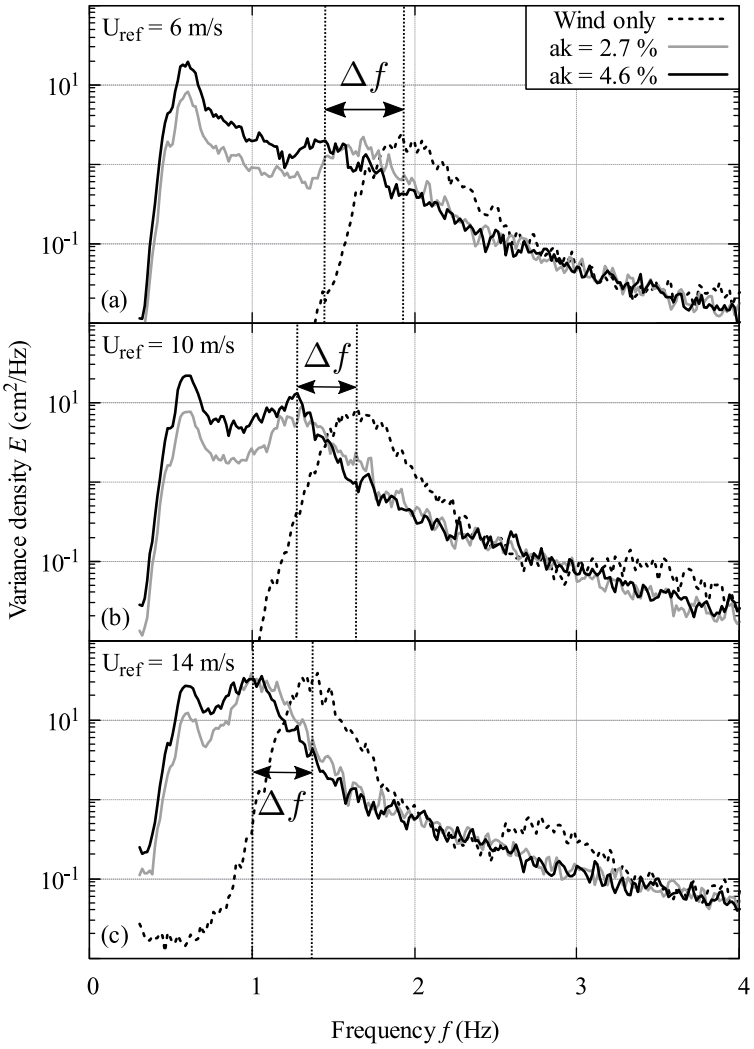

Figure 4.1: Laboratory measurements of variance density spectra with and without irregular paddle waves of steepness ak and peak frequency $f_p = 0.6$ Hz for three wind velocities U_{ref} at fetch 30 m (maximal fetch).

This downshift tends to increase with increasing paddle-wave steepness. By fitting the vertical profile of the horizontal wind velocity with a logarithmic profile method (see Monin and Obukhov (1954)), Villefer et al. (2021) found that the friction velocity at the air/sea interface $u_\star$ had a tendency to increase in the presence of a background following paddle-waves. This tendency can be retained as a first hypothesis to explain the above-mentioned downshift as a result of an increase of the momentum transfer from the wind to the waves with paddle-waves. The following numerical simulations are analyzed given these observed experimental features.

4.2.2 SHOWEX in-situ observations in North Carolina continental shelf

The second dataset considered for model's validation is an event that happened during the Shoaling Waves Experiment (SHOWEX) conducted in the North Carolina continental shelf (east coast of the

USA) from August to December 1999. Six Datawell Directional Waverider (DDW) buoys (Ardhuin et al., 2003a,b) were deployed along a cross-shelf transect going from 5 to 80 km (X1 to X6) to the coastline (see Fig. 4.2) to obtain the wave spectra and bulk parameters. Three Air–Sea Interaction Spar (ASIS) buoys (Graber et al., 2000) permitted to obtain the wind properties and additional wave measurements (Bravo, Yankee and Romeo buoys in Fig. 4.2). Buoys and stations of the National Data Buoy Center (NDBC) and the U.S. Army Corps of Engineers (USACE) provided extra data about the oceanic and atmospheric conditions.

On 3rd November 1999, a 10 m/s wind (U_{10}), coming from the land (westerly wind, orange arrow in Fig. 4.2), was blowing steadily and uniformly over a time period of 5 hours from 12:00 to 17:00 East-Coast Standard Time (EST). This led to wind wave generation close to idealized fetch-limited conditions with a wind directed at 10 to 30 degrees relative to the normal to the coast (i.e. slightly oblique wind). An additional southeasterly swell system (blue arrow in Fig. 4.2) with a peak period $T_p \simeq 10$ s and a significant wave height $H_s \simeq 1$ m was nearly opposed to the local wind. This event, first chosen by Ardhuin et al. (2007) to validate the spectral wave model WAVEWATCH III (WW3) (Tolman and Chalikov, 1996; Tolman, 2002), provides rare observations of fetch-limited conditions, in the presence of a background swell, with a large set of wave sensors to assess wind wave growth with fetch.

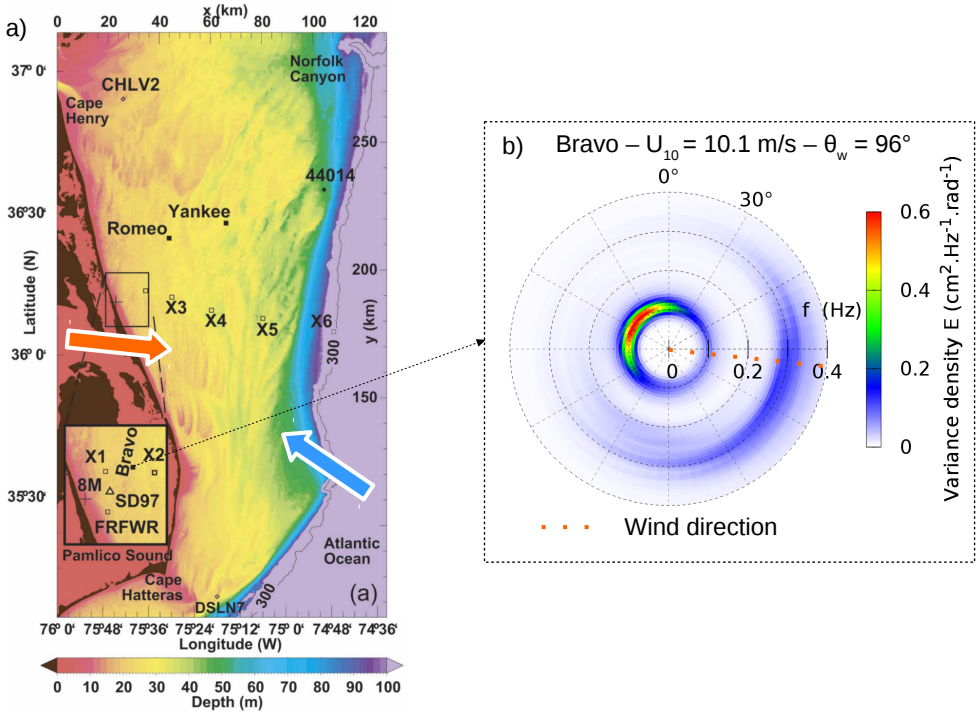

Figure 4.2: (a) Bathymetry of the North Carolina shelf and locations of wave measurements during the SHOWEX campaign (1999) with a directional spectrum (b), obtained from the MLM and averaged from 12:00 to 17:00 (EST), at Bravo (ASIS-type buoy) illustrating the wind and wave conditions. The orange and the blue arrows depict wind and swell directions respectively. The left part of this picture was taken from Ardhuin et al. (2007).

The wave spectra calculated from the wave buoys measurements, for instance at Bravo in Figure 4.2, depicted the evolution of two well-defined wave systems: the low frequency part with swell energy decreasing from offshore to the coast and the high frequency (HF) part with wind waves growing with fetch from X1 to X6. Looking at Bravo directional spectrum in Figure 4.2, one can observe that the wind wave peak is not exactly aligned with the mean wind direction (orange dots): the main wind wave components are slightly deviated towards the alongshore direction (i.e. $\theta \simeq 160°$). This observation, within the framework of this particular event, received two different interpretations in the literature. On the one hand, it was associated to slanting-fetch conditions (i.e. the obliquity of the wind direction relative to the normal to the coast) and to wave refraction by Ardhuin et al. (2007). The turning of the wind wave peak due to slanting-fetch conditions is further described in Pettersson et al. (2010). It is interesting to remark that the wind wave peak mean direction simulated with WW3 in Ardhuin et al. (2010), including the wave dissipation model they developed, showed a 25° bias towards the alongshore direction. On the other hand, Zhang et al. (2009) associated the turning of the wind wave peak towards the alongshore direction to a wind stress angle deviated from the wind direction because of surface currents.

Following Ardhuin et al. (2007) in the case of a slanting fetch, the dimensionless fetch in the wind direction is defined extending Eq. 4.1a as $X^* = Xg/(\cos\theta_w U_{10}^2)$, where θ_w is the wind direction with respect to the normal to the coast and X is the distance perpendicular to the coast. The idealized fetch-limited condition, the specific directional properties of the observed spectra and the comparison with WW3 results (Ardhuin et al., 2010, 2007) provide a valuable database to assess the performances of the present simulations.

4.3 Parameterization of the 3rd generation wave model

TOMAWAC is a 3G wave model (developed by EDF R&D) using unstructured spatial grid of the oceanic domain for solving the action balance equation (Benoit et al., 1996). To serve that purpose, the model simulates the evolution of the action density directional spectrum at each node of a spatial computational grid. The balance equation of wave action density is solved for each component (f_i, θ_j), with discrete frequencies f_i and directions θ_j. Each component of the action density spectrum changes in time and space under the effects of wave propagation and software-modelled physical processes. Based on the considerations in Ardhuin et al. (2007), the current is not taken into account in the present study. Thereby, only the evolution of the surface elevation variance spectrum $E(t, \boldsymbol{x}, f, \theta)$, at a location $\boldsymbol{x}$ and a time t, is considered using the following equation:

$$\frac{dE}{dt} = Q \tag{4.2}$$

The left hand size of the equation is the kinematic part and the right hand size gathers the contributions from the physical processes modeled using source and sink terms. Following Ardhuin et al. (2007), bottom friction dissipation is considered as negligible, here, so that Q is formulated as in deep water conditions:

$$Q = Q_{\text{in}} + Q_{\text{ds}} + Q_{\text{nl}} \tag{4.3}$$

corresponding to the processes of wind energy input Q_{in}, dissipation through white-capping Q_{ds} and

nonlinear 4-wave interactions Q_{nl}. In the code, each process has several models and formulations that can be adapted to the particularities of the studied case. The different source/sink terms used in the course of this study are described below from the most to the less known physical mechanisms.

Q_{nl} is the only source term that has been formulated theoretically (Hasselmann, 1962; Zakharov, 1968) as a Boltzmann integral for resonant interactions between quadruplets of surface gravity waves, as said above. Among the methods that have been developed to calculate an approximated solution, the above-mentioned two methods are used here: DIA ($Q_{\mathrm{nl}}^{\mathrm{DIA}}$) and the more accurate, as well as computationally heavier, GQM ($Q_{\mathrm{nl}}^{\mathrm{GQM}}$). The GQM algorithm, as implemented in TOMAWAC with the default configuration, needs about 50 times the DIA CPU time to compute Q_{nl}.

The transfer of momentum from the wind to the sea Q_{in} is based on Miles' feedback mechanism and Janssen's quasi-linear theory for modelling the ocean/atmosphere interaction (Janssen, 1991, 2004), and denoted $Q_{\mathrm{in}}^{\mathrm{J}}$.

Lastly, the selected dissipation terms are van der Westhuysen (2007) term $Q_{\mathrm{ds}}^{\mathrm{VDW}}$, combining a saturation model (van der Westhuysen et al., 2007) and Komen et al. (1984)'s model, and Ardhuin et al. (2010) term $Q_{\mathrm{ds}}^{\mathrm{ST4}}$ (ST4 referring to WW3 nomenclature). This latter sink term is a combination of different dissipation terms formulated as $Q_{\mathrm{ds}}^{\mathrm{ST4}} = Q_{\mathrm{sat}} + Q_{\mathrm{bk,cu}} + Q_{\mathrm{swell}} + Q_{\mathrm{turb}}$. For the following simulations, the swell dissipation due to the resistance of the air Q_{swell} (Q_{out} in Ardhuin et al. (2010)) and the dissipation associated to surface turbulence Q_{turb} are considered as negligible. Particularly, Q_{swell} is not expected to have a significant effect on swell dissipation over the typical distances (150 km maximum) in the spatial domain considered here. Only the saturation term Q_{sat} and breaking cumulative term $Q_{\mathrm{bk,cu}}$ (i.e. the dissipation of short waves by long breaking waves) are considered. The modification of $Q_{\mathrm{in}}^{\mathrm{J}}$ and $Q_{\mathrm{nl}}^{\mathrm{DIA}}$ parameterizations described in Ardhuin et al. (2010) dissipation terms are included when $Q_{\mathrm{ds}}^{\mathrm{ST4}}$ is activated. Regarding $Q_{\mathrm{in}}^{\mathrm{J}}$, it consists in the inclusion of a sheltering effect, accounting for the effect of a background swell on the wind wave generation, by adapting the calculation of the friction velocity, somewhat like Chen and Belcher (2000) suggested. Amongst the parameterizations developed for $Q_{\mathrm{ds}}^{\mathrm{ST4}}$, we chose to use the T471f (The WAVEWATCH III (R) Development Group (WW3DG), 2019) which corresponds to the one used in WW3 at global scale adapted to Climate Forecast System Reanalysis (CFSR) wind files.

To reproduce both laboratory and in-situ SHOWEX observations, different sets of parameterizations for the source/sink terms are compared:

- VDW: $Q^{\mathrm{VDW}} = Q_{\mathrm{in}}^{\mathrm{J}} + Q_{\mathrm{ds}}^{\mathrm{VDW}} + Q_{\mathrm{nl}}^{\mathrm{DIA}}$, associated to blue color in figures of results,
- ST4: $Q^{\mathrm{ST4}} = Q_{\mathrm{in}}^{\mathrm{J}} + Q_{\mathrm{ds}}^{\mathrm{ST4}} + Q_{\mathrm{nl}}^{\mathrm{DIA}}$, associated to orange color,
- ST4+GQM: $Q^{\mathrm{ST4+GQM}} = Q_{\mathrm{in}}^{\mathrm{J}} + Q_{\mathrm{ds}}^{\mathrm{VDW}} + Q_{\mathrm{nl}}^{\mathrm{GQM}}$, associated to red color.

These parameterizations will be compared with observations associated to gray scale colors.

4.4 Hindcast of laboratory experiments

4.4.1 Numerical specifications

A first series of simulations of the wind wave tunnel experiments led to some adjustments of the source/sink terms parameterizations. First, the wave growth limiter is deactivated. This limiter is generally used to guarantee the numerical stability of the calculation which, in our case, appears to be unnecessary with a small time step of 0.1 s. Secondly in Q_{in}^{J}, the friction velocity at the air/sea interface, for each wind speed U_{ref}, is forced to be constant and equal to the laboratory measured one in the "wind only" case, for simulations with and without paddle-waves. Without this forcing, the model tends to overestimate the friction velocity. In addition, the deep water approximation is adopted since it was shown by Villefer et al. (2021) that the dissipation due to bottom friction is relatively low.

Lastly, since the spectral wave model is not meant for the simulation of strictly unidirectional waves, the laboratory paddle-waves are modelled with a very narrow directional energy distribution:

$$E(f,\theta) = \frac{E(f)}{\Delta}\ \cos^{20}(\theta - \theta_0) \tag{4.4}$$

with $\theta \in [\theta_0 - \pi/2, \theta_0 + \pi/2]$ and Δ is a normalization factor to ensure that the integral of the angular spreading function over $[-\pi, \pi]$ is equal to 1. It was further verified that the following results with this representation of paddle-waves are not sensitive to the directional discretization. Yet, such a definition might change the nonlinear interactions between both wave systems that occurred in the wind wave tank. Therefore, the following results must be analysed in light of the present directional definition of the paddle-wave system.

4.4.2 Results

Hindcasts of laboratory measurements (i.e. without any kinematic similarity) are not common in the literature. Booij et al. (2001) and Holthuijsen et al. (2000b) made an attempt to simulate Donelan (1987) laboratory observations with the SWAN model (Booij et al., 1999). They showed significant limitations of 3G wave models to simulate wind wave generation and dissipation processes at laboratory scale. Indeed, wave models are exclusively parameterized for wave hindcasting or forecasting at global, regional or coastal scales. However, as Shemer (2019) showed, wave generation in wind wave tunnels is, to a great extent, comparable to in situ wind wave growth. Thus, using the advantages of the well-controlled laboratory environment can be a powerful way to validate 3G wave models.

Since the paddle-waves and the wind had the same direction in the tank, we focus on 1D (omnidirectional) wave spectra in this case. Figure 4.3 depicts the observed spectra at a fetch 30 m by comparisons with the simulated ones. Columns and rows separate the different values of the steepness ak of irregular paddle-waves and the different wind speeds, respectively.

Overall, the simulations are in good agreement with the observed spectra in the presence of a JONSWAP-type paddle-waves. On the other hand, in "wind only" conditions, the spectral wind

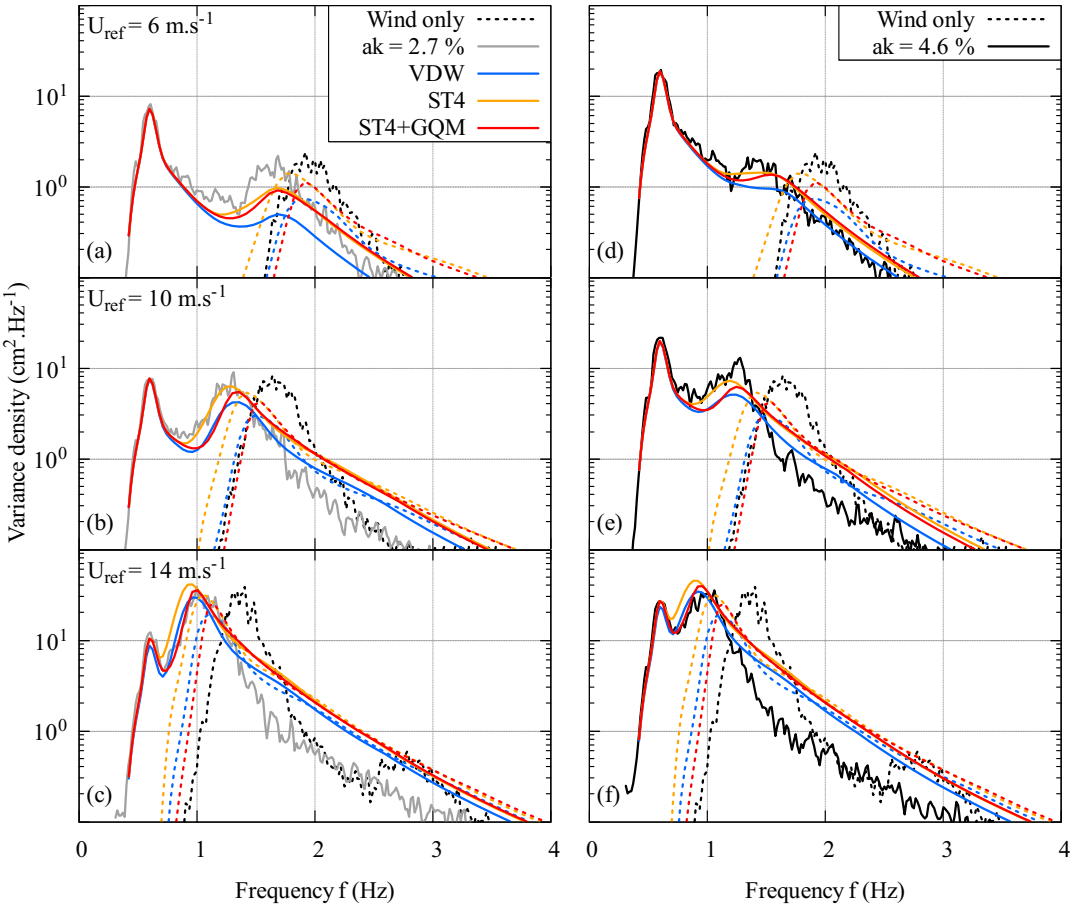

Figure 4.3: Variance density spectra with and without irregular paddle-waves of steepness ak and peak frequency $f_p = 0.6$ Hz for several wind speeds (on rows) at a fetch of 30 m. Color lines (blue, orange and red) correspond to simulations with different sets of source/sink terms and black and grey lines refer to the observations.

wave peak is underestimated in terms of energy and peak frequency. Booij et al. (2001) and Holthuijsen et al. (2000b) raised a similar issue when simulating wind-wave growth from laboratory observations with SWAN. The most interesting point to highlight might be that, in the simulations, the various model variations seem to reproduce a wind wave peak frequency downshift in the presence of background long-waves. This numerically simulated downshift is however less pronounced than in the experiment.

It can be noted that the energy levels of the HF tail are overestimated in the simulations with $U_{\text{ref}} = 10$ and 14 m/s (colored lines in Figs. 4.3.b,c,e and f) even if the variance density decrease rate at HF is consistent with the observations (grey scale). For those wind speeds, there is an increasing difference between the simulations and the observations from the wind wave peak to higher frequencies. It shows a lack of accuracy of the simulations in reproducing the well-known overshoot behavior (Barnett and Sutherland, 1968) associated to wind wave growth. At lower wind speed (Figures 4.3.a and d), this overshoot is less pronounced and the HF tails seem rather well reproduced by the simulations including the long-waves. But it is not the case for the wind wave peak (colored dotted lines) which is underestimated in all panels. Overall, the simulation of an

accurate energy level for both the wind wave peak and the HF tail seems to be a barrier when using 3G wave models at such small scale.

The different models described in section 4.3 show different levels of performances in reproducing the observed spectra. First, the VDW set is the only parameterization depicting a slight underestimation of the low-frequency wave energy at the highest wind-speed. This is due to the limitation of Komen et al. (1984)'s parameterization partly included in VDW. At higher frequencies, VDW generally underestimates the energy of the wind wave peak with and without the long-waves. Such a behavior reveals an over dissipation of the wind-sea system in $Q_{\mathrm{ds}}^{\mathrm{VDW}}$. Regarding the "wind only" case, VDW simulates a wind wave peak frequency that tends to be shifted toward low frequencies by comparison with the observations.

At the largest wind speed $U_{\mathrm{ref}} = 14$ m/s, all the models tend to have an excessively energetic wind wave peak in the cases with long-waves and an excessively low wind wave peak frequency in "wind only" conditions. As highlighted in Villefer et al. (2021), the limitation of the techniques to measure the wind velocity profile could lead to the calculation of an excessive value of the friction velocity. Since the friction velocity forcing is taken from the experimental value, the wind wave peak energy and frequency can be expected to be respectively over- and under-estimated at higher wind speeds.

ST4 parameterization seems to better estimate the wind wave peak energy than VDW both with and without long waves, but still depicts a largely downshifted peak frequency for the "wind only" case. With a more accurate resolution for the 4-wave interactions with GQM, the simulations in "wind only" conditions give a better compromise in terms of energy level and peak frequency. The differences between ST4 with DIA and ST4 with GQM is well illustrated in the simulations with long-waves in Figures 4.3.a and d. The red spectra (GQM) depict a slightly narrower wind wave peak than the orange spectra (DIA). Simulating narrower spectra is a well known property when improving the accuracy of the method for solving the 4-wave interactions (Benoit, 2005). Finally, considering the simulations with and without long-waves, ST4+GQM might be the parameterization showing the best overall performances in reproducing the bimodal spectra observed in Marseilles' wind wave tank.

Figure 4.4 is obtained by separating the wind waves from the paddle-waves using a decomposition of the sea state into two JONSWAP spectra fitted using a method presented in Villefer et al. (2021). It tempers the agreement between the simulated and the observed wind wave peak energy illustrated in Figure 4.3. In Figure 4.4.a, the 3G wave model overestimates the wind wave energy at all fetches with an exception at maximal fetch. Nevertheless, the simulated wind wave energy variations with fetch show a slope similar to Kahma and Calkoen (1992) formula and close to the observations. Regarding the simulated wind waves peak frequency variations with fetch, the model reproduces rather well the observed bimodal sea states in terms of magnitude and slope. However, the simulated variation of the wind wave peak frequency without paddle-waves (dotted lines in Fig. 4.4.b), clearly different from the corresponding observations (black squares), is similar to the observations with paddle-waves (black circles).

This latter issue, also observed in Figure 4.3, is linked to the difficult question of triggering wind wave growth in 3G wave models. The wind wave growth initialisation commonly used following Cavaleri and Malanotte Rizzoli (1981) was not adapted for wave simulation at laboratory scale in

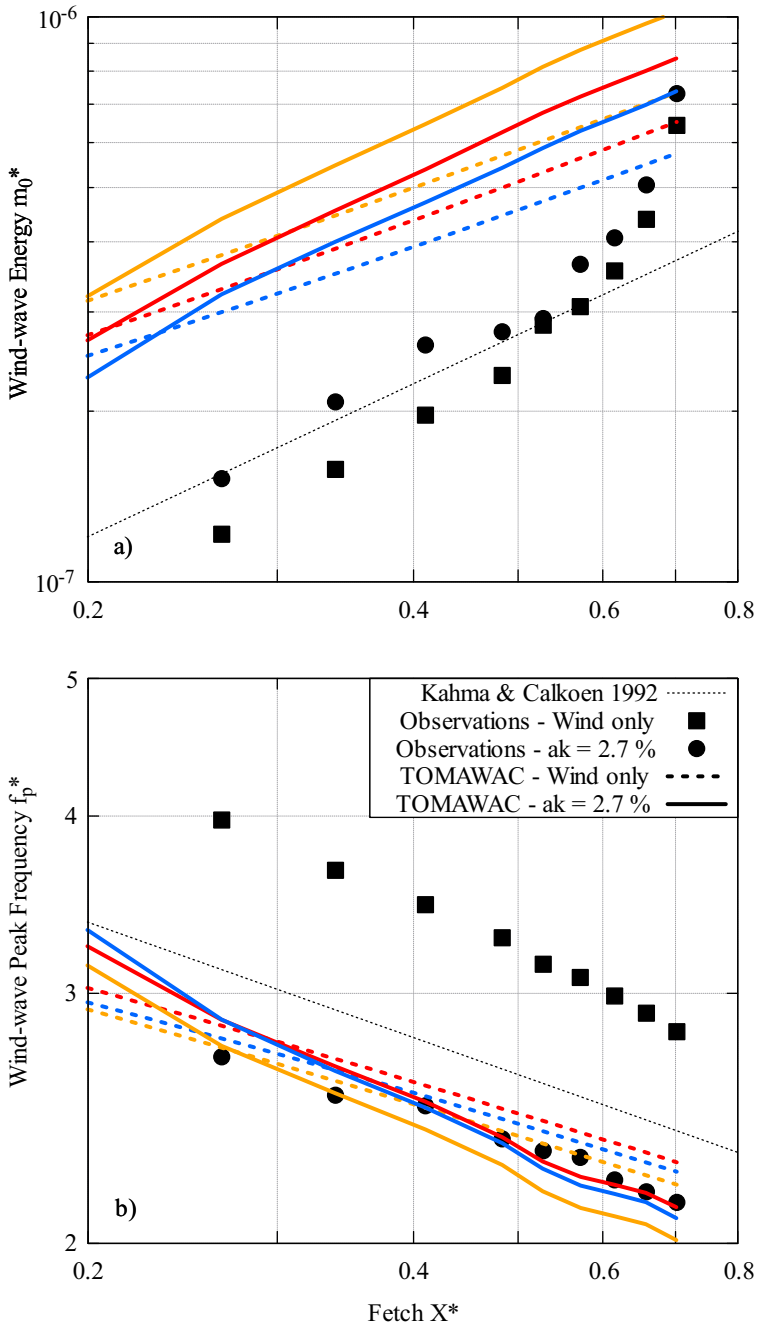

Figure 4.4: Variations of the observed and simulated wind wave dimensionless energy (a) and peak frequency (b) with dimensionless fetch compared to Kahma and Calkoen (1992)'s empirical law for a wind speed $U_{\text{ref}} = 14$ m/s and irregular paddle waves with $ak = 2.7$ %. TOMAWAC's parameterizations are differentiated using colors: VDW in blue, ST4 in orange and ST4+GQM in red. The black points refer to the observations.

our case (not shown). Thus, we triggered wind wave growth by using the measured wind wave spectrum at a fetch 5 m as an input boundary condition in our simulations.

A difference is observed between the horizontal location of the HF peak of colored plain-line spectra and the corresponding peak of dotted-line spectra in Figure 4.3, especially at high wind

speed. This difference is observed, once again, in Figure 4.4.b between the dashed and plain color lines. Hence, the downshift of the wind wave peak in the presence of long-waves, first observed during the laboratory experiments (Villefer et al., 2021), is observed once again in the simulations to a smaller extent. To further characterize this phenomenon, Figure 4.5 illustrates the differences between its observations in laboratory (black dots) and their simulations (colored dots).

In laboratory, the downshift does not result in a modification of the wind wave energy. Hence, it implies a reduction of the wind wave steepness. This was illustrated, in a figure similar to Figure 4.5 in Villefer et al. (2021), by the distance to Toba's law (Toba, 1997). Wind waves' steepness increases when the points overtake Toba's law from above. According to Figure 4.5, at medium and high wind speed, the points are more gathered in the simulations than in the observations. Particularly, the most pronounced differences are in "wind only" conditions with the points corresponding to observed wind waves located above Toba's law contrary to the simulations. Thus, the model fails to reproduce the high steepness of the wind waves in "wind only" conditions.

For each wind speed and for all the parameterizations, the simulations exhibit a clear tendency to be horizontally distributed. The width of the distribution increases when the wind speed decreases, in agreement with the observations. The horizontal distribution shows that the wave models simulate wind waves with the same energy but a different peak frequency whether they are generated with or in absence of paddle-waves. Although, in "wind only" conditions, simulated wind waves are less steep than in laboratory, the simulations succeed in reproducing the wind wave frequency downshift happening when long-waves are added to the sea state.

In Villefer et al. (2021), the increase of the wind wave friction velocity in the presence of long waves was considered as a possible factor to explain the downshift. According to the simulations in which the friction velocity is kept constant with and without long waves, this factor is proved not to be the only one explaining the downshift.

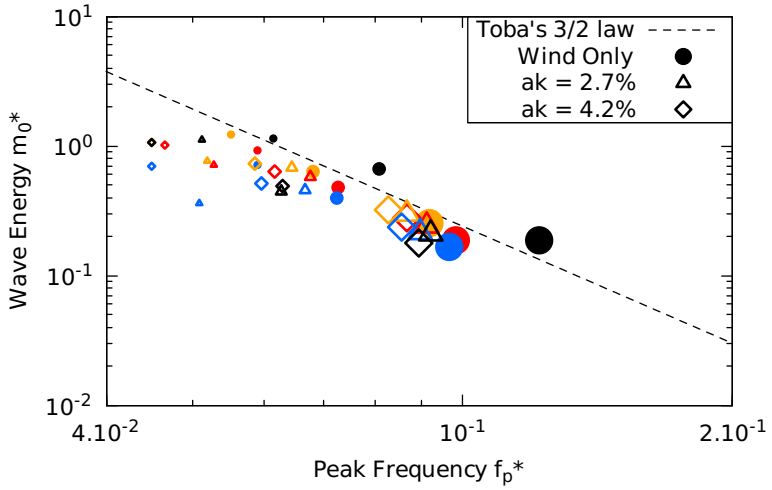

Figure 4.5: Variations of the wind waves's dimensionless energy with the dimensionless peak frequency for different reference wind speeds compared to Toba's 3/2 law. The dot size refers to the wind speed (small $U_{\text{ref}} = 6$ m/s; medium $U_{\text{ref}} = 10$ m/s; large $U_{\text{ref}} = 14$ m/s) and the color refers to the sets of source/sink terms. The black points refer to the observations.

Overall, the simulations are in rather good agreement with the observed frequency spectra in cases including paddle-waves. Therefore, the narrow energy directional distribution selected to model the unidirectional paddle-waves does not seem to disturb the nonlinear interactions between both wave systems. The general underestimation of the wind wave peak in "wind only" conditions seems to result from an over-dissipation in the wind wave frequency range. The wind waves observed in the wind wave tank, especially in "wind only" conditions, are very steep. The saturation limits defined by Ardhuin et al. (2010) and van der Westhuysen (2007) might then be too restrictive for young laboratory wind waves, according to their wave age. Hence, the saturation limit might be more relevant with a definition including a function of wave age. This could allow having a more pronounced overshoot in the spectra and an accurate numerical estimation of the energy levels for both the wind wave peak and the HF tail. This saturation limit is less problematic for wind waves in the presence of longer waves since their steepness is reduced due to the background long-waves. The mechanisms at play in this steepness reduction will be further investigated in the following.

4.5 Hindcast of SHOWEX experiment

4.5.1 Numerical specifications

The bathymetry for the North Carolina continental shelf was taken from the GEneral Bathymetric Chart of the Oceans (GEBCO) publicly available bathymetry data sets. The different domains are discretized as follows:

- Spatial: irregular mesh with an average resolution of 500 m.
- Temporal: constant time step of 30 s.
- Frequency: 40 frequencies with a logarithmic distribution ($f_n = f_1.q^{n-1}$) over the range $[0.04; 0.72]$ Hz.
- Directional: regular mesh with 36 directions (every 10°).

It was checked that halving the spatial resolution from 500 m to 250 m does not change the simulated spectra, the spatial mesh convergence is thus satisfied.

The wind field is taken from the CFSR time series in open-access in the National Oceanic and Atmospheric Administration (NOAA) website. Figure 4.6 gives an overview of the numerical spatial domain colored with the wind velocity (65,000 nodes). It depicts the wind acceleration when the distance to the coast increases. The swell frequency spectra from the measurements at the X6 buoy (offshore) are imposed as boundary condition on the offshore side of the spatial domain. The unstable atmospheric boundary layer is not taken into account in the simulations. These atmospheric conditions would result in a slight wind wave growth amplification (see Ardhuin et al. (2007) for more details). Therefore, this amplification is ignored in our case since the default numerical settings consider a neutral atmospheric boundary layer.

When using Q^{ST4}, it was found that imposing a parametric HF tail was not necessary to obtain a variance density smooth f^{-4} decrease rate. This decrease rate has been largely discussed in the

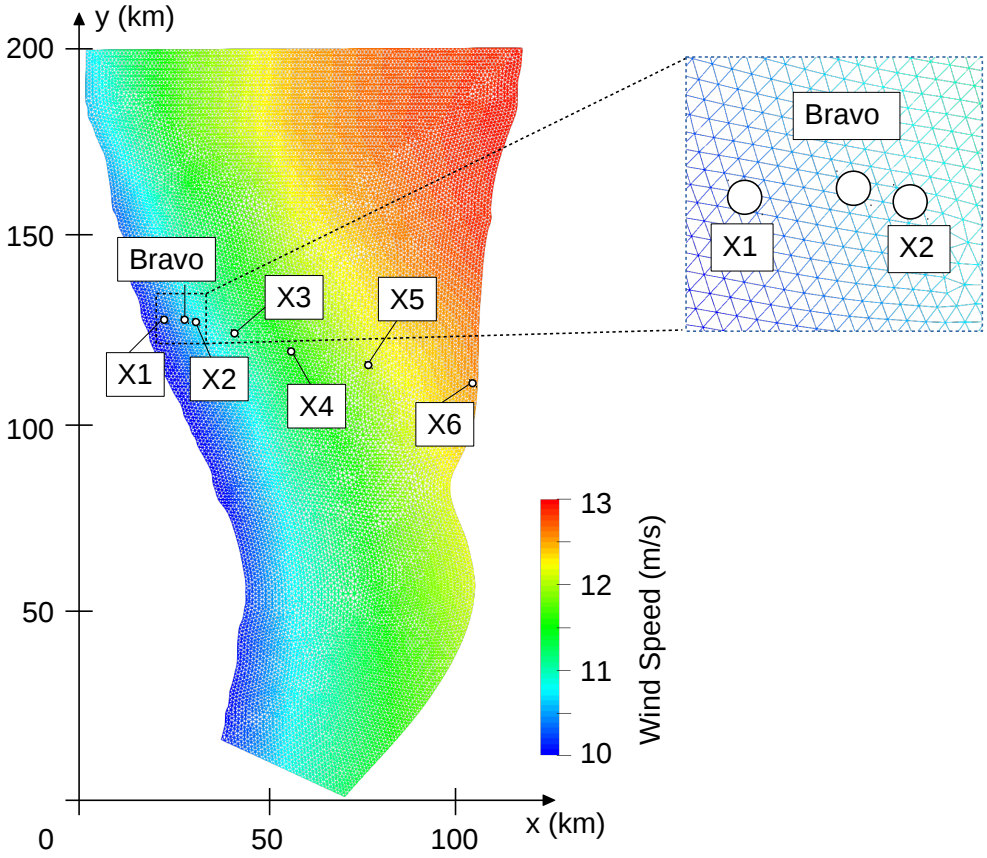

Figure 4.6: TOMAWAC's spatial domain showing the wind speed and the irregular mesh adopted for the simulations of the SHOWEX campaign.

literature (Toba, 1973) and is supported by numerous observations (Kawai et al., 1977). Furthermore, the deactivation of the parametric tail was required to obtain spatially converged results (not shown).

When using $Q^{\mathrm{ST4+GQM}}$, neither the parametric HF tail nor the wave growth limiter were activated. These features are commonly used respectively to insure the physical shape of the spectrum at high frequencies and to guarantee the numerical stability of the calculations due to the physical shortcomings of the model parameterizations. Having numerically stable simulations without using these tools is a proof of the physical relevance of the ST4+GQM parameterization.

4.5.2 Results

In section 4.4, the numerical model has proved to be quite adapted, with a friction velocity forcing, for reproducing the laboratory bimodal sea states. The purpose of our work is to assess the extent at which laboratory observations by Villefer et al. (2021) can be transported at coastal scale. Hence, it is necessary to verify the model's performances for simulating bimodal sea states at coastal scale.

This validation step is based on the evaluation of TOMAWAC's performances in reproducing the spatial characteristics of wind wave growth over an opposing background swell within the scope of the SHOWEX campaign.

Figure 4.7 depicts the simulated wind wave energy and peak frequency variations with fetch. These variations are compared to the SHOWEX observations and Kahma and Calkoen (1992) law for stable stratification obtained from a collection of laboratory and ocean data.

In the observations, one can distinguish two kinds of gray circles referring to two spectral methods for separating wind waves from swell. The open circles refer to Ardhuin et al. (2007)'s analysis considering the wind-sea energy at frequencies above the first maximum of the directional spread over frequencies. The solid circles refer to a spectral separation method based on JONSWAP-type spectra fitted on the observed bimodal spectra from Villefer et al. (2021). This method is also used to obtain the simulated wind wave energy and peak frequencies. Hence, the model's results are compared to the observations according to the full circles in the following. The vertical distance between solid and empty circles at each fetch, in Figure 4.7, depicts the degree of arbitrariness existing between methods for separating swell and wind waves.

In Figure 4.7.a, each parameterization reproduces energy variations in agreement with SHOWEX observations and the empirical laws for the energy and the peak frequency. However, the wind wave energy level is systematically overestimated in the simulations especially by VDW at a medium fetch. This systematic overestimation can be explained, to some extent, by the choice of the wind hindcast file. A finer setting of the parameterizations' design parameters, such as Alday et al. (2021) did by modifying the wind input and dissipation parameters for global scale applications, could improve the quality of the estimated energy level. For example, Ardhuin et al. (2007) TEST443 parameterization for ST4 (black triangles in Figure 4.7) is in close agreement with the observations (open circles). It should be noted that GQM was activated without changing any dissipation or wind input settings originally calibrated for DIA method. Performing global hindcasts would be necessary to further improve GQM performances by adopting a finer setting for GQM parameters. Recently, Beyramzadeh and Siadatmousavi (2022) implemented the GQM method in WW3 and performed hindcasts on hurricanes observed in the Gulf of Mexico. Their conclusion, similar to ours, is that a redesign and a recalibration of Q_{in} and Q_{ds} would be necessary to fully benefit from GQM's improvements.

Regarding Figure 4.7.b, ST4+GQM (red lines) clearly outperforms the parameterization using DIA method in reproducing the downshift of the wind wave peak frequency with fetch. The frequency variation depicted by the red curve is in agreement with SHOWEX observations and the empirical law. The differences with parameterizations based on DIA appear at short fetch with an underestimation of the peak frequency. This initial underestimation results in reduced variations that eventually give an accurate peak frequency at longer fetch.

Figure 4.8 shows the spatial evolution of frequency spectra at buoys Bravo, X3 and X6 (respectively the 2^{nd}, 4^{th} and last locations relative to increasing fetch in Figure 4.7). The features observed in Figure 4.7 are encountered again in Figure 4.8 with the overestimation of the wind wave energy and the accurate estimation of the wind wave peak frequency by ST4+GQM. The swell peak is rather well reproduced in the simulations. VDW parameterization shows a stronger dissipation of the swell with fetch resulting from the dissipation term partly based on Komen et al. (1984). In

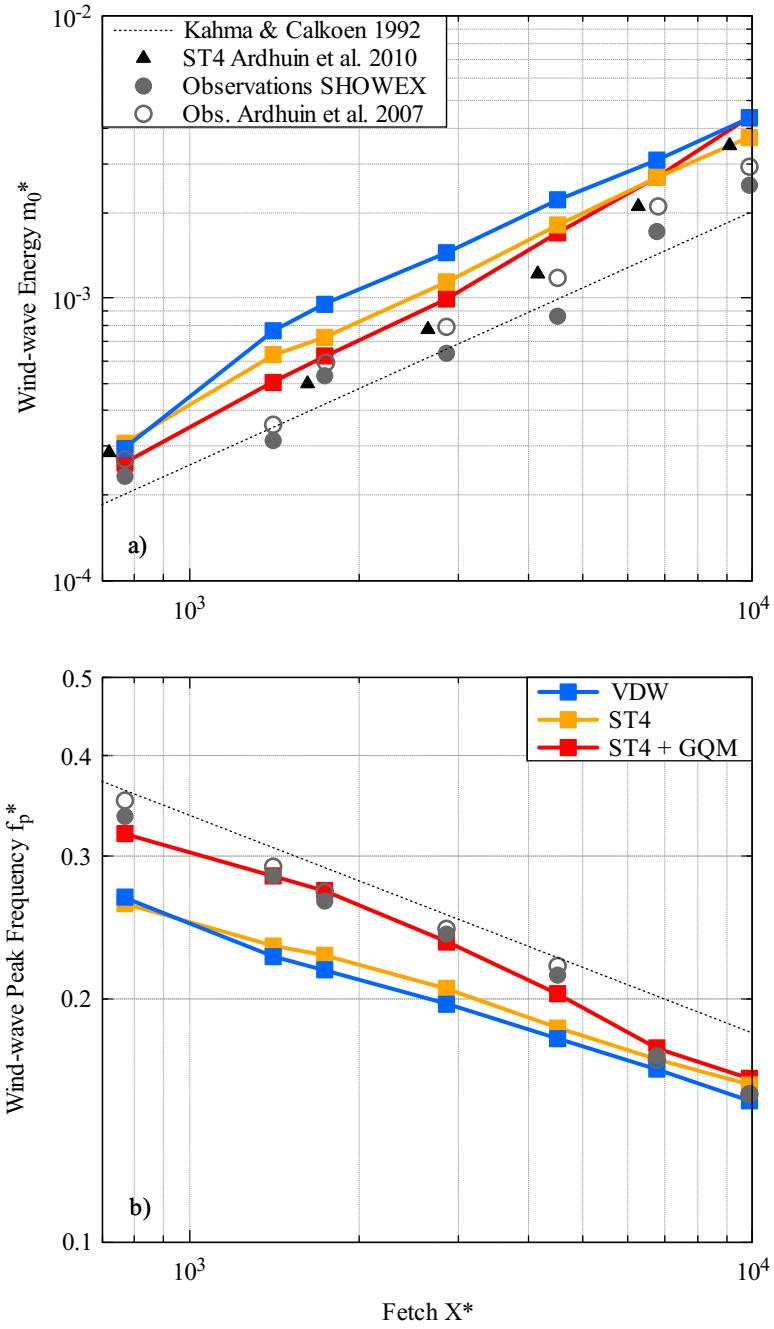

Figure 4.7: Variations of the wind wave dimensionless energy (a) and peak frequency (b) with dimensionless fetch (with increasing fetch: X1, Bravo and X2 to X6) compared to Kahma and Calkoen (1992)'s empirical law during SHOWEX campaign on Nov. 3, 1999, 12-17 EST. Color point-lines (blue, orange and red) correspond to simulations with different sets of source/sink terms. Black and grey point-lines refer to the observations.

Figures 4.8.a and b, the ST4+GQM simulations (red spectra) overestimate the HF side of the swell peak degrading the agreement with the observations. This overestimation can either result from the 4-wave interactions or from a lack of dissipation of the HF part of the swell in the shoaling process. The overestimation eventually disappears at maximal fetch (Fig. 4.8.c).

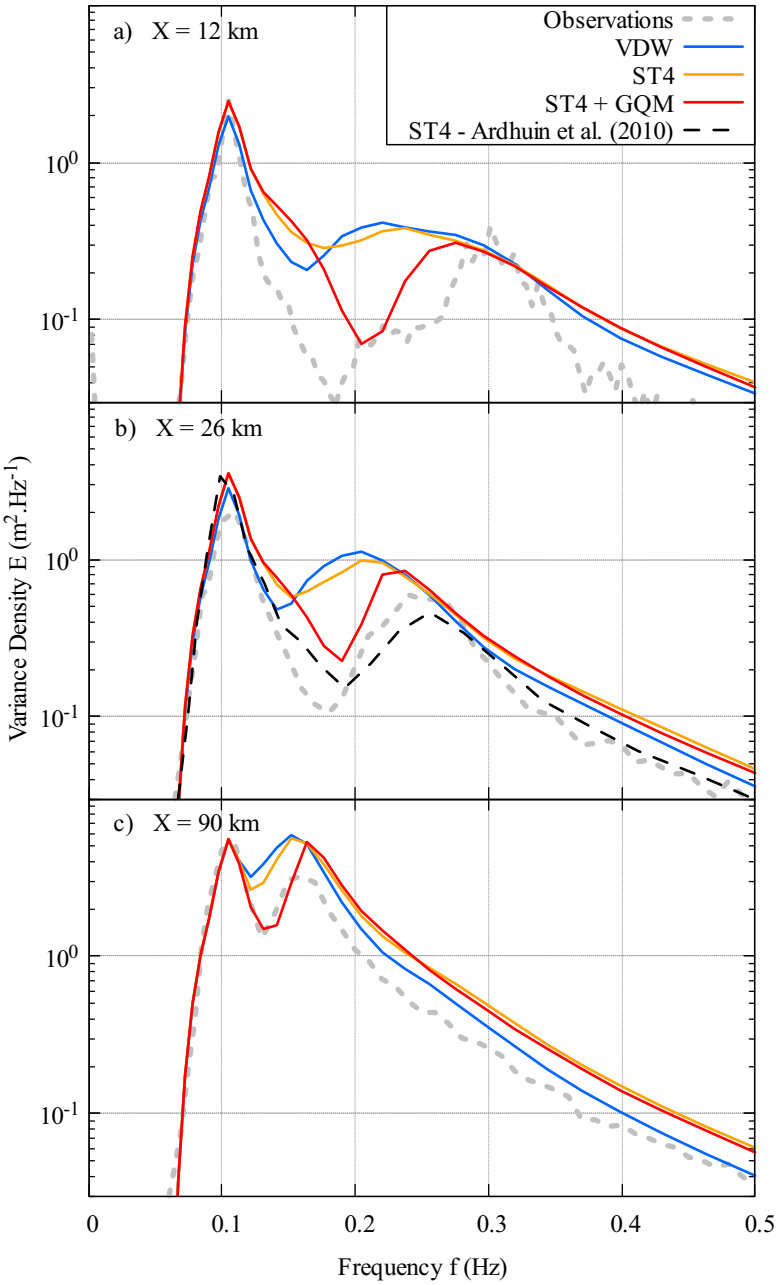

Figure 4.8: Spatial evolution of the variance density spectrum with buoys Bravo ($X = 12$ km), X3 ($X = 26$ km) and X6 ($X = 90$ km) during SHOWEX campaign on Nov. 3, 1999, 12-17 EST. Color lines (blue, orange and red) correspond to simulations with different sets of source/sink terms, grey dotted-lines refer to the observations and black dashed-line to Ardhuin et al. (2007) simulation.

Another proof of ST4+GQM performances is illustrated by the width of the simulated spectra. While VDW and ST4 parameterizations depict a rather large wind wave peak in Figures 4.8.a and b, ST4+GQM gives a narrower peak which is more representative of the observed spectra.

Figure 4.9 shows a set of observed and simulated directional spectra at Bravo location. One should keep in mind that the methods to obtain directional spectra from buoy measurements such as gauge

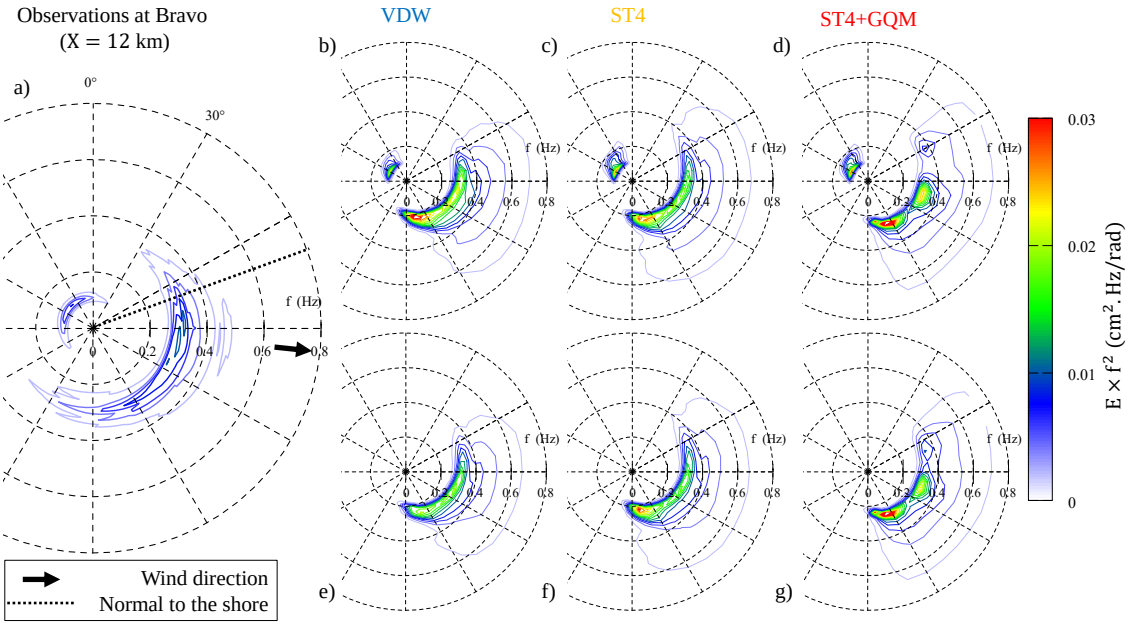

Figure 4.9: Directional variance density spectra multiplied by the frequency squared at Bravo (ASIS-type buoy) according to observations using the MLM (a) and to simulations with (b to d) or without (e to g) swell. The normal to the shore is 70° and the mean wind direction is 96°.

arrays (ASIS) or single-point systems (DDW) only give an estimation of the directional properties. The energy distribution along frequencies and directions can vary between the different methods. Here, the directional spectra from the observations are obtained using the Maximum Likelihood Method (MLM). A classification of methods to analyse directional wave spectra was performed by Benoit et al. (1997).

In Figure 4.9, the original directional spectra are multiplied by the squared frequency to highlight the energy of the wind waves. Directional spectra from simulations with and without swell are plotted to assess the extent at which swell impacts the wind wave direction. Looking at the observations in Figure 4.9.a, the equilibrium range (clear blue) is slightly deviated from the wind direction towards the alongshore direction. However, the wind wave peak (dark blue-green color) direction is aligned with wind direction.

Using the same SHOWEX event, this deviation has been addressed by Ardhuin et al. (2007) and Zhang et al. (2009). First, by observing the wind wave mean directions, Ardhuin et al. (2010, 2007) associated this deviation to the slanting fetch properties. They observed a similar but amplified wind wave deviation in their models with a significant bias, compared to SHOWEX observations, towards the alongshore direction. This amplification was even more marked with a saturation-based dissipation term.

Zhang et al. (2009) argued that the slanting fetch has the property to deviate the wind wave peak but not the waves in the equilibrium range. According to them, the waves in the equilibrium range are deviated due to the wind stress angle that can be shifted from the wind direction by the presence of ocean currents.

In the present simulations, no current is taken into account and no shifting of the wave equilibrium

range is observed in the corresponding spectra plotted in Figure 4.9. The numerically estimated wave equilibrium range has the same direction as the wind in all parameterizations. However, according to VDW and ST4 parameterizations with and without swell, the wind wave peak direction has a bias of about 30° in the alongshore direction. This bias is certainly due to the slanting fetch properties somehow amplified by the numerical model. VDW is the only parameterization showing a clear wind wave energy amplification in the presence of swell. This amplification is another consequence of the use of Komen et al. (1984)'s dissipation term with a background swell.

The differences between DIA method and GQM to take into account the 4-wave interaction in a sea state including wind waves are well illustrated in Figure 4.9. According to Figures 4.9.d and g, the wind wave peak simulated with ST4+GQM differs from VDW and ST4 in terms of directional distribution of the wave energy near the wind wave peak. Three peaks can be distinguished. The main peak (i.e. the more energetic in red) follows the alongshore propagation tendency observed in VDW and ST4, while the secondary peak (i.e. yellow) is aligned with the wind direction. Lastly, the third peak is directed offshore. Overall, with the presence of the secondary peak, GQM+ST4 slightly improves the agreement between the numerical model and the observations. Regarding the mutual influences between swell and wind wave peaks, the wave systems do not seem to have significant effects on each other.

In Figure 4.10, the frequency spectra, mean directions and directional spreadings simulated with ST4+QM are compared to the observations at two values of fetch: 26 km and 89 km (buoys X3 and X6, respectively). At buoy X3, the simulated and observed wind wave peak frequencies are identical (Fig. 4.10.a). However, the distribution of the wind wave energy is slightly shifted towards HFs in the simulation. A similar shift is encountered regarding the mean direction and the directional spread (Fig. 4.10.b and c). Hence, as observed in Figure 4.9, the simulated mean direction is still slightly overestimated in the alongshore direction. In Figure 4.10.c, the simulated wind wave directional spreading is overestimated by about 10°.

At buoy X6, the simulated wind wave peak is in rather good agreement with the observations regarding the main direction and the angular spread (Fig. 4.10.e and f). Yet, the simulated peak frequency is still shifted towards HFs. Compared to the simulations in Figure 4.9, Figure 4.10 proves that the model shows better performances in reproducing the directional properties at a larger fetch, where the influence of the slanting fetch configuration decreases.

The simulations at laboratory and coastal scales prove that the chosen parameterizations are sufficiently accurate to reproduce both laboratory and coastal observations. Among the parameterizations, the aforementioned results showed that ST4+GQM slightly outperforms simulations with DIA: at laboratory scale in terms of peak frequency variations with fetch and at coastal scale in terms of the directional distribution of the wave energy. ST4+GQM is used in the next section on a generic case to study the effect of swell on wind wave growth at coastal scale.

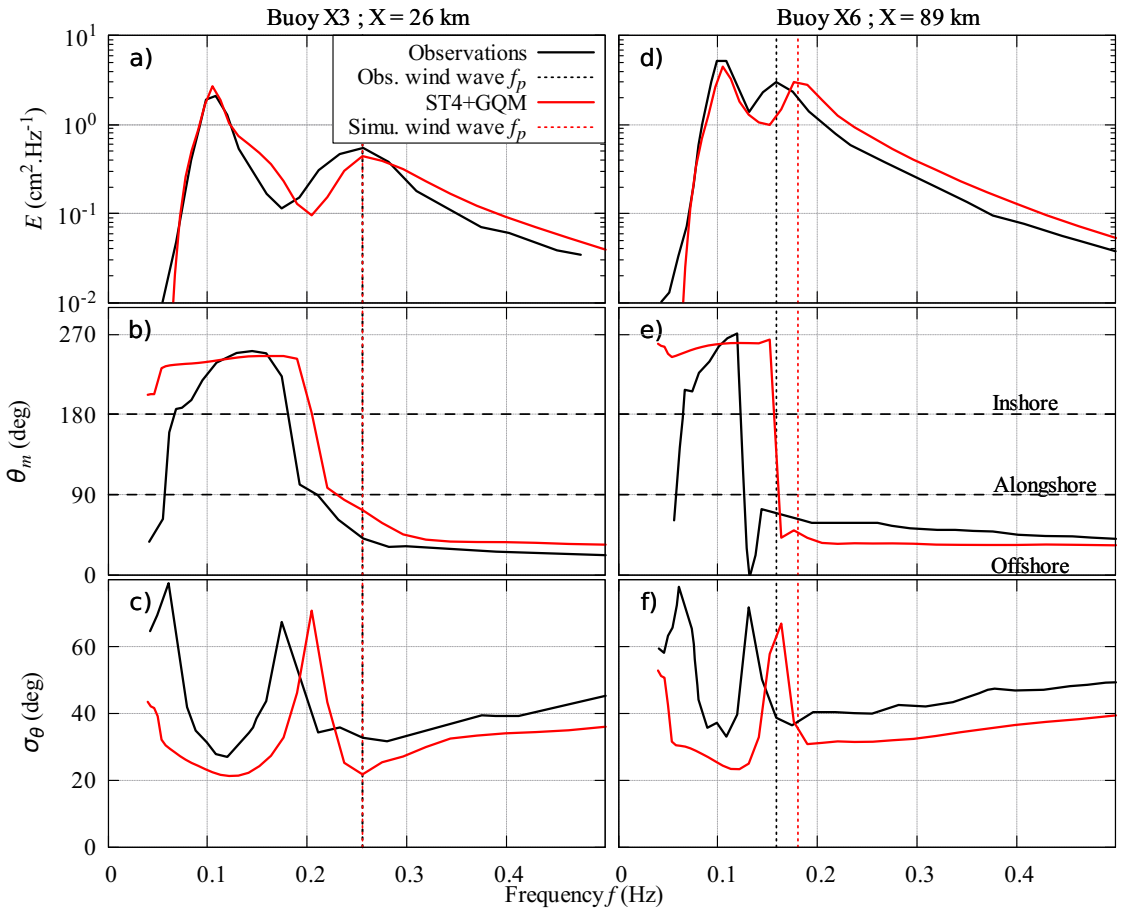

Figure 4.10: Simulated (red lines) and observed (black lines) (a,d) frequency spectra, and both as a function of frequency, (b,e) mean directions and (c,f) directional spreadings on 3 Nov. 1999 (averages over the 12:00–17:00 EST time interval) at two values of fetch: 26 km (on the left) and 89 km (on the right). Only the simulation using ST4+GQM set is displayed. The red and black vertical dotted lines correspond to the simulated and observed (resp.) wind wave peak frequencies.

4.6 Application to the study of wind wave growth over swell

4.6.1 Numerical specifications

A generic mesh was created to study wind wave growth over a background following swell. The maximal fetch for this study was set to 60 km. The mesh resolution is 500 m. The selected generic atmospheric conditions are in such a way that a wind at a velocity $U_{10} = 12$ m/s is blowing over a swell (JONSWAP-type) with a 10 s peak period propagating in the wind direction. Simulations were run with six swell energy levels ranging from no swell to a swell with a significant wave height $H_{m0} = 2$ m. The swell energy levels are identified in Figures 4.11 and 4.12 by swell energy percentages (i.e. 0 to 100 % corresponding to 0 to 2 m wave height ; for instance, 40 % is equivalent to a swell with $H_{m_0} = \sqrt{0.4} * 2 = 1.26$ m).

Two test cases were selected. In both cases, the ST4+GQM parameterization is used and the simulations are run with the six different swell magnitudes. The purpose of the first case is

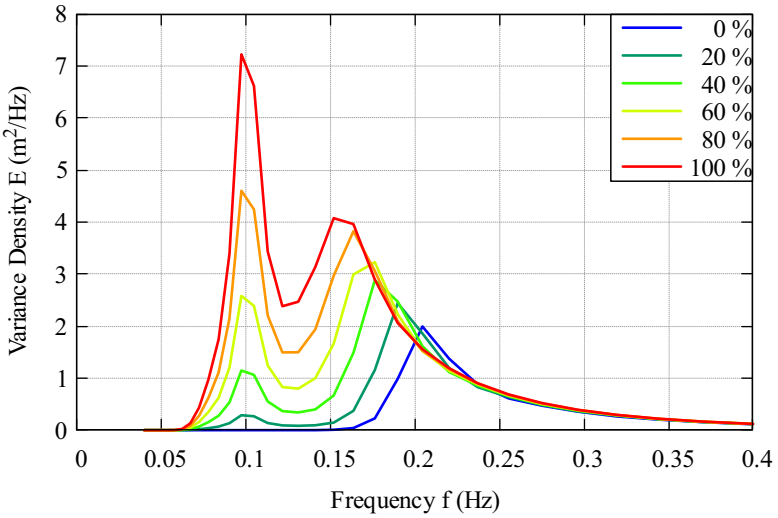

Figure 4.11: Downshift of the wind wave's variance density spectra in the presence of swell using TOMAWAC at a fetch 50 km. The swell is characterized by different energy levels identified by percentages: 0 % and 100 % respectively relate to no swell and to a 2 m high swell (H_{m0}).

to let the wave model handle the whole wind wave generation process and to observe the final results when the sea state reaches a stationary state. For this first case, only the swell, given the aforementioned percentage, is present in the initial condition of the simulations. Figure 4.11 shows the corresponding stationary spectra. The second test case, inspired by Masson (1993) study, aims at observing the source term balance for specific sea states consisting in the addition of two JONSWAP spectra. As illustrated in Figure 4.12.a, one is the swell system with $f_p = 0.1$ Hz and six different energy levels and the other one represents a wind wave system with $f_p = 0.2$ Hz (5 s peak period) and $H_{m0} = 1$ m. In Figure 4.12.a, the wind wave energy levels are slightly affected by swell energy. This is due to the addition of the energy in the HF tail of the JONSWAP swell spectrum. Considering $Q_{\text{in}} + Q_{\text{ds}}$ and Q_{nl}, the source term balance is calculated and given in Figures 4.12.b and c.

4.6.2 Results

As mentioned above, the wind wave modifications in the presence of swell are difficult to observe in the ocean and in coastal areas. This is partly due to the complex notion of fetch when dealing with vast areas of water and winds varying both in space and in time. Here, we suggest using a numerical model to overcome the problem. Figure 4.11 proves that, given the parameterizations and hypotheses on which our simulations are based with the use of TOMAWAC, the wind wave generation is largely modified with a background swell.

Given the constant wind speed (U_{10}), the only parameter changing between the different simulations (i.e. different colors) in Figure 4.11 is the swell height. The downshift of the wind wave peak frequency with increasing swell height is clear with the wind wave peak frequency varying from 0.2 Hz to almost 0.15 Hz equivalent to a variation from 5 to 6.7 s in terms of peak period. This downshift observed in Figure 4.11 is in agreement with the downshift observed during the

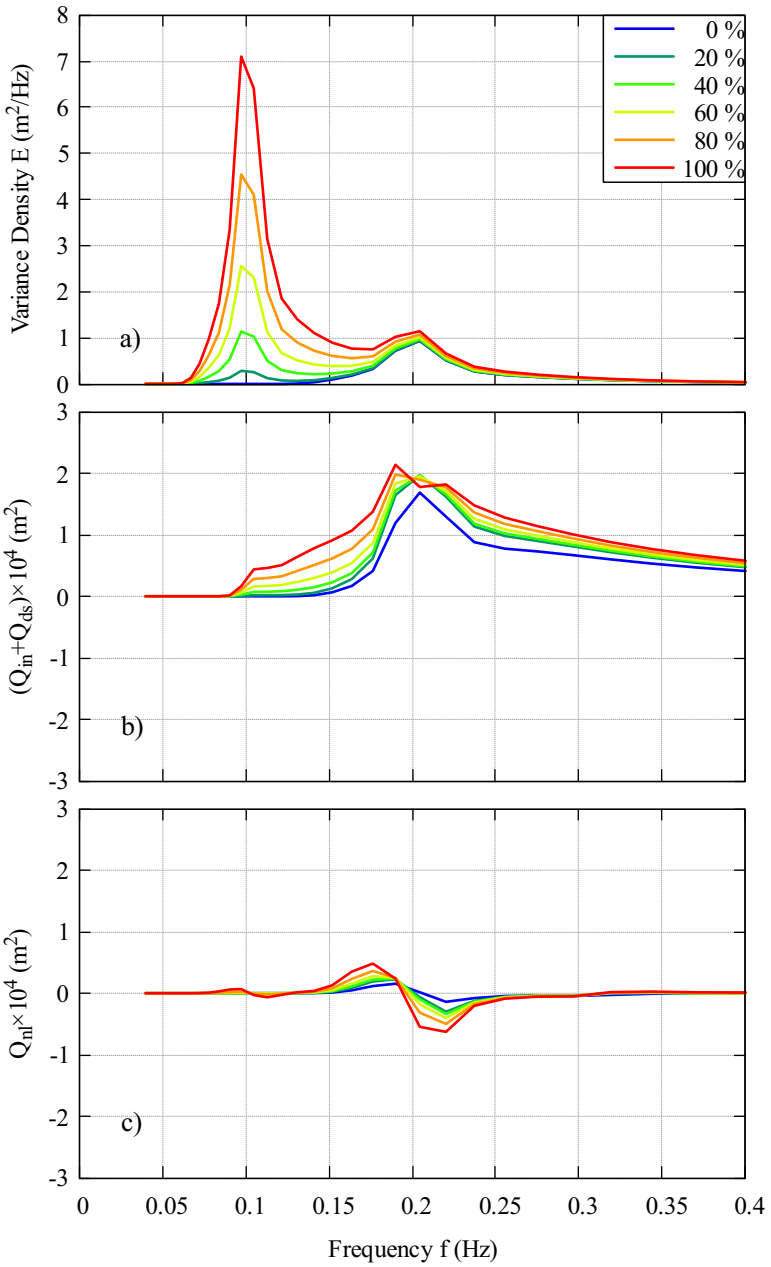

Figure 4.12: Bimodal wave spectra with different swell intensity (a) with the associated $Q_{in} + Q_{ds}$ balance (b) and non-linear transfer Q_{nl} (c).

laboratory experiments (Fig. 4.1).

In order to further analyse the physical processes leading to the downshift, the source terms involved in TOMAWAC simulations are investigated in Figure 4.12. This separation of the physical processes is inspired from Masson (1993) study in which the nonlinear coupling between swell and wind waves was examined. Here, the influence of the balance between the wind energy input and the whitecapping dissipation is studied in addition to the 4-wave interactions term.

According to Figure 4.12.b, the balance between Q_{in} and Q_{ds} is positive: wave generation prevails over wave dissipation so wave components are only growing. Hence, at the stage considered in Figure 4.12, the wave spectra did not reach an equilibrium state. The observation of this duration-limited stage is necessary to identify the processes leading to the downshift. In Figure 4.12.b, the most striking effect of the swell energy on wind wave growth is the large wind wave generation on the HF side of the swell peak. A significant amount of energy is added to the wave system in the frequency range between the swell and the wind wave peaks. Such wave generation on the low frequency part of the wind wave peak facilitates the wind wave frequency downshift. This observation is in agreement with Villefer et al. (2021) hypothesis. According the them, the energy continuum brought by the swell HF tail would initiate wind wave growth at a lower frequency than in absence of swell.

Figure 4.12.c recalls Masson (1993) study on nonlinear coupling between swell and wind waves. As said above, according to this latter reference, 4-wave interactions are involved in the wind wave evolution when the ratio of swell to wind wave frequency is greater than 0.6. In our case, this ratio is 0.5. In Figure 4.12.c, Q_{nl} shows slight variations accounting for the slight differences in wind wave energy levels (see Fig. 4.12.a). Apart from these variations, the swell does not seem to have a significant effect on the 4-wave interactions term that could have a notable effect on wind wave growth. This latter assertion is in agreement with Masson's ratio.

The present analysis could be completed by studying the magnitude of the downshift as a function of the spectral width of the swell peak. It comes from the present analysis that the HF tail of the swell peak artificially increases the fetch available for wind wave growth by initiating wave generation at a lower frequency than without swell. However, in many cases, swell spectral peaks do not carry much energy in the HF range. Given the latter analysis, the observed downshift is therefore expected to be reduced with a sharper and narrower swell peak. Hence, further analysis could be performed by testing different shapes for the swell peak with a narrow Gaussian shape, for instance. This is left for future work.

Overall, studying the influence of swell on wind wave generation based on the use of a spectral wave model with a generic domain enables to gain insights on the physical processes at play in the wind wave growth process for complex sea state conditions. However, this insight may be biased due to the limitations and the large extent of empiricism involved in the physical processes modelled in such numerical models (see e.g. Cavaleri et al. (2007)). Although the general shape of the wave spectrum has been reproduced to some extent by the numerical model at laboratory and coastal scales, the source and sink terms combination is not validated. There is a multitude of combinations between generation and dissipation terms that might lead to the observed spectra. Yet, the gap between the understanding of the physical processes and their mathematical formulations as source and sink terms in 3G wave models is constantly decreasing.

The present analysis, involving wind wave tank experiments and numerical simulations, is still rather exploratory and could be continued to assess the effect of several physical parameters on wind wave growth in more diverse configurations. Parameters such as the wind direction relative to the swell direction, the water depth or the atmospheric stability could be investigated, among others.

4.7 Extension of the results to real ocean waves

A downshift of the wind wave peak frequency was observed in Marseilles' wind wave tunnel when long paddle-waves were added into the wave system (Villefer et al., 2021). To which extent these laboratory observations can be upscaled at coastal scale with swell instead of paddle-waves? This is not an easy question since the long paddle-waves generated in wind wave tunnels have a wave age radically smaller than typical ocean swell. In the present paper, the method chosen to address the question is based on the use of a 3G spectral wave model. The initial hypothesis is that if the numerical model can faithfully reproduce the laboratory experiments (i.e the frequency downshift) and the evolution of a bimodal sea states (i.e. combining wind waves and swell) at a coastal scale, it can be used to upscale the laboratory experiment to the coastal scale. And by decomposing the physical processes at play when wind waves grow, the model can help to identify the physical processes responsible for the downshift.

The first stage of our methodology was to evaluate TOMAWAC performances in reproducing bimodal sea states at laboratory and coastal scales. Amongst the different parameterizations, the combination ST4+GQM gives, on average, the best agreement between simulations and observations. Overall, ST4+GQM shows a rather faithful reproduction of the observations both in terms of wave energy and peak frequency variations with fetch. Nevertheless, there are two main limitations of the model:

- at laboratory scale, the model largely underestimates the wind wave peak energy in wind only conditions (i.e. without paddle-waves),
- at coastal scale, in the presence of slanting fetch conditions of the selected event (SHOWEX campaign), the model succeeds only partially in simulating the directional distribution of the wind wave energy.

Yet, one interesting feature is the numerical simulation of a downshift similar to the experiments at laboratory scale, to a lesser extent though.

The second stage of our methodology consisted in creating a generic coastal domain to upscale the laboratory experiments at coastal scale. The first test case (Fig. 4.11) reveals a marked wind wave peak frequency downshift, increasing with swell intensity. According to the simulations, the wind wave peak period can be shifted by more than 1 s when a background swell is present. This wave period shift would have significant effects on the design of breakwaters or offshore structures, for instance. In a second test case (Fig. 4.12), we took advantage of the separation of the physical processes (i.e. Q_{in}, Q_{ds} and Q_{nl}) to identify the source and sink terms responsible for the spectral downshift. The wind input term is the best candidate given the wave generation happening on the low frequency part of the wind wave peak in the presence of swell. This wind wave generation at frequencies lower than without swell appears to be due to the continuum of energy brought by the swell peak in the HF range.

The methodology described in the present study is essentially based on the wave model reliability in modelling the physical processes at play when wind waves grow. This validity was evaluated to a large extent by performing comparisons between the numerical model results and wave ob-

servations. Such a verification makes our methodology more consistent, but the results must be appreciated in light of the validation stage we performed.

4.8 Conclusion

The performances of a 3G wave model were assessed for the simulation of bimodal sea state conditions at laboratory and coastal scales. Three sets of parameterizations for the source and sink terms were tested and compared with the observations at both scales. The similarity between the different sets lies in the modelling of the dissipation by whitecapping using a saturation based model. The latter choice results from the limitations of Komen et al. (1984) dissipation model in bimodal sea state conditions highlighted in several references (e.g. Ardhuin et al., 2007).

The ST4+GQM combination, recently and originally developed in TOMAWAC, uses a highly accurate method (GQM) to compute the nonlinear 4-wave interactions (Benoit, 2005; Gagnaire-Renou et al., 2010). Within this set, GQM is combined with the recent and largely adopted ST4 parameterization for the whitecapping dissipation sink term (Ardhuin et al., 2010). Compared to the other sets based on the DIA method, ST4+GQM simulations are roughly 50 times longer than the other sets due to the CPU time to compute Q_{nl} with GQM.

Overall, all the sets of parameterizations showed good performances for the reproduction of the frequency spectra by comparison with the observations at both scales. The ST4+GQM combination, albeit computationally demanding, showed two interesting facets:

- at laboratory scale, it differentiates from the other sets with a very accurate reproduction of the wind wave peak frequency variations with fetch,
- at coastal scale, it is the set showing the best agreement in terms of directional properties by comparison with the observations.

In addition to these two facets, simulations with ST4+GQM can be run without imposing any diagnostic HF tail and without using any wave growth limiter. Lastly, the ST4+GQM set was used to investigate the relevance of a physical phenomenon observed at laboratory scale, within a bimodal sea state combining two wind wave systems, at coastal scale within a bimodal sea state combining swell and wind waves.

To improve the results of the present study, it would be necessary to remove the friction velocity forcing, adopted for the simulations at laboratory scale. Recent studies aimed to improve the calculation of the friction velocity by further including the effects of nonlinearity with Janssen and Bidlot (2021) revision of Janssen (1991) source term or with the use of a wave boundary layer model as in Du et al. (2017). To further improve the directional properties of the simulated spectra, Romero (2019) proposed an anisotropic parameterization of the dissipation by whitecapping showing promising directional properties.

The use of 3G spectral wave models at laboratory scale could permit to further validate the different parameterizations for the source and sink terms in idealized conditions. Lastly, the simulations on a generic coastal domain could be continued to investigate wind wave growth with a background

swell considering several aspects such as the relative angle between swell and wind direction, the presence of a variable depth, the directional spread of the swell system, etc.

Acknowledgments

Antoine Villefer acknowledges the financial support of his PhD research program provided by the French ANRT (Association Nationale de la Recherche et de la Technologie) with CIFRE grant number 2019-1257. The authors thank Dr. Fabrice Ardhuin (LOPS, UMR 6523, Brest, France) and Pr. William Drennan (RSMAS, Miami, FL, USA) for providing the SHOWEX data, and Dr. Hubert Branger (IRPHE, UMR 7342, Marseilles, France) and Dr. Jeffrey Harris (ENPC/LHSV, Chatou, France) for many fruitful discussions.

Chapter 5

Wave overtopping of smooth and rock-armoured breakwaters in bimodal sea-state conditions

by A. Villefer, M. Benoit, D. Violeau, M. Teles and C. Luneau

Submitted to Coastal Engineering

Le débit de franchissements par les vagues est un paramètre essentiel pour la conception des protections côtières. Son estimation précise est primordiale pour trouver un équilibre entre un niveau de sécurité satisfaisant et un impact limité sur l'environnement. Une série d'expériences en laboratoire a été réalisée dans le but d'améliorer les méthodologies existantes (e.g. EurOtop 2018) pour estimer les débits de franchissements dans des conditions d'états de mer bimodaux (i.e. combinant houle et clapot). Deux types de revêtements ont été testés sur la pente de la digue : une surface lisse et une surface composée d'enrochements. Nos résultats prouvent que la plupart des méthodologies existantes donnent une estimation correcte des débits de franchissements dans des conditions bimodales en présence d'une pente lisse. Cependant, la caractérisation des états de mer à l'aide d'une cambrure caractéristique de l'état de mer met en évidence certaines tendances dans les résultats. Ces tendances sont confirmées et amplifiées en présence d'enrochements. Dans ce cas, le débit de franchissements mesuré est significativement surestimé par les formules empiriques (type EurOtop (Van der Meer et al., 2018)), en particulier pour des conditions d'état de mer présentant une cambrure caractéristique élevée, correspondant à une forte proportion de clapot dans l'énergie totale de l'état de mer. Deux méthodes, basées sur la cambrure caractéristique de l'état de mer, sont suggérées afin d'améliorer les estimations des débits de franchissements en présence de digues lisses et avec enrochements.

Abstract

The mean wave overtopping rate is an essential parameter to design coastal protections. Estimating it with a high precision is primordial to find a balance between a satisfactory safety level and a limited impact on the environment. A series of laboratory experiments were carried out with the aim of improving the existing methodologies (e.g. EurOtop 2018) to estimate the wave overtopping discharge in bimodal sea states conditions (i.e. combining swell and wind waves). Two types of slope roughness surfaces were tested: a smooth and an armoured rubble one. Our results prove that most existing methodologies are rather adapted to estimate wave overtopping in bimodal conditions in the presence of a smooth slope. However, some trends in the results can be associated to the combination of both wave systems characterized by a representative wave steepness. These trends are confirmed and amplified in the presence of the armour rubble slope. In that case, the measured wave overtopping rate can be significantly overestimated especially for sea state conditions with a high representative wave steepness, corresponding to a high wind wave proportion in the sea state energy. Two methods to take into account the effect of bimodal sea state conditions are suggested in order to improve the wave overtopping rate estimations with smooth and armoured rubble breakwaters.

5.1 Introduction

Storms occurring in coastal areas can lead to both extreme Mean Water Levels (MWL), due to a large storm surge, and extreme sea state conditions. In these conditions, waves can overtop coastal protections causing important flooding of coastal inland zones, cities, etc. In order to protect those coastal areas against such hazards, protections like breakwaters, sea-walls or dikes are usually built. In the scientific literature, numerous references (CIRIA, 2007; Pullen et al., 2007; TAW, 2002; Van der Meer et al., 2018) give recommendations to design these protections. Based on the admissible wave overtopping rate and the wave conditions that can be encountered in a specific coastal area, these references propose empirical formulas to determine the dimensions and characteristics of the protection.

During these extreme events, it is quite common to observe swell in addition to wind waves near the coast (Mason et al., 2008; Thompson et al., 2018). The swell is a wind wave system generated offshore that lengthen by propagating over long distances under the influence of a wind forcing and wave interaction processes up to the coast. This latter wave system has a longer period than the wind waves, generated near the coast by a local wind, and can also differ in terms of heights and directions. Yet, the above mentioned references give the overtopping rate estimation as a function of a single wave height, period and direction.

The objective of the present paper is to assess the validity of the use of a single wave height, period and direction to estimate the wave overtopping rate in such bimodal sea state conditions. Few series of experiments have been carried out using sea-wall models in wave tanks with the same purpose (Hawkes, 1999; Hedges and Shareef, 2002; Kashima et al., 2010; Orimoloye et al., 2021). All these previous studies based their research on sea walls with a smooth slope. One novelty of the present series of experiments is to extend previous studies to the common case of

a rock-armoured breakwater. With that goal, a breakwater model was set in the OSU Institut Pythéas wave tank in Marseilles (France). Due to the wave tank configuration, wind waves and swell were generated in the same direction normal to the breakwater crest. In such conditions, the wave overtopping rates are usually higher than similar wave conditions (i.e. equal periods and significant wave heights) with a direction oblique to the breakwater crest. Hence, the relative direction between the swell, the wind waves and the normal to the breakwater's crest is not further considered here. The experimental set up was such that wave overtopping rates were measured relatively to the crest freeboard R_c, distance between the crest level and the MWL, and the sea state conditions (H_s, T_m) with H_s the significant wave height and T_m the representative period (Fig. 5.1). A standard slope of 2:3 (vertical:horizontal) was selected for the model. Two types of slope surface roughness were tested: a smooth and an armoured rubble one. An example of standard armoured rubble breakwater in a French harbour is given in Figure 5.2.

In the wave tank, the wavemaker could generate two wave systems permitting to measure the mean wave overtopping rate over unit length of the sea wall q for a large variety of unimodal and bimodal sea states characterized by one or two couple(s) (H_s, T_m). The wave overtopping rates thus measured are compared to the estimated ones according to reference empirical formulas.

Different methods permit to empirically estimate the wave overtopping rate as a function of the coastal site characteristics and the wave properties. Although these methods differ in many ways, all are based on the following dimensional analysis:

$$q = f(g, H_s, L_m, R_c, \alpha) \tag{5.1}$$

where g is the acceleration due to gravity, L_m is the representative wave length and α the angle characterizing the breakwater slope (Fig. 5.1).

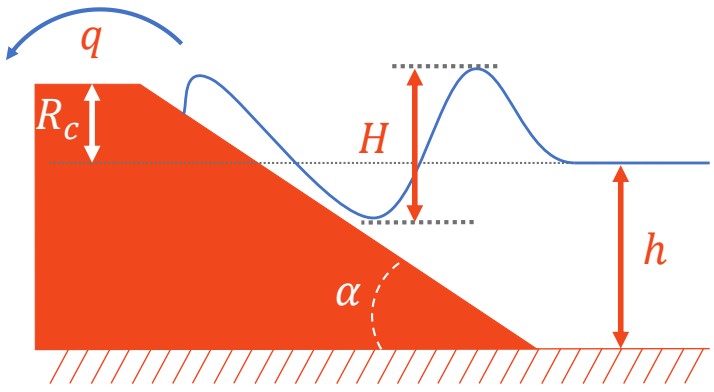

Figure 5.1: Sketch of the wave overtopping process over a breakwater with a slope $\tan\alpha = 2/3$.

The infinite depth dispersion relation is used to define the representative wave length $L_m = gT_m^2/(2\pi)$. Following Pullen et al. (2007) and Van der Meer et al. (2018) (referred to as EurOtop (2007) and EurOtop (2018) respectively in the following), the latter dispersion relation is used whatever the water depth to allow the definition of a representative wave steepness in the following. In addition, we make the hypothesis that the wave overtopping rate does not explicitly

Figure 5.2: Photograph of an armoured rubble-mound breakwater (in La Pallice harbour, La Rochelle, France) similar to the model considered in the present study (photo: Hubert Branger).

depend on the local water depth h. According to Eq. (5.1), the wave overtopping rate is only function of two base quantities, namely length and time. Hence, the Vaschy-Buckingham theorem (Vaschy, 1892) proves the existence of 4 non-dimensional variables to describe the physical process, *e.g.*:

$$\frac{q}{\sqrt{gH_s^3}} = F\left(\frac{R_c}{H_s}, \frac{H_s}{L_m}, \tan\alpha\right) \tag{5.2}$$

The following notations are chosen:

$$q^* = \frac{q}{\sqrt{gH_s^3}} \quad ; \quad R_c^* = \frac{R_c}{H_s} \quad ; \quad s_m = \frac{H_s}{L_m}$$

In the literature, several formulas to estimate the wave overtopping rate can be identified. Most of them are based on the exponential function. One of the first formulations, introduced by Owen (1980), is:

$$q^*\sqrt{\frac{s_m}{2\pi}} = a_O \exp\left(-b_O \frac{R_c^*}{\gamma_{f,O}}\sqrt{\frac{s_m}{2\pi}}\right) \tag{5.3}$$

with (a_O, b_O) a couple of parameters depending on the breakwater slope (i.e. on α) and $\gamma_{f,O}$ a factor characterizing the slope roughness (the values of these parameters are given in a table by Owen (1980)).

Following Owen (1980), Hedges and Reis (1998) developed a model on the basis of a simple theoretical wave overtopping model for regular waves. Although this model is more soundly based on physics than most empirical formulas from the scientific literature, it lacks of validation regarding the wave overtopping rate in the presence of an armoured rubble breakwater. Therefore it will not be used in the present study.

A second and largely adopted formulation, introduced by Van der Meer and Janssen (1995) and

developed through TAW (2002) and later EurOtop (2007,2018), is defined as:

$$q^* \sqrt{\frac{s_m}{\tan\alpha}} = a_{EM} \exp\left(-b_{EM}\left[\frac{R_c^*}{\gamma_{f,E}}\frac{\sqrt{s_m}}{\tan\alpha}\right]^c\right) \tag{5.4}$$

with a maximum given by

$$q^* = a_{ES} \exp\left(-b_{ES}\left[\frac{R_c^*}{\gamma_{f,E}}\right]^c\right) \tag{5.5}$$

with $\xi = \tan\alpha/\sqrt{s_m}$ the breaker parameter (or Iribarren number). The values of (a_{EM}, b_{EM}), (a_{ES}, b_{ES}) and c are given in EurOtop (2018). In particular, the main evolution between EurOtop (2007) and EurOtop (2018) regarding Eqs. (5.4) and (5.5) is that $c = 1$ in the 2007 version and $c = 1.3$ in the 2018 version. When $\xi > 2$ (approximately), i.e. the waves are not steep enough to break on the breakwater, they rather surge. In such conditions, q^* calculated with Eq. (5.4) is greater than q^* calculated with Eq. (5.5). Hence, Eq. (5.5) is used instead of Eq. (5.4).

Eqs. (5.3), (5.4) and (5.5) have been written in the framework of the present study. In the presence of slanting waves or if a berm precedes the breakwater, other influence factors can be included in the same manner as γ_f in the above formulas.

Although Eqs. (5.3), (5.4) and (5.5) take into account a single period and significant wave height to describe the sea state, several attempts were made to include the effect of the combination of two wave systems. Considering both unimodal and bimodal sea states, Van Gent (2000) found that the mean period $T_{m_{-1,0}} = m_{-1}/m_0$, defined using the spectral moments m_{-1} and m_0, is the most representative period to estimate q^*.

To further take into account bimodal sea state effects on wave overtopping, Van der Werf and Van Gent (2018) modified Eq. (5.4) based on the experimental study of the effects of oblique wind waves and swell on wave overtopping of a breakwater characterized by a smooth and impermeable 1:4 slope. They introduced a relative freeboard crest $R_c' = R_c - 0.5H_{m_0,\mathrm{s}}$, with $H_{m_0,\mathrm{s}}$ the swell significant wave height in place of R_c in Eq. (5.4). According to this new definition, the crest freeboard decreases relatively to half the swell significant wave height in bimodal sea state conditions. Hence, for a given bimodal sea state, the wave overtopping rate calculated according to Van der Werf and Van Gent (2018) is higher than the one given by Eq. (5.4). However, Van der Werf and Van Gent (2018) modification is not relevant in our case since the selected crest freeboard can be such as $R_c < 0.5H_{m_0,\mathrm{swell}}$ leading to negative crest freeboards.

Recently, Orimoloye et al. (2021) investigated the effects of bimodal wave conditions on wave overtopping considering 3 breakwater slopes: 1:3, 2:3 and a vertical wall. They introduced a parameterization of (a_{ES}, b_{ES}) as a function of the swell energy proportion in the total sea state energy and the breakwater slope. Overall, they observed that the wave overtopping rate increases with increasing swell proportion. Their method is valid in the conditions tested in the present study but might be questionable for sea states with larger wave periods. Indeed, this definition does not include the physical difference between swell and wind waves that is the difference in peak period of the two wave systems. Hence, for instance, if one wants to estimate the wave overtopping rate associated to a bimodal sea state including peak periods of 8 and 15 s on one hand and 5 and 8 s on the other hand, according to Orimoloye et al. (2021)'s formula, the 8 s wave system is a wind wave system in the former case and a swell system in the latter.

Both Van der Werf and Van Gent (2018) and Orimoloye et al. (2021) formulas to calculate the wave overtopping rate in bimodal sea state conditions were developed using laboratory experiments. The physical model described in the present work is complementary to Orimoloye et al. (2021) study with the investigation of the effect of roughness elements on the breakwater slope. Furthermore, we aim at improving the universality of the characterization of the wind waves and swell combination to estimate the wave overtopping rate.

The experimental set-up including the characteristics of the breakwater model, the tested wave series and the measurement techniques are introduced in section 5.2. In section 5.3, the resulting measurements with the smooth slope and with the armoured rubble slope are analysed successively, and then summarized to be accessible as a unique dataset for future studies. Based on the analysis of the results, section 5.4 suggests a new scaling including the representative wave steepness as a key parameter to improve wave overtopping estimations for sloping structures. Section 5.6 concludes the present study by summarizing the main observations and suggesting complementary studies to further include the effect of bimodal sea state conditions in the wave overtopping rate calculation with smooth and armoured rubble slopes.

5.2 Experimental set-up

5.2.1 Specifications at prototype scale

In this section 5.2.1, the dimensions are specified at prototype scale in order to better picture the breakwater and the sea state characteristics. The breakwater dimensions and the sea state conditions at model scale (1:25, using Froude similitude), based on the facility characteristics, are specified in the following sections.

The selected breakwater has a 2:3 slope (V:H) and a total height (from the seabed to the breakwater crest, see Figure 5.1) of $h + R_c = 20$ m. The core of the structure is impermeable. The wave overtopping rate is measured for a smooth slope and a rock-armoured slope. The armoured rubble slope consists in a 2-layer underlayer made of stones from 0.3 to 1.1 t (with a nominal diameter $D_{\mathrm{n,u}} = 0.5 - 0.75$ m) covered by a 2-layer rock armour made of stones from 1.1 to 2.6 t ($D_{\mathrm{n,a}} = 0.75 - 1$ m). The total thickness of the stone layers (i.e. the permeable layers) is $2D_{\mathrm{n,u}} + 2D_{\mathrm{n,a}} \sim 3$ m. Relative to the smooth slope, these rocky layers lead to increased wave damping by adding roughness, porosity and permeability properties to the slope.

A low crest freeboards range is selected such as $0.4 < R_c^* < 2.0$. The lower bound of this range corresponds to an extremely high MWL typical of stormy conditions combined with a high tide for instance. This selected range permits to compare our results to those of Victor et al. (2012), who made a similar choice of low crest freeboard range in addition to steep slopes in their experiments. Their work led to a modification of (a_{ES}, b_{ES}) in Eq. (5.5) in these conditions. This modification is included in EurOtop (2018).

The waves selected in the present study are irregular and long-crested, described using a significant wave height H_s $(= H_{m_0})$ and a peak period T_p. Given the chosen slope ($\tan\alpha = 2{:}3$) and the typical swell peak period (i.e. $T_p \sim 10$ s), EurOtop (2018) suggests that the corresponding wave

Series	Swell		Wind waves	
	$H_{m_0,\mathrm{s}}$ (cm)	$T_{\mathrm{p,s}}$ (s)	$H_{m_0,\mathrm{ww}}$ (cm)	$T_{\mathrm{p,ww}}$ (s)
A	5.6	1.67	-	-
B	-	-	5.2	1
C	4.8	1.67	4.8	1
D	3.6	1.67	4.4	1
E	3.6	1.67	4.0	0.77
F	3.6	1.67	2.4	0.66
G	3.6	1.67	2.0	0.56
H	3.0	1.67	5.4	1

Table 5.1: Different wave conditions at the wavemaker used during the experiments. Wave heights and periods are given at model scale (1:25).

overtopping rate does not depend on the wave period. Hence, only one swell peak period $T_{p,s} = 8.3$ s is selected in the present study. According to Villefer et al. (2021), the wind wave period can be modified in the presence of following long paddle-waves. Following these recent results, different wind wave peak periods are selected between 2.8 and 5 s. The significant wave heights selected in the present study vary between 0.5 and 1.4 m. One of the objectives here is to investigate the effect of the wind wave period on the wave overtopping process, and resulting mean discharge.

5.2.2 The facility

The series of experiments was carried out in the OSU Institut Pytheas wind wave tank in Marseilles (France). The wave tank is 40 m long and 2.6 m wide. Due to the facility properties, the depth (h in Figures 5.1 and 5.3) could only vary between 0.72 and 0.74 m. Considering the specifications given in section 5.2.1, this latter constraint determined the choice of a 1:25 model scale. The different combinations of swell and wind wave systems tested in the present study are given at model scale in Table 5.1. It is important to specify that the wind feature of the facility was not used in the present experiments: all the wave series introduced in Table 5.1 are run without wind.

The wave series properties in Table 5.1 have been used to calculate a JONSWAP spectrum (Hasselmann et al., 1973) for each wave system. For bimodal sea states, the wind wave and swell respective spectra have been added to obtain a double peaked spectrum. Based on the spectra corresponding to each series and using a random phases distribution, the time series of surface elevation was obtained and converted into a wavemaker signal. The whole procedure from the desired wave spectrum to the corresponding wavemaker signal is given in more details by Villefer et al. (2021). The piston-type wavemaker was able to accurately reproduce the 8 sea states listed in Table 5.1. However, the wavemaker is not equipped with an active wave absorption system. Hence, waves partially reflected by the breakwater model are partially reflected back by the wavemaker.

These reflections can become an issue if the wave energy significantly increases over the duration of a run. Hence, the question was investigated by performing an analysis of the evolution in time of the significant wave height calculated for a series of 300 waves $H_{m_0,300}$ from 0 to 300, 300 to 600 and 600 to 900 number of waves (based on the sea state peak period) relatively to the significant wave height calculated for the whole series of 1000 waves H_{m_0} (detailed results not shown here for brevity). Except for the most reflective case with the highest freeboard ($R_c^* \simeq 1.5$), the smooth

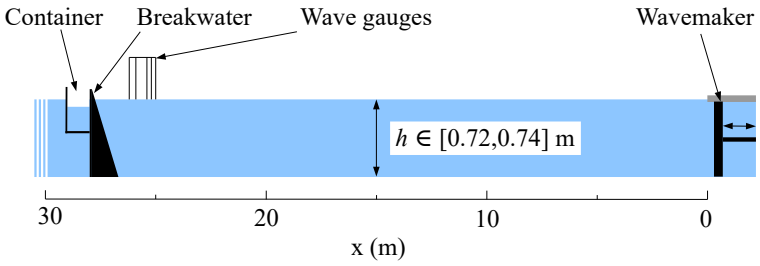

Figure 5.3: Sketch of the wave tank showing the experimental set-up. The vertical exaggeration is $\times 5$.

slope and $T_p = 1$ s, for which $H_{m_0,300}$ is 6 % lower than H_{m_0} for the first 300 waves, all the values of $H_{m_0,300}$ are included within ± 5 % of the H_{m_0} value (and most often within ± 3 % of the H_{m_0} value). Therefore, the sea states tested in the present study can be considered as stationary (i.e. the significant wave height variations during each run are negligible).

5.2.3 The breakwater model

The breakwater model has been installed in the wave tank at a distance of about 27 m from the wavemaker (Figs. 5.3 and 5.4) for practical aspect in order to be visible through the 5-m-long clear glass situated at $x = 25$ m. Figure 5.4 gives an illustration to better picture the breakwater shape and the different slope surfaces. Regarding the armoured rubble slope, it is important to note that the present model is built with an impermeable core covered with two main rock layers: one under-layer and one armoured layer.

Figure 5.4: Photograph of the breakwater with smooth (left) and armoured rubble (right) slopes.

Given the constraint that the water depth could only vary within a 2 cm range in the wave flume, the breakwater crest level was adapted such that $0.4 < R_c^* < 2.0$. Four removable wooden boards with 1.5 cm width were shaped and placed on the breakwater crest (see Fig. 5.5), allowing to test 5 freeboards over the range $[1.5, 9.5]$ cm with 1 mm precision. The resulting difference in the length of the horizontal part of the crest, depending on the freeboard setting (see Fig. 5.5), is assumed

to have no influence on wave overtopping.

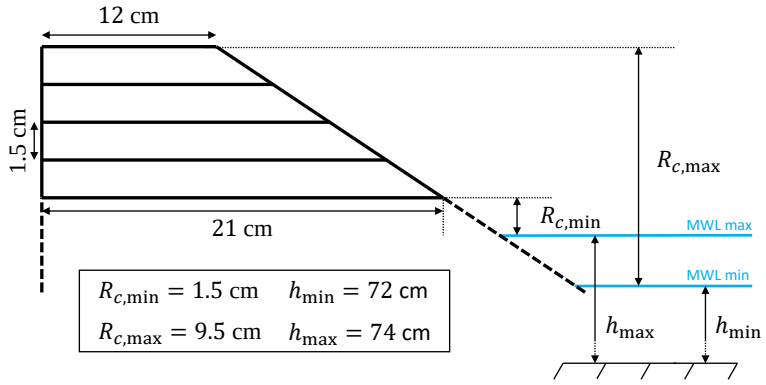

Figure 5.5: Sketch of the profile of the breakwater's crest showing the different freeboards tested at model scale. This figure is not to scale.

The wave conditions, given at model scale in Table 5.1, were identified by their representative wave steepness $s_{m-1,0}$ using $T_{m-1,0}$ defined in introduction. Examples of incident spectra, measured at a distance of 1 m before the breakwater toe (Fig. 5.7), are plotted for the series A to H in Figure 5.6.

5.2.4 Measurements

Before each run, the freeboard crest level and MWL were measured using a vertical ruler. During a run, a sea state selected in Table 5.1 was generated for a 30 min duration so that more than 1000 waves reached the breakwater (i.e. according to the swell peak period which is the largest peak period in the generated wave systems). This consideration is in accordance with EurOtop (2018) recommendations in order to avoid significant variations in extreme statistics.

Part of the wave energy was reflected by the breakwater and by the wavemaker, especially in the presence of the smooth slope. To take into account the induced reflections, wave generation using the wavemaker began 5 min before starting the measurements of the free-surface elevation and the wave overtopping rate, so that incident sea state conditions at the toe of the breakwater could be considered as statistically stationary, as discussed in Section 5.2.2 In order to separate the incident from the reflected waves, a reflection analysis was performed with a linear least-square algorithm for unidirectional waves initially developed by Goda and Suzuki (1976). In the present study, the reflection analysis is systematically performed based on free-surface elevations measured by a grid of 5 wave gauges (Figs. 3.3 and 3.7) following Zelt and Skjelbreia (1992). The distances between the gauges were chosen based on the generated peak wavelength. This set of wave gauges, combined with the reflection analysis, permitted to obtain the incident wave spectrum for each sea state condition, from which H_{m_0} and $T_{m-1,0}$ were then calculated (see Table 5.2).

The overtopping water volume was collected in a container over a 74 cm width located at the center of the breakwater crest (Fig. 5.7). Inside the water container, a pump was connected to a water-meter to obtain the mean overtopping rate q averaged over a 30 min duration at the end of each run (Figs. 5.1,5.3 and 5.7).

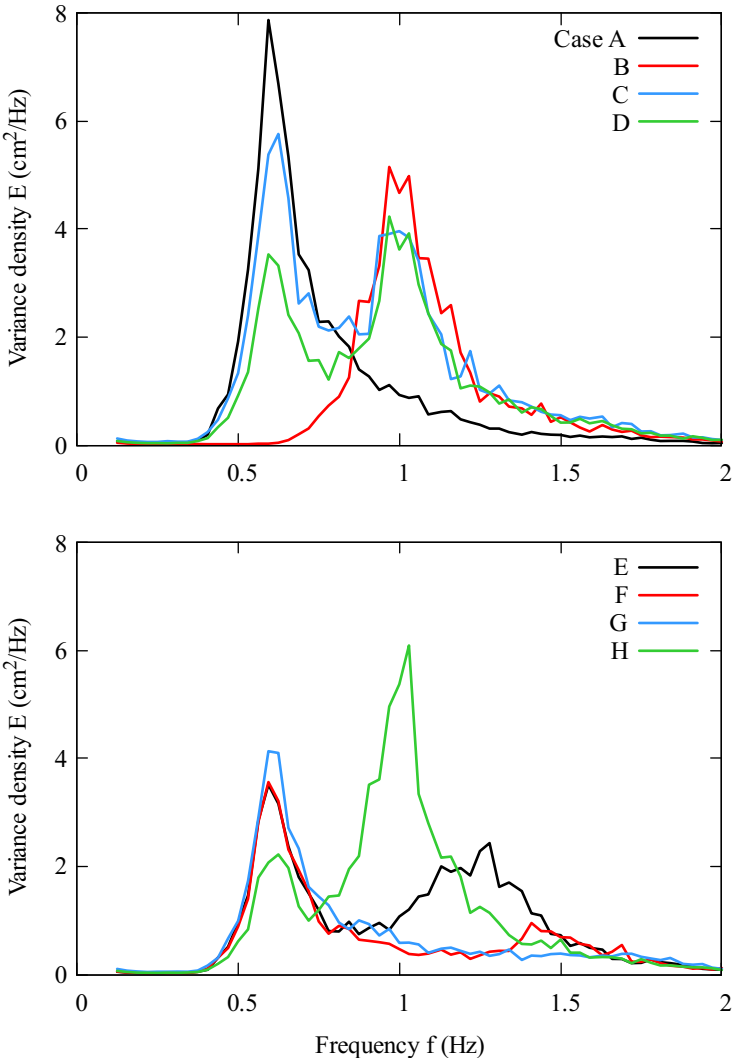

Figure 5.6: Variance density spectra at model scale corresponding to experimental series A to H, whose parameters can be found in Table 5.1.

Table 5.2 shows the ranges of significant wave height and the representative wavelengths obtained with the reflection analysis. For each case, the significant wave heights are clearly higher with the smooth slope due to lower damping on both the breakwater and the wavemaker sides. In addition, the reflection coefficient associated to a given case tended to be higher with higher freeboards (but not systematically).

A single representative wavelength is calculated for each case since it was verified that it did not vary significantly (less than 5% of the values given in Table 5.2) with the different freeboard settings and slope surfaces. Although the dispersion relation in deep water is generally used to obtain a representative wavelength for the design of breakwaters, Table 5.2 also shows wavelengths obtained with the dispersion relation in intermediate and shallow water (ISW) depths. It appears that both wavelength values are sufficiently close, so the deep water dispersion relation approximation can be adopted in the present study to simplify the definition of the representative steepness.

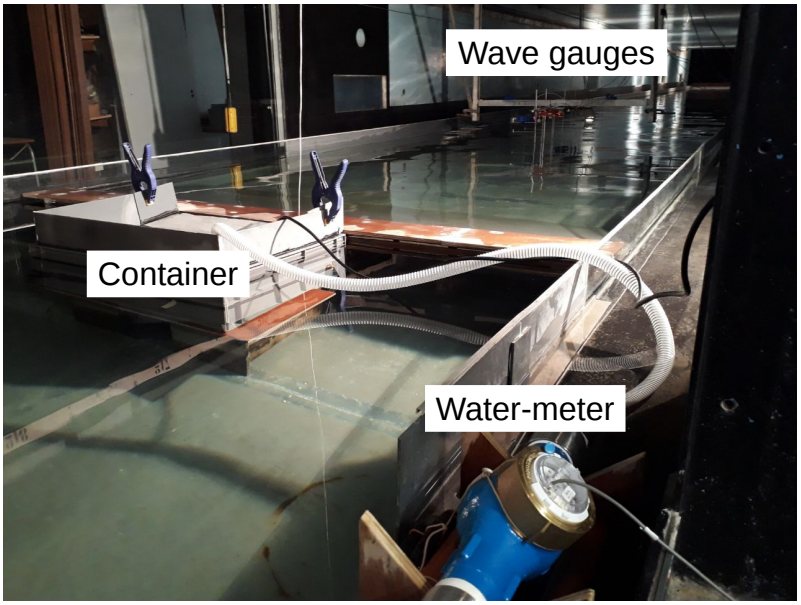

Figure 5.7: Photograph of the measurement set-up (taken from the rear side of the breakwater).

Case	Smooth slope $[H_{m_0,\min}, H_{m_0,\max}]$ (cm)	Rock-armoured slope $[H_{m_0,\min}, H_{m_0,\max}]$ (cm)	$L_{m_{-1,0}}$ (m)	$L^{\text{ISW}}_{m_{-1,0}}$ (m)
A	$[5.89, 6.16]$	$[5.55, 5.77]$	3.3	3.0
B	$[5.39, 5.92]$	$[5.14, 5.31]$	1.4	1.4
C	$[6.82, 7.09]$	$[6.48, 6.68]$	2.4	2.3
D	$[6.15, 6.41]$	$[5.30, 5.91]$	2.1	2.1
E	$[5.60, 5.78]$	$[5.89, 5.47]$	2.0	2.0
F	$[4.67, 4.84]$	$[4.34, 4.56]$	2.5	2.4
G	$[4.53, 4.79]$	$[-, -]$	2.8	2.6
H	$[6.45, 6.51]$	$[5.86, 6.11]$	1.9	1.9

Table 5.2: Ranges of the measured incident sea state characteristics corresponding to each case: H_{m_0} minimum and maximum, $L_{m_{-1,0}}$ and $L^{\text{ISW}}_{m_{-1,0}}$ the wavelengths obtained with the dispersion relation in deep water conditions and in intermediate and shallow water (ISW) depth conditions respectively

According to Frostick et al. (2011), the significant wave heights involved in the present study (between 4 and 7 cm, see Table 5.2) are in the lower range of recommended values to avoid the effect of water surface tension ($H_{m_0} > 5$ cm). Yet, since in most cases, the significant wave heights are either about or greater than 5 cm and the representative wavelengths are always larger than 1.4 m, the results of the present study are assumed to be free from surface tension effects.

5.3 Results

Each point in Figure 5.8 (smooth slope) and 5.9 (armoured rubble slope) results from a 30 min run with a sea state from table 5.1. In these figures, the results are compared with different parameterizations of the empirical formula defined by Eq. (5.5) (given that $\xi > 2$ is always verified

in the present study) with the following sets of parameters:

- EurOtop (2018)
  $(a_{ES}, b_{ES}, c_{ES}) = (0.09, 1.5, 1.3)$
- Victor et al. (2012)
  $(a_{ES}, b_{ES}, c_{ES}) = (0.088, 1.65, 1.3)$
- Orimoloye et al. (2021)
  $(a_{ES}, b_{ES}, c_{ES}) = (0.090, 1.62, 1.3)$ for a sea state dominated by a swell system and $(0.076, 1.91, 1.3)$ for a sea state dominated by a wind wave system

Other set of parameters can be found in EurOtop (2007) and TAW (2002) but they have not been plotted here since EurOtop's (2018) set of parameters is more adapted to our measurements, especially for low freeboards. In the listed set of parameters, $\gamma_{f,E} = 1$ for a smooth slope and $\gamma_{f,E} = 0.4$ with the armoured rubble slope. It is important to note that the wave period is not included in Eq. (5.5). In addition, for the EurOtop (2018) parameterization, a 90% confidence interval is plotted using dotted lines. Hence, the relative wave overtopping rates falling out of this range represent 10% of the observations.

It was found that Owen (1980)'s method was overestimating the wave overtopping rates by a factor going from 3 to 7 in the presence of swell for the smooth slope and by factors higher than 7 with the armoured rubble slope (not shown). Hawkes (1999) already noticed that Owen (1980)'s method, that assumes an indefinitely increasing overtopping rate with increasing wave period, leads to an overestimation of the overtopping rate by a factor up to 5. Consequently, Owen (1980)'s method is not adapted in the present study.

5.3.1 Smooth slope

in Figure 5.8, one can observe a general agreement between our results and the empirical formulas. All the points obtained in the present experiments fall into the EurOtop (2018) confidence interval. Victor et al. (2012)'s parameterization is in slightly better agreement when R_c^* is low. This is not surprising since the latter parameterization has been designed to estimate the wave overopping rates at low freeboard. Orimoloye et al. (2021) observed an increased wave overtopping rate with an increasing swell energy proportion in the sea state. Our results are in agreement with Orimoloye et al. (2021)'s observations for a relative freeboard lower than 1 in Figure 5.8. In particular, Orimoloye et al. (2021)'s parameterizations, in blue and red dashed lines, give a rather accurate estimation of the wave overtopping rate in that range.

However, by taking a closer look, the points corresponding to wind waves (i.e. red triangles in Figure 5.8) tend to describe a slightly different slope than those corresponding to swell. In addition, the slope described by the red points is somehow different from the slope given by the different parameterizations of Eq. (5.5). The points corresponding to bimodal sea states (i.e. series C to H) are inserted between the points corresponding to pure swell (blue circles) and pure wind waves (red triangles).

It is quite interesting to note that the motivation that lead to change the c parameter from 1 to

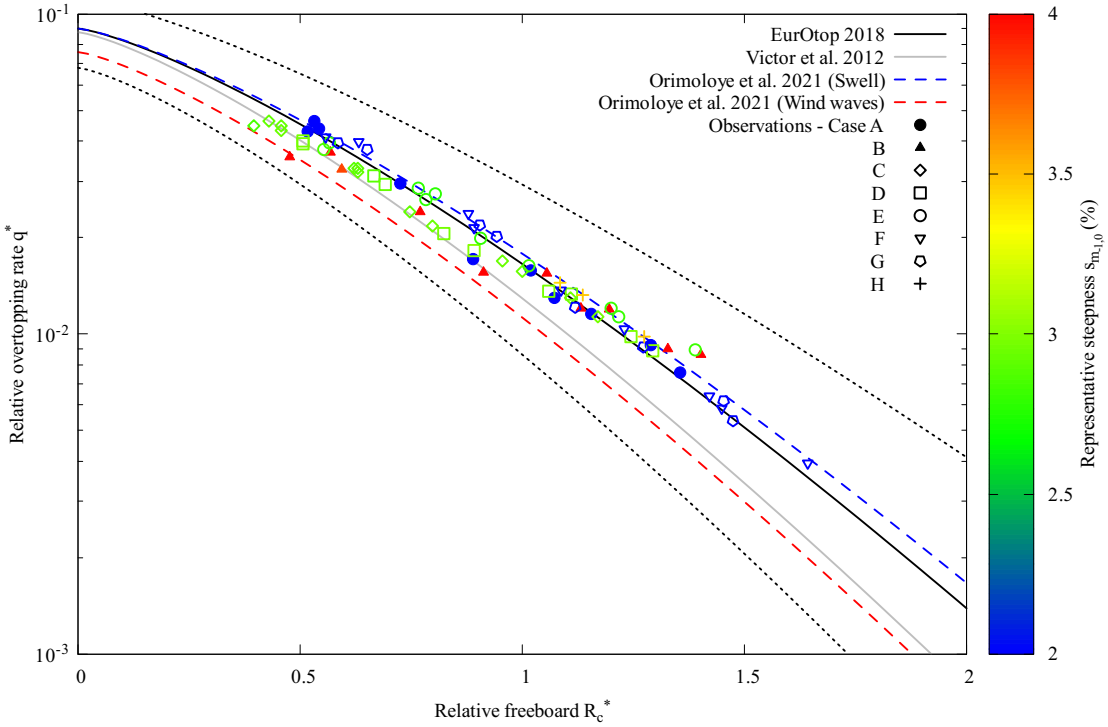

Figure 5.8: Relative wave overtopping rate as a function of the relative freeboard with a smooth slope. The points are the present experimental results colored by the representative wave steepness s_m characterizing each sea state. The lines correspond to different parameterizations of the empirical formula defined by Eq. (5.5).

1.3 between EurOtop (2007) and EurOtop (2018) is not relevant in our series. According to our results in Figure 5.8, each series seems to follow a straight line that would correspond to $c = 1$ in Eq. (5.5). The fact that different sea states, identified by their representative wave steepness, describe different straight lines is even more marked with the armoured rubble slope.

5.3.2 Armoured rubble slope

The results obtained with the armoured rubble breakwater are given in Figure 5.9 similarly to Figure 5.8. The series G, that appears in Figure 5.8, has been removed in the present case due to the negligible wave overtopping rates. Also, it is quite interesting to see that for an equivalent wavemaker signal, series B is steeper in Figure 5.8 (red color) than in Figure 5.9 (orange color). This is due to wave damping in the presence of the armoured rubble slope limiting the wave reflection thus reducing the incident significant wave height. It is important to note that EurOtop (2018) and Orimoloye et al. (2021) parameterizations in Figure 5.9 include a roughness factor $\gamma_f = 0.4$. According to Table 6.2 given in EurOtop (2018), the recommended roughness factor in the present case (i.e. for a rock armour made of 2 armoured layers covering an impermeable core) is 0.55. The value of 0.4 has been determined in order to better fit the present results in Figure 5.9. Hence, our model efficiency regarding wave damping is higher than estimated by EurOtop (2018). Overall, no value of γ_f can give satisfactory estimations of q^* in Figure 5.9: low γ_f values deteriorate the

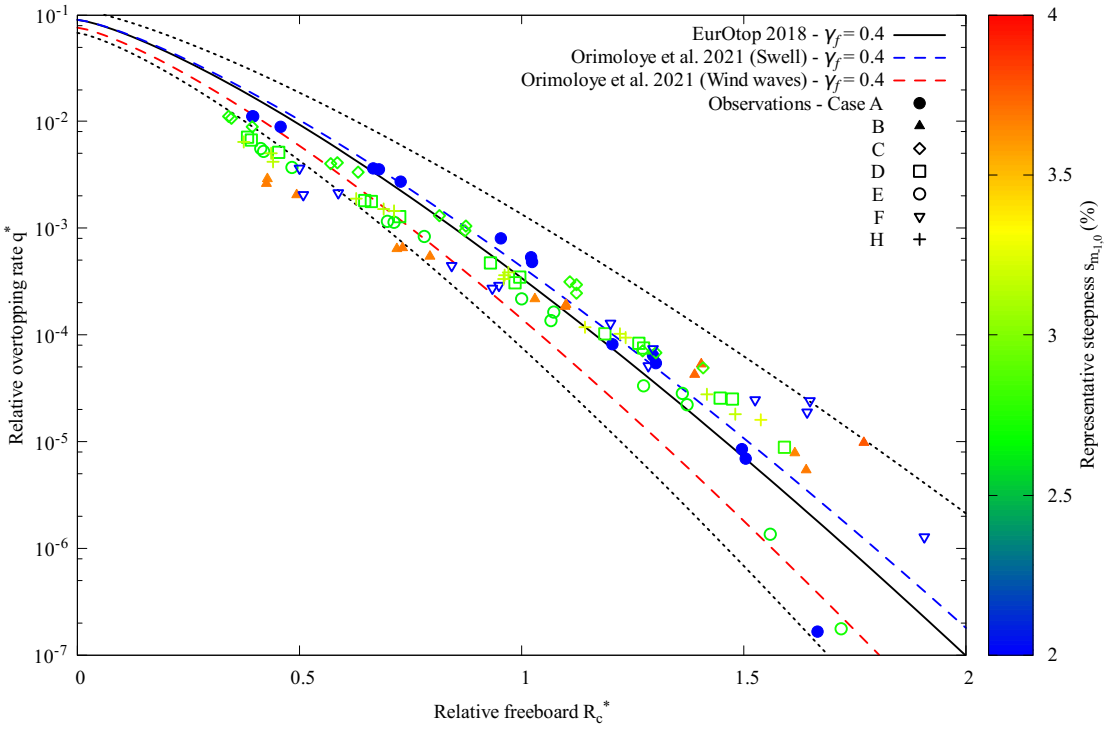

Figure 5.9: Relative wave overtopping rate as a function of the relative crest freeboard with a armoured rubble slope. The points are the present experimental results colored by the representative wave steepness s_m characterizing each sea state. The lines correspond to different parameterizations of the empirical formula defined by Eq. (5.5) with a roughness factor $\gamma_f = 0.4$.

estimations at high relative freeboards and high values deteriorate the estimations at low relative freeboards.

Although the chosen roughness factor is rather low in Figure 5.9 compared to recommendations, when R_c^* is lower than 0.75, a large number of points fall below the lower bound of the 90% confidence interval of EurOtop (2018). In particular, these points are generally associated to sea states characterized by a high representative wave steepness, corresponding to series with a significant wind wave proportion in the sea state energy (i.e. series B, C, D, E and H). These results suggest that with an armoured rubble slope, Eq. (5.5) should include a wave steepness parameter. This latter assumption is further developed in section 5.4. Furthermore, the observations suggest that wind waves are more effectively damped by the armoured layers than the swell. In Figure 5.9, Orimoloye et al. (2021) wind wave parameterization (red dashed line) gives slightly better (i.e. lower) estimations than EurOtop (2018) but still largely overestimates wave overtopping in sea state conditions with a significant wind wave energy proportion.

Series F slightly hampers our general observation with low overtopping rate at low freeboard although it corresponds to a sea state with a low wind wave energy relatively to the swell energy. This latter result suggests that even with a very small wind wave component in a bimodal sea state, the overtopping rate is drastically reduced. However, series F include swell and wind wave with rather small significant wave heights. Therefore, capillarity forces can affect the results. But

series F might show a first limitation for describing the wind waves and swell combination with a representative wave steepness. For lack of any better parameter, the representative wave steepness is still considered as a satisfactory parameter to describe the results obtained in the present study with wave series from Table 5.1.

In Figure 5.9, the linear variations described by each wave series previously observed in Figure 5.8 are amplified. In particular series A (blue circles), corresponding to pure swell conditions, depicts a significantly steeper slope than series B (orange triangles) with pure wind wave conditions. These different slopes observed in Figure 5.9 show a lower overtopping rate with wind waves than with swell for low freeboards ($R_c^* < 1$). At higher freeboards ($R_c^* > 1$), the trend is inverted: wind waves lead to larger overtopping rate than swell. This being said, it is important to note that the vertical error associated with the wave overtopping rate measurements for the points in the range $R_c^* > 1.5$ and $q^* < 10^{-1}$ in Figure 5.9 can go up to a factor 4. This latter remark added to the fact that low freeboard corresponds to extreme sea states give more importance to the study of the low freeboard values and high overtopping rates than high freeboard values and low overtopping rates.

5.3.3 Discussion and summary

Figure 5.10 summarizes the observations made in the previous sections on smooth and armoured rubble slopes by showing the ratio between the measured and predicted wave overtopping rates according to EurOtop (2018). It is clear in Figure 5.10.a that the empirical formula tends to underestimate the overtopping discharge corresponding to a sea state with a high representative wave steepness but this overestimation is not significant. Figure 5.10.b shows the same trend but with a larger vertical distribution due to the presence of the armoured rubble slope with an exception with the wave series F as noticed in the previous paragraph. Consequently, the overestimation of the wave overtopping rate by the empirical formula challenges the EurOtop (2018) parameterization validity. Given the limited number of configurations tested here, it would be impossible to find a correction for the EurOtop (2018) that would be universal by using our data only. For that purpose, gathering more data in as many configurations as possible (e.g. different slope angles, different kinds of slope surface, etc.) would be necessary for operational needs. In the present section, we suggest giving a synthesis of our results so they can be further used to improve EurOtop (2018) parameterization in a more universal approach.

For that purpose, the couple of parameters $(a_{\mathrm{ES}}, b'_{\mathrm{ES}})$, with $b'_{\mathrm{ES}} = b_{\mathrm{ES}}/\gamma_f$, from Eq. (5.5) was fitted by a nonlinear least-square method on the measured values of $log(q^*)$ as a function of R_c^* for each wave series (associated to a representative wave steepness value). The parameters $(a_{\mathrm{ES}}, b_{\mathrm{ES}})$ corresponding to each wave series for both the smooth and armoured rubble slope are plotted as a function of the representative wave steepness in Figure 5.11. Then, a least-square method was applied a second time in order to obtain straight lines fitting the variations of parameters (a_{ES}, b_{ES}) with $s_{m_{-1,0}}$ for each slope surfaces. The $(a_{\mathrm{ES}}, b_{\mathrm{ES}})$ parameters in red color (armoured rubble slopes) have been fitted after removing the red point corresponding to wave series F at bottom left of the clouds of red points.

The equations of the red and black lines fitted in Figure 5.11 are given below and are valid over the range of representative wave steepness at play in the present study, namely for $0.01 < s_{m_{-1,0}} < 0.04$.

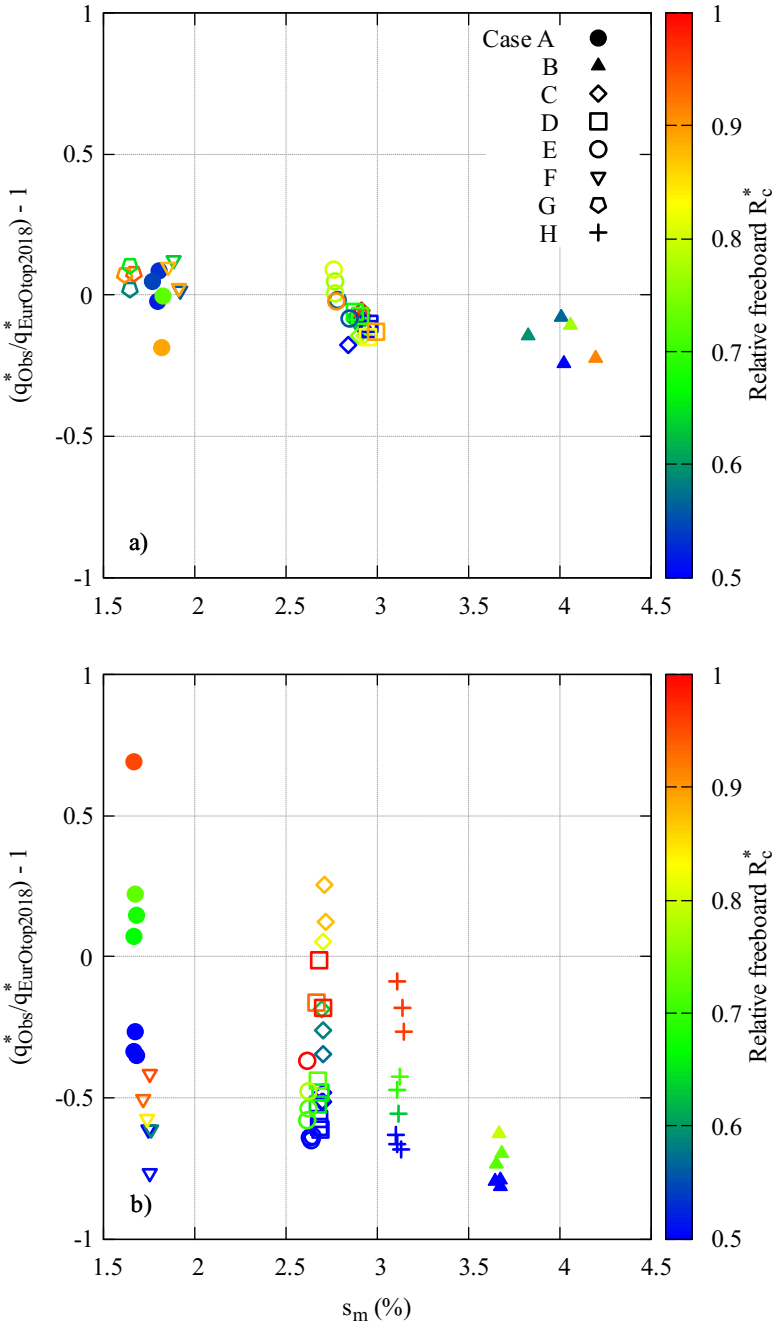

Figure 5.10: Ratio between the measured and predicted wave overtopping rates according to EurOtop (2018) with the smooth slope (a) and the armoured rubble slope (b). Only the points satisfying the condition $R_c^* < 1$ have been plotted.

The parameterizations for the smooth slope curves (black) are:

$$\begin{cases} -1.44 s_{m_{-1,0}} + 0.12 &= a_{\text{ES,smooth}} \\ -11.42 s_{m_{-1,0}} + 1.71 &= b_{\text{ES,smooth}} \end{cases} \tag{5.6}$$

The parameterizations for the armoured rubble (AR) slope curves (red) are:

$$\begin{cases} -2.43 s_{m_{-1,0}} + 0.09 &= a_{\mathrm{ES,AR}} \\ -41.16 s_{m_{-1,0}} + 4.13 &= b_{\mathrm{ES,AR}} \end{cases} \tag{5.7}$$

It should be highlighted that $s_{m_{-1,0}}$ given in Eqs. (5.6) and (5.7) is not in percent (unlike $s_{m_{-1,0}}$ given in the figures). Eqs. (5.6) and (5.7) must be seen as a synthesis of the experimental results obtained in the present study. The corresponding curves are depicted in Figure 5.12 and show a significant improvement over EurOtop (2018) parameterization. Eqs. (5.6) and (5.7) are only valid in the present configuration, namely with a 2:3 slope and the selected type of armoured rubble slope. If one wants to improve EurOtop (2018) parameterizations using a larger dataset, our results can be approximated using (a_{ES}, b_{ES}) values given in Eqs. (5.6) and (5.7) by applying them in Eq. (5.5).

Figure 5.11 confirms the close agreement between our results with a smooth slope and EurOtop (2018) parameterization. in Figure 5.11.a, the differences regarding a_{ES} with the armoured rubble slope (red points) compared to the value given by EurOtop (2018) formula (black dotted line) are highlighted. With an appropriate value for a_{ES} such as the one given by the red line in Figure 5.11.a, Figure 5.11.b shows that $\gamma_f = 0.55$ would be an appropriate roughness coefficient to take into account the armoured rubble slope selected in the present study.

Overall, the straight red lines plotted in Figure 5.11 and parameterized by Eq. (5.7) are rather steep and might not be appropriate out of the scope of the present configuration. Such parameterizations of the couple of parameters (a_{ES}, b_{ES}) slightly improve the wave overtopping rate estimations for the maximum formula (i.e. Eq. (5.5), when $\xi > 2$) in few configurations such as a varying slope angle (Victor et al., 2012) or with different swell energy proportions (Orimoloye et al., 2021). Yet, it was observed in the present study that the wave overtopping rate vertical distribution observed with the armour rubble slope at low freeboards (Fig. 5.9) is linked to the sea state representative wave steepness. However, Eq. (5.5) does not include a sea-sate roughness parameter. In order to improve the wave overtopping estimations in a more robust way, it might be necessary to continue to investigate the non-dimensional numbers at play in the overtopping process in the same vein as the different formulations suggested by Owen (1980), Van der Meer and Janssen (1995) and Hedges and Reis (1998).

5.4 Towards a new scaling

Similar figures such as figures 5.8 and 5.9 have been plotted (but not shown here) with Hedges and Reis (1998) and Owen (1980)'s definitions for q^* and R_c^*, that include a wave steepness parameter. With both definitions, a significant vertical distribution of the wave overtopping rate, even larger than observed in Figure 5.9, was noticed at low freeboards with the armoured rubble slope for the different wave conditions.

This section aims to investigate a new scaling for q^* and R_c^* that would be adapted to our results both with the smooth and the armoured rubble slope. Our starting point, basing on the observa-

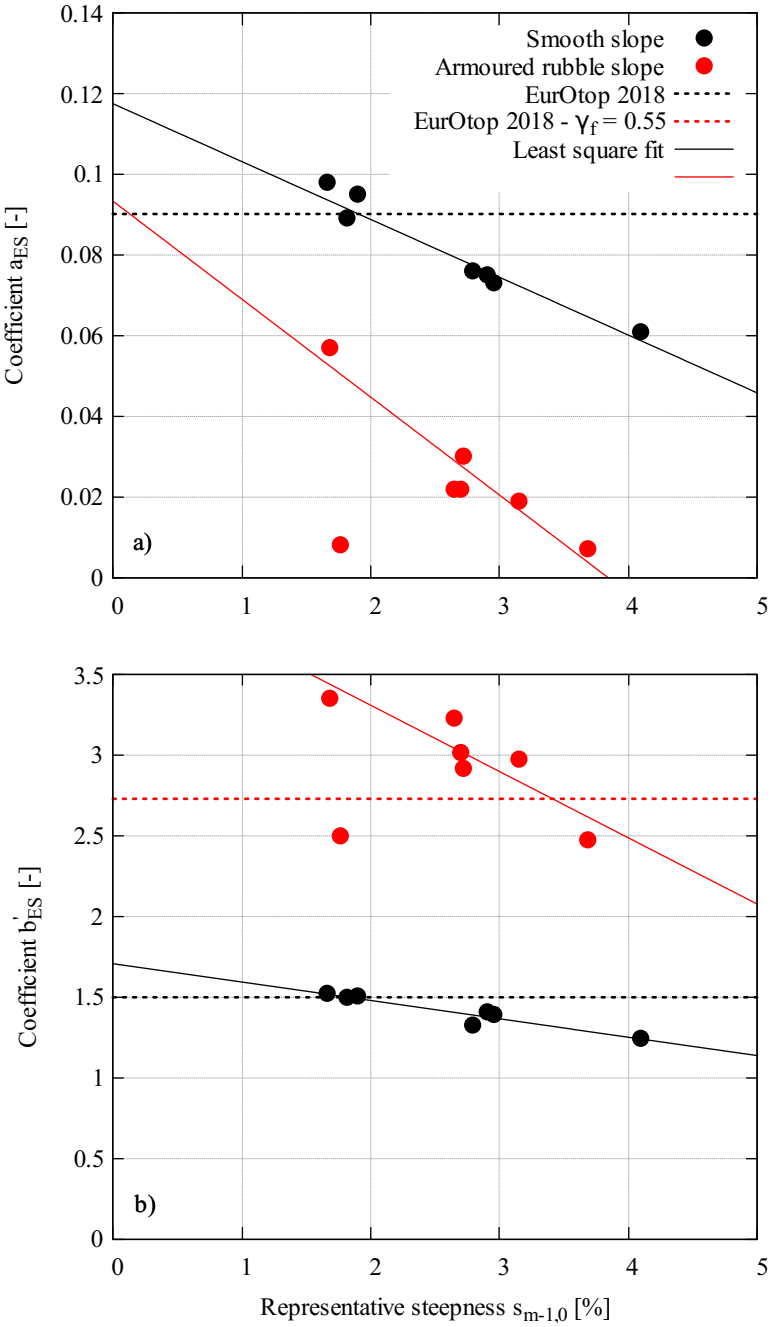

Figure 5.11: Parameters a_{ES} (a) and b'_{ES} (b), with $b'_{ES} = b_{ES}/\gamma_f$, as a function of the representative wave steepness for the smooth (black) and the armoured rubble slope (red). Comparison is made with EurOtop (2018) parameters and a least-square fit is performed on the experimental results. The paremeterizations corresponding to the fitted black and red curves are given in Eqs. (5.6) and (5.7) respectively.

tions of the experimental results, was to assume that the representative wave steepness should be included in the scaling. In a quite straightforward way, R_c^* and q^* have been re-defined as follows:

$$R_c^{*'} = R_c^* s_{m-1,0}^{n_x} \quad ; \quad q^{*'} = q^* s_{m-1,0}^{n_y} \tag{5.8}$$

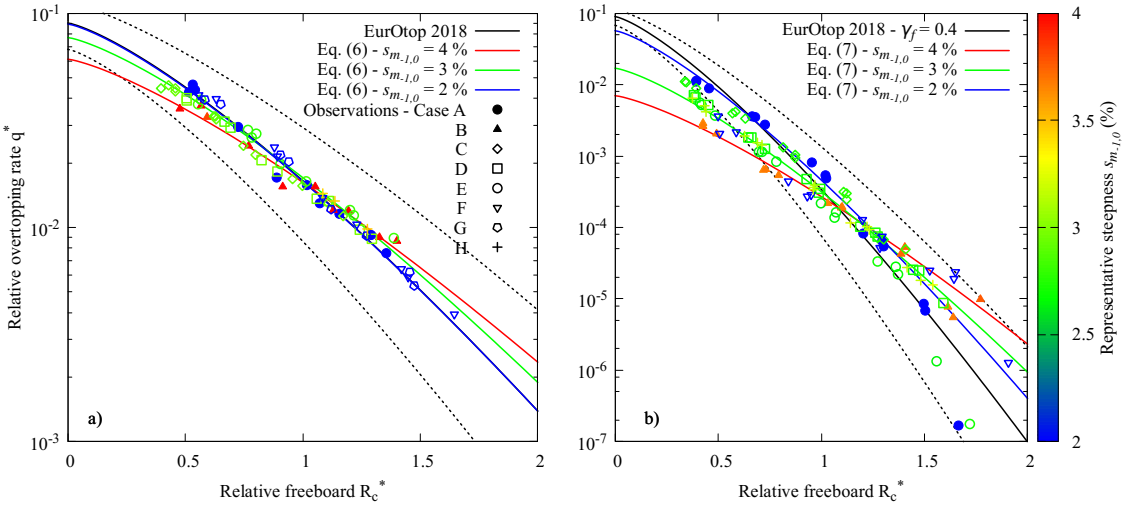

Figure 5.12: Relative wave overtopping rate as a function of the relative freeboard with a smooth slope (a) and an armoured rubble slope (b). The blue, green and red lines show improvements using Eqs. (5.6) and (5.7) with $s_{m_{-1,0}} = 0.02$, 0.03 and 0.04 respectively, by comparison with EurOtop (2018) formula.

with (n_x, n_y) a couple of (real) powers of $s_{m_{-1,0}}$.

Then, (n_x, n_y) is determined in such a way that it reduces the vertical dispersion of the wave overtopping rates at low freeboards. Following this optimisation process, two couples of values were found: (-0.5,1) for the smooth slope and (-0.5,3) for the armoured rubble slope. Using this new scaling, Eq. (5.5) becomes:

$$q^{*'} = a_{NS} \exp\left(-b_{NS} R_c^{*'}\right) \tag{5.9}$$

Given that the overtopping rate variations corresponding to each series can be associated to straight lines (see figures 5.13 and 5.14), the parameter c in Eq. (5.5) was set equal to 1. The wave overtopping rate as a function of the relative freeboard is plotted according to the new scaling. In addition, the couple (a_{NS}, b_{NS}) in Eq. (5.9) is fitted on the results for both smooth and armoured rubble slopes.

With a smooth slope, unlike Figure 5.8, the straight line described by the results from each wave series are collinear in Figure 5.13. This alignment does not alter the very narrow vertical distribution already observed in Figure 5.8. This is highlighted in Figure 5.13 by a very narrow 90% confidence interval in dotted lines.

Again in Figure 5.14, with the armoured rubble slope, the points corresponding to each wave series describe collinear and straight lines no matter the sea state representative wave steepness. This latter observation is an important improvement by comparison with Figure 5.9. Another improvement is the narrow vertical distribution at low freeboards illustrated in Figure 5.14. The narrow confidence interval (in dotted line) at low freeboards confirms this observation. At higher freeboards, the confidence interval tends to widen in a more significant way than in Figure 5.13. This is not surprising given the fact that, with the armoured rubble slope, the points at high

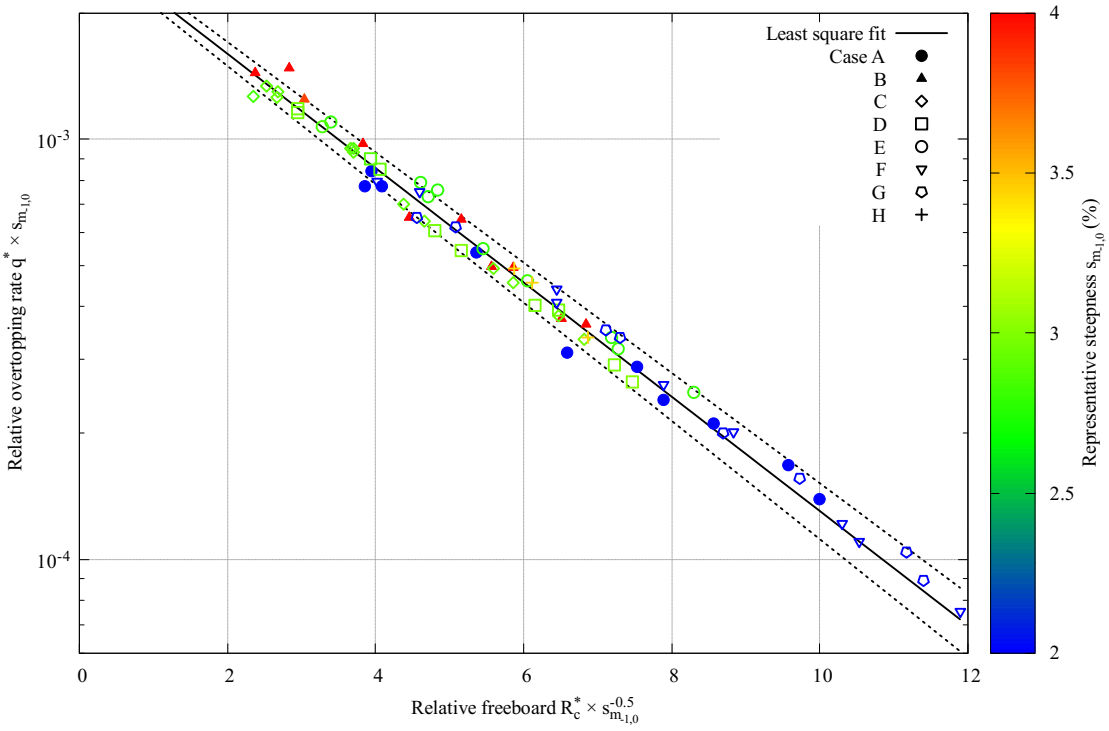

Figure 5.13: New scaling of the relative wave overtopping rate as a function of the relative freeboard with a smooth slope. The points are the experimental results colored by the representative wave steepness $s_{m_{-1,0}}$ characterizing each sea state. The black solid line corresponds to a least-square fit of Eq. (5.9) with the 90% confidence interval in dotted lines.

freeboards match with very low overtopping rates inducing a scatter in the vertical distribution.

Figures 5.15 (using linear scale) and 5.16 (using log scale) illustrate the improvement brought by the new definitions of the relative wave overtopping rate and freeboards to scale our results with a comparison between the scaling based on Eq. (5.5) (first column) and the scaling according to Eq. (5.9) suggested in the present study (second column). For that purpose, the parameters (a_{ES}, b'_{ES}) and (a_{NS}, b_{NS}) (using Eqs. (5.5) and (5.9) respectively) are fitted using a least-square method on the present experimental results.

The parameters used in Figures 5.15 and 5.16 are the following:

- Smooth slope (Figs. 5.15.a and 5.16.a)
  $(a_{ES}, b'_{ES}) = (0.0774, 1.38)$
- Smooth slope (Figs. 5.15.b and 5.16.b)
  $(a_{NS}, b_{NS}) = (0.00287, 0.305)$
- Armoured rubble slope (Figs. 5.15.c and 5.16.c)
  $(a_{ES}, b'_{ES}) = (0.0225, 3.04)$
- Armoured rubble slope (Figs. 5.15.d and 5.16.d)
  $(a_{NS}, b_{NS}) = (1.08e-06, 0.865)$

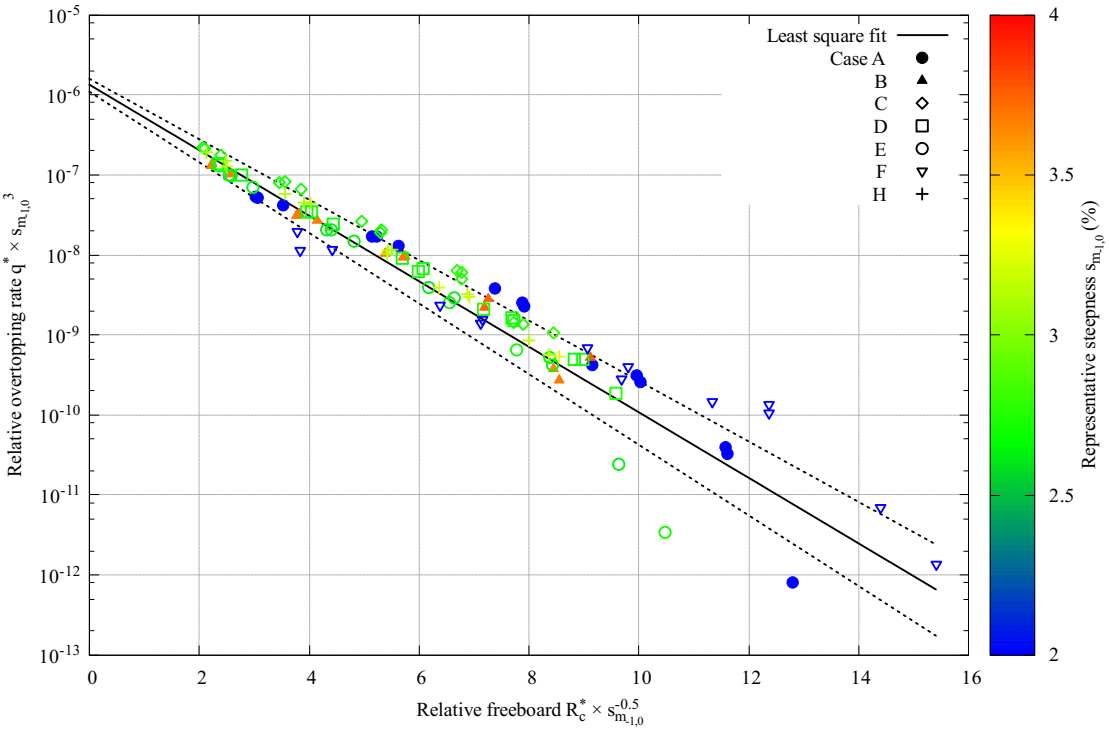

Figure 5.14: New scaling of the relative wave overtopping rate as a function of the relative freeboard with a rock-armoured slope. The points are the experimental results colored by the representative wave steepness $s_{m_{-1,0}}$ characterizing each sea state. The solid black line corresponds to a least-square fit of Eq. (5.9) with the 90% confidence interval in dotted lines.

Different skill scores to quantify the general agreement between the estimated and the measured overtopping discharges according to the different scalings are displayed in Figure 5.15: the bias, the Root Mean Square Error (RMSE) and the Scatter Index (SI, also named "normalized RMSE"), defined as:

$$\text{Bias} = \frac{1}{n}\sum(q_{estimated} - q_{measured}) \tag{5.10}$$

$$\text{RMSE} = \sqrt{\frac{1}{n}\sum(q_{estimated} - q_{measured})^2} \tag{5.11}$$

$$\text{SI} = \sqrt{\frac{\sum(q_{estimated} - q_{measured})^2}{\sum q_{measured}^2}} \tag{5.12}$$

where n is the number of points (i.e. q measurements) in each sub-figure of Figure 5.15. The bias expresses the model tendency to over or underestimate the measurements, while the RMSE indicates the data dispersion (both having the unit of q). The SI gives a normalized quantification of the error; among the three indicators, it is the only one permitting to compare Eqs (5.5) and (5.9) performances between the smooth and the armoured rubble slope (upper and lower rows in Figure 5.15).

Looking at the upper row corresponding to the smooth slope results (Fig. 5.15-5.16.a and b),

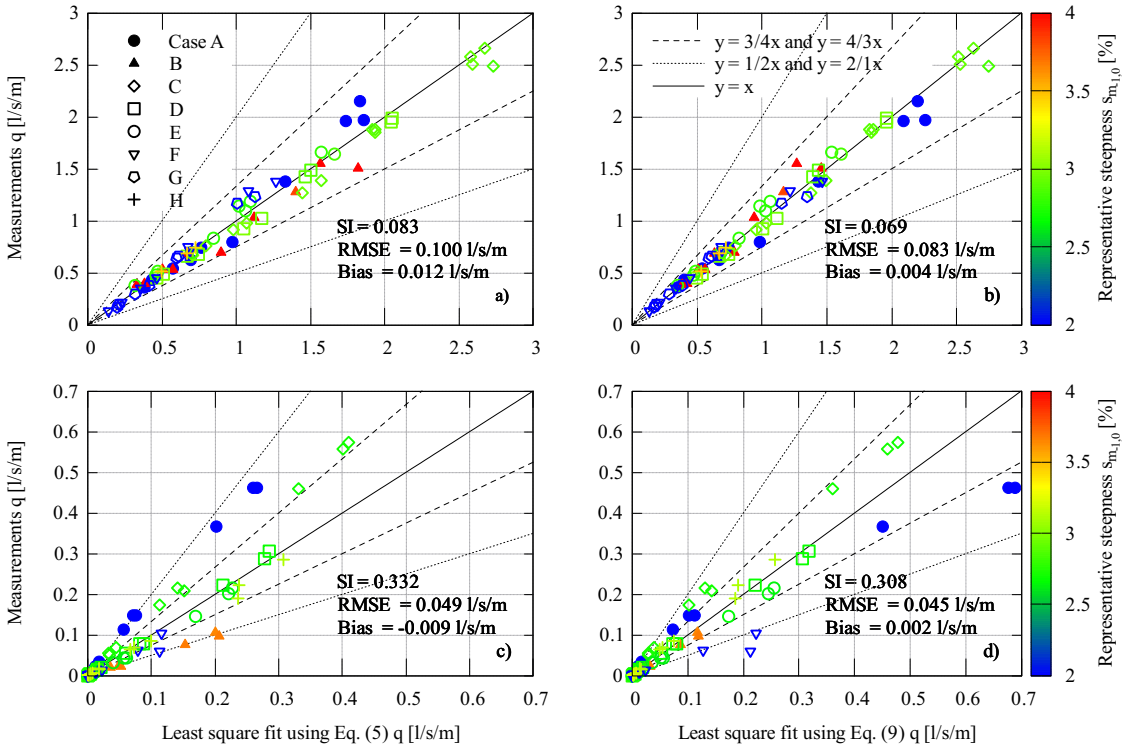

Figure 5.15: Wave overtopping data at model scale for smooth (upper row) and armoured rubble slope (lower row), showing the level of agreement between the measurements and the estimations according a least-square fit using Eq. (5.5) (left column) and a least-square fit using Eq. (5.9) suggested in the present study (right column).

Eqs. (5.5) and (5.9) give a correct estimated value with all of the points falling between $y = 3/4x$ and $y = 4/3x$ lines both at high and low overtopping rates (Fig. 5.16). The level of agreement seems slightly better with Eq. (5.9) scaling with a narrower point distribution around $x = y$ line. This graphical observation is confirmed by the value of the different indicators which are lower in Figure 5.15.b than in Figure 5.15.a.

With the rock-armoured slope, the lower row of Figure 5.16 shows that the differences between both scaling are more marked at large overtopping rates. In addition, the difference between the level of agreement of both scaling methods is more significant with the armoured rubble slope (Fig. 5.15.c and d). in Figure 5.15.c, the overtopping corresponding to a pure swell (blue points) and pure wind waves (orange points) are respectively underestimated and overestimated (resp. following $y = 2/1x$ and $y = 1/2x$ lines). in Figure 5.15.d, the separation between pure swell and pure wind waves is less marked, with most points falling within or near the interval between $y = 4/3x$ and $y = 3/4x$ lines. Again, wave series F is making an exception as it was previously noticed. Overall, the lower values of all 3 skill scores in the right column in Figure 5.15 prove that the scaling suggested in the present study performs better than the one given in Eq. (5.5). For instance, the bias is divided by 3 and the SI reduced from 8.3% to 6.9% for the smooth slope, while the bias is divided by more than 4 and the SI reduced from 33.2% to 30.8% for the rock-armoured slope. The comparison of the SI between the upper and lower rows (resp. Fig. 5.15.a,b and Fig. 5.15.c,d) indicates that the estimations are much more accurate when considering a smooth slope.

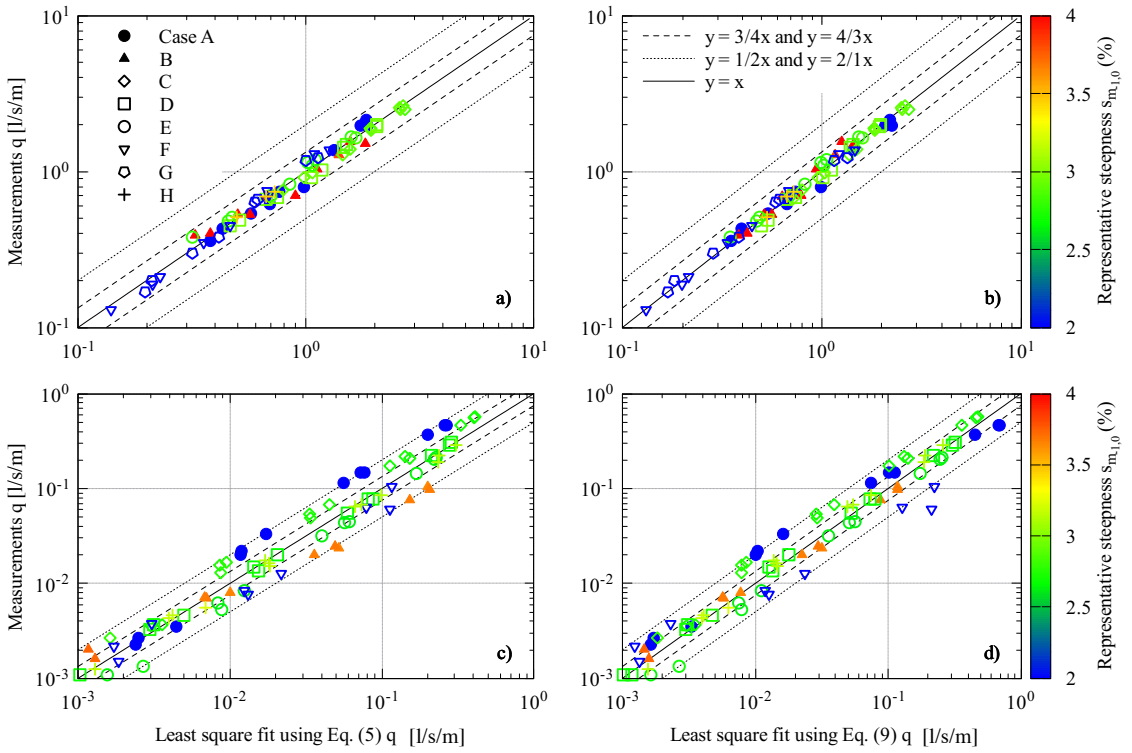

Figure 5.16: Same as Figure 5.15 but using logarithmic axes.

When observing Figure 5.15, the scaling from Eq. (5.9) is more adapted to our results both with the smooth and armoured rubble slope than Eq. (5.5) scaling. However, this new scaling (i.e. Eq. (5.9)) has been designed to fit our single set of results whereas Eq. (5.5) has proven to be representative of a large number of configurations through the years. In addition, to obtain a narrow distribution of our results in Figures 5.13 and 5.14, the couple (n_x, n_y) had to be different between both slope surfaces. Yet, one could think of introducing a new roughness factor γ_f that, instead of dividing R_c^*, would divide n_y in the presence of a rough slope surface. In the present study, we could define $\gamma_f = 0.33$ in order to have a relation between the different n_y used for the different slope surfaces. The physical basis behind this latter use of γ_f can be explained with the fact that it was found that the armoured rubble slope damps more efficiently the waves with a short wavelength (i.e. short wave periods). Eventually, the ratio between the rocks or layers characteristic length (at the slope surface) and the representative wavelength of the sea state might be added in the dimensional analysis performed in Eq. (5.1) since it might have an importance to explain the wave overtopping processes in the presence of an armoured rubble slope. For that purpose, it would be necessary to carry out an experimental study using rocks with different diameters and values of underlayer and armour permeability.

5.5 Discussion

EurOtop (2018) overtopping formula for non-breaking waves (Eq. (5.5)) appears appropriate for estimating wave overtopping rates in the presence of a smooth slope but shows major limitations for rock-armoured breakwater in sea state conditions with a large proportion of wind waves (i.e. a high representative wave steepness). Yet, this formula, that does not take into account the wave period, showed the best agreement with our results among the different empirical formulas proposed in the scientific literature. Hence, in coastal areas where wind waves are predominant, the crest level of a rock-armoured breakwater with a steep slope designed according to the EurOtop 2018 recommendations might be oversized considering the present results.

To overcome the observed limitations, a generic method to improve the EurOtop formula consists in adapting the design parameters a_{ES} and b_{ES} to our results. This method was used in Victor et al. (2012) and Orimoloye et al. (2021). They expressed the parameters as a function of the breakwater slope and the swell proportion respectively. In the present study, Eqs. (5.6) and (5.7) show the expression of a_{ES} and b_{ES} parameters, as a function of the representative wave steepness, based on our results. According to our observations and the above references, a_{ES} and b_{ES} should be at least function of (i) the breakwater slope (Victor et al., 2012), (ii) the slope surface properties (e.g. roughness, porosity and permeability) and (iii) the bimodality of the sea state (e.g. with the representative steepness). It makes the definition of the parameters rather complex, therefore hard to adapt for an operational use. In addition, this approach is empirical to a large extent. Yet, Eqs. (5.6) and (5.7) could be directly applied at prototype scale with a dike having a similar configuration as our model.

The second method suggested in this study is based on dimensional analysis. Our purpose was to find a stronger physical basis for the definition of the relative wave overtopping rate and the relative freeboard. With the scaling suggested in Eq. (5.8) and within the present study, the parameters a_{NS} and b_{NS} only depend on the slope surface properties (e.g. roughness, porosity and permeability). With a validation process on different breakwater slopes, it can be foreseen that a_{NS} and b_{NS} should also depend on the slope. The main improvement with this second method is that it shows good performances to fit our results (Figs. 5.13 and 5.14) without adapting a_{NS} and b_{NS} to the bimodal sea states properties. Unlike Figures 5.8 and 5.9 based on EurOtop scaling, Figures 5.13 and 5.14 show a significant reduction of the vertical distribution of the relative measured wave overtopping rate at low relative freeboards. Considering that low relative freeboards correspond to extreme events, it is essential for the efficiency of the breakwater design to accurately estimate wave overtopping rates within this range. This narrowing of the vertical distribution of experimental points with the new scaling is confirmed by looking at Figures 5.15 and 5.16, and associated skill scores in Figure 5.15.

5.6 Conclusion

A series of experiments was conducted in the OSU Institut Pythéas wave tank in Marseilles (France) with the objective to assess and to improve the accuracy of the wave overtopping prediction formulas in bimodal sea states conditions according to different references in the literature. For

that purpose, a breakwater at a 1/25 model scale and with a 2:3 slope was set in the wave tank to measure the wave overtopping rate for different freeboard heights with sea states combining different proportions of swell and wind waves. In particular, the measurements were carried out for two types of slope surface roughness: a smooth and a rock-armoured one. The measured overtopping rates have been plotted by comparison with predictions from state-of-the-art formulas.

The experimental results with the smooth slope are quite well estimated by the different parameterizations based on Eq. (5.5). However, the results distribution suggests a dependence on the sea state representative wave steepness, which is not taken into account in Eq. (5.5). This dependence is confirmed by the results with the armoured rubble slope. In that latter case, the different parameterizations based on Eq. (5.5) are largely overestimating the wave overtopping rate corresponding to conditions with a significant wind wave proportion in the total sea state energy. In the present series of experiments, such wave conditions were associated to medium and high representative wave steepness values. Therefore, the results suggest that the presence of a rock-armoured layer at the slope surface damps more efficiently waves with a short wavelength, such as wind waves, than a long swell. In order to improve the existing formula for estimating the wave overtopping in the present configuration (i.e. bimodal sea state conditions with a rock-armoured slope), two options were suggested.

The first option would be to find an adapted parameterization for the couple of parameters (a_{ES}, b_{ES}) to be used within Eq. (5.5) in the same vein as Victor et al. (2012) and Orimoloye et al. (2021) did with respectively varying slope angle and varying swell proportion in the sea state. This option would require to gather a large number of data in order to find a parameterization for (a_{ES}, b_{ES}) that would be robust in a large number of configurations. With that objective, a first parameterization of (a_{ES}, b_{ES}) as a function of $s_{m_{-1,0}}$ has been proposed with Eqs. (5.6) and (5.7). This latter parameterization should be seen as a summary of our results for a future use in a study with a larger scope that would unify the different existing parameterizations of (a_{ES}, b_{ES}).

The second option would consist in finding a new scaling for predicting the wave overtopping rate. This option is based on the observation that, although the representative wave steepness seems to play a significant role in the wave overtopping process (especially with a rock-armoured slope), it is not taken into account in Eq. (5.5). In Eq. (5.8), a new scaling has been proposed by including the representative wave steepness parameter in the non-dimensional wave overtopping rate and freeboard definitions given in Eq. (5.5). Using the same exponential formulation as Eq. (5.5) with the latter definitions, the parameters (a_{NS}, b_{NS}) in Eq. (5.9) were fitted using a least-square method. A comparison between Eqs. (5.9) and (5.5) was performed. The new scaling shows slightly better performances than the previous one on which EurOtop (2018) is based. In particular, in the presence of a rock-armoured slope, the wave overtopping rates due to pure wind waves and pure swell are better estimated using Eq. (5.9).

Although the second option might seem a bit naive, the results shown in Figures 5.8 and 5.9 prove Eq. (5.5) limitations for estimating the wave overtopping in bimodal sea states conditions with a large freeboard range. A parameter characterizing the bimodal sea state should be included in the calculation of the wave overtopping rate in those conditions. Our choice was the use of a representative wave steepness that proved to be rather adapted in the present experiments.

Further studies must be performed in order to validate the use of the steepness parameter to take into account the bimodal sea state properties in the wave overtopping rate calculation. As it was shown previously, either a new parameterization of the formula currently used in EurOtop (2018) or a new scaling for the relative wave overtopping rate and freeboard should be further investigated with a larger dataset. Finally, the armoured rubble slope seemed to have different damping properties between the different wave series. A study comparing the wave damping with different wave periods could be performed with various slope surfaces (e.g. with different roughness and porosity properties) in order to clarify the relation between the rock properties and the overtopping rate corresponding to different incident wavelengths for instance or wave steepness values.

Acknowledgments

Antoine Villefer acknowledges the financial support of his PhD research program provided by the French ANRT (Association Nationale de la Recherche et de la Technologie) with CIFRE grant number 2019-1257. The authors thank Dr. Hubert Branger (IRPHE, UMR 7342) for his invaluable help to conceive and build the model and Dr. Jeffrey Harris (ENPC/LHSV) for many fruitful discussions in the course of this study. Thanks are due to Pr. Dominic Reeve (Faculty of Science & Engineering, Swansea University) for providing additional explanations in response to our queries about the work presented in Orimoloye et al. (2021).

Chapter 6

Numerical modelling of wave overtopping in bimodal sea-state conditions with neptune_cfd

Le code neptune_cfd, résolvant les équations de Navier-Stokes (NS) pour les écoulements multiphasiques, est utilisé pour simuler numériquement les expériences réalisées avec le modèle réduit de digue, décrites dans le Chapitre 5. L'originalité de neptune_cfd réside dans la résolution d'un système d'équations de NS pour chaque fluide, soit ici l'eau et l'air, modélisés par une approche eulérienne. De plus, la structure de la digue est intégrée au domaine numérique à l'aide d'une méthode de porosité variable permettant de s'affranchir des contraintes de maillages. Une première étude de convergence a mis en évidence les enjeux de l'utilisation d'un tel code afin de trouver un équilibre entre coût de calcul et précision des résultats. Malgré une sous-estimation de l'énergie des vagues par le code, la forme générale des spectres bimodaux obtenus est proche de celle observée en laboratoire, au moins pour des fréquences inférieures à 1,5 Hz environ. Par ailleurs, nous avons constaté que les débits adimensionnels de franchissements par les vagues résultant des simulations présentent des ordres de grandeur cohérents avec les observations, mais sont systématiquement sous-estimés d'un facteur 1.5 environ. Cependant, la distribution des débits de franchissements relatifs aux différents cas d'essai (A à G) est très proche de la distribution des observations. Cela a permis de retrouver qualitativement les tendances observées en laboratoire, et notamment que, à faible hauteur de franc bord adimensionnelle, la houle occasionne des franchissements plus importants que le clapot.

Abstract

The neptune_cfd code, solving the Navier-Stokes (NS) equations for multiphase flows, is used to numerically simulate the experiments carried out with the breakwater model (smooth slope only), as described in Chapter 5. The originality of neptune_cfd lies in the resolution of a system of NS equations for each fluid, i.e. here water and air, modeled by an Eulerian approach. The structure of the breakwater is integrated into the numerical domain using a Time and Space Dependent Porosity (TSDP) method to overcome the mesh constraints. A first convergence study highlighted the challenges of using such a code in order to find a balance between computational cost and accuracy of results. Despite an underestimation of the wave energy by the code, the general shape of the bimodal spectra obtained is close to that observed in the laboratory, at least for frequencies lower than about 1.5 Hz. Furthermore, we found that the relative wave overtopping rates resulting from the simulations have orders of magnitude consistent with the observations, but are systematically underestimated by a factor of about 1.5. However, the distribution of wave overtopping rates for the different test cases (A to G) is very close to the distribution of the observations. The trends observed with the physical model are qualitatively recovered: at low freeboard, swell causes larger wave overtopping rates than wind-waves.

6.1 Introduction

In the context of the climate crisis, the occurrence and the intensity of storms, associated to strong winds, are assumed to increase in the short term (IPCC AR6 report, Chapter 11, 2022). Hence, the protection of coastal facilities must be constantly updated considering the state of the art in terms of methodologies and extreme events statistics. Coastal protections are generally designed based on the estimation of the wave overtopping discharge. To guarantee the safety of a coastal facilities, the wave overtopping rate q must remain under an acceptable limit considering the most severe sea-state conditions at a specific coastal location.

The wave overtopping processes have mainly been investigated using physical models in a large number of configurations and sea-state conditions. By gathering the results of numerous physical experiments, empirical formulas have been developed to estimate the wave overtopping rate as a function of the breakwater dimensions and the sea-state conditions (e.g. Pullen et al., 2007; TAW, 2002; Van der Meer et al., 2018). This methodology is highly parameterized in order to take into account a large number of configurations. However, shortcomings of the formulas are regularly highlighted, such as in Chapter 5. The series of physical experiments performed in Chapter 5 revealed a limitation of the existing formulas regarding the estimation of wave overtopping rates in bimodal sea-state conditions. Two methods were suggested to improve the current methodology but they need a further validation, for instance by carrying out additional series of physical experiments. However, such physical experiments include several limitations due to many factors. The most obvious factor is the scaling effects: for instance, the wind influence on the wave overtopping process cannot be properly investigated at model scale due to the impossibility to satisfy both Froude and Reynolds similitudes. Other factors relative to the intrinsic experimental conditions such as the unwanted wave reflection or frictions on the sides of a tank limits the accuracy of the

model.

Studying wave overtopping process with numerical models as a complementary tool to physical experiments was motivated by the possibility to emancipate from the above listed constraints intrinsic to physical models. However, among the different numerical models families commonly used to predict wave overtopping, the choice of a particular model must be done depending on the expected level of accuracy and available computing resources and time.

The numerical models used within this scope are separated into 3 main families with different approximation, sets of governing equations and solving techniques. These models can be sorted from the less to the most computationally expensive as follows:

1. Phase-averaged and depth-averaged spectral wave models such as SWAN (Booij et al., 1999) or Xbeach-surfbeat (Roelvink and Costas, 2019),
2. Phase-resolving and depth-averaged models separated in 3 sub-families:
   - Nonlinear shallow water (NSW) equations (non-dispersive Saint-Venant equations) such as AMAZON (Hu et al., 2000),
   - NSW equations with an added non-hydrostatic pressure correction term such as SWASH (Suzuki et al., 2017) and XBeach-NH (Smit et al., 2010),
   - Boussinesq or Serre-Green-Naghdi type equations (partially dispersive and weakly to fully nonlinear) such as BOSZ (Roeber and Cheung, 2012) and FUNWAVE (Kirby et al., 1998).
3. Phase-resolving and depth-resolving models solving Navier-Stokes (NS) equations either with a mesh-based Eulerian approach such as OpenFOAM (Jasak et al., 2007) or a meshless Lagrangian approach such as DualSPHysics (Altomare et al., 2021).

Lashley et al. (2020) performed a benchmark study on wave overtopping at dikes with shallow mildly sloping foreshores with the purpose to compare 6 models representing each above-listed family. They showed that the accuracy of the wave overtopping estimations is not systematically improved with complex models requiring a long computational time (i.e. NS-based models). In particular, OpenFOAM (the NS-based model selected in their study) showed limitations regarding wave propagation. According to them the differences in terms of computational time between phase-averaged/depth-averaged models and NS-based models can reach a factor of 10^4.

Hence, depth-averaged models are computationally efficient numerical models permitting the study of a large range of configurations and providing accurate statistics by simulating series of 1000 waves (e.g. recommendation from Van der Meer et al. (2018)) in a rather short computational time. However, the study of complex breakwater geometries or multiphysical problems (e.g. involving water and air flows) can only be parameterized in these models.

The depth-resolving models, by solving NS equations, are expected to overcome the latter limitations. A large number of studies using such models showed interesting performances in reproducing complex breakwater geometries such as the presence of roughness elements on a breakwater slope (Chen et al., 2021), wave overtopping over a fixed cylinder (Esteban et al., 2022) and wave overtopping over a multi level breakwater (Han et al., 2018). Other processes including turbulence

effects (e.g. wave breaking, vortices) or the influence of air-entrainment in the estimation of wave loads have been modelled (Bozorgnia et al., 2014; Gruwez et al., 2020; Musa et al., 2017). In the above-listed references, several codes are used, such as OpenFOAM, Star-CCM+, ANSYS-Fluent and FLOW3D.

Yet, NS models require a much longer computational time than models from the first two families to simulate an equivalent physical duration. Hence, the computational time is commonly reduced by simulating less than 1000 waves, thus degrading the statistical representativity. In addition to the higher computational cost, NS models often require the design of complex meshes that can be rather time consuming. Since one set of NS equations governs the motion of a single fluid, it is necessary to adopt a method to define two fluids, namely air and water, characterized by their densities and viscosities. The most common approach is the Volume Of Fluid (VOF) method. The different model families regularly need to be compared to data obtained with physical models to verify their performances. After this validation process, the numerical models can be used to simulate wave overtopping at prototype scale.

In the present study, we chose to use neptune_cfd, a multi-phase code based on NS equations. neptune_cfd falls in the third family itemized above. Two sets of mass and momentum balance equations, following Eulerian specifications, are solved to account for both fluids. Although air and water have their own velocity fields (whole domain), the code relies on a method based on a single pressure field for both fluids. neptune_cfd permits one to simulate physical processes, such as the propagation of irregular waves and the depth-induced wave breaking, necessary for the study of wave overtopping. In particular, the code includes an Immersed Boundary Method with discrete forcing - the time-and-space-dependant porosity (TSDP) method (Benguigui et al., 2018) - to define complex breakwaters shapes without meshing constraints. The TSDP method was used to define the numerical breakwater model. The numerical simulations performed in this chapter aim at testing the capacity of the numerical model to simulate the series of experiments described in Chapter 5. Considering the results presented in Chapter 5, the influence of the wave period on wave overtopping will be investigated with the numerical model.

Section 6.2 introduces the software neptune_cfd with the specific features to account for free-surface flow modelling and permitting the breakwater design with the TSDP method. The selected method to handle wave generation together with the absorption of the waves reflected by the breakwater is presented in Section 6.4. A description of the model set-up, giving an insight of the different inputs and outputs, is provided in section 6.5. The performances of the numerical model to simulate bimodal sea-states on the one hand, and wave overtopping rates on the other hand, are discussed in Section 6.6. The performances and weaknesses of the model are summarized in Section 6.8 with perspectives to further increase the accuracy in future studies.

6.2 Multiphase model

6.2.1 Equations solved by neptune_cfd

neptune_cfd is a code dedicated to multiphase flows developed within the NEPTUNE project (Coste et al., 2007; Guelfi et al., 2007), funded by a consortium including several French companies

(EDF, CEA, Framatome and IRSN). Its originality lies in the use of a multi-fluid approach by solving a set of mass, momentum and energy balance equations for each fluid on the basis of a pressure correction method (Ishii, 1975). In the present study, the number of fluids N is such as $N = 2$: namely air and water. Regarding the numerical aspects, neptune_cfd is a collocated finite-volume model integrated in Code_Saturne system (www.code-saturne.org). Hence, neptune_cfd is provided with Code_Saturne high performance computing features such as an adaptive time step and permits one to perform fully unsteady calculations.

The balance equations are solved for each phase k ($k \in [1, N]$). The definition of a volume fraction α_k permits to locate the evolution of the different phases in time. Within a cell, the conservation relations for mass and volume result in the following property:

$$\sum_{k=1}^{N} \alpha_k = 1 \tag{6.1}$$

In the present study, each fluid remains in its initial phase (gas for air and liquid for water): there is no phase transition. Considering only adiabatic processes, the mass and momentum balance equations can be simplified for each phase k:

$$\begin{aligned} \frac{\partial(\alpha_k \rho_k)}{\partial t} + \boldsymbol{\nabla} \cdot (\alpha_k \rho_k \boldsymbol{U}_k) &= 0 \\ \frac{\partial (\alpha_k \rho_k \boldsymbol{U}_k)}{\partial t} + \boldsymbol{\nabla} \cdot (\alpha_k \rho_k \boldsymbol{U}_k \boldsymbol{U}_k) &= -\alpha_k \boldsymbol{\nabla} \boldsymbol{P} + \alpha_k \rho_k \boldsymbol{g} + \boldsymbol{\nabla} \cdot \overline{\overline{\tau}}_k + \sum_{p=1 \ p \neq k}^{N} \boldsymbol{M}_{p \to k} \end{aligned} \tag{6.2}$$

with ρ the density, $\boldsymbol{U}$ the velocity, P the pressure, $\overline{\overline{\tau}}$ the Reynolds-stress tensor, $\boldsymbol{g}$ the gravity and $\boldsymbol{M}$ the momentum transfer to the phase k.

Here, both air and water are considered as incompressible. Since the types of fluids and phases involved can significantly vary from one study to the other (going from flows with air entrainment to free-surface flow study for instance), several models are available to account for the interfacial momentum transfers between the phases. In the case of free-surface flows, a specific interface tracking method for Eulerian-Eulerian approach, called the Large Interface Model (LIM), is adopted (Coste, 2013).

6.2.2 Free-surface tracking method: Large Interface Model (LIM)

The study of wave overtopping process requires the modelling of a free-surface flow. The interface extends over a large number of cells mostly in the horizontal direction. The simulation of such a large interface requires the use of specific features such as interface recognition and interfacial transfer of momentum (e.g. viscous drag and form drag). The Large Interface Model (LIM) (Coste, 2013; Lavieville and Coste, 2008) was developed and implemented in neptune_cfd with that purpose. It can handle either smooth, wavy or rough interfaces. A method based on the gradient of liquid fraction is implemented within the LIM to tackle the interface recognition.

The interface recognition consists in the computation of a refined liquid fraction gradient, based on harmonic or anti-harmonic interpolated values of liquid fraction on the faces between the cells (Lavieville and Coste, 2008). The resulting refined gradient permits a detection of the cells includ-

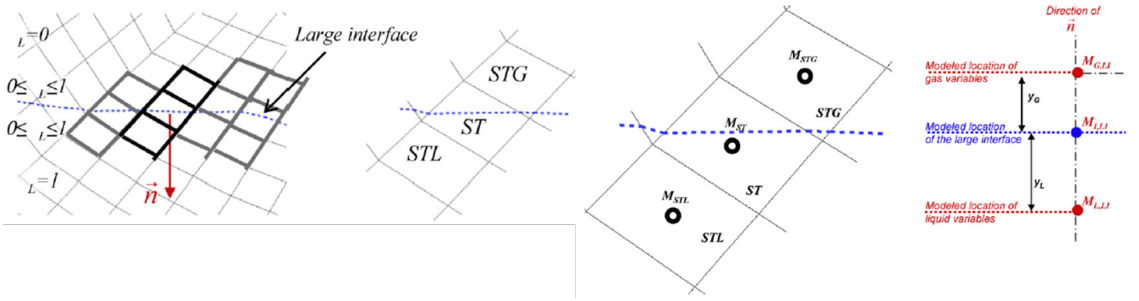

Figure 6.1: Left: example of a generic mesh showing different stencils (black and gray) cut by the interface (dotted line). Right: example of stencil. Scheme from Coste (2013).

ing the interface. Specific closure laws for such interfaces are defined within a three-cell stencil around the large interface position. The stencil includes the full liquid and full gas cells located on both sides of the cell including interface, relative to the interface normal direction (see Fig. 6.1). This stencil is used to define a law similar to a wall law on both sides of the interface. Therefore, the interface acts like a physical boundary separating the physical processes relevant to each phases. In addition, such a model limits the impact of the mesh on the interface.

6.3 Immersed boundary method to define the breakwater shape

When studying gravity stratified flow, Cartesian meshes are commonly used to accurately model the horizontal free-surface. However, the use of Cartesian meshes becomes a constraint when including solids with complex geometries inside the numerical domain. The integration of such complex shapes in Cartesian meshes requires one to find a balance between the quality of the free-surface flow modelling, the accuracy of the solid definition and the computational cost (Peskin, 1972). In the present study, the breakwater model properties are included in the numerical domain by using a discrete-forcing immersed boundary method developed by Benguigui et al. (2018) based on Mittal and Iaccarino (2005) work. The TSDP permits one to perform calculations with an easily-adaptable breakwater shape and by using a Cartesian mesh. Consequently, the breakwater is not physically meshed but defined with a Lagrangian solid fraction on the Cartesian grid.

First, as illustrated in Figure 6.2, a porosity field is defined. The mesh cells are identified as follows:

- Inner part of the solid: porosity value is 0,
- Outer part of the solid (i.e. fluid): porosity value is 1,
- Including the interface fluid-solid: porosity value lies strictly between 0 and 1.

The cells including the interface are processed to associate a specific scheme on both sides of the interface. In these cells, the interface is approximated as a straight line (a plane in 3D). Similarly to the LIM, a recognition function is necessary to identify the solid/fluid distribution within the cut cells (i.e. cut by the interface). Then, the interface properties can be reconstructed.

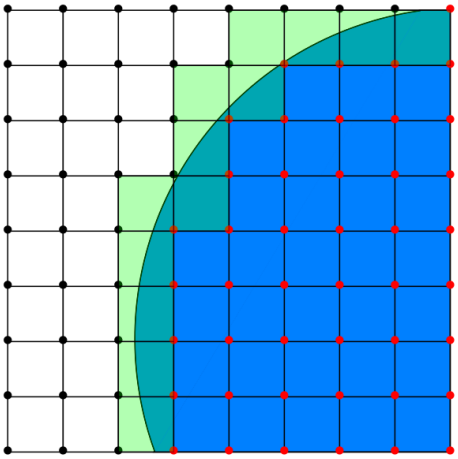

Figure 6.2: Generic mesh showing a solid (blue) and a fluid part (white). The Cartesian grid shows the three types of cells: inner part of the solid, outer part of the solid or including the interface. The ones including the interface are shaded in green color. (Figure from Benguigui et al. (2018))

The solid considered in the present study is the smooth slope breakwater model used during previous laboratory experiments (Chap. 5). The porosity field $\varepsilon_p(\boldsymbol{x})$ is defined at the initialization step. In the present study, the porosity ε_p is only function of space $\boldsymbol{x}$ and defined as follows:

$$\varepsilon_p(\boldsymbol{x}) = 1 - \alpha_s(\boldsymbol{x}) \tag{6.3}$$

with α_s the volume fraction of the solid. Assembling Equations (6.1), that does not include porosity, with (6.3), one finds:

$$\sum_{k=1}^{N} \alpha_k(\boldsymbol{x}, t) = \varepsilon_p(\boldsymbol{x}) \tag{6.4}$$

Equation (6.4) insures no mass transfer between the solid body (where the porosity is 0 so neither water or air are present) and fluids. Within the framework of the finite-volume theory, the porosity is computed for a cell I by using the following relation:

$$\varepsilon_p(\boldsymbol{x}_I) = \frac{\text{fluid volume in the cell } I}{\text{total volume of the cell } I} \tag{6.5}$$

6.4 Wave modelling

6.4.1 Irregular waves

The simulation of irregular (i.e. multichromatic) waves was performed on the basis of the linear wave theory (also named Airy theory or Stokes first-order theory). The linear theory is rather adapted in the present case given the low wave steepnesses considered in the present study (see Chap. 5). Here, the free-surface elevation η and the velocity potential ϕ are expressed considering waves in the plane Oxz (x and z are the horizontal and vertical axis respectively) with $z = 0$ the mean water level. According to the linear wave theory, the free-surface elevation and the velocity

potential are expressed as sums of N independent wave components:

$$\begin{cases} \eta(x,t) &= \sum_{n=1}^{N} A_n \cos(k_n x - \omega_n + \psi_n) \\ \phi(x,z,t) &= \sum_{n=1}^{N} \frac{gA_n}{\omega_n} \frac{\cosh(k_n(h+z))}{\cosh(k_n h)} \sin(k_n x - \omega_n t + \psi_n) \end{cases} \tag{6.6}$$

with h the water depth, A the amplitude, k the wavenumber, ω the angular frequency, ψ the phase and n the index referring to the wave component n. The corresponding orbital velocities are obtained from the velocity potential such as:

$$\begin{cases} u(x,z,t) &= \frac{\partial \phi}{\partial x} &= \sum_{n=1}^{N} \frac{gA_n k_n}{\omega_n} \frac{\cosh(k_n(h+z))}{\cosh(k_n h)} \cos(k_n x - \omega_n t + \psi_n) \\ w(x,z,t) &= \frac{\partial \phi}{\partial z} &= \sum_{n=1}^{N} \frac{gA_n k_n}{\omega_n} \frac{\sinh(k_n(h+z))}{\cosh(k_n h)} \sin(k_n x - \omega_n t + \psi_n) \end{cases} \tag{6.7}$$

In the present study, the N wave components are determined using the incident spectra resulting from the reflection analysis algorithm used during the experiments described in Chapter 5. The spectra include 86 wave components ($N = 86$) equally distributed over the frequency range $f_n \in [0.3, 3]$ Hz with $\mathrm{d}f \simeq 0.031$ Hz. The wavenumbers are determined using the dispersion relation: $\omega^2 = gk\tanh(kh)$.

A well-known property of wave generation according to the linear theory is an induced current in the wave direction: the so-called Stokes drift (Longuet-Higgins, 1956). In the present numerical domain with rather small dimensions, the Stokes drift involved a rapid increase of the water level. Hence, a return current had to be applied to counter the water level rise. The Stokes drift associated to each simulated wave spectrum was estimated using an iterative algorithm calculating the drift and correcting the wavenumbers (using the dispersion relation) at each step until it reached stable values for both the drift and the wavenumbers.

In addition to the return current to counterbalance the Stokes drift U_d, a current U_o was also applied to account for the water level decrease due to wave overtopping. The method to estimate the numerical wave overtopping rates is defined in the following. For the purpose of the present study, currents were applied by modifying the wave orbital velocities displayed in Equation (6.7):

$$\begin{cases} U(x,z,t) &= U_\mathrm{d} + U_\mathrm{o} + u(x,z,t) \\ W(x,z,t) &= w(x,z,t) \end{cases} \tag{6.8}$$

with $U_\mathrm{d} < 0$ and $U_\mathrm{o} > 0$, so that the mean Eulerian mass transport was zero.

6.4.2 Numerical wave generation method

To have comparable results between the numerical and physical models, the incident waves in front of the breakwater must be statistically similar. Since the numerically-generated waves correspond to the incident wave spectrum obtained from the experiments, it is necessary to handle the absorption of the waves reflected by the breakwater in the numerical model. The generation

and absorption are performed using a combination of a Dirichlet boundary condition (BC) and a relaxation zone illustrated in Figure 6.4.

At $x = 0$, the following Dirichlet BCs are applied for $z \leq \eta(x = 0, t)$:

$$\begin{cases} \alpha_{\mathrm{w}} = 1 \text{ and } \alpha_{\mathrm{a}} = 0 \\ U_0(z,t) = U(x = 0, z, t) \\ W_0(z,t) = W(x = 0, z, t) \end{cases} \tag{6.9}$$

with α_{w} and α_{a} the water (liquid) and air (gas) phases respectively. For $z > \eta(x = 0, t)$, $\alpha_{\mathrm{a}} = 1$ and U_0 and W_0 velocities are zero.

The relaxation zone was located between $x = 0$ and $x = 5$ m. Its length $L_{\mathrm{r}} = 5$ m was slightly longer than the longest peak wavelength λ_p in this study (λ_p,max = 3.67 m). The relaxation zone method consists in including a source term in the dynamic part (right-hand side) of the momentum conservation equation (Eq. (6.2)) to correct the simulated velocity so it smoothly tends to a target velocity when $x \to 0$. In this zone, it is important to highlight that only the velocities are corrected: the volume fractions are the ones computed by the software. A factor $\chi(x)$ is used to handle the weighting of the velocity correction within the relaxation zone. Here, it is defined as follows:

$$\chi(x) = \frac{e^{\left(\frac{L_{\mathrm{r}} - x}{L_{\mathrm{r}}}\right)^2} - 1}{e - 1} \tag{6.10}$$

were e is the exponential constant so that, in the present study, $\chi(0) = 1$ and $\chi(L_r) = 0$. The target velocities applied within the zone correspond to the velocities given by the linear wave theory (Eq. (6.7)). For more details about the expression of the source term, one can refer to Perić and Abdel-Maksoud (2018).

6.5 Numerical set-up

In this section, the calculation domain is described by introducing the time and space discretizations and by presenting the different inputs and outputs of the model. An illustration of wave overtopping with the numerical set-up adopted in the present study is shown in Figure 6.3. One can observe the free-surface corresponding to an irregular sea-state during a wave overtopping event.

6.5.1 Mesh

Since only unidirectional waves were considered during the physical experiments, the numerical mesh is designed in 2D in the plane Oxz. The mesh design described in this section is a result of several preliminary simulations that aimed at finding a good balance between sufficiently accurate wave generation and absorption processes together with computing considerations. The objective was to simulate a physical time of 500 s in a computational time below 3 days with a parallel computation on 48 CPUs provided by the EDF R&D computational center. The selected physical time is taken from Chen et al. (2021) who considered similar (or longer) wave periods as in the present study. They found that experimental runs with 250 to 350 waves (depending on the

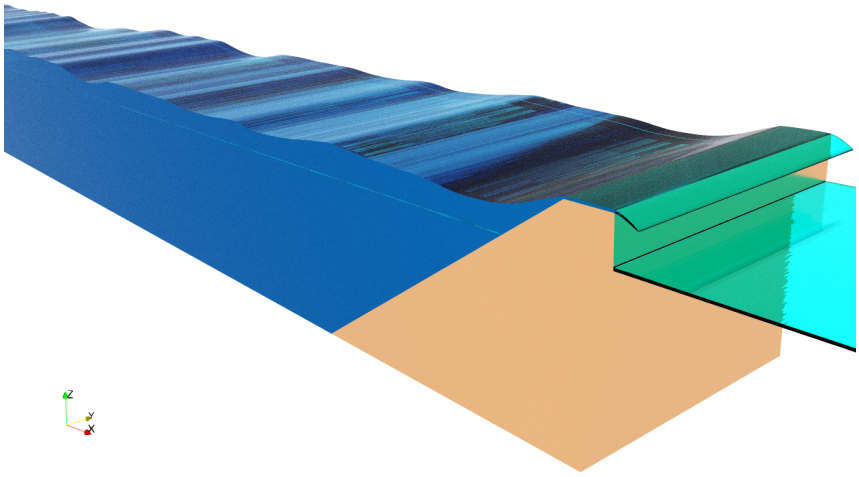

Figure 6.3: Snapshot of the 2D numerical wave tank with the breakwater and the water container during a simulation with Case E and $R_c = 5.1$ cm. It is important to note that there is only one cell along the y-axis.

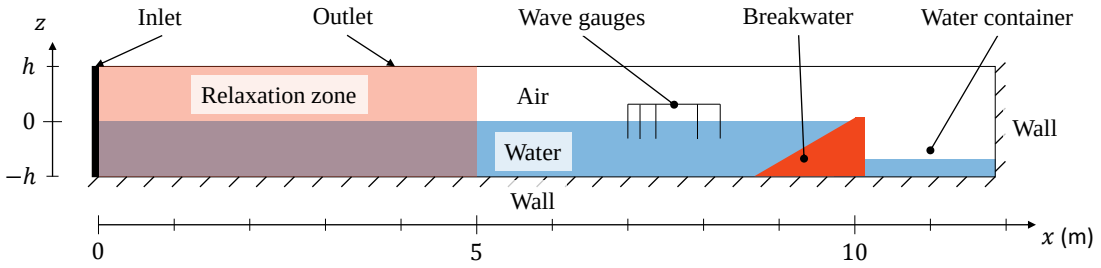

Figure 6.4: Definition sketch of the numerical set-up.

wave periods), corresponding to 500 s time series, lead to a maximum error of 15 % in the wave overtopping rate estimations compared to runs with 1000 waves.

Although the water depth h could vary between 0.72 and 0.74 m during the experiments, here we assumed that defining $h = 0.73$ m as a constant value does not impact the results. In addition to the water depth, the parameters considered to define the default mesh dimensions are the following:

- Maximum peak wavelength: $\lambda_{\max} = 3.67$ m (corresponding to a peak frequency $f_p = 0.6$ Hz),
- Design wavelength: $\lambda_{\mathrm{ww}}^{\mathrm{dsg}} = 1.55$ m (corresponding to a peak frequency $f_p = 1$ Hz),
- Maximum free-surface elevation: $\eta_{\max} = 0.1$ m,
- Design significant wave height: $H_{m_0}^{\mathrm{dsg}} = 0.065$ m,
- Breakwater length along the x-axis: $L_{\mathrm{bw}} = 1.338$ m,
- Container length along the x-axis: $L_{\mathrm{c}} = 1.80$ m.

The dimensions of the numerical domain, illustrated in Figures 6.4 and 6.5, are the following:

- Horizontal total length: $L_{x,\text{tot}} = L_\text{r} + \lambda_\text{max} + L_\text{bw} + L_c = 11.808$ m,
- Vertical total height: $L_{z,\text{tot}} = 2 \times h = 1.46$ m.

As shown in Figure 6.4, the origin of the x-axis coincides with the left-hand side of the domain and the origin of the z-axis coincides with the free-surface at rest.

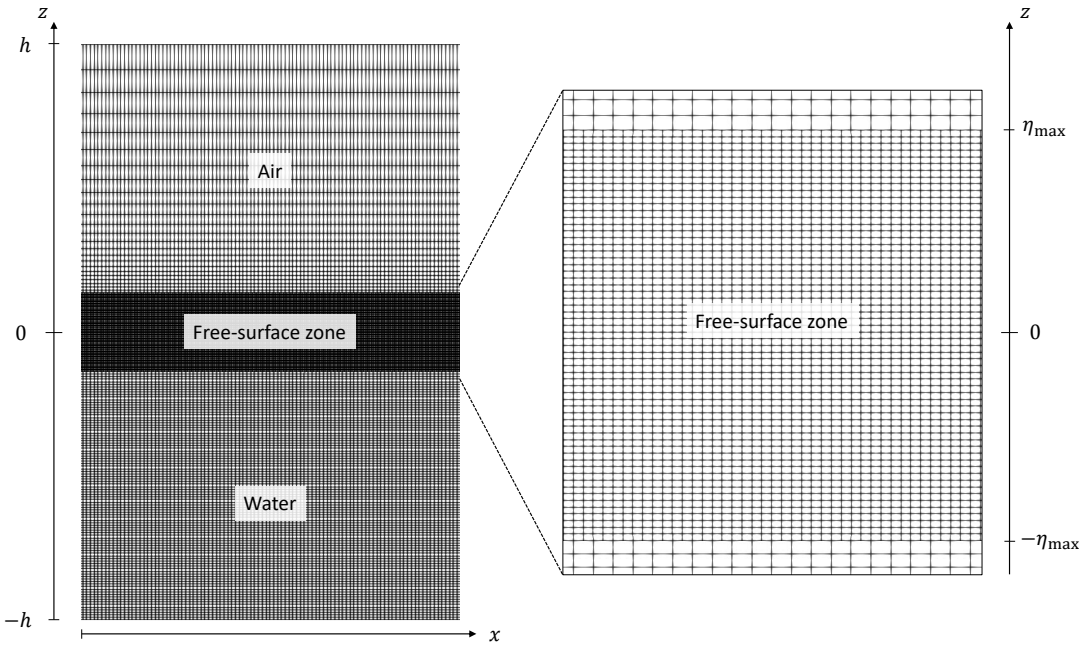

Figure 6.5: Section of the default mesh adopted in the present study with a zoom on the refined free-surface zone (right-hand side).

Regarding the cells dimensions, the mesh has been divided in 3 parts along the z-axis (Fig. 6.5):

- The free-surface zone ($z \in [-\eta_\text{max}, \eta_\text{max}]$) with $\text{d}x = \lambda_\text{ww}^\text{dsg}/N_x$ and $\text{d}z = H_{m_0}^\text{dsg}/N_z$
- The air zone ($z \in [\eta_\text{max}, h]$) with $\text{d}x = \lambda_\text{ww}^\text{dsg}/(0.5N_x)$ and $\text{d}z = H_{m_0}^\text{dsg}/(0.5N_z)$ at $z = \eta_\text{max}$ with a geometrical increase with a ratio of 1.101 up to $z = h$,
- The water zone ($z \in [-h, -\eta_\text{max}]$) with $\text{d}x = \lambda_\text{ww}^\text{dsg}/(0.5N_x)$ and $\text{d}z = H_{m_0}^\text{dsg}/(0.5N_z)$

The air zone is defined so that the top of the numerical domain is sufficiently far from the free-surface to prevent effects of the BC on wave propagation. As displayed in the right-hand side of Figure 6.5, the above settings resulted in a non conformal mesh: the free-surface zone is twice as fine as the adjacent zones. The default values determining the cells dimensions are $N_x = 320$ and $N_z = 20$.

In the following, a convergence analysis is performed based on the simulated wave overtopping rates and significant wave heights with finer meshes. It is found that the default mesh is rather coarse and would need to be refined to improve the numerical results. Yet, interesting trends are observed with the results obtained using the default mesh by comparison with the results from the

physical model. Hence, the use of the default mesh should be seen as a necessary step to initiate a mesh optimization effort with the purpose to use it for an operational use.

6.5.2 General settings

First, the adaptive time step feature is activated and based on a maximum Courant number value of 1 for both the water and the air phases with an initial time step $\mathrm{d}t = 0.005$ s. In addition to the Inlet BCs defined in Section 6.4, two additional BCs are defined and illustrated in Figure 6.4:

- Wall BC (velocities equal to zero): applied at the bottom and at the right end of the numerical tank,
- Inlet/Outlet BC (imposed pressure): applied on the roof of the numerical tank.

Furthermore, no turbulence models were applied in the present study.

The initialisation of the calculation consisted in defining the velocity, air and water volume fractions and the porosity fields in space as follows:

$$\begin{cases} \alpha_{\mathrm{w}} = 1 \text{ for } z < \eta(x, t = 0) \text{ with } x < 10 \text{ m} \\ U_{\mathrm{initial}}(\boldsymbol{x}) = U(\boldsymbol{x}, t = 0) \\ W_{\mathrm{initial}}(\boldsymbol{x}) = W(\boldsymbol{x}, t = 0) \end{cases} \tag{6.11}$$

Equation (6.1) imposes that $\alpha_{\mathrm{a}} = 1$ when $\alpha_{\mathrm{w}} = 0$. Hence, there is no water in the container at $t = 0$. Then, the porosity field is defined as follows: $\varepsilon_{\mathrm{p}}(\boldsymbol{x}) = 0$ for $\boldsymbol{x}$ in the orange zone displayed in Figure 6.4.

6.5.3 Model inputs

Another advantage of defining the breakwater shape with the porosity method comes up with the setting of the breakwater freeboard R_c. During the physical experiments, the freeboard was measured before each run. Hence, the freeboard was set for each simulation of a run with neptune_cfd by changing a single parameter in the porosity settings.

During the experiments in the wave tank, the incident wave spectrum was obtained for each run. Therefore, for a given wavemaker signal, the measured incident wave spectrum could slightly vary from one run to the next. In the present simulations, both unimodal and bimodal spectra were simulated based on the incident spectra measured during the experiments. In each simulation, corresponding to a single run from the physical experiments, the corresponding incident measured spectrum was numerically generated. These spectra are separated in eight different cases sorted from A to G, illustrated in Figure 6.6.

6.5.4 Model outputs

Since the numerical model aims at reproducing the physical model, the main outputs we focus on are the wave overtopping rate and the incident wave spectrum.

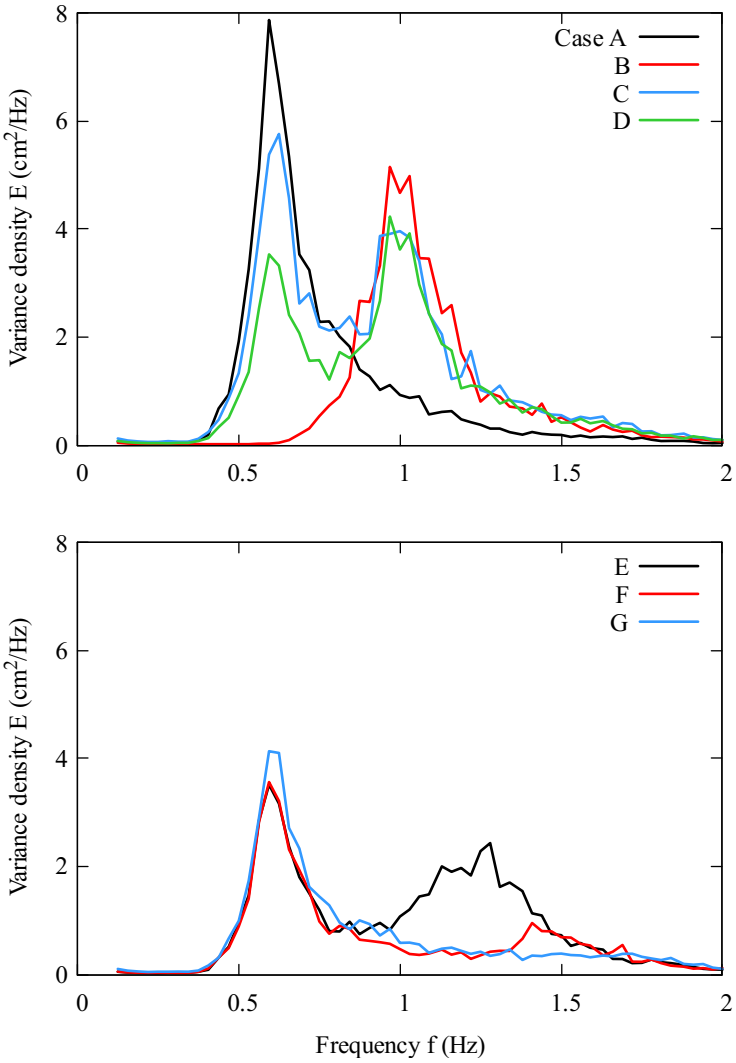

Figure 6.6: Examples of variance density spectra measured during the physical experiments corresponding to series A to G, whose parameters can be found in Table 5.1.

The wave overtopping discharge was collected in a container located behind the breakwater (Figs. 6.4 and 6.3). Then, an algorithm permitted to calculate the mean wave overtopping rate evolution as a function of the simulated physical time as shown in Figure 6.7. The wave overtopping induced a decrease of the water level in the numerical tank. To counter the decrease, the instantaneous wave overtopping rate calculated by the algorithm was re-injected (after $t = 30$ s, so the current was not too strong) as a current distributed over the water column added to U (Eq. (6.8)). Given the low magnitude of the overtopping rate relatively to the water depth, we made the hypothesis that the re-injection did not impact the results. With the combination of the return current to account for the Stokes drift and for the wave overtopping, the mean water level in the wave tank was kept constant. To account for the variations of the overtopping rate with time, the retained wave overtopping rate was obtained by averaging its value between 480 and 500 s.

Like in the experiments, a set of 5 numerical wave gauges, located in front of the breakwater (Fig. 6.4), permitted to obtain the incident spectrum using the same reflection analysis (Goda and

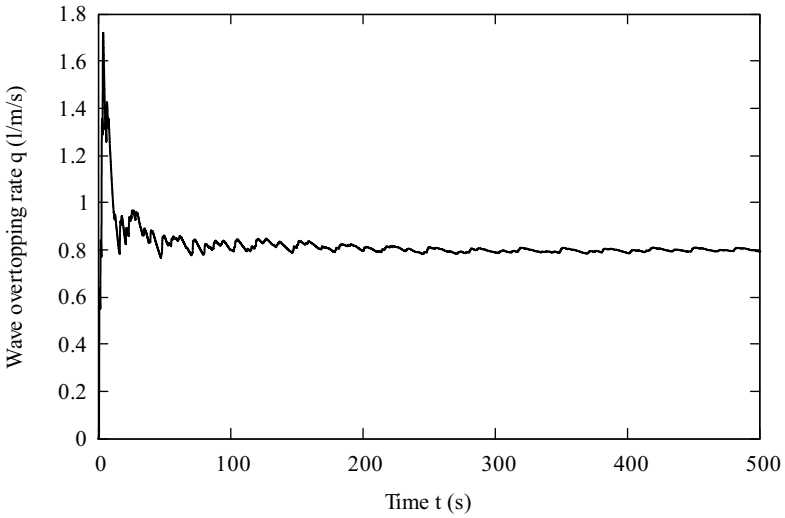

Figure 6.7: Evolution of the wave overtopping rate as a function of time over 500 s for Case B with a freeboard $R_c = 3.2$ cm.

Suzuki, 1976). The main difference with the physical experiments lies in the duration of the water surface elevation records: 1800 s with the physical model and 500 s with the numerical model. Thus, the numerical spectra are noisier (i.e. have a larger variability) than the experimental ones.

6.6 Validation of the model

6.6.1 Convergence analysis

A convergence analysis was carried out in order to assess the performances of the default mesh to yield an accurate estimation of q and H_{m_0}. Hence, 4 finer meshes (illustrated in Figure 6.8) have been designed by multiplying the default values of N_x and N_z with a coefficient C_{xz}:

- $C_{xz} = 1.25$: $N_x = 400$ and $N_z = 25$,
- $C_{xz} = 1.5$: $N_x = 480$ and $N_z = 30$,
- $C_{xz} = 1.75$: $N_x = 560$ and $N_z = 35$,
- $C_{xz} = 2$: $N_x = 640$ and $N_z = 40$.

Simulations were performed with these different mesh refinements using a wave spectrum from Case E with a freeboard $R_c = 5.1$ cm as inputs. Case E was selected on the basis of its high wind-wave peak frequency: it was considered as the most challenging wave spectrum to simulate with the wave model. For the convergence analysis relative to the mesh refinement, the maximum simulated time is $t_{\max} = 320$ s due to the high computational cost of the mesh corresponding to $C_{xz} = 2$.

Figure 6.9 shows the sensibility of the simulated wave overtopping rate as a function of the relative freeboard depending on the mesh definition and the simulated time. As a reminder of the previous

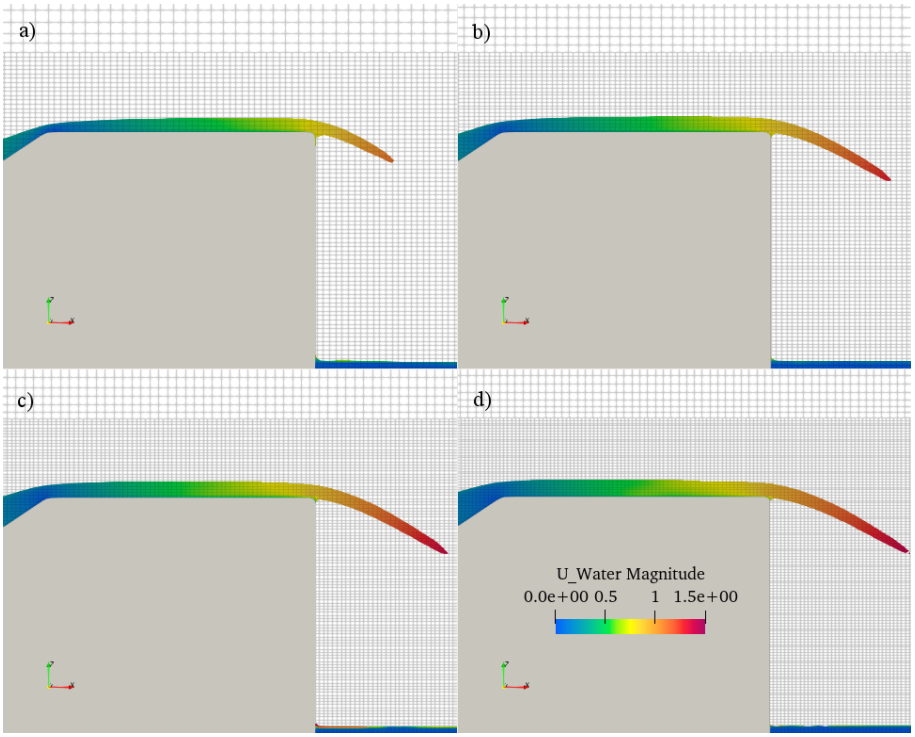

Figure 6.8: Snapshot of numerical wave overtopping for different meshes: a) $C_{xz} = 1.25$, b) $C_{xz} = 1.5$, c) $C_{xz} = 1.75$, d) $C_{xz} = 2$.

chapter, R_c^* and q^* follows EurOtop definition (Pullen et al., 2007; Van der Meer et al., 2018):

$$q^* = \frac{q}{\sqrt{gH_{m_0}^3}} \quad ; \quad R_c^* = \frac{R_c}{H_{m_0}}$$

In this chapter, the new scaling suggested in Chapter 5 is not used. The mesh's refinement is described using a number of cells per wavelength N_x (see the above itemization). Among the mesh parameters, N_x is assumed to have most significant impact on the accuracy of the numerically generated waves.

In Figure 6.9.a, the difference between the blue (default mesh) and red (finest mesh) points shows that the default mesh is not fine enough to accurately estimate the wave overtopping rate and the significant wave height. The aimed value for q^* and R_c^* are given by the laboratory observations with the black square. By increasing the mesh refinement the simulated q^* and R_c^* get somewhat closer to the observed value. However, by observing Figure 6.9.b (zoom on Fig. 6.9.a), it is not clear that the simulated values tend to the observed one. It seems to rather converge toward a position with R_c^* equivalent to the observation but with a lower q^*. In addition to the convergence analysis regarding the mesh definition, a further analysis of the relaxation zone length could be performed in order to improve the wave simulation to obtain better estimations of H_{m_0}.

In addition, Figure 6.9.b shows that the values of q^* and R_c^* does not significantly vary depending on the simulated time $t_{\max}$ by comparing the circles and triangles. Yet, it can be observed that the simulated time tends to have a larger impact on the results when the mesh refinement increases.

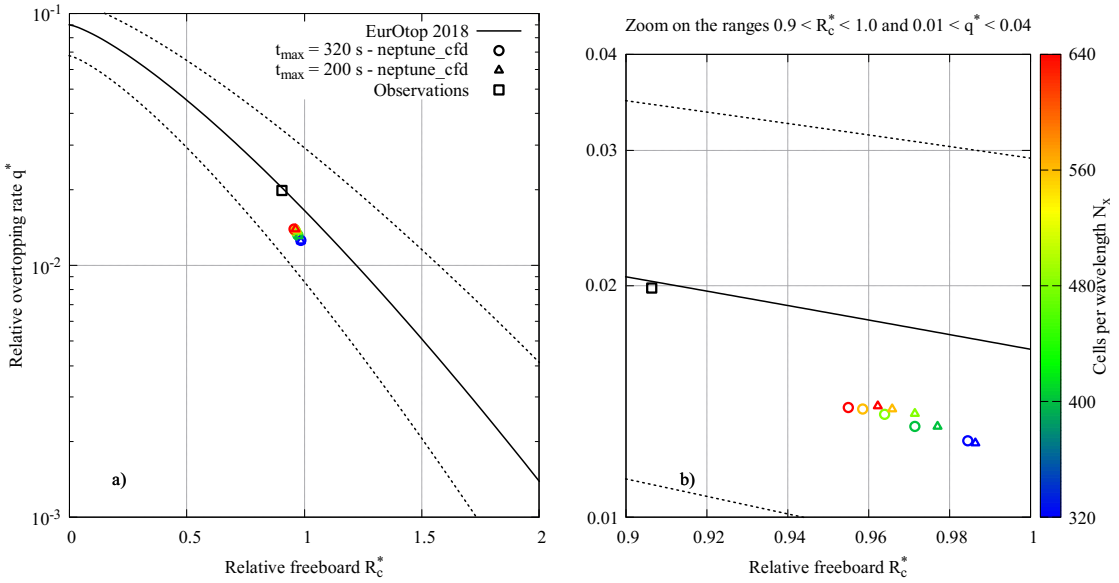

Figure 6.9: Relative wave overtopping rate as a function of the relative freeboard corresponding to Case E with a constant freeboard $R_c = 5.1$ cm for several mesh definitions and for two different simulated time $t_{\max}$ compared to the observations (black). b) is a close-up view of a) on the ranges $0.9 < R_c^* < 1.0$ and $0.01 < q^* < 0.04$.

For a given number of CPU, the computational time relative to the calculation with $N_x = 640$ (finest mesh) is 8 times longer than with $N_x = 320$ (default mesh). This computational time could be reduced using an efficient parallelizing of the computation and by increasing the CPU numbers. Yet, the improvement of the results with finer meshes is rather small considering the increase in terms of computational cost. To be able to perform simulation on a relatively short computational time (500s simulated within 3 days), simulations performed with the default mesh ($N_x = 320, N_z = 20$) are shown in the following sections.

The convergence analysis was also performed regarding the accuracy of the wave generation in neptune_cfd by analyzing wave spectra in Figures 6.10 and 6.11. Figure 6.10 illustrates the dependency of the wave frequency spectra on the mesh definition. Based on Figure 6.10.a, it is rather clear that the spectrum simulated with the finest mesh (red color) is not significantly different from the one with the default mesh (blue color). Figure 6.10.b shows that the differences relative to the mesh definition increases with the frequency. Hence, the mesh refinement does not significantly improve the simulated spectra below 2 Hz. The low energy levels of the waves components in the high-frequency tail are not expected to have a significant impact on the wave overtopping process.

Overall, Figure 6.10 shows that the general shape of the spectrum is reasonably well simulated by neptune_cfd by comparison with the observations at least over the range [0 : 1.5] Hz. However, even with the finest mesh, the simulated spectra lack of energy at the swell and wind-wave peak frequencies and in the high frequency (HF) tail.

Figure 6.11 illustrates the influence of the simulated time on the spectral analysis. For that purpose, spectra obtained from a simulation with Case E are plotted after different simulated times from $t_{\max} = 100$ to 500 s. In both Figures 6.11.a and b, the most significant differences occur between

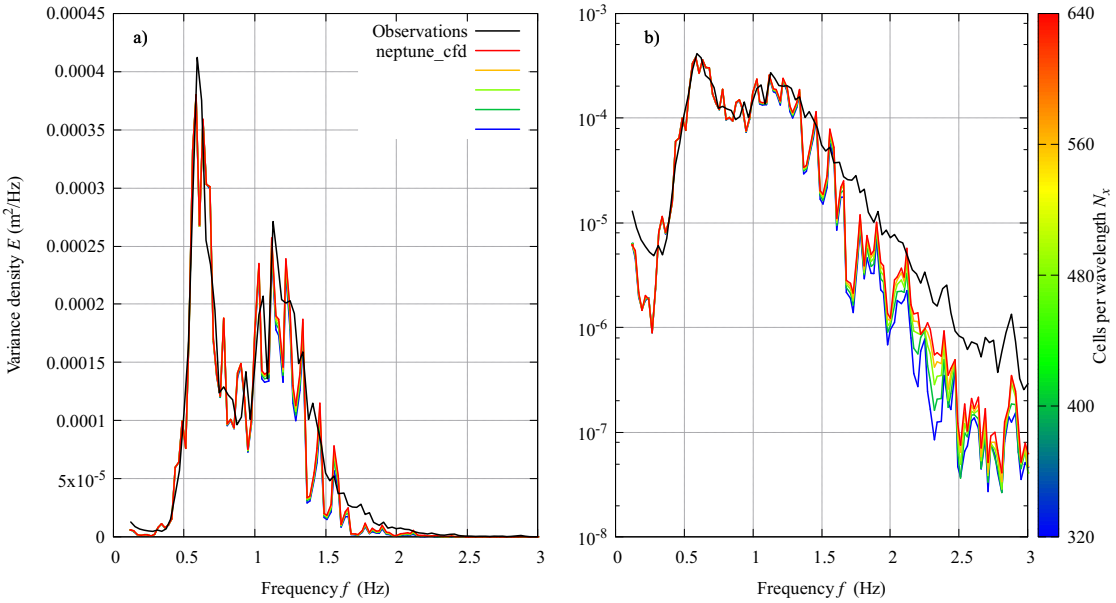

Figure 6.10: Variance density spectra corresponding to Case E with a constant freeboard $R_c = 5.1$ cm obtained after $t = 320$ s for different mesh definitions. The spectra are plotted with linear (a) and logarithmic (b) vertical scales.

the spectra obtained at $t_{\max} = 100$ and 200 s. Above $t_{\max} = 200$ s, the increasing simulated time tends to smooth the general shape of the spectra. Figure 6.11.b shows that this smoothing effect is rather uniform along the frequencies.

6.6.2 Simulated wave spectra

The accurate simulation of irregular waves corresponding to bimodal sea-states with a NS solver was one of the challenges of the present study. Figure 6.12 illustrates neptune_cfd performances to reproduce the experimental spectra. The general shape of the spectra are rather well reproduced up to frequencies of 1.2 Hz. However, the simulated swell peaks at 0.6 Hz are divided in two sub-peaks leading to an underestimation of the swell energy compared to the observations. The total energy of the simulated spectra are around 10 % less energetic than the experimental ones. At higher frequencies, the wind-waves peaks are rather well simulated in terms of magnitude but are much noisier than the observations above 1 Hz. As discussed in the previous section, the noise could be reduced by performing longer computations to simulate a longer physical time. In Figure 6.12 from Cases C to G, the HF part ($f \geq 1.2 - 1.5$ Hz) of the spectra are clearly underestimated in the simulations. In particular for Case F, the wind-wave peak merges with the HF tail of the swell peak. This latter underestimation might partly be overcome with a finer mesh (Fig. 6.10). But since the wave components satisfying $f \geq 2.5$ Hz correspond to low energy magnitudes, the accuracy of the simulated waves in this range may not be essential for an accurate simulation of the wave overtopping rates. Hence, improving the fidelity of the simulated wave overtopping rate compared to the observations would consist in improving the simulated intensity of the wave components near the spectral peaks (up to 2.5 Hz in the present study).

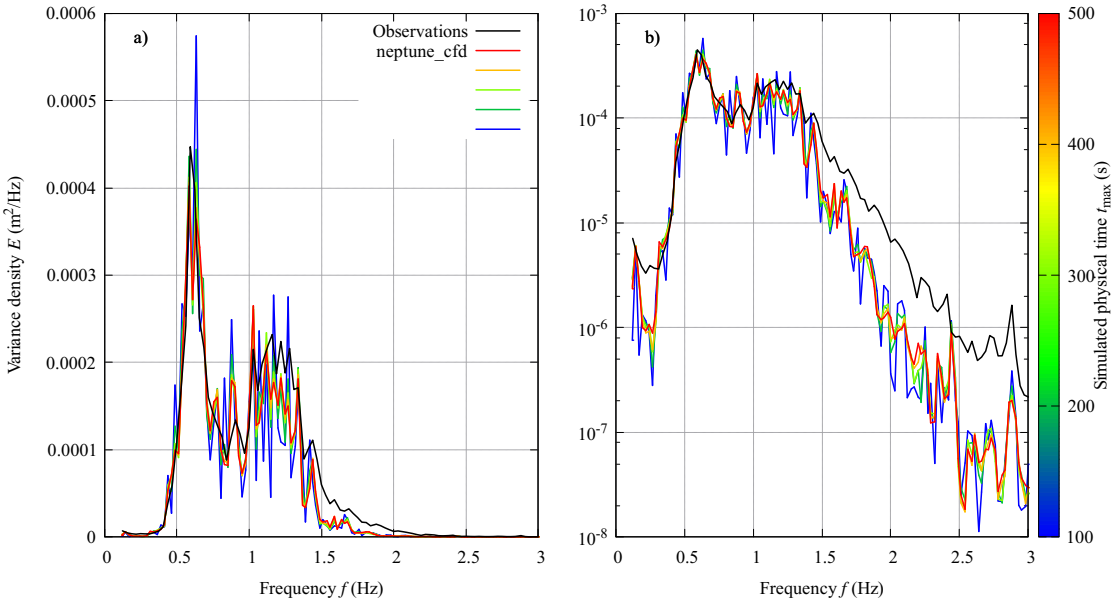

Figure 6.11: Variance density spectra corresponding to Case E with a constant freeboard R_c = 4.5 cm obtained after different simulated time $t_{\max}$ with the default mesh (i.e. $C_{xz} = 1$). The spectra are plotted with linear (a) and logarithmic (b) scales.

6.6.3 Wave overtopping

Figure 6.13 shows the relative wave overtopping rate as a function of the relative freeboard obtained with neptune_cfd simulations (colored symbols) by comparison with the laboratory observations (grey symbols). At first sight, it is clear that the numerical model underestimates q^* and overestimates R_c^*. This recalls the behaviour observed with Case E in the previous section.

Although the colored points are shifted to the south-east of the grey ones, it is interesting to note that the numerical results distribution is very similar to the observations. In particular, the increasing overtopping rate magnitude with decreasing representative wave steepness at low freeboard, emphasized in Chapter 5 (see Fig. 5.7), can be observed in Figure 6.13 by comparing the red triangles (Case A) and the full blue circles (Case B). The bimodal sea-states, corresponding to an intermediate wave representative steepness (green points), are located between the points corresponding to high (red) and low (blue) steepnesses.

The comparison of the numerical results with EurOtop (2018) (Van der Meer et al., 2018) confirms the underestimation of the wave overtopping rates yielded by neptune_cfd. However, as discussed in the previous Chapter, the numerical results are another proof that the motivation that lead to change the c parameter from 1 to 1.3 between EurOtop (2007) (Pullen et al., 2007) and EurOtop (2018) is not relevant in our series.

6.7 Discussion

In the previous sections, an underestimation of the incident simulated wave energy was observed in addition to an underestimation of the wave overtopping rates. In the present section, a discussion

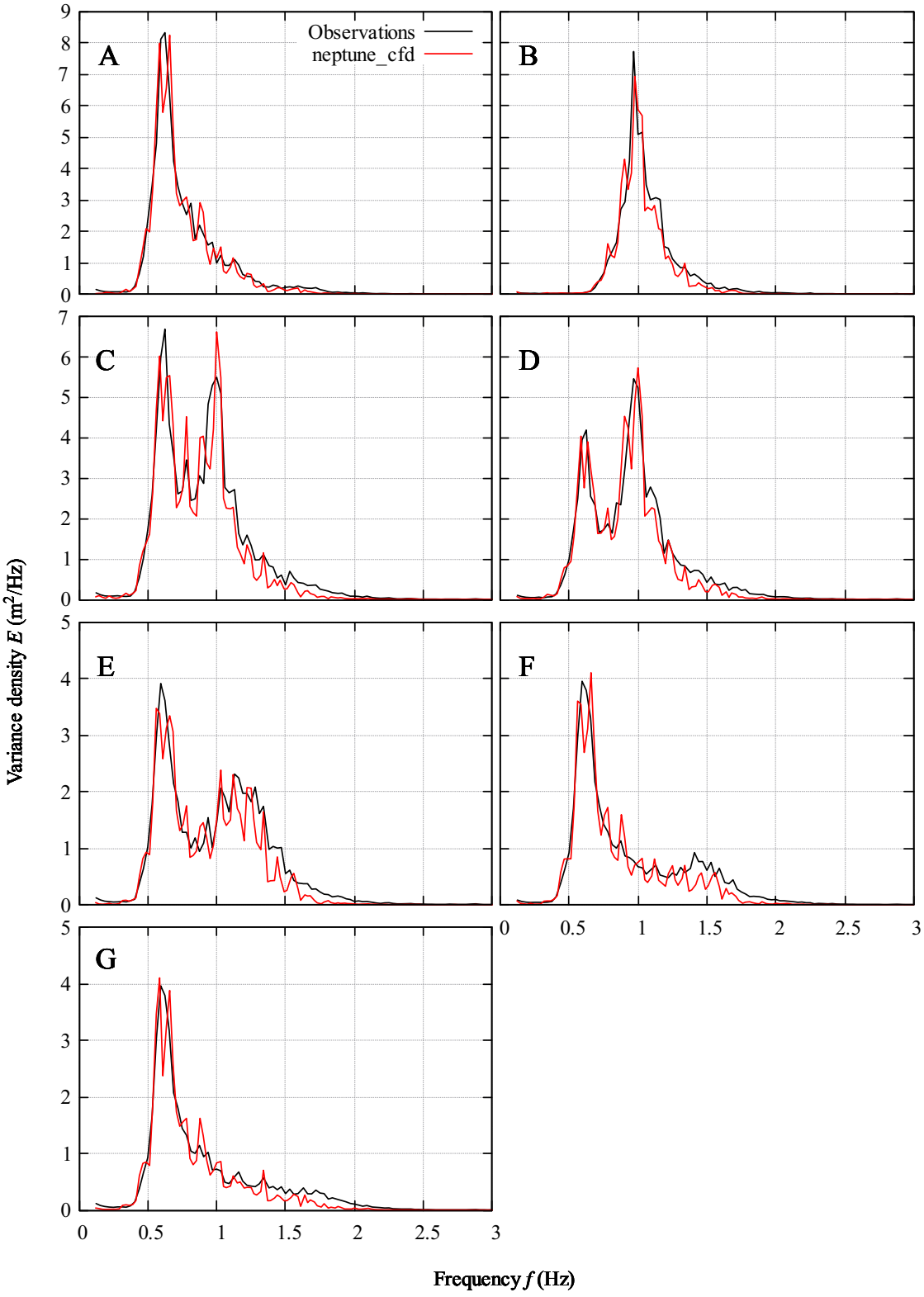

Figure 6.12: Comparison between observed and simulated variance density spectra corresponding to runs with Case A to G with the default mesh (i.e. $C_{xz} = 1$) obtained with $t_{\max} = 500$ s.

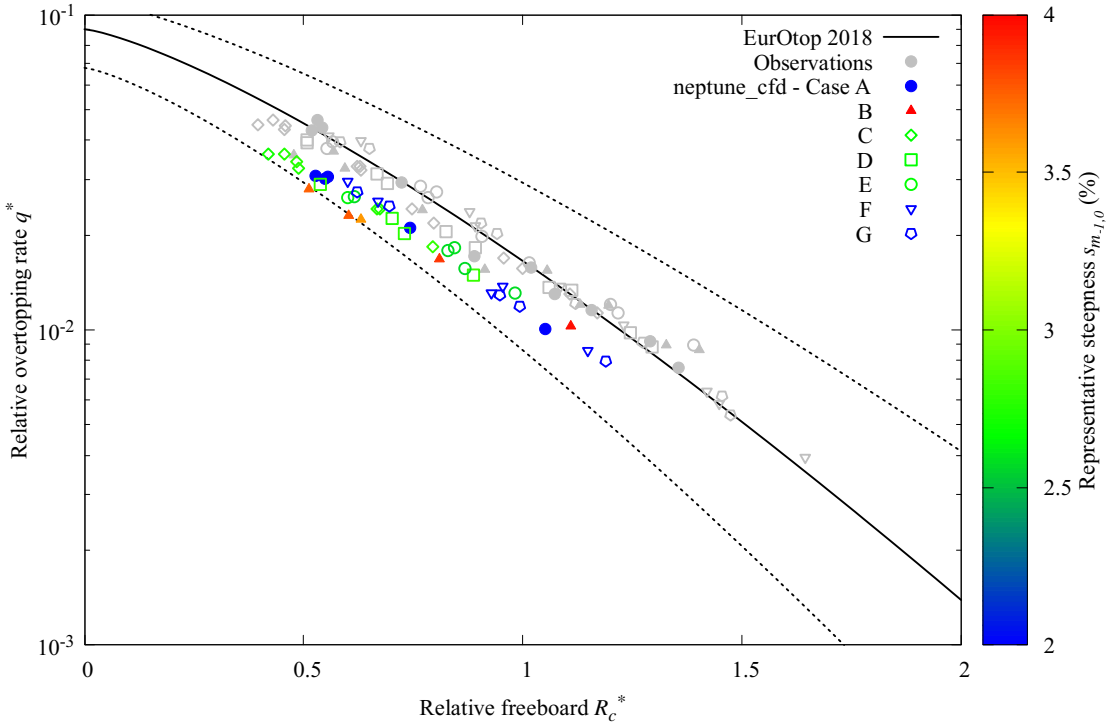

Figure 6.13: Comparison between observed (grey) and simulated (colors) relative wave overtopping rates as a function of relative freeboard obtained with the default mesh (i.e. $C_{xz} = 1$). The simulations with neptune_cfd are colored by the representative wave steepness $s_{m_{-1,0}}$ characterizing each sea-state. The lines correspond to EurOtop formula (Van der Meer et al., 2018).

is proposed about the possible origins of the underestimation and its impact on the relevance of using numerical models to improve or complement the wave overtopping empirical formulas.

Figure 6.14 supports the discussion by showing a spectrum (red) obtained at the Inlet of the numerical domain (see Fig. 6.4) by comparison with the underestimated incident spectrum (blue) at the toe of the breakwater and the spectrum from the observations with the physical model (black). Hence, Figure 6.14 highlights that wave energy is lost between the Inlet BC and the toe of the breakwater. This energy loss can have different origins.

First, it can arise for numerical reasons associated with the NS solver (space and time resolution, numerical methods, etc). In addition to the mesh refinement and the simulated time previously discussed, the relaxation zone might also play a significant part. A sensitivity study could be performed to assess the quality of both wave generation and wave reflection as a function of the relaxation zone length. An extended relaxation zone should permit to force the wave orbital velocity profile over a longer distance so that the waves might be more energetic at the toe of the breakwater. Furthermore, different weighting functions χ could be tested to increase the forcing magnitude within the zone. However, a stronger velocity forcing might deteriorate the absorption property of the relaxation zone.

Secondly, the energy loss might have physical origins. Waves are generated according to the linear theory although NS equations are fully nonlinear. The energy loss might question our assumption

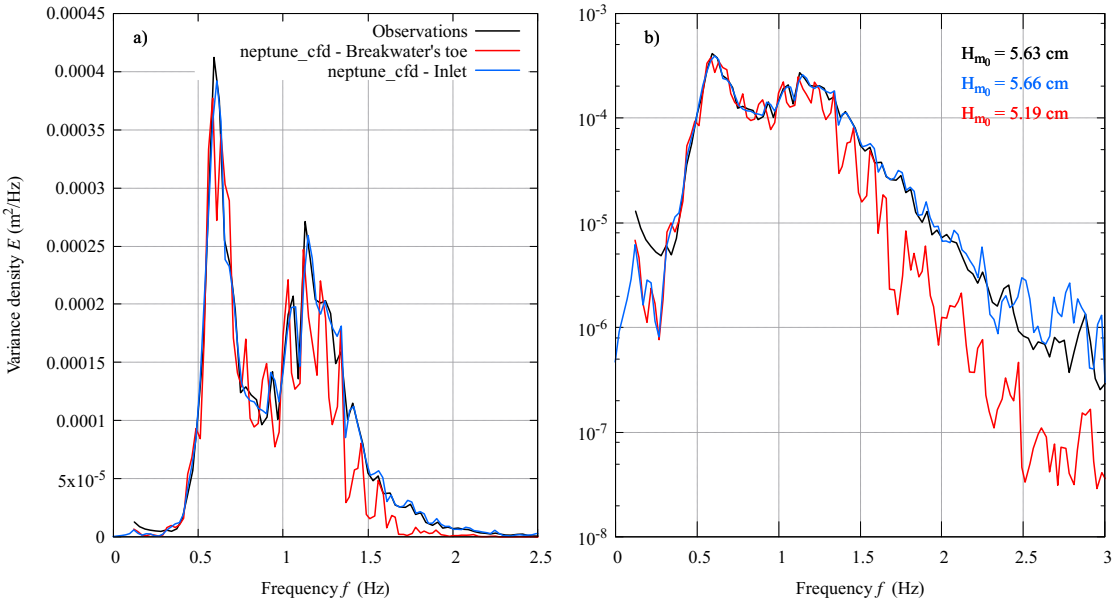

Figure 6.14: Variance density spectra corresponding to Case E with a freeboard $R_c = 5.1$ cm obtained over a simulated time $t_{\max} = 500$ s with the default mesh (i.e. $C_{xz} = 1$). The simulated spectra obtained at the Inlet BC (i.e. $x = 0$, blue color) and the incident spectra at the toe of the breakwater (red color) are compared to the spectrum from the observations (black color). Both linear (a) and logarithmic (b) scales are displayed.

that the linear wave theory is adapted in the present study. The incident waves near the exit of the relaxation zone (i.e. $x \simeq 5$ m) might no longer satisfy the linear theory (at the difference with waves observed at $x = 0$) since the computed velocities (with NS equations) predominate over the targeted velocities (from the linear theory). This linear-nonlinear transition could have a damping effect on the wave energy. A partial solution might be to force wave velocities with the second order Stokes' theory to smooth the transition from target to computed wave orbital velocities. The effect of air-water mixing during wave breaking is also missing in the numerical model.

By comparison with the unimodal spectra simulated using OpenFOAM in Chen et al. (2021) (Fig. 7 in the article), neptune_cfd shows rather comparable performances. The novelty and the main challenge of the present study is to accurately simulate wave components over a large range of frequencies due to the presence of two wave systems characterized by two peak frequencies.

Regarding the pertinence to perform numerical simulations in addition to physical experiments, the present results proved the performances of a numerical model to reproduce qualitatively the trends observed in a laboratory. If one circumvents the above limitations, neptune_cfd could be used in the future as an exploratory tool to investigate the relevance to perform physical experiments on a given research topic. It can also be used to assess the physical limitations of scale model experiments by comparison with the prototype scale (studying scale effects like viscous and surface tension forces). Finally, by further improving the wave overtopping rate simulation, the code could be used with a rather good level of accuracy to investigate wave overtopping under configurations that cannot be modelled with physical experiments. For instance, such experiments could be the investigation of the wind effect on wave overtopping at the prototype scale.

6.8 Conclusion

A numerical model based on a multi-fluid approach using neptune_cfd software was designed in order to reproduce a series of experiments on wave overtopping over a breakwater model at laboratory scale. Only the case of a smooth slope (impermeable) breakwater was considered here. One of the novelty of our approach was to use a multi-fluid code based on NS equations to study the wave overtopping of a generic coastal protection designed with a porosity method. Furthermore, the wave overtopping process was studied in bimodal sea-state conditions with a combination of swell and wind-waves. The simulation of such sea-states combines the challenges to accurately simulate irregular sea-states with a NS model and to obtain an accurate wave simulation over a sufficiently large range of energetic frequencies due to the combination of long and short waves (i.e. swell and wind-waves).

It was found that the relative wave overtopping rates resulting from neptune_cfd simulations are consistently underestimated compared to the observations, by a factor of about 1.5. However, the distribution of the overtopping rates relative to the different cases (A to G) is qualitatively close to the distribution of the laboratory results. This similar distribution permits the observation of a decrease of the wave overtopping rate with increasing wave representative steepness as observed with the physical model. Overall, the numerical model was able to simulate the shape of bimodal spectra over the range $[0, 1.5]$ Hz, i.e. about 1.5 times the target peak frequency of the wind-wave component. Yet, the simulated spectral contour was rather noisy leading to an underestimation of some wave components, such as at the swell peak frequency. Hence, the numerical model underestimates the total energy of the sea-state (characterized by H_{m_0}) at the toe of the breakwater.

Based on a convergence analysis, several avenues have been identified to improve the accuracy of the simulated wave overtopping rates. First, an optimization of the mesh is necessary in order to improve the default mesh without increasing too much the already high computational cost. Secondly, improving the computational efficiency, by carrying several sensibility analysis for instance, should permit to simulate a longer physical time. Longer physical time series should have the effect to smooth the obtained numerical wave spectra.

Furthermore, the relaxation zone properties (e.g. the length and the weighting factor) on the quality of the numerical wave spectra have not been investigated, but might play an important role on the quality of the numerical wave spectra. The implementation of a wave generation according to second order Stokes' wave theory (i.e. by further including the effects of nonlinearity) might improve the efficiency of the wave generation. In addition, the use of the TSDP method to define the breakwater shape within the numerical domain could be extended to define a porous layer on the breakwater slope with permeable and roughness properties to account for a rock-armour. This way, the numerical simulations could be compared to the experimental results with the rock-armoured breakwater described in Chapter 5.

Acknowledgments

Thanks are due to William Benguigui (EDF R&D, MFEE) for providing the initial numerical settings permitting to perform the above simulations and for its invaluable assistance with the use of neptune_cfd.

Chapter 7

Conclusions and perspectives

L'objectif principal de la thèse était d'étudier les processus physiques en jeu lors de la submersion des protections côtières par les vagues dans des conditions d'état de mer combinant houle et clapot. Le premier volet, couvrant la caractérisation des états de mer bimodaux, a été traité à l'aide d'expériences réalisées dans le canal-soufflerie de l'OSU Institut Pythéas à Marseille ainsi que de simulations numériques avec le code spectral d'état de mer TOMAWAC. Le canal-soufflerie a permis d'observer un décalage de la fréquence pic du clapot causé par la présence de longues vagues irrégulières mécaniquement générées se propageant dans la direction du vent. Les performances du code spectral ont ensuite été évaluées pour la reproduction des essais en canal-soufflerie ainsi que pour la simulation d'observations à l'échelle côtière. On a ensuite pu aborder le second volet, visant l'étude des processus de submersions de protections côtières. Dans un premier temps, une seconde série d'essais a été réalisée dans le canal-soufflerie pour étudier l'influence de la présence d'états de mer bimodaux sur les débits de franchissements d'un modèle de digue d'abord lisse, puis recouvert d'une carapace en enrochements. En particulier en présence d'enrochements, les observations ont montré que les franchissements sont d'autant plus importants que la proportion de houle dans l'état de mer est élevée. Des pistes d'améliorations des formules d'estimation des franchissements ont été proposées sur la base des observations. Enfin, les performances du code multiphasique neptune_cfd pour la simulation des franchissements ont été évaluées par comparaison avec les mesures expérimentales. De telles simulations ont pour objectif, à terme, de compléter les données expérimentales dans des configurations complexes difficiles à mettre en oeuvre à l'échelle d'un laboratoire. Des perspectives ont été proposées pour continuer d'améliorer la prévision des états de mer ainsi que leur prise en compte dans l'estimation des débits de franchissement.

The main objective of the present thesis was to investigate the physical processes at play during the submersion of coastal protections by waves in sea-state conditions combining swell and wind-waves. From an industrial perspective, the purpose of this investigation is to assess the validity and possibly improve the reference methodology to estimate the wave overtopping of coastal protections as a function of the sea-state characteristics in bimodal sea-state conditions. The objective of this thesis is motivated by considerations of safety and efficiency to protect the nuclear power plants near the sea. Economical aspects are rather important given the expensive cost of the installation of coastal protections that falls on communities' or industries' finance. Meanwhile, a compromise must be found between the economical and environmental reasons regarding the visual and ecological impact of such installation along the coast.

To meet the objective, the organization of the present thesis is divided into two themes:

1. Characterization of bimodal sea-states: wind-wave generation and propagation in the presence of a background swell.

2. Study of wave overtopping: submersion of coastal protection by waves in bimodal sea-state conditions.

The first theme relates to physical oceanography while the second theme concerns coastal engineering. Both themes include experiments in a physical model used to investigate the physical processes at play and to assess the performances of a numerical model.

7.1 Summary of the conclusions

7.1.1 Characterization of bimodal sea-states

The OSU Institut Pythéas wind-wave tunnel was selected as a starting point of our study to investigate the physical processes that take place when wind-waves are combined with a long paddle-waves. Wind-wave, generated by the air-flow, could be combined with regular (i.e. monochromatic) or irregular (i.e. JONSWAP-type) mechanically generated waves. Similar experiments, largely documented in the scientific literature, have been carried out since the mid-20^{th} century with the wind-wave tunnels' breakthrough. The main observation resulting from these previous studies was a wind-wave energy reduction in the presence of a following paddle-waves (e.g. Donelan, 1987). This finding was confirmed in the first series of experiments performed in the course of the present thesis. However, assessing the extent to which the wind-wave reduction phenomenon could occur at prototype scale in the presence of real ocean swell characterized by a largely higher wave age than paddle-waves is still an open question.

The novelty of our approach was to investigate wind-wave growth in the presence of following irregular paddle-waves instead of monochromatic paddle-waves. Although the energy distribution over a larger frequency range complicates the identification of the physical processes, irregular waves have the advantage to be a more realistic representation of real ocean waves. In these conditions, the wind-wave peak frequency without paddle-waves was found to be shifted towards lower frequencies in the presence of irregular paddle-waves. In other words, the presence of long

irregular paddle-waves lengthens wind-waves. The observed downshift of the wind-wave peak frequency can be associated with several physical processes:

- The high-frequency wave components brought by the paddle-wave spectrum high-frequency tail initiate wind-wave growth at a lower frequency than in the absence of paddle-waves,
- The estimated friction velocity was found to slightly increase in the presence of irregular paddle-waves, that could induce a slightly accelerated wind-wave growth.

Contrary to the observations with long monochromatic paddle-waves, no strong energy reduction of the wind-wave peak was observed in the presence of long irregular paddle-waves.

An original separation method, initiated by Mackay (2011), was used to obtain the wind-wave energy and peak frequency evolution with fetch in the presence of irregular paddle-waves. Whereas the evolution of wind-wave energy and peak frequency with fetch observed in most laboratory experiments is faster than in open oceans, it was found that the presence of irregular paddle-waves triggers a wind-wave growth much more similar to that observed at prototype scale. The observed wind-wave growth follows Kahma and Calkoen (1992) empirical formula established using ocean wave data. Regarding wind-wave growth energy and peak frequency evolution with fetch, the data acquired during this first series of experiments are summarized in Table 3.1 for further use by the scientific community.

As formulated above, evaluating the extent to which the downshift observed in the laboratory can occur at prototype scale is not trivial. For that purpose, the methodology adopted in the present thesis was to use a 3rd generation (3G) spectral wave model with the following hypothesis: if the model can faithfully simulate bimodal spectra at both laboratory and coastal scales, then it can be used to assess the extent to which a phenomenon observed at laboratory scale can occur at prototype scale (e.g. coastal scale). Additionally, in 3G wave models, the physical processes involved in wind-wave growth are decomposed in source and sink terms that can be used to identify the physical process(es) responsible for the downshift.

Operational 3G wave models are very powerful tools to predict the general characteristics of a sea-state, such as the significant wave height and the peak period, from global to coastal scale. However, the performances of these models are still questionable for predicting accurate frequency and frequency-direction spectra, especially in the cases where several wave systems, such as swell and wind-waves, coexist at a specific location. The performances of three sets of source and sink terms were evaluated at laboratory and coastal scales. The selected sets include recent parameterizations for the dissipation by whitecapping, appropriate for simulating bimodal sea-states (Ardhuin et al., 2010; van der Westhuysen, 2007). Regarding the nonlinear 4-wave interactions term, the performances of the quasi-exact Gaussian Quadrature Method (GQM) (Gagnaire-Renou et al., 2010) were evaluated for the first time on bimodal sea-states simulation as an alternative to the commonly used DIA method. As a first validation stage of our methodology, TOMAWAC performances were evaluated against the results obtained during the first series of experiments.

Using a 3G model at a laboratory scale is a novel approach since such models are originally designed to simulate oceanic and coastal sea-states. The first simulations at a laboratory scale revealed a large overestimation of the friction velocity at the air-sea interface, a crucial parameter in the calculation of the wind-wave generation source term. Hence, it was necessary to force the

friction velocity to be constant and equal to the one estimated from the measurements. Overall, all the parameterizations faithfully reproduced the bimodal sea-state conditions obtained during the experiments. However, the agreement with the observations is questionable for wind-only conditions with an underestimated wind-wave peak frequency in the simulations. But even with this underestimation, a slight downshift of the wind-wave peak-frequency is observed in the simulations when the paddle-waves are added to the sea-state. While the different sets of source/sink terms are comparable for wind-wave energy estimation, the set combining ST4 (a recent and widely used wave dissipation sink term developed by Ardhuin et al. (2010)) and GQM performs slightly better regarding the simulated wind-wave peak frequency evolution with fetch.

The second stage of the validation consisted in verifying the performances of a 3G wave model for reproducing bimodal spectra observations at a coastal scale. Following Ardhuin et al. (2007), an event from the SHOWEX campaign, on the North Carolina continental shelf (USA), was selected for that purpose. In particular, the selected event permitted to assess the directional properties of the simulated spectra against the estimated directional spectra obtained from the observations. Again, among the different sets of source and sink terms, the set combining ST4 and GQM gives the best estimation of the peak frequency evolution with fetch. Additionally, this set shows promising performances for simulating the wind-wave peak width in the frequency space and the directional distribution of the wave energy. Overall, the model seems to faithfully simulate bimodal spectra at both laboratory and coastal scales showing promising results with the set combining ST4 and GQM. The validation part of our latter hypothesis was then considered satisfied.

The last stage of our methodology in using a 3G wave model to upscale a phenomenon observed in the laboratory consisted of the simulation of wind-wave growth with swell over a generic spatial domain with typical coastal scale dimensions. The downshift of the wind-wave peak frequency was observed in the simulation and increased with swell intensity. Furthermore, the observation of the contribution of the source and sink terms permitted us to attribute the downshift to the wind input source term. This latter observation confirmed our first hypothesis that the high-frequency wave components brought by the swell spectrum high-frequency tail initiate wind-wave growth at a lower frequency than in the absence of swell. However, the validity of these latter results essentially relies on the validation stage performed as the first part of our methodology. Hence, these results must be acknowledged in light of the forces and weaknesses of 3G spectral wave models.

As a summary of the first theme of the present thesis, a series of experiments carried out in a wind-wave tunnel revealed a downshift of the wind-wave peak frequency in the presence of a background swell. To assess the extent to which this phenomenon can occur at a coastal scale, a methodology based on the use of a 3G spectral wave model was developed. The model displayed promising performances in the simulation of bimodal spectra both at laboratory and coastal scales. The application of this powerful tool on a generic coastal domain showed that the downshift observed in the wind-wave tunnel can be expected to happen at a coastal scale as well. In particular, the simulations displayed a wind-wave peak period that could vary from 5 s without swell to 6.5 s with a strong swell. At a given coastal location, the presence of swell could significantly change the wind-wave spectrum. These changes may have an impact on coastal flooding estimations.

7.1.2 Study of wave overtopping

Reference formulas for estimating the wave overtopping rate in bimodal sea-state conditions are mostly based on laboratory experiments involving unimodal sea-state conditions only. Our main motivation was to assess and improve the validity of the reference formulas (e.g. Van der Meer et al. (2018)) for estimating the wave overtopping rate in bimodal sea-state conditions. The starting point of our approach consisted in carrying out the second series of experiments with the installation of a 1:25 scale coastal protection model in the OSU Institut Pythéas wind-wave tunnel. In the framework of the wave overtopping study, only the wave tank was used: the influence of wind on wave overtopping is left for future studies. The selected coastal protection type was a breakwater with a 2:3 (vertical:horizontal) slope and an impermeable core with either a smooth or a rock-armoured surface. Extreme conditions were considered so that the selected range of relative freeboard varied between 0.4 (i.e. the breakwater freeboard is lower than half the significant wave height) to more than 2.

In the presence of a smooth slope, we found that different formulas based on the EurOtop scaling perform rather well in estimating the measured wave overtopping rate in both unimodal and bimodal sea-state conditions. However, by identifying the different sea-state conditions with a representative wave steepness, clear trends are observed with a larger overtopping rate in sea-state conditions dominated by the swell system. Yet, all the results fell into the 90% confidence range of the EurOtop formula.

On the contrary with the rock-armoured slope, the latter trends are amplified and, in sea-state conditions dominated by the wind-wave system combined with low relative freeboards, the experimental results fall out of the 90% confidence range. Hence, in such conditions, the reference formulas largely overestimate the wave overtopping rate.

Our results are thus challenging the validity of the reference formulas for estimating the wave overtopping on a relatively common breakwater profile with a rock-armour. Two methods are proposed to improve these estimations:

- by modifying the existing formulas with coefficients expressed as a function of the representative wave steepness of the sea-state,
- by developing a new scaling including the representative wave steepness in the definitions of both the relative wave overtopping rate and the relative freeboard.

These methods outline two ways of including the results of the present thesis in a practical formula to improve the predictions of the wave overtopping rate. The first method, which would be the easiest one to implement, would require a larger amount of data to set the coefficients, so the formula could be used with confidence in a wide range of configurations (various slopes, types of rock-armour, etc). In the second method, more soundly based on physics, the use of the representative wave steepness would need to be validated with more diverse sea-state conditions such as in the presence of a steeper swell (that could not be generated in our experiments due to the limitations of the wave-maker). Behind the second method, the main idea is to highlight that a parameter characterizing the bimodal sea-state should be included in the calculation of the wave overtopping rate in the case of rock-armoured breakwater with a quite steep slope.

Additionally, the increased differences between the wave overtopping relative to swell and wind-waves for the smooth and the rock-armoured breakwater suggest that the rock-armour damps more efficiently the shorter wavelengths. One can imagine that a ratio of the wavelength over a typical distance, to be defined, describing the armour-layers (e.g. the mean nominal diameter of the rocks) might explain the observed differences between the overtopping relative to wind-waves and swell.

Finally, the series of experiments carried out with the coastal protection model reveals limitations of the reference formula for the estimation of the wave overtopping rates considering a rock-armoured breakwater. Possible improvements to the formula are suggested but would require a long validation process using a large data-set acquired on a larger number of breakwater configurations. Such data can be gathered in different ways:

- by collecting data from previous experiments,
- by performing new experiments,
- through the use of a validated numerical model.

Here, the neptune_cfd software was used to numerically reproduce the experiments with the breakwater physical model, considering the smooth slope configuration only. The reproduction of the physical experiments by the numerical model permitted to observe similar trends as in the experiments regarding the decreasing wave overtopping rate with increasing wave representative steepness. However, by comparison with the observations, the numerical model's results show an underestimated significant wave height at the toe of the structure on one hand, and a systematic underestimation of the relative overtopping rate, by a factor of about 1.5, on the other hand.

7.2 Perspectives

7.2.1 Characterization of the sea-state

- The first series of experiments aimed at characterizing the generation and propagation of wind-waves in the presence of monochromatic and irregular swell. The downshift of the wind-wave peak-frequency observed due to the presence of irregular swell could be further investigated with a dedicated series of experiments. In a future series of experiments, the wind profile could be measured with a hot wire anemometer instead of a hot film anemometer to estimate the friction velocity using the eddy correlation method instead of the logarithmic profile method. The eddy correlation method permits to obtain a more accurate estimation of the friction velocity (according to Donelan et al. (1997), for instance) to perform a quantitative comparison between the observed downshift and the modification of the wind characteristics. Further analysis of the wind-wave downshift as a function of the swell steepness, peak frequency, and spectral width, for instance, would be interesting to further characterize the phenomenon.
- Simulations with a wave model were performed using state-of-the-art models regarding the wave dissipation and 4-wave interactions terms. Since Janssen (1991) wave generation source

term overestimates the friction velocity at the laboratory scale, recent developments regarding this source term might improve our simulations. Janssen and Bidlot (2021) suggest further including the effects of nonlinearity to improve Janssen (1991) source term. This recent development might improve the friction velocity calculation in the presence of waves characterized by a low wave age like a typical laboratory swell. Another recent development to improve the estimated friction velocity is based on the use of a wave boundary layer model, as in Du et al. (2017) for instance.

- A generic numerical domain was used to study wind-wave generation with different swell intensities at a coastal scale based on the performances of a 3G wave model. This study could be extended to more diverse configurations to further use the advantages of the numerical model to characterize bimodal sea-state conditions. These diverse conditions could be the following:
  - variable depth: the extension of GQM for intermediate depth and shallow water cases would be a requirement in these conditions.
  - effects of currents: Zhang et al. (2009) noticed that the presence of current can change the orientation of the wind stress, thus changing the directional properties of wind-waves.
  - a varying angle between swell and wind directions: Mitsuyasu and Yoshida (1991) observed an increase of the wind-wave height in the presence of an opposing swell in a wind-wave tunnel. It would be interesting to investigate the evolution of the downshift depicted in Chapter 3 as a function of the angle between the swell and the wind directions since such conditions cannot be modelled with a wind-wave tunnel.
- The SHOWEX campaign data used for the 3G wave model validation at coastal scale display rather gentle bimodal sea-state conditions. To further validate the wave model for the simulation of bimodal sea-states, more severe wave conditions, for instance during a hurricane in which several wave systems coexist, could be simulated with the ST4+GQM set.
- Beyramzadeh and Siadatmousavi (2022), who implemented the GQM method in WAVEWATCH III, performed simulations of hurricanes in the Gulf of Mexico and pointed out the necessity to better calibrate Q_{in} and Q_{ds} when using GQM, as they are currently calibrated to compensate for the shortcomings of the DIA method. This was also noticed in the present thesis with the hindcast of the SHOWEX campaign. A future study could include the simulation of the bimodal sea-states observations during the SHOWEX campaign combined with a hurricane hindcast to perform the required calibration.

7.2.2 Study of wave overtopping

- In Chapter 5, wave overtopping rates were measured in sea-state conditions combining swell and wind-waves. Since there are no wind-waves without wind, an important parameter to consider in a future series of experiments is the wind enhancement effect on overtopping discharge. Only a few series of experiments have been performed on the topic (e.g. de Rouck et al., 2005; de Waal et al., 1996; Pullen et al., 2009; Ward et al., 1996) resulting in the

definition of a multiplying factor function of the wave overtopping rate only to estimate the wave overtopping rate in the presence of wind. A future series of experiments could permit the investigation of the influence of wind speed and the breakwater shape (e.g. vertical wall, rubble mound) on the wave overtopping rate in windy conditions.

- As stated in the summary of conclusions, future experiments could be performed to validate the scaling developed subsequently to the second series of experiments with the breakwater. The main validation process would consist in testing different breakwater slopes α with and without a rock-armoured surface and assessing the performances of the new scaling in these conditions. A parameter $\tan\alpha$ could then be included in the scaling by using the Iribarren number (surf similarity parameter) instead of the representative steepness.

- During the series of experiments with the rock-armoured breakwater, observations showed that short wavelengths (wind-waves) tend to be more efficiently damped than long wavelengths (swell). These observations suggest that a parameter, such as a representative rock size characterizing the rock-armour type, might be required in the dimensional analysis performed in Chapter 5. To identify the relevant parameter, future experiments could consist in the study of the wave overtopping rate over a breakwater covered with different types of armour layers in sea-state conditions with variable peak periods. For instance, different types of armour layers could be tested: rocks with different layers configurations, Antifer cubes, tetrapodes, accropodes, etc.

- To validate new developments for the estimation of the wave overtopping rate, numerical models can permit to avoid or complement long and costly laboratory experiments. Although neptune_cfd showed promising performances to reproduce the results obtained with the physical model, it requires important computational resources resulting in rather long and costly simulations. Hence, the comparison of neptune_cfd with a simpler wave model (see Section 6.1), associated to a lower computational cost, on the present experimental dataset would be of interest.

- The use of the porosity method to design the numerical breakwater model with neputne_cfd paves the way for the design of a rock-armoured breakwater using the porosity method to reproduce the permeability, roughness and porosity properties within the numerical model. Such numerical simulations could be compared to our laboratory results with the rock-armoured breakwater described in Chapter 5.

Bibliography

Alday, M., Accensi, M., Ardhuin, F., and Dodet, G. A global wave parameter database for geophysical applications. Part 3: improved forcing and spectral resolution. *Ocean Modelling*, 166:101848, 2021.

Altomare, C., Gironella, X., and Crespo, A. J. Simulation of random wave overtopping by a WCSPH model. *Applied Ocean Research*, 116:102888, 2021. doi: https://doi.org/10.1016/j.apor.2021.102888.

Alves, J.-H. G. M. and Banner, M. Performance of a saturation-based dissipation-rate source term in modeling the fetch-limited evolution of wind waves. *Journal of Physical Oceanography*, 33: 1274–1298, 2003.

Ardhuin, F. Ocean waves in geosciences, 2021.

Ardhuin, F. and Orfila, A. *Wind waves*, chapter 14, pages 393 – 422. Florida State University Libraries, 2018. ISBN 9781720549970.

Ardhuin, F., Herbers, T., Jessen, P., and O'Reilly, W. Swell transformation across the continental shelf. Part ii: validation of a spectral energy balance equation. *Journal of Physical Oceanography*, 33:1940–1953, 2003a.

Ardhuin, F., Herbers, T., O'Reilly, W., and Jessen, P. Swell transformation across the continental shelf. Part i: attenuation and directional broadening. *Journal of Physical Oceanography*, 33:1921 – 1939, 2003b.

Ardhuin, F., Rogers, E., Babanin, A., Filipot, J.-F., Magne, R., Roland, A., Van Der Westhuysen, A. J., Queffeulou, P., Lefevre, J.-M., Aouf, L., and Collard, F. Semiempirical dissipation source functions for ocean waves. Part i: definition, calibration, and validation. *Journal of Physical Oceanography*, 40:1917 – 1941, 2010.

Ardhuin, F.and Herbers, T., van Vledder, G., Watts, K., Jensen, R., and Graber, H. Swell and slanting-fetch effects on wind wave growth. *Journal of Physical Oceanography*, 37:908 – 931, 2007.

Babanin, A. *Breaking and dissipation of ocean surface waves*. Cambridge University Press, 2011. doi: 10.1017/CBO9780511736162.

Bailey, T., Ross, L., Bryant, M., and Bryant, D. Predicting wind wave suppression on irregular long waves. *Journal of Marine Science and Engineering*, 8:619, 2020.

Barnett, T. P. and Sutherland, A. J. A note on an overshoot effect in wind-generated waves. *Journal of Geophysical Research*, 73(22):6879 – 6885, 1968.

Benetazzo, A., Cavaleri, L., Ma, H., Jiang, S., Bergamasco, F., Jiang, W., Chen, S., and Qiao, F. Analysis of the effect of fish oil on wind waves and implications for air-water interaction studies. *Ocean Science*, 15(3):725 – 743, 2019.

Benguigui, W., Doradoux, A., Lavieville, J., Mimouni, S., and Longatte, E. A discrete forcing method dedicated to moving bodies in two-phase flow. *International Journal for Numerical Methods in Fluids*, 88(7):315 – 333, 2018. doi: https://doi.org/10.1002/fld.4670.

Benoit, M. Evaluation of methods to compute the non-linear quadruplets interactions for deep-water wave spectra. In *Proceedings of the 5th International Symposium on Ocean Waves Measurement and Analysis (WAVES'2005), 3–7 July 2005, Madrid (ESP).*, number 52, page 10. American Society of Civil Engineering, 2005.

Benoit, M. Implementation and test of improved methods for evaluation of nonlinear quadruplet interactions in a third generation wave model. In *Proceedings of the 30th International Conference on Coastal Engineering (ICCE'2006), 3-8 September 2006, San Diego (CA, USA)*, pages 526 – 538, 2006.

Benoit, M., Marcos, F., and Becq, F. Development of a third generation shallow-water wave model with unstructured spatial meshing. In *Proceedings of the 25th International Conference on Coastal Engineering (ICCE'1996), Orlando (FL, USA)*, pages 465 – 478. American Society of Civil Engineers, 1996.

Benoit, M., Frigaard, P., and Schäffer, H. Analyzing multidirectional wave spectra: a tentative classification of available methods. In *Proceedings of the 1997 IAHR conference, San Francisco (CA, USA)*, pages 131 – 158, 1997.

Beyramzadeh, M. and Siadatmousavi, S. M. Skill assessment of different quadruplet wave-wave interaction formulations in the WAVEWATCH-III model with application to the Gulf of Mexico. *Applied Ocean Research*, 127:103316, 2022. doi: https://doi.org/10.1016/j.apor.2022.103316.

Bidlot, J., Janssen, P. A. E. M., and Abdalla, S. A revised formulation of ocean wave dissipation and its model impact. Technical report, ECMWF Tech. Rep. Memo. 509, Reading, United Kingdom, 27 pp., 2007.

Booij, N. and Holthuijsen, L. The effects of swell and wave steepness on wave growth and depth-induced wave breaking. In *Proceedings of the 7th International Workshop on Wave Forecasting and Hindcasting, Banff (CAN)*, 2002.

Booij, N., Ris, R. C., and Holthuijsen, L. H. A third-generation wave model for coastal regions: 1. Model description and validation. *Journal of Geophysical Research: Oceans*, 104(C4):7649 – 7666, 1999.

Booij, N., Holthuijsen, L. H., and Haagsma, I. J. The effect of swell on the generation and dissipation of wind sea. In *4th International Symposium on Ocean Wave Measurement and Analysis, San Francisco (USA)*, pages 501 – 506, 2001.

Bozorgnia, M., Eftekharian, A., and Lee, J. J. CFD modeling of a solitary wave overtopping breakwater of varying submergence. In *Proceedings of the 34th Conference on Coastal Engineering (ICCE'2014), Seoul (KOR)*, volume 1, page 7, 2014. doi: 10.9753/icce.v34.waves.7.

Bretherton, F. P., Garrett, C. J. R., and Lighthill, M. J. Wavetrains in inhomogeneous moving media. *Proceedings of the Royal Society of London. Series A. Mathematical and Physical Sciences*, 302(1471):529–554, 1968. doi: 10.1098/rspa.1968.0034.

Bretschneider, C. L. The generation and decay of wind waves in deep water. *Eos Trans. AGU*, 33 (3):381 – 389, 1952. doi: 10.1029/TR033i003p00381.

Cavaleri, L. The oceanographic tower acqua alta — activity and prediction of sea states at venice. *Coastal Engineering*, 39(1):29 – 70, 2000. doi: https://doi.org/10.1016/S0378-3839(99)00053-8.

Cavaleri, L. and Malanotte Rizzoli, P. Wind wave prediction in shallow water: theory and applications. *Journal of Geophysical Research: Oceans*, 86(C11):10961 – 10973, 1981.

Cavaleri, L., Alves, J.-H. G. M., Ardhuin, F., Babanin, A. V., Banner, M., Belibassakis, K. A., Benoit, M., Donelan, M. A., Groeneweg, J., Herbers, T. H. C., Hwang, P. A., Janssen, P. A. E. M., Janssen, T., Lavrenov, I. V., Magne, R., Monbaliu, J., Onorato, M., Polnikov, V., Resio, D., Rogers, W. E., Sheremet, A., McKee Smith, J., Tolman, H. L., van Vledder, G., Wolf, J., and Young, I. Wave modeling - the state of the art. *Progress In Oceanography*, 74:603 – 674, 2007.

Chen, G. and Belcher, S. E. Effects of long waves on wind-generated waves. *Journal of Physical Oceanography*, 30:2246 – 2256, 2000.

Chen, W., Warmink, J. J., van Gent, M. R. A., and Hulscher, S. J. M. H. Numerical modelling of wave overtopping at dikes using OpenFOAM®. *Coastal Engineering*, 166:103890, 2021. doi: https://doi.org/10.1016/j.coastaleng.2021.103890.

CIRIA. *The Rock Manual: The Use of Rock in Hydraulic Engineering, 2nd ed.* C683, CIRIA, London, 2007.

Coantic, M. and Bonmarin, P. The air-sea interaction simulation facility at the institut de mécanique statistique de la turbulence. *Atmospheric Technology*, 7:72 – 79, 1975.

Coantic, M. and Favre, A. Activities in, and preliminary results of, air–sea interactions research at I.M.S.T. *Advances in Geophysics*, 18:391 – 405, 1975.

Coantic, M., Ramamonjiarisoa, A., Mestayer, P., Resch, F., and Favre, A. Wind-water tunnel simulation of small-scale ocean-atmosphere interactions. *Journal of Geophysical Research*, 86: 6607 – 6626, 1981.

Coste, P. A large interface model for two-phase cfd. *Nuclear Eng Design*, 225:38 – 50, 2013.

Coste, P., Pouvreau, J., Morel, C., Lavieville, J., Boucker, M., and Martin, A. Modelling turbulence and friction around a large interface in a three-dimension two-velocity Eulerian code. In *Proceedings of the 12th International Topical Meeting on Nuclear Reactor Thermal Hydraulics (NURETH-12), Pittsburgh (USA), 30 Sept. - 4 Oct. 2007.*, 2007.

de Rouck, J., Geeraerts, J., Troch, P., Kortenhaus, A., Pullen, T., and Franco, L. New results on scale effects for wave overtopping at coastal structures, the CLASH programme. Technical Report TLJ700600, Ghent University, 2005.

de Waal, J. P., Tönjes, P., and van der Meer, J. W. Wave overtopping of vertical structures including wind effect. In *Proceedings of the 25th International Conference on Coastal Engineering (ICCE'1996), Orlando (FL, USA)*, pages 2216 – 2229, 1996. doi: 10.1061/9780784402429.172.

Donelan, M. A. The effect of swell on the growth of wind waves. In *Johns Hopkins APL Technical Digest*, volume 8, pages 18 – 23, 1987.

Donelan, M. A., Hamilton, J., and Hui, W. H. Directional spectra of wind-generated waves. *Philosophical Transactions of the Royal Society of London. Series A, Mathematical and Physical Sciences*, 315:509–562, 1985.

Donelan, M. A., Drennan, W. M., and Katsaros, K. The air-sea momentum flux in conditions of wind sea and swell. *Journal of Physical Oceanography*, 27:2087 – 2099, 1997.

Donelan, M. A., Haus, B. K., Plant, W. J., and Troianowski, O. Modulation of short wind waves by long waves. *Journal of Geophysical Research: Oceans*, 115:C10003, 2010.

Dorn, W. G. V. Boundary dissipation of oscillatory waves. *Journal of Fluid Mechanics*, 24(4):769 – 779, 1966.

Du, J., Bolaños, R., and Guo Larsén, X. The use of a wave boundary layer model in SWAN. *Journal of Geophysical Research: Oceans*, 122(1):42–62, 2017.

Esteban, G., Aristondo, A., Izquierdo, U., Blanco, J., and Pérez-Morán, G. Experimental analysis and numerical simulation of wave overtopping on a fixed vertical cylinder under regular waves. *Coastal Engineering*, 173:104097, 2022. doi: https://doi.org/10.1016/j.coastaleng.2022.104097.

Filipot, J.-F. and Ardhuin, F. A unified spectral parameterization for wave breaking: From the deep ocean to the surf zone. *Journal of Geophysical Research: Oceans*, 117(C00J08), 2012. doi: https://doi.org/10.1029/2011JC007784.

Frigaard, P., Helm-Petersen, J., Klopman, G., Stansberg, C. T., Benoit, M., Briggs, M. J., Miles, M., Santats, J. C., Schäffer, H. A., and Hawkes, P. J. IAHR list of sea-state parameters – An update for multidirectional waves. In *Proceedings of the IAHR Seminar on Multidirectional Waves and their Interactions with Structures, San-Francisco (CA, USA)*, pages 15 – 24, 1997.

Frostick, L. E., McLelland, S. J., and Mercer, T. G. *Users guide to physical modelling and experimentation: experience of the HYDRALAB network.* IAHR design manual. CRC press., 2011.

Gagnaire-Renou, E. *Progress in spectral wave modeling using a quasi-exact method for nonlinear wave-wave interactions.* PhD thesis, Université du Sud Toulon Var, 2009.

Gagnaire-Renou, E., Benoit, M., and Forget, P. Ocean wave spectrum properties as derived from quasi-exact computations of nonlinear wave-wave interactions. *Journal of Geophysical Research: Oceans*, 115:C12058, 2010.

Gelci, R., Cazalé, H., and Vassal, J. Prévision de la houle. la méthode des densités spectroangulaires. *Bull. Inform. Comité Central Océanogr. Etude Côtes*, 9:416 – 435, 1957.

Goda, Y. and Suzuki, T. Estimation of incident and reflected waves in random wave experiments. *Proceedings of the 15th International Conference on Coastal Engineering (ICCE'1976), Honolulu, Hawaii (USA)*, 1(15):47, 1976. doi: 10.9753/icce.v15.47.

Graber, H. C., Terray, E. A., Donelan, M. A., Drennan, W. M., Leer, J. C. V., and Peters, D. B. ASIS—A new Air–Sea Interaction Spar buoy: design and performance at sea. *Journal of Atmospheric and Oceanic Technology*, 17(5):708 – 720, 2000.

Grigorieva, V. G. and Badulin, S. I. Wind wave characteristics based on visual Observations and satellite altimetry. *Oceanology*, 56:19 – 24, 2016. doi: https://doi.org/10.1134/S0001437016010045.

Gruwez, V., Altomare, C., Suzuki, T., Streicher, M., Cappietti, L., Kortenhaus, A., and Troch, P. Validation of RANS Modelling for Wave Interactions with Sea Dikes on Shallow Foreshores Using a Large-Scale Experimental Dataset. *Journal of Marine Science and Engineering*, 8(9), 2020. doi: 10.3390/jmse8090650.

Guelfi, A., Bestion, D., Boucker, M., Boudier, M., Fillion, P., Grandotto, M., Hérard, J.-M., Hervieu, E., and Peturaud, P. NEPTUNE: A new software platform for advanced nuclear thermal hydraulics. *Nuclear Science Engineering*, 15(3):281 – 324, 2007.

Han, Z., Liu, Z., and Shi, H. Numerical study on overtopping performance of a multi-level breakwater for wave energy conversion. *Ocean Engineering*, 150:94 – 101, 2018. doi: https://doi.org/10.1016/j.oceaneng.2017.12.058.

Hasselmann, K. On the non-linear energy transfer in a gravity-wave spectrum. Part 1. General theory. *Journal of Fluid Mechanics*, 12(4):481 – 500, 1962.

Hasselmann, K. On the non-linear energy transfer in a gravity-wave spectrum. Part 3. Evaluation of the energy flux and swell-sea interaction for a Neumann spectrum. *Journal of Fluid Mechanics*, 15(3):385 – 398, 1963.

Hasselmann, K. On the spectral dissipation of ocean waves due to white capping. *Boundary-Layer Meteorology*, 6:107 – 127, 1974.

Hasselmann, K., Barnett, T. P., Bouws, E., Carlson, H., Cartwright, D. E., Enke, K., Ewing, J. A., Gienapp, H., Hasselmann, D. E., Kruseman, P., Meerburg, A., Muller, P., Olbers, D. J., Richter, K., Sell, W., and Walden, H. Measurements of wind-wave growth and swell decay during the Joint North Sea Wave Project (JONSWAP). *Deutches Hydrographisches Institut*, 8:1 – 95, 1973.

Hasselmann, S., Hasselmann, K., Allender, J. H., and Barnett, T. P. Computations and parameterizations of the nonlinear energy transfer in a gravity-wave specturm. Part ii: parameterizations of the nonlinear energy transfer for application in wave models. *Journal of Physical Oceanography*, 15(11):1378 – 1391, 1985.

Hauser, D., Tison, C., Amiot, T., Delaye, L., Corcoral, N., and Castillan, P. SWIM: The first spaceborne save scatterometer. *IEEE Transactions on Geoscience and Remote Sensing*, 55(5): 3000 – 3014, 2017. doi: 10.1109/TGRS.2017.2658672.

Hawkes, P. J. Mean overtopping rate in swell and bimodal seas. *Proceedings of the Institution of Civil Engineers - Water, Maritime and Energy*, 136(4):235 – 238, 1999. doi: 10.1680/iwtme.1999.31987.

Hedges, T. S. and Reis, M. T. Random wave overtopping of simple sea walls: a new regression model. *Proceedings of the Institution of Civil Engineers - Water, Maritime and Energy*, 130(1): 1 – 10, 1998. doi: 10.1680/iwtme.1998.30223.

Hedges, T. S. and Shareef, M. Predicting seawall overtopping by bimodal seas. In *Proceedings of the 28th International Conference on Coastal Engineering (ICCE'2002), Cardiff (Wales, UK)*, pages 2153 – 2164. World Scientific, 2002. doi: 10.1142/9789812791306_0181.

Holthuijsen, L. H. *Waves in oceanic and coastal waters*. Cambridge University Press, 2007. doi: 10.1017/cbo9780511618536.

Holthuijsen, L. H., Ris, R. C., Booij, N., and Cecchi, E. Swell and whitecapping - a numerical experiment. In *Proceedings of the 27th International Conference on Coastal Engineering (ICCE'2000), Sydney (AUS)*, pages 346 – 354. ASCE, 2000a.

Holthuijsen, L. H., Ris, R. C., Booij, N., and Cecchi, E. Swell and whitecapping - a numerical experiment. In *Proceedings of the 27th International Conference on Coastal Engineering (ICCE'2000), Sydney (AUS)*, pages 346–354. ASCE, 2000b.

Hu, K., Mingham, C., and Causon, D. Numerical simulation of wave overtopping of coastal structures using the non-linear shallow water equations. *Coastal Engineering*, 41(4):433 – 465, 2000. doi: https://doi.org/10.1016/S0378-3839(00)00040-5.

Hwang, P. A., García-Nava, H., and Ocampo-Torres, F. J. Observations of wind wave development in mixed seas and unsteady wind forcing. *Journal of Physical Oceanography*, 41:2343 – 2362, 2011.

Ishii, M. Thermo-fluid dynamic theory of two-phase flow. *NASA Sti/recon Technical Report A*, 75:29657, 1975.

Janssen, P. A. E. M. Quasi-linear theory of wind-wave generation applied to wave forecasting. *Journal of Physical Oceanography*, 21:1631 – 1642, 1991.

Janssen, P. A. E. M. *The interaction of ocean waves and wind*. Cambridge University Press, 2004.

Janssen, P. A. E. M. and Bidlot, J.-R. On the consequences of nonlinearity and gravity-capillary waves on wind-wave interaction. Technical report, ECMWF Tech. Rep. Memo. 882, Reading, United Kingdom, 40 pp., 2021.

Jasak, H., Jemcov, A., Tukovic, Z., et al. OpenFOAM: A C++ library for complex physics simulations. In *International workshop on coupled methods in numerical dynamics*, volume 1000, pages 1 – 20, 2007.

Kahma, K. K. and Calkoen, C. J. Reconciling discrepancies in the observed growth of wind-generated waves. *Journal of Physical Oceanography*, 22(12):1389 – 1405, 1992.

Kashima, H., Hirayama, K., and Hasegawa, I. Experimental study on wave overtopping rate of long period swell on seawall. *Journal of Japan Society of Civil Engineers, Serie B2*, 66(1):716 – 720, 2010. doi: 10.2208/kaigan.66.716.

Kawai, S., Okada, K., and Toba, Y. Field data support of three-seconds power law and $gu * \sigma^{-4}$-spectral form for growing wind waves. *Journal of the Oceanographical Society of Japan*, 33:137 – 150, 1977.

Kimmoun, O. and Branger, H. A Particle Image Velocimetry investigation on laboratory surf-zone breaking waves over a sloping beach. *Journal of Fluid Mechanics*, 588:353–397, 2007.

Kirby, J. T., Wei, G., Chen, Q., Kennedy, A. B., and Dalrymple, R. A. FUNWAVE 1.0: fully non-linear Boussinesq wave model-Documentation and user's manual. *Research report NO. CACR-98-06*, 1998.

Kitaigorodskii, S. Application of the theory of similarity to the analysis of wind generated wave motion as a stochastic process. *Izv. Akad. Nauk SSSR, Ser. Geofiz.*, 1:105 – 117, 1961.

Komen, G. J., Hasselmann, S., and Hasselmann, K. On the existence of a fully developed wind-sea spectrum. *Journal of Physical Oceanography*, 14:1271 – 1285, 1984.

Komen, G. J., Cavaleri, L., Donelan, M. A., Hasselmann, K., Hasselmann, S., and Janssen, P. A. E. M. *Dynamics and modelling of ocean waves*. Cambridge University Press, 1994.

Lashley, C. H., Zanuttigh, B., Bricker, J. D., van der Meer, J., Altomare, C., Suzuki, T., Roeber, V., and Oosterlo, P. Benchmarking of numerical models for wave overtopping at dikes with shallow mildly sloping foreshores: Accuracy versus speed. *Environmental Modelling & Software*, 130:104740, 2020. doi: https://doi.org/10.1016/j.envsoft.2020.104740.

Lavieville, J. and Coste, P. Numerical modeling of liquid-gas stratified flows using two-phase eulerian approach. In *Proceedings of the 5th International Symposium on Finite Volumes for Complex Applications, Aussois, France*, pages 8 – 13, 2008.

Lavrenov, I. *Wind-waves in oceans: dynamics and numerical simulations*. Springer, 2003.

Lavrenov, I. V. Effect of wind wave parameter fluctuation on the nonlinear spectrum evolution. *Journal of Physical Oceanography*, 31(4):861 – 873, 2001.

Le Merle, E. *Étude des propriétés physiques des vagues océaniques à partir d'observations par radar aéroporté à ouverture réelle*. PhD thesis, Physique Atmosphérique et Océanique, Université Paris Saclay (COmUE), 2019.

Longuet-Higgins, M. S. Mass transport in water waves. *Philosophical Transactions of the Royal Society A.*, 245(903):535 – 581, 1956.

Mackay, E. Modelling and description of omnidirectional wave spectra. In *European Wave & Tidal Energy Conference EWTEC 2011*. University of Southampton, UK, 2011.

Marean, C. W., Bar-Matthews, M., Bernatchez, J., Fisher, E., Goldberg, P., Herries, A. I. R., Jacobs, Z., Jerardino, A., Karkanas, P., Minichillo, T., Nilssen, P. J., Thompson, E., Watts, I., and Williams, H. M. Early human use of marine resources and pigment in South Africa during the Middle Pleistocene. *Nature*, 449(7164):905 – 908, 2007. doi: 10.1038/nature06204.

Mason, T., Bradbury, A., Poate, T., and Newman, R. Nearshore wave climate of the English Channel evidence for bimodal seas. In *Proceedings of the 31st International Conference on Coastal Engineering (ICCE'2008), Hamburg (DEU)*, pages 605 – 616. World Scientific, 2008. doi: 10.1142/9789814277426_0051.

Masson, D. On the nonlinear coupling between swell and wind waves. *Journal of Physical Oceanography*, 23:1249 – 1258, 1993.

Miles, J. W. On the generation of surface waves by shear flows. *Journal of Fluid Mechanics*, 3:185 – 204, 1957.

Mitsuyasu, H. Interactions between water waves and wind (1). *Rep. Inst. Appl. Mech. Kyushu Univ.*, 14:67 – 88, 1966.

Mitsuyasu, H. and Rikiishi, K. The growth of duration-limited wind waves. *Journal of Fluid Mechanics*, 85(4):705 – 730, 1978.

Mitsuyasu, H. and Yoshida, Y. The effect of swell on the growth of wind waves. *Elsevier Oceanography Series*, 54:381 – 392, 1991.

Mittal, R. and Iaccarino, G. Immersed boundary methods. *Annual Review of Fluid Mechanics*, 37 (1):239 – 261, 2005. doi: 10.1146/annurev.fluid.37.061903.175743.

Monin, A. S. and Obukhov, A. M. Basic laws of turbulent mixing in the surface layer of the atmosphere. *Tr. Akad. Nauk SSSR Geophiz. Inst.*, 24:163 – 187, 1954.

Montagne, R. Le service de prédiction de la houle au maroc. *Annales Hydrographiques*, pages 157 – 186, 1922.

Musa, M. A., Maliki, A. Y., Ahmad, M. F., Sani, W. N., Yaakob, O., and Samo, K. Numerical simulation of wave flow over the overtopping breakwater for energy conversion (obrec) device. In *Procedia Engineering, 10th International Conference on Marine Technology (MARTEC'2016), Dhaka (BGD)*, volume 194, pages 166 – 173, 2017. doi: https://doi.org/10.1016/j.proeng.2017.08.131.

Orimoloye, S., Horrillo-Caraballo, J., Karunarathna, H., and Reeve, D. E. Wave overtopping of smooth impermeable seawalls under unidirectional bimodal sea conditions. *Coastal Engineering*, 165:103792, 2021.

Owen, M. Design of seawalls allowing for wave overtopping. Technical report, EX924 HR Wallingford, UK, 1980.

Perić, R. and Abdel-Maksoud, M. Analytical prediction of reflection coefficients for wave absorbing layers in flow simulations of regular free-surface waves. *Ocean Engineering*, 147:132 – 147, 2018. doi: https://doi.org/10.1016/j.oceaneng.2017.10.009.

Peskin, C. Flow patterns around heart valves: a numerical method. *Journal of Computational Physics*, 10(2):252 – 271, 1972. doi: https://doi.org/10.1016/0021-9991(72)90065-4.

Pettersson, H., Kahma, K. K., and Tuomi, L. Wave directions in a narrow bay. *Journal of Physical Oceanography*, 40(1):155 – 169, 2010.

Phillips, O. M. On the generation of waves by turbulent wind. *J. Fluid Mech*, 2:417 – 445, 1957.

Phillips, O. M. The equilibrium range in the spectrum of wind-generated waves. *Journal of Fluid Mechanics*, 4(4):426 – 434, 1958. doi: 10.1017/S0022112058000550.

Phillips, O. M. and Banner, M. L. Wave breaking in the presence of wind drift and swell. *Journal of Fluid Mechanics*, 66:625 – 640, 1974.

Pierson, W. J.; Neuman, G. and James, R. W. *Practical methods for observing and forecasting ocean waves by means of wave spectra and statistics.* H.O Pub;603. U.S. Naval Hydrographic Office, Washington, DC, 1955.

Pierson, W. J. and Moskowitz, L. A. Proposed spectral form for fully developed wind seas based on the similarity theory of s. a. kitaigorodskii. *Journal of Geophysical Research*, 69:5181 – 5190, 1964.

Pullen, T., Allsop, N. W. H., Bruce, T., Kortenhaus, A., Schüttrumpf, H., and Van der Meer, J. W. *EurOtop wave overtopping of sea defences and related structures: assessment manual.* Boyens Medien GmbH, 2007.

Pullen, T., Allsop, N. W. H., Bruce, T., and Pearson, J. Field and laboratory measurements of mean overtopping discharges and spatial distributions at vertical seawalls. *Coastal Engineering*, 56(2):121 – 140, 2009. doi: https://doi.org/10.1016/j.coastaleng.2008.03.011.

Reul, N., Branger, H., and Giovanangeli, J. P. Air-flow structure over short-gravity breaking water waves. *Boundary Layer Meteorology*, 126(3):477 – 505, 2008.

Roeber, V. and Cheung, K. BOSZ (Boussinesq ocean and surf zone model). In *Proceedings of the 2011 NTHMP Model Benchmarking Workshop. NOAA*, 2012.

Roelvink, D. and Costas, S. Coupling nearshore and aeolian processes: XBeach and duna process-based models. *Environmental Modelling & Software*, 115:98–112, 2019. doi: https://doi.org/10.1016/j.envsoft.2019.02.010.

Romero, L. Distribution of surface wave breaking fronts. *Geophysical Research Letters*, 46(17 - 18):10463 – 10474, 2019. doi: https://doi.org/10.1029/2019GL083408.

Shabani, B., Ware, P., and Baldock, T. E. Suppression of wind waves in the presence of swell: a physical modeling study. *Journal of Geophysical Research: Oceans*, 127(5):e2021JC018306, 2022. doi: https://doi.org/10.1029/2021JC018306.

Shemer, L. On evolution of young wind waves in time and space. *Atmosphere*, 10(9):562, 2019.

Smit, P. B., Stelling, G. S., Roelvink, D., van Thiel de Vries, J., McCall, R., van Dongeren, A., Zwinkels, C., and Jacobs, R. XBeach: Non-hydrostatic model: Validation, verification and model description. *Delft University of Technology and Deltares*, 2010.

Snyder., R. L., Dobson, F. W., and Elliot, J. A. Array measurements of atmospheric pressure fluctuations above surface gravity waves. *Journal of Fluid Mechanics*, 102:1 – 59, 1981.

Suzuki, T., Altomare, C., Veale, W., Verwaest, T., Trouw, K., Troch, P., and Zijlema, M. Efficient and robust wave overtopping estimation for impermeable coastal structures in shallow foreshores using SWASH. *Coastal Engineering*, 122:108 – 123, 2017. doi: https://doi.org/10.1016/j.coastaleng.2017.01.009.

Sverdrup, H. U. and Munk, W. H. Wind sea and swell: Theory of relations for forecasting. *H.O. Pub. 601, US Navy Hydrographic Office, Washington, DC*, page 44, 1947.

Sverdrup, H. V. and Munk, W. H. Breakers and surf: Principles in forecasting. Technical report, Hydrogrphic Office, U.S. Navy, Publ. No. 235., 1944a.

Sverdrup, H. V. and Munk, W. H. Wind waves and swell: Principles in forecasting. Technical report, Hydrogrphic Office, U.S. Navy, Misc. 11, 215., 1944b.

TAW. Wave run-up and wave overtopping at dikes. Technical report, Technical Advisory Committee on Flood Defence, Delft, The Netherlands, 2002.

The WAVEWATCH III (R) Development Group (WW3DG). User manual and system documentation of wavewatch iii (r) version 6.07. Technical report, Tech. Note 333, NOAA/NWS/NCEP/MMAB, College Park, MD, USA, 465 pp + Appendices., 2019.

Thompson, D. A., Karunarathna, H., and Reeve, D. E. An analysis of swell and bimodality around the south and south-west coastline of England. *Natural Hazards and Earth System Sciences Discussions*, [preprint]:1 – 28, 2018. doi: 10.5194/nhess-2018-117.

Toba, Y. Local balance in the air-sea boundary processes. iii on the spectrum of wind waves. *Journal of the Oceanographical Society of Japan*, 29:209 – 220, 1973.

Toba, Y. The 3/2-power law for ocean wind waves and its applications. In *Advances in coastal and ocean engineering*, volume 3, pages 31 – 65. World Scientific, 1997.

Tolman, H. and Chalikov, D. Source terms in a third-generation wind wave model. *Journal of Physical Oceanography*, 26:2497 – 2518, 11 1996. doi: 10.1175/1520-0485(1996)026⟨2497:STIATG⟩2.0.CO;2.

Tolman, H. L. Distributed memory concepts in the wave model WAVEWATCH III. *Parallel Computing*, 28:35 – 52, 2002.

TOMAWAC User manual. Version v8p3. TELEMAC-MASCARET Modelling System. www.opentelemac.org, 2022.

Van der Meer, J. W. and Janssen, J. Wave run-up and wave overtopping at dikes. In *Wave Forces on Inclined and Vertical Wall Structures. ASCE. Chap. 1*, pages 1 – 27. Ed. N. Kobayashi and Z. Demirbilek., 1995.

Van der Meer, J. W., Allsop, N. W. H., Bruce, T., De Rouck, J., Kortenhaus, A., Pullen, T., Schüttrumpf, H., Troch, P., and Zanuttigh, B. *EurOtop: Manual on wave overtopping of sea defences and related sturctures - An overtopping manual largely based on European research, but for worlwide application (2nd edition)*. EurOtop Manual, 2018.

Van der Werf, I. M. and Van Gent, M. R. A. Wave overtopping over coastal structures with oblique wind and swell waves. *Journal of Marine Science and Engineering*, 6(4):149, 2018. doi: 10.3390/jmse6040149.

van der Westhuysen, A. *Advances in the spectral modelling of wind waves in the nearshore*. PhD thesis, Delft University of Technology, Delft, The Netherlands, 2007.

van der Westhuysen, A. J., Zijlema, M., and Battjes, J. A. Nonlinear saturation-based whitecapping dissipation in SWAN for deep and shallow water. *Coastal Engineering*, 54(2):151 – 170, 2007. doi: https://doi.org/10.1016/j.coastaleng.2006.08.006.

Van Gent, M. R. A. Wave run-up on dikes with shallow foreshores. In *Proceedings of the 27th International Conference on Coastal Engineering (ICCE'2000), Sydney (AUS)*, volume 3, pages 2030 – 2043. American Society of Civil Engineering, 2000.

Vaschy, A. Sur les considérations d'homogénéité en physique. (in french). *Réponse à une note de M. Clavenad, comptes rendus des séances de l'Académie des Sciences*, 115:597–599, 1892. (in french).

Victor, L., Van der Meer, J. W., and Troch, P. Probability distribution of individual wave overtopping volumes for smooth impermeable steep slopes with low crest freeboards. *Coastal Engineering*, 64:87 – 101, 2012.

Villefer, A., Benoit, M., Violeau, D., Luneau, C., and Branger, H. Influence of following, regular, and irregular long waves on wind-wave growth with fetch: an experimental study. *Journal of Physical Oceanography*, 51(11):3435 – 3448, 2021.

Vincent, C. L., Thomson, J., Graber, H. C., and Collins III, C. O. Impact of swell on the wind-sea and resulting modulation of stress. *Progress in Oceanography*, 178:102164, 2019.

WAMDI Group. The WAM Model—A Third Generation Ocean Wave Prediction Model. *Journal of Physical Oceanography*, 18:1775 – 1810, 1988.

Ward, D. L., Zhang, J., Wibner, C. G., and Cinotto, C. M. Wind effects on runup and overtopping of coastal structures. In *Proceedings of the 25th International Conference on Coastal Engineering (ICCE'1996), Orlando (FL, USA)*, pages 2206 – 2215, 1996. doi: 10.1061/9780784402429.171.

Welch, P. The use of fast fourier transform for the estimation of power spectra: a method based on time averaging over short, modified periodograms. *IEEE Transactions on Audio and Electroacoustics*, 15(2):70–73, 1967.

Wright, J. W. The wind drift and wave breaking. *Journal of Physical Oceanography*, 6:402 – 405, 1976.

Young, I. and Babanin, A. *Ocean Wave Dynamics*. World Scientific, 2020. doi: 10.1142/11509.

Zakharov, V., Badulin, S., Hwang, P., and Caulliez, G. Universality of sea wave growth and its physical roots. *Journal of Fluid Mechanics*, 780:503 – 535, 2015.

Zakharov, V. E. Stability of periodic waves of finite amplitude on the surface of a deep fluid. *Journal of Applied Mechanics and Technical Physics*, 9:190 – 194, 1968.

Zelt, J. A. and Skjelbreia, J. E. Estimating incident and reflected wave fields using an arbitrary number of wave gauges. *Proceedings of 23rd International Conference on Coastal Engineering (ICCE'1992), Venice (ITA)*, 1(23):777 – 789, 1992. doi: 10.1061/9780872629332.058.

Zhang, F. W., Drennan, W. M., Haus, B. K., and Graber, H. C. On wind-wave-current interactions during the shoaling waves experiment. *Journal of Geophysical Research: Oceans*, 114:C1018, 2009.